LEABHARLANN CHOLÁISTE NA TRÍONÓIDE, BAILE ÁTHA CLIATH
Ollscoil Átha Cliath

TRINITY COLLEGE LIBRARY DUBLIN
The University of Dublin

Terms and Conditions of Use of Digitised Theses from Trinity College Library Dublin

Copyright statement

All material supplied by Trinity College Library is protected by copyright (under the Copyright and Related Rights Act, 2000 as amended) and other relevant Intellectual Property Rights. By accessing and using a Digitised Thesis from Trinity College Library you acknowledge that all Intellectual Property Rights in any Works supplied are the sole and exclusive property of the copyright and/or other IPR holder. Specific copyright holders may not be explicitly identified. Use of materials from other sources within a thesis should not be construed as a claim over them.

A non-exclusive, non-transferable licence is hereby granted to those using or reproducing, in whole or in part, the material for valid purposes, providing the copyright owners are acknowledged using the normal conventions. Where specific permission to use material is required, this is identified and such permission must be sought from the copyright holder or agency cited.

Liability statement

By using a Digitised Thesis, I accept that Trinity College Dublin bears no legal responsibility for the accuracy, legality or comprehensiveness of materials contained within the thesis, and that Trinity College Dublin accepts no liability for indirect, consequential, or incidental, damages or losses arising from use of the thesis for whatever reason. Information located in a thesis may be subject to specific use constraints, details of which may not be explicitly described. It is the responsibility of potential and actual users to be aware of such constraints and to abide by them. By making use of material from a digitised thesis, you accept these copyright and disclaimer provisions. Where it is brought to the attention of Trinity College Library that there may be a breach of copyright or other restraint, it is the policy to withdraw or take down access to a thesis while the issue is being resolved.

Access Agreement

By using a Digitised Thesis from Trinity College Library you are bound by the following Terms & Conditions. Please read them carefully.

I have read and I understand the following statement: All material supplied via a Digitised Thesis from Trinity College Library is protected by copyright and other intellectual property rights, and duplication or sale of all or part of any of a thesis is not permitted, except that material may be duplicated by you for your research use or for educational purposes in electronic or print form providing the copyright owners are acknowledged using the normal conventions. You must obtain permission for any other use. Electronic or print copies may not be offered, whether for sale or otherwise to anyone. This copy has been supplied on the understanding that it is copyright material and that no quotation from the thesis may be published without proper acknowledgement.

LIQUID PHASE EXFOLIATION AND DISPERSION OF TWO DIMENSIONAL MATERIALS

Rónán Smith

A thesis submitted for the degree of
Doctor of Philosophy

Supervised by Prof. Jonathan Coleman
Chemical Physics of Low Dimensional Nanostructures Group
School of Physics
Trinity College Dublin

2014

To my sister Aoife,

for paving the way.

DECLARATION

I declare that this thesis has not been submitted as an exercise for a degree at this or any other university and it is entirely my own work.

I agree to deposit this thesis in the University's open access institutional repository or allow the library to do so on my behalf, subject to Irish Copyright Legislation and Trinity College Library conditions of use and acknowledgement.

Elements of this work that have been carried out jointly with others or by collaborators have been duly acknowledged in the text wherever included.

Rónán Smith

Rónán Smith

ABSTRACT

Over the last few years, it has become clear that due to their high surface area and novel properties, two dimensional materials will be extremely useful both for fundamental studies and for a range of applications. Previous work has shown that graphene can be produced in large quantities by exfoliation of graphite in certain solvents or surfactants. Of these methods, surfactant dispersion is perhaps the most promising because the use of toxic solvents is avoided. Although previous work has shown that such methods give reasonably large quantities of good-quality graphene, there is still much scope for improvement as well as further investigation.

To improve the concentration and quality of surfactant-stabilized nanosheet dispersions, it is critical to gain an understanding of the stabilization process. Such an understanding will aid surfactant choice and process optimization, resulting in better dispersions. To that end, this work studies the dispersibility of graphene in a range of surfactants. The effect of surfactant choice on exfoliation state is investigated by TEM analysis of the dispersed material showing little difference between dispersions. Most importantly, a relationship between surfactant choice and dispersed concentration has been established. It appears that for ionic surfactants, the concentration is largely controlled by the zeta potential of the surfactant-coated graphene sheet scaling linearly with the repulsive electrostatic potential barrier. Similarly, for non-ionic surfactants, the concentration scales linearly with a repulsive potential barrier that has steric origins.

Control over the dimensions of the material produced will be critical for many future applications of liquid phase exfoliations. The flakes produced have a significant spread in both lateral flake size and number of layers that has so far proved difficult to control through adjustment of processing conditions. In this work, size selection column chromatography has been used to separate a typical aqueous graphene dispersion into several fractions according to their average lateral flake size. The separation has been confirmed by means of TEM analysis and Raman spectroscopy. Effectively, this process has allowed for a 100% increase in the average flake size of a graphene dispersion through the removal of smaller flakes.

In addition to graphite, a wide range of inorganic layered compounds exist such as transition metal dichalcogenides and oxides. These materials span a range of electronic and physical properties making them exciting materials for study. This research extends existing liquid phase processing techniques to include inorganic layered materials. The dispersions are characterised using electron and optical microscopy techniques. The effect of varying processing parameters is investigated for surfactant stabilised MoS_2 and MnO_2 showing good control over dispersed concentration and temporal stability.

Liquid phase exfoliation allows dispersions to be cast into thin films using vacuum filtration. The addition of nanotubes to MoS_2 films is shown to increase the conductivity over six orders of magnitude. These hybrid films have a show improved power factor for thermoelectric devices as well as having good columbic efficiency and cyclability when tested as a cathode material for Li-Ion batteries. Finally the electrochemical response of MnO_2 thin films and hybrids is also tested.

"It isn't all over; everything has not been invented; the human adventure is just beginning."
(Gene Roddenberry)

ACKNOWLEDGEMENTS

First and foremost I would like to thank Professor Jonathan Coleman for giving me the opportunity to further my scientific education. None of this work would have been possible without his support, insight and infectious enthusiasm. I'm very grateful to him for the time I spent here in the group.

Over the years in trinity I have been fortunate enough to work with some truly excellent scientists as well as people and chief among them is Dr. Niall McEvoy (honorary contrarian to the Coleman group). From my first day his mix of cynicism and good nature has kept me on the straight and narrow. We are a collaborative bunch and I have been helped in some way by all the Coleman group members (Damien, Umar, Arlene, Sophie, Graeme, Rickard, Phil, Keith, Eswar, Evelyn, Fiona, Karen and Marguerite) but would especially like to thank Dr. Paul King and Dr. Mustafa Lotya for their help and supervision and Dr. Peter May for all the kind words. In my final year I have had the pleasure of collaborating with Dr. Claudia Backes and Tom Higgins and hope to do so for many years to come. I wish the best of luck to the new crop of Sebastian, Conor, David and Andrew. I would also like to thank all the Blau, Duesberg and MI members for their support, particularly Denise, Darren, Paula, Trevor, Eddie and Anna for helping me settle in.

The technical and admin staff in the school of physics have been really helpful from day one, Robbie, Pa, Sam and Ciara, I'll miss you now they have moved me to CRANN. The folks down in the CMA will be sick of the sight of me after the many hours of microscopy they have had to endure so special thanks to Neal, Heath and Amanda for their patience. All the football over the years has kept me sane in the sometimes cruel world of postgraduate research so thanks to all the lads who took part especially Rob and Ronan for organising a lot of games.

Outside of research I have had a tremendous amount of support from some wonderful friends. Anna, thanks for all the notes and words of encouragement, James and Shane for all the late night debates and Eithne for all the wonderful years to look back on and forward to. Finally I would like to thank my brothers and sisters, to whom I sincerely owe any success I may enjoy and Gill with whom I hope to share

PUBLICATIONS

Aspects of the work presented in this thesis have appeared previously in the following publications. Publications containing major contributions from material in this thesis are marked with *.

1. Backes, C., Smith, R.J., McEvoy, N., Berner, N.C., Nerl, H.C., O'Neill, A., King, P.J., Higgins, T., Hanlon, D., Scheuschner, N., Maultzsch, J., Duesberg, G.S., Nicolosi1, V., Coleman, J.N. Using Edge and Confinement Effects for in situ Determination of Size and Thickness of Liquid Exfoliated Nanosheets. (Under Review) Nature Communications. *
2. Paton, K.R., Varrla, E., Backes, C., Smith1, R.J., Khan, U., O'Neill, A., Boland, M., Lotya, M., Istrate, O., King, P.J., Higgins, T., Barwich, S., May, P., Puczkarski , P., Ahmed, I., Moebius, Pettersson, H., Long, E., Coelho, J., O'Brien, S.E., McGuire, E.K., Sanchez, B.M., Duesberg, G.S.,McEvoy, N., Pennycook, T.J., Downing, C., Crossley, A., Nicolosi, V., Coleman, J.N. Scalable production of large quantities of defect-free, few-layer graphene by shear exfoliation in liquids. Nature Materials, 2014
3. Finn, D.J., Lotya, M., Cunningham, G., Smith, R.J., McCloskey, D., Donegan, J.F., Coleman, J.N. Inkjet deposition of liquid-exfoliated graphene and MoS_2 nanosheets for printed device applications. Journal of Materials Chemistry C 2014
4. Fahimi, A., Jurewicz, I., Smith, R.J., Sharrock, C.S., Bradley, D.A., Henley, S.J., Coleman, J.N., Dalton, A.B. Density controlled conductivity of pristine graphene films. Carbon 2013, 54, 435-443
5. Smith, R.J., King, P.J., Wirtz, C., Duesberg, G.S., Coleman, J.N. Lateral size selection of surfactant-stabilised graphene flakes using size exclusion chromatography. Chemical Physics Letters, 2012, 531, 169-172. *
6. Smith, R.J., King, P.J., Lotya, M., Wirtz, C., Khan, U., De, S., O'Neill, A., Duesberg, G.S., Grunlan, J.C., Moriarty, G., Chen, J., Wang, J., Minett, A.I., Nicolosi, V., Coleman, J.N. Large-scale exfoliation of inorganic layered compounds in aqueous surfactant solutions. Advanced Materials 2011, 23, 3944-3948. *

7. Coleman, J.N., Lotya, M., O'Neill, A., Bergin, S.D., King, P.J., Khan, U., Young, K., Gaucher, A., De, S., Smith, R.J., Shvets, I.V., Arora, S.K., Stanton, G., Kim, H.-Y., Lee, K., Kim, G.T., Duesberg, G.S., Hallam, T., Boland, J.J., Wang, J.J., Donegan, J.F., Grunlan, J.C., Moriarty, G., Shmeliov, A., Nicholls, R.J., Perkins, J.M., Grieveson, E.M., Theuwissen, K., McComb, D.W., Nellist, P.D., Nicolosi, V. Two-dimensional nanosheets produced by liquid exfoliation of layered materials. Science, 2011, 331, 568-571.

8. Smith, R.J., Lotya, M., Coleman, J.N. The importance of repulsive potential barriers for the dispersion of graphene using surfactants. New Journal of Physics, 2010, 12. *

9. Lotya, M., Hernandez, Y., King, P.J., Smith, R.J., Nicolosi, V., Karlsson, L.S., Blighe, F.M., De, S., Zhiming, W., McGovern, I.T., Duesberg, G.S., Coleman, J.N. Liquid phase production of graphene by exfoliation of graphite in surfactant/water solutions. Journal of the American Chemical Society, 2009, 131, 3611-3620.

CONTENTS

LIST OF FIGURES

LIST OF ACRONYMS

AFM: Atomic Force Microscopy

BNNR: Boron Nitride Nano-Ribbon

CF: Centrifugation

CHP: Cyclohexylpyrrolidone

CMC: Critical Micelle Concentration

CNT: Carbon Nanotube

CPG: Controlled Pore Glass

CPO: Cyclopentanone

CTAB: Cetyltrimethyl Ammoniumbromide

CVD: Chemical Vapour Deposition

DLVO: Derjaguin–Landau–Verwey–Overbeek

DMA: N,N-dimethylacetamide

DOC: Sodium Deoxycholate

GNR: Graphene Nano-Ribbon

GO: Graphene Oxide

h-BN: Hexagonal Boron Nitride

HOPG: Highly Ordered Pyrolytic Graphene

HRTEM: High Resolution Transmission Electron Microscopy

ITO: Indium Tin Oxide

LDS: Lithium Dodecyl Sulfate

MWNT: Multi-Walled Carbon Nanotube

NIR: Near Infrared

NMP: N-methyl-2-pyrrolidone

PET: Polyethylene Terephthalate

PMMA: Polymethyl Methacrylate

rGO: Reduced Graphene Oxide

SC: Sodium Cholate

SDBS: Dodecylbenzenesulfonic acid

SDS: SodiumDodecylsulfate

SEM: Scanning Electron Microscopy

STEM: Scanning Transition Electron Microscopy

SWNT : Single Walled Carbon Nanotube

TDOC Sodium Taurodeoxycholate

TEM: Transmission Electron Microscopy

TGA: Thermogravimetric Analysis

TMD: Tranisition Metal Dichalcogenide

TMO: Transition Metal Oxide

TTAB: Tetradecyltrimethylammonium Bromide

UV: Ultra Violet

vdW: van der Waals

XPS: X-ray Photoelectron Spectroscopy

1

MOTIVATION AND THESIS OUTLINE

Throughout history, technological progress has always been limited by the materials available. The level of control over the physical properties of a material is the determining factor for the range of its application. Properties such as thermal & electrical conductivity as well as elasticity and transparency are extremely important for many modern applications and careful regulation of these often requires manipulation on the smallest of scales. It is this need for greater control that has spawned such intense research into nanoscience. This field can in itself be considered a bottom-up approach to understanding and shaping the world around us by manipulating materials at a fundamental level.

In the 50 years since Richard Feynman gave his famous "there is plenty of room at the bottom" speech, nanoscience has become an enormous field encompassing physics, chemistry, biology and engineering. All of these disciplines seek to exploit nanoscale effects or structures to address current and future needs with some of the world's biggest problems having possibly the smallest of solutions. Over the past 30 years there have been several breakthroughs in the study of nanostructured materials beginning with the discovery of zero-dimensional Fullerenes in 1985 [1]. This was quickly followed by the discovery of one-dimensional nanotubes [2] and eventually two-dimensional nanosheets [3]. With these new structures came new physics and hence a new frontier for possible applications. Two dimensional materials in particular have been proposed for use in polymer reinforcement, high performance electronics, gas sensing, solar cells, supercapacitors, batteries, fuel cells and hydrogen evolution.

The main aim of this thesis is the large scale production of two-dimensional materials. This is explored using liquid phase techniques to produce dispersions of nanosheets stabilised by a surfactant coating. While this process has already been established for Graphene, this work extends this method to produce dispersions of layered inorganic materials such as transition metal dichalcogenides and oxides. Control over the quality as well as quantity of material produced will be key to any future applications. This work attempts to gain insight into the mechanisms for dispersion of these materials by careful control over the parameter base for processing. The ability to control the morphology and composition of nanostructures incorporating these materials is also essential. To that end, the dispersions studied in the main body of this research have been cast into thin films of pristine and hybrid materials. These films have been initially tested for a number of applications such as thermoelectrics, Li-ion batteries, supercapacitors as well as catalysis. It is hoped that this research will form the basis for further study into liquid phase processing of layered materials for future applications. A brief outline of each chapter is given below

Chapter 2: Materials and Background

An overview of carbon and inorganic nanomaterials is given. The history and physical properties of each material is discussed in detail as well as current and future applications. The process of liquid phase exfoliation is also introduced and discussed with regard to carbon nanotubes and graphene.

Chapter 3: Colloidal Theory

The basic concepts of colloidal theory are introduced. DLVO theory is discussed with particular emphasis on the source of repulsive potentials allowing for the stabilization of two dimensional sheets in aqueous environments.

Chapter 4: Methods and Characterisation

All experimental techniques as well as methods for characterisation used in this thesis are outlined and discussed.

Chapter 5: Dispersion of Graphene in Aqueous Surfactant Media

Dispersibility of graphene in a range of surfactants is assessed using dispersed concentration as a metric. Temporal stability as well as exfoliation state are also examined for each dispersion. The dispersed concentration is linked to the size of the repulsive potential barrier created by the surfactant coating.

Chapter 6: Lateral Size Selection of Surfactant Stabilized Graphene Dispersions using Size Exclusion Chromatography

Size exclusion chromatography is used to segregate nanosheets according to lateral dimensions. The resulting fractions are characterised using TEM and Raman analysis. Control over the average flake length is demonstrated.

Chapter 7: Exfoliation of Inorganic Layered Compounds in Aqueous Surfactant Media

MoS_2 is dispersed in aqueous surfactant media using ultrasonication. The resulting dispersions are characterised using, electron microscopy and optical spectroscopy. This method is also extended to other layered inorganic materials such as $MoTe_2$, $MoSe_2$, WS_2, $NbSe_2$ and BN. MoS_2 thin films and hybrids are tested for application in thermoelectrics and Li-ion batteries.

Chapter 8: Exfoliation of Manganese Oxide in Aqueous Surfactant Media

MnO_2 is dispersed in aqueous surfactant media using ultrasonication. The resulting dispersions are characterised using, electron microscopy and optical spectroscopy. MnO_2 thin films and hybrids are tested for application in supercapacitors.

Chapter 9: Ongoing and Future Work

A summary of current research being undertaken is given. Changes in the absorbance spectra for MoS_2 dispersions of varying size and thickness are examined in order to generate a metric. Size selected dispersions of MoS_2 are also tested for hydrogen evolution catalysis. Finally, promising methods for production of nanostructures with controlled morphology and increased porosity are discussed.

2

MATERIALS AND BACKGROUND

2.1 INTRODUCTION

This chapter introduces and discusses all materials examined and used in this thesis. The physical properties of each material are discussed with particular emphasis on current and future applications. The various production methods are also compared with specific consideration to the advantages and deficiencies for each process.

The nanomaterials used in this thesis are broken up into two main categories: Carbon nanomaterials and inorganic layered compounds. The first section will deal with carbon nanotubes and Graphene while the second will deal with transition metal dichalcogenides and transition metal oxides. This chapter also reviews the previous work on liquid phase production of carbon nanomaterials that has formed the basis for the work presented in this thesis.

2.2 CARBON NANOMATERIALS

Carbon is one of the most important and hence most intensely studied elements in the universe. It's versatility in forming chemical bonds has made it pivotal to all known life on earth. Carbon has four valence electrons meaning it can readily form bonds with other carbon atoms as well as a wide range of other elements. This versatility leads to the enormous amount of permutations of complex molecules present in all life forms and critical to biological processes.

Elemental carbon occurs naturally in both graphite and diamond. Diamond is composed of a rigid network sp^3 hybridized atoms tetragonally arranged to give a three dimensional crystal structure as shown in Figure 2.1a. Graphite on the other hand consists of a stacked array of 2 dimensional lattices held together by weak van der Waals interactions. Each sp^2 hybridized carbon is atom is triagonally arranged giving a planar hexagonal sheet. While these represent the most abundant forms of

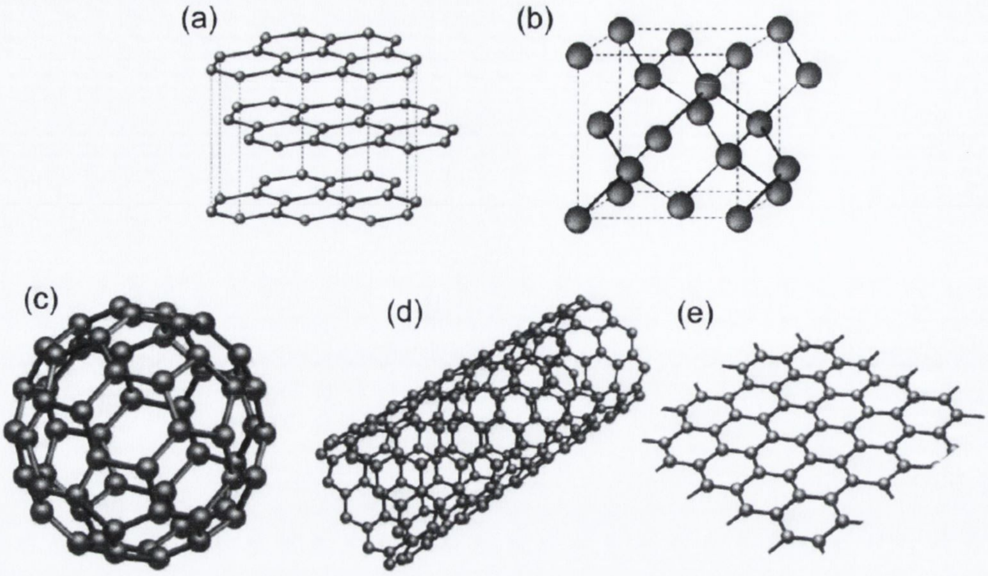

Figure 2.1: Atomic structures of (a) Graphite and (b) Diamond (c) 0-D Buckminsterfullerene (d) 1-D Carbon Nanotube (e) 2-D Graphene Sheet [4]

elemental carbon, the discovery of the zero dimensional carbon allotrope C_{60} in 1985 by Kroto et al, paved the way for further research in carbon nanostructures of other dimensionalities[1].

2.2.1. *Carbon Nanotubes*

Carbon nanotubes were first observed experimentally by Iijima et al in 1991 in material produced by arc burning graphite rods[2]. Nanotubes, as shown in Figure 2.1 consist of a rolled up sheet of sp^2 hybridized carbon atoms. They can be either single walled (SWNTs) or multi walled (MWNTs) in configuration with the latter consisting of several concentrically arranged cylinders. SWNTs have diameters of 1 to 2 nm while MWNTs have diameters ranging from 10 to 30nm with anything above this considered to be a carbon nanofibre. Both types can have lengths up to hundreds of microns and exhibit drastically different electrical and physical properties from bulk graphite. It is these unique physical and electrical properties that have driven the intense research into CNT synthesis and device testing.

Nanotubes are extremely mechanically robust with a measured ultimate tensile strength of 60GPa and a young's modulus of up to 1TPa [5]. These impressive mechanical properties coupled with a high aspect ratio make them an ideal filler material for reinforced composites. The 1-D geometry of CNTs allows for ballistic

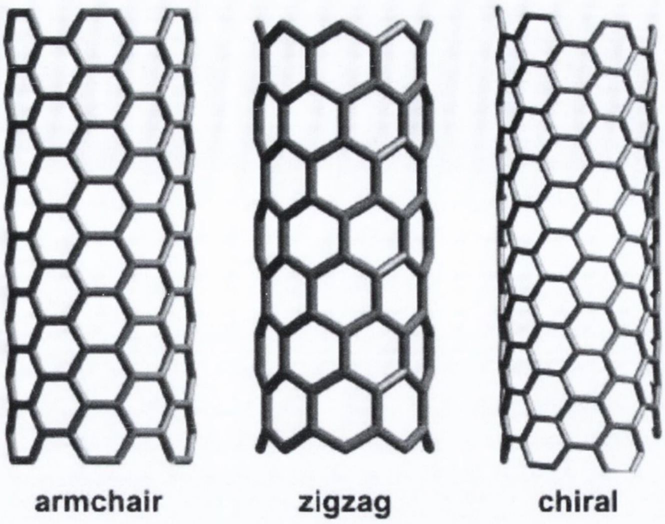

Figure 2.2: Different geometries of CNTs

conduction with mobilities of the order of 10^5 cm^2/Vs [6]. The lack of scattering for charge carriers in CNTs minimizes resistive heating allowing them to support massive current densities on the order of 10^9 A/cm^2 [7]. CNTs can be metallic or semiconducting depending on how the sheet of carbon atoms is rolled up. Figure 2.2 shows the 3 possible geometries for CNTs. While all of the armchair variety as well as some zigzag are metallic, the remaining CNTs are semiconducting with a diameter dependent band gap [8]. In addition, the predicted thermal conductivity of CNTs is of the order of 6000 WmK^{-1}. This combination of impressive electrical, mechanical and thermal properties makes CNTs an exciting material for a range of applications and fundamental research.

Early production methods followed Iijima's initial experiments using modified arch discharge reactors originally designed for fullerene synthesis [2, 9]. However, more recently laser ablation and chemical vapour deposition (CVD) have been used [10]. Arc discharge and laser ablation can both produce large quantities; however the material produced comes in a powder form. By contrast CVD grows nanotubes by decomposition of a gas, most commonly carbon monoxide [11] over metal catalyst particles. This allows for patterned growth at catalyst sites as well as excellent control over the length and diameter of tubes produced. Although all these methods produce high quality material, there is always some contamination from the metal catalysts used or from amorphous carbon. More importantly the material produced is a mixture of both the metallic and semiconducting types. Recent work has shown that these two species can be separated using chemical treatment [12].

Once produced, CNTs can be used in a range of applications. They have been used a filler materials for polymer composites with enhanced electrical and mechanical properties [10, 13], while the addition of small amounts of CNTs to metal can also improve the tensile strength [14]. The extremely small radius of SWNTs makes them ideal for use as tips in scanning probe microscopy, offering increased spatial resolution [15]. The tuneable band gap and low electron scattering for CNTs makes them a highly attractive material for microelectronics, specifically field effect transistors however greater control over the diameter, chirality and patterning is required in order to make these applications feasible. CNTs have been used as gas sensors with doping and functionalization allowing for increased sensitivity and selectivity[16]. These sensors can also be useful in biotechnology for DNA and protein detection as well as drug delivery [13].

Perhaps most relevant for this thesis, is the application of CNTs in energy storage. CNTs have already begun to be used in Li-ion batteries for mobile devices [13]. The active material in the electrodes for these batteries can often suffer from poor electrical conductivity or mechanical degradation after extensive cycling. A small wt% of CNTs increases the electrical conductivity of these electrodes while simultaneously enhancing the structural integrity. Recent work has also shown CNTs to be a promising material for supercapacitors as the active material themselves [17] or as embedded current collecting networks for pseudocapacative materials with low intrinsic electrical conductivity [18].

One of the biggest challenges for use of CNTs in any application besides production costs is their tendency to form bundles. The van der Waals interaction between the individual tubes and the bundles themselves promote entanglement. This bundling strongly inhibits the superlative properties of the individual tubes. Bundles are much less useful for mechanical reinforcement as stress is not uniformly applied to the individual tubes unless they are completely coated by the polymer. This means that CNT's present in a bundle tend to slip over each other upon the application of stress greatly reducing their effectiveness as reinforcing filler. Bundling can also increase the percolation threshold for conducting networks of CNTs as well as reducing the

Figure 2.3: A sheet of graphene can be cut up, rolled or stacked to form all other dimensionalities: 0D Fullerenes, 1D Nanotubes and 3D Graphite [19]

available surface area, both of which are undesirable affects for energy storage systems. Recent work on liquid phase processing has proven successful in effectively debundling CNTs for use in such applications. It has been shown that CNTs can be efficiently debundled and stabilized by sonication in aqueous surfactants[20-24], polymer dispersions[25, 26] or appropriate solvents[27, 28]. Some of this work will be discussed in more detail in Section 2.2.3.

2.2.2. *Graphene*

2.2.2.1 *Isolation*

Graphene is the name given to a monolayer (or few layers) of carbon atoms packed tightly into a two-dimensional honeycomb lattice and can be considered the basic building block for graphitic materials of all other dimensionalities (Figure 2.3). This planar form of carbon arises from the hybridisation of the 2s $2p_x$ and $2p_y$ orbitals, forming 3 sp^2 orbitals with a bond angle of 120 degrees between them. This means that the atoms are covalently bonded to one another in plane while the sheets are only weakly bound out of plane by van der Waals forces. This makes it far easier to break the bonds between sheets than the atoms themselves and hence enabled the isolation of graphene from highly ordered pyrolytic carbon (HOPG) by simple micromechanical cleavage.

The isolation of graphene in 2004 by Geim and co-workers from the university of Manchester [29] sparked a fundamental shift in the research priorities of groups around the world. Over the next few years the number of publications on graphene increased at an exponential rate with the larger scientific community seeking to investigate and exploit the properties of this new kind of material. Initial tests on micromechanically cleaved samples revealed a host of novel properties such as room temperature quantum Hall Effect [30] and breakdown of the Born-Oppenheimer approximation[31]. Although some research was aimed towards isolating single sheets of graphite[32], until 2004, graphene was widely thought to be thermodynamically unstable and considered a purely academic material with uses in theoretical modelling [19]. The impact and importance of the discovery of stable, isolated sheets of graphene was recognised by the awarding of the 2010 Nobel Prize for physics to both Geim and Novosolov.

2.2.2.2 *Properties & Applications*

Much like CNTs, graphene displays incredible physical properties that differ significantly from those of bulk graphite. Graphene has a very high thermal conductivity on the order of 3000 WmK^{-1} [33] and is completely impermeable to any gases [34] but it is its electrical and mechanical properties that are most responsible for it being dubbed a ‘miracle material’.

Graphene is what is known as a zero gap semiconductor. While the valence and conduction bands for metals tend to overlap, semiconductors are characterised by the gap between these bands. In Graphene however, the valence and conduction bands touch at just two points known as Dirac points. At these points, the electrons behave as relativistic particles known as Dirac Fermions. Like photons, these particles always move at a speed that is independent of their energy. The Dirac fermions in graphene move at a speed of about 300 times less than the speed of light [35].

The high quality of the material means that it has an extremely low defect density. The absence of these scattering centres vastly improves the charge transport in graphene with carrier mobilities of over 200,000 cm^2/Vs reported [36] Such high carrier mobilities are maintained at carrier concentrations greater than 1012 cm^{-2}, meaning that transport is essentially ballistic over micron length scales at room temperature [19]. This is what enables graphene to have such a low sheet resistance at such a low thickness. The ambipolar field effect observed for graphene also allows the electron or hole concentrations to be tuned at room temperature by the applied gate bias [19]. With such incredible electrical properties, graphene is a promising material for the semiconductor industry with 100GHz transistors already fabricated [37].

In 2008, Lee et al. measured both the stiffness and strength of a graphene monolayer showing it to be the strongest material known to man [38]. This nano-indentation method measured a Young's modulus of 1 TPa with an intrinsic strength of 130 GPa making it up to 100 times stronger than steel. The improvement in mechanical properties when compared with nanotubes coupled with the large decrease in production cost meant that graphene became the ideal choice as a filler material for polymer nanocomposites [39, 40].

Although graphene absorbs a significant amount of visible light per monolayer (2.3%) [41], the combination of its impressive transport properties and mechanical robustness, have fuelled a great deal of research into its possible use as a transparent conductor. The current industry standard, indium tin oxide (ITO) is used in wide variety of applications requiring both high electrical conductivity and transparency such as flat panel displays, touch screens and photovoltaics but suffers from two main drawbacks. The first is that the material itself is in short supply and hence the cost is rapidly increasing. Secondly, ITO is a ceramic making it very easy to fracture under low strains. These fractures lead to a large decrease in electrical conductivity thus causing device failure at low stresses. While this is not a large problem for rigid devices, the brittle nature of the material makes it unsuitable for use in the flexible displays or devices that are envisaged to be required for future applications. Graphene however has a fracture strain that is ten times greater than that for ITO. In addition, in 2010, Bae et al [42] were able to produce large area sheets of graphene with transparency of about 90% and sheet resistance of about 40 Ωsq^{-1} meeting minimum industry requirements [43]. These properties coupled with the flexibility of the sheets makes graphene a possible replacement for ITO in the next generation of devices.

Due to its 2D geometry, graphene has a very high specific surface area with a theoretical limit of 2630 m^2/g. The combination of this high surface area as well as

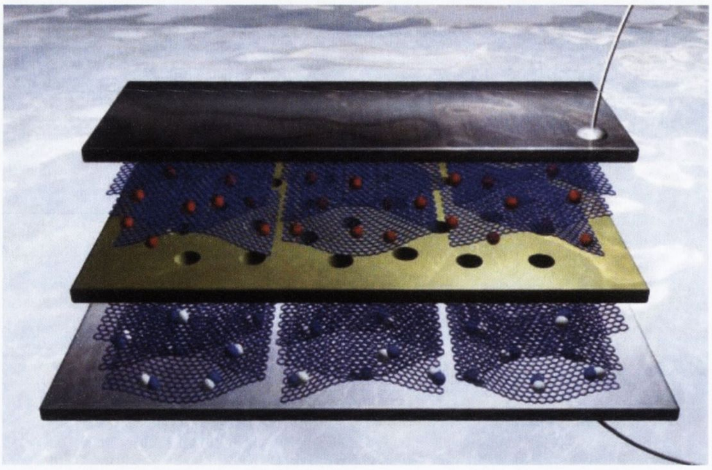

Figure 2.4: Graphene based supercapacitor: two high-surface-area graphene electrodes (blue and purple sheets) are separated by a membrane (yellow) [44].

low sheet resistance makes graphene an interesting material for energy storage. The most obvious applications involve graphene replacing industry standard carbon materials such as carbon black and activated carbon. The layered structure of graphene means that it can be used to intercalate lithium reversibly between the sheets and hence makes it a promising material for use in Li-ion batteries. The high thermal conductivity of graphene may also help improve the current loads in such batteries as the heat generated could be dissipated more quickly[44]. A high surface area porous assembly of graphene sheets such as that shown in Figure 2.4 is ideal for supercapacitor devices. Supercapacitors store energy in an electrochemical double layer with graphene based devices showing impressive capacitance, power and energy densities [45]. Graphene has also been used as a platform for platinum catalysts in fuel cells. Graphene improves catalysis compared to the standard carbon black used in these devices by reducing the particle size of the platinum [46]. It would appear that graphene has the potential to outperform and hence supersede traditional carbon materials for energy storage applications.

The high surface to mass ratio of graphene sheets also makes them ideal for gas sensing. All atoms in single layer graphene can be considered surface atoms and hence can adsorb gas molecules giving the material the highest sensing area per unit volume[47]. Graphene's high carrier mobility and low electrical noise mean that small changes in the sheet resistance caused by the adsorption of molecules can easily be detected. This has led to the first ever single molecule adsorption detection in 2007 using graphene based sensors, highlighting the phenomenal sensitivity of such devices [48].

Although the list of graphene's superlative qualities seems to stretch on and on, like nanotubes, industrial applications have been slow to get off the ground. The main problem with exploiting the unique electrical, mechanical and thermal properties of graphene lies with its production. Applications seeking to take advantage of graphene's electrical properties require high quality, defect free material. Control over the number of layers and lateral dimensions of the sheet are extremely important for any transparent electrode applications as well as polymer reinforcement. With all these requirements in mind, many different methods for production of graphene emerged and with the main processes discussed in the next section.

2.2.2.3 *Production methods*

The initial production of graphene involved isolation from a parent crystal (HOPG) using micromechanical cleavage. This 'scotch tape' method involves peeling thin layers of graphite away from a bulk sample using adhesive tape. The material is then deposited onto a silicon substrate with a 300nm oxide layer using the same adhesive tape with mono and few-layer material identified using an optical microscope. Despite the apparent crudity of this method, it has produced the highest quality material to date and is the production method of choice for most of the fundamental research into graphene's physical properties. Although micromechanical cleavage can produce mono and few-layer material up to microns in length, it is laborious and has an extremely low yield. These mono and few-layer sheets represent a tiny fraction of the particles cleaved from the HOPG with the rest being ordinary graphite. This means that there is very little scalability in this method and hence many competing routes for synthesis emerged soon after graphene's discovery.

Reduction of silicon carbide

De Heer et al pioneered work on an epitaxial method to produce graphene by reduction of silicon carbide (SiC) wafers [49]. Silicon carbide is a relatively common material that is used for high power electronics. It was found that silicon desorbs from the surface of the SiC wafers around 1000°C in ultrahigh vacuum leaving behind islands of graphitised carbon. These islands initially consisted of randomly oriented layers, however, recent work has shown good control over the number of layers grown [50]. Although the quality of the graphene can be very high and at sizes up to hundreds of microns, there are significant drawbacks to this method of production. The high temperatures required, limit the range of substrates that can be used and are not directly compatible with silicon electronics. The high cost of processing conditions and lack of versatility in the method means that epitaxial graphene will probably be limited to use in niche high end electronics such as high frequency transistors [37].

Chemical Vapour Deposition

Perhaps one of the most exciting processing methods in terms of its good production cost/quality balance is chemical vapour deposition (CVD). This involves exposing a thin transition metal layer such as platinum[51], ruthenium[52] or copper [53] to a hydrocarbon gas (most commonly methane) under pressure at high temperatures. A second process gas is typically used to catalyse a reaction between the hydrocarbons and the transition metal substrate. Li et al have suggested their process to be self-limiting due to the low solubility of carbon in the copper films used, making large area growth of a single layer possible [53]. Indeed recent work has reported the production of square meters of monolayer graphene sheets on copper foils [42]. The quality of the graphene produced by CVD can be very good with sheets shown to exhibit the half integer quantum hall effect and high electron mobilities seen in mechanically exfoliated samples [54]. This means that the growth of graphene on metal surfaces could have a number of applications. The high thermal and electrical conductivities of the sheets could allow CVD grown graphene to be used to enhance current copper interconnects used in integrated circuits. The complete impermeability of graphene may also allow it to be used in anti-corrosive coatings.

Although there are large energy requirements for this process, the ability to transfer the resulting films on to a range of substrates makes it a much more viable option for widespread application compared to epitaxial grown graphene. This transfer process is by no means straightforward and requires the metal support foil to be etched away after transfer to an adhesive polymer support as shown in Figure 2.5. This process can

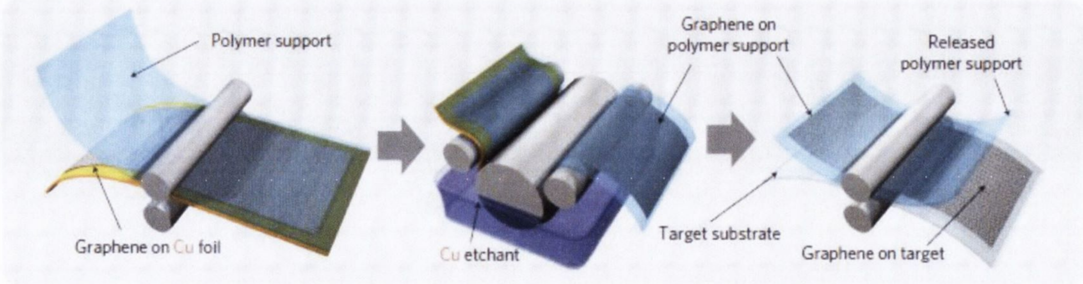

Figure 2.5: Diagram of roll based transfer of Graphene grown on copper foil to a target substrate using a polymer support and copper etchant[42].

damage the graphene in terms its electrical and mechanical properties and hence improvements in the transfer process will be required before CVD graphene can be widely used [44]. Greater control over the grain boundaries and crystallographic orientation of the layers would also be of great benefit. Despite these drawbacks, CVD grown graphene is already suitable for use in transparent conducting applications such as touch screens with Bae et al reporting sheet resistance values as low as $30\Omega/\text{sq.}$ for 90% transparency [42]. These values were for a film transferred to a flexible substrate of polyethylene terephthalate (PET) suggesting CVD grown graphene could be a viable replacement for ITO in the next generation of flexible devices.

Chemical Assembly of organic precursors

Another bottom up approach to graphene is the chemical assembly of macromolecules [55, 56]. These polyaromatic hydrocarbons have a benzene based structure similar to that of graphene allowing them to be used as building blocks to construct larger graphene sheets. This process has allowed the synthesis of graphene nanoribbons (GNRs) however their size has been greatly limited by the size of the organic macromolecules used to assemble them. As the molecular weight of these precursors is increased, the solubility of the molecule decreases and also promotes an increase in side reactions [56] greatly complicating proccessability. While the size limitations make organic synthesis of graphene unappealing for the majority of applications, the process enables production of ribbons with well-defined size and edge structures.

Liquid Phase Methods

All of the bottom up methods previously discussed produce very small masses of graphene and are simply not suitable for a range of applications such as composite materials. CVD and SiC epitaxy are both limited by the processable substrate dimensions while chemical assembly is limited by the size of the macromolecules available. Because of these obvious drawbacks, a large amount of research has focused on top down techniques whereby graphene is isolated in dispersion from bulk graphite similar to mechanical exfoliation but with much greater yields and proccessability. While all the methods differ significantly in their processing conditions they all have the same common idea. The cohesive energy barrier between layers must be overcome while also stabilising the resulting individual or few layer structures against their natural tendency to re-aggregate.

The earliest attempt at graphene dispersion revolved around chemical modification of graphite in order to weaken the interlayer interactions. This method is by no means a new one and dates back to 1859 [57] long before anyone was interested in isolating graphene. The most common technique involves oxidation of graphite and was perfected by Hummers in 1957 whereby potassium permanganate, sodium nitrate and sulphuric acid are used to attach hydroxyl groups and other functionalities onto the basal plane of the graphite [58]. The presence of the hydroxyl, carboxyl and epoxy groups strongly affect the graphite affinity with water turning hydrophobic graphite into hydrophilic graphite oxide. In 2006, Stankovich et al produced dispersions of mono and few-layer graphene in water by using a modified version of Hummers method. The water dispersible graphite oxide produced by this method was mildly sonicated breaking the weak interlayer attractions and exfoliating the material to form graphene oxide (GO). Further improvements were made by oxidising graphite intercalates whereby exfoliation is improved by the presence of molecules between the graphene layers of the starting graphite [59].

While this method easily produces readily dispersible mono and few-layer material in large quantities, it is important to note the graphene oxide is quite different from graphene due to the presence of functional groups. Oxidation of the graphene sheets, alters the electronic structure making them insulating or semiconducting. In addition, the impressive mechanical properties are lost with a reported 80% reduction in modulus compared to pristine graphene[60]. Many groups have attempted to

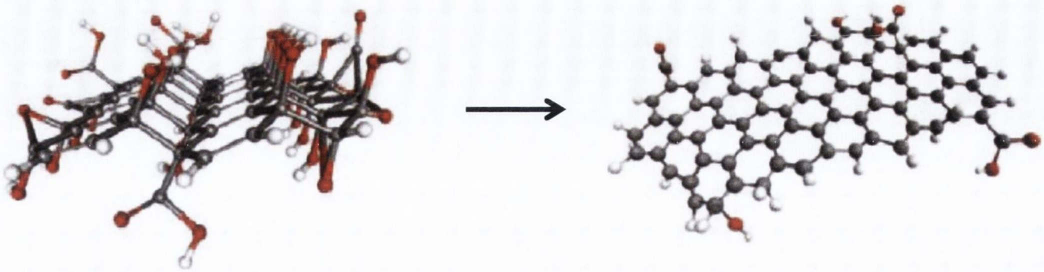

Figure 2.6: Molecular model of graphene oxide (left) and reduced graphene oxide (right). Carbon in grey, oxygen in red and hydrogen in white. Adapted from [61]

convert GO back to pristine graphene using various post treatments with varying success [61-67]. These methods can involve ultraviolet assisted photocatalytic [68] and hydrazine [69] reduction or thermal shock [70] using high temperature annealing (>1000°C) but none are capable of completely removing the functional groups. This means that although the electrical properties of GO can be improved by post treatments, this method is unsuitable for preparation of pristine material. This coupled with the harsh oxidising agents required and high temperatures used in reduction seriously limits the potential of this technique. From the above discussion it is clear that a less destructive method capable of producing pristine graphene is required. A breakthrough involving such a method will be discussed in the next section and forms the basis for this thesis.

2.2.3. *Liquid Phase Exfoliation of Carbon Nanomaterials*

As discussed earlier, one of the biggest challenges for application of nanotubes involves overcoming their tendency to form bundles. To address this issue several liquid phase techniques to both debundle and disperse nanotubes were developed and perfected. These can be categorized into two strategies: Dispersion using favourable solution energetics by careful selection of solvents and stabilization using electrostatic or steric repulsion in aqueous surfactant media. Dispersion in a polymer is also possible.

2.2.3.1 *Solvent based Exfoliation*

The simplest way to debundle and disperse nanotubes is in a suitable solvent. This is assisted by ultrasonication and centrifugation. SWCNTs have been successfully dispersed in a range of amide solvents such as N-methyl-2-pyrrolidone (NMP), N,N-dimethylacetamide (DMA), cyclopentanone (CPO) and cyclohexylpyrrolidone(CHP) [71-73]. Although in some solvents both the temporal stability and fraction of isolated individual tubes can be quite high [27, 28, 74], for the vast majority of solvents, this is not the case. Thus in order to minimise aggregation and sedimentation in these dispersions it is important to develop and understanding of the factors affecting a solvent's suitability for dispersion of CNTs. To that end several studies were performed to explore the energetics of CNT dispersions using solubility parameters to compare good and bad solvents [75-77].

It is important at this point to consider the thermodynamics involved in mixing CNTs with a solvent. Whenever two chemical compounds are mixed there will be an overall change in both the entropy (s) and enthalpy (H) of the system. In general when adding a solute to a solvent, solubility is thermodynamically favourable if the free energy of mixing (ΔG_{mix}) is negative

$$\Delta G_{mix} = \Delta H_{mix} - T\Delta S_{mix} \qquad (2.1)$$

where ΔH_{mix} and ΔS_{mix} are the enthalpy and entopy of mixing respectively. Since mixing will increase the disorder of the system and hence ΔS_{mix} is always positive. Although positive values of ΔS_{mix} are beneficial for keeping ΔG_{mix} below zero, the ΔS_{mix} for large rigid particles like CNTs is very small. This means that the enthalpy change associated with mixing CNTs and a given solvent must be minimised (i.e. ΔH_{mix} must be close to zero) in order for it to be thermodynamically favourable. In 2006 Bergin et al approximate expression, based on van der Waals type interactions, for ΔH_{mix} (per solvent volume V_{mix}) when nanotubes are dispersed in a solvent

$$\frac{\Delta H_{mix}}{V_{mix}} \approx \frac{2}{R_{bun}} \ \delta_{NT} - \delta_{Sol} \ {}^{2}V_f \qquad (2.2)$$

where R_{bun} is the radius of the dispersed nanotube bundles and V_f is the nanotube volume fraction. More importantly δ_{NT} and δ_{Sol} are the square roots of the nanotubes

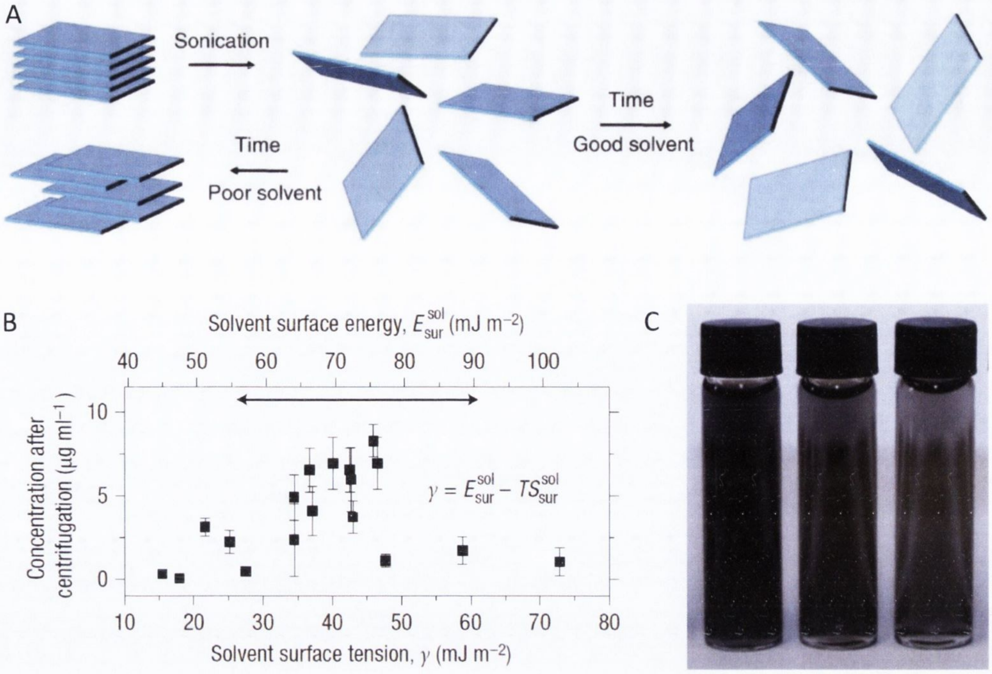

Figure 2.7: (a) Sonication assisted exfoliation. The layered crystal is sonicated in a solvent, resulting in exfoliation and nanosheet formation. In good solvents the exfoliated nanosheets are stabilized against reaggregation. For bad solvents reaggregation and sedimentation will occur. (b) Graphite concentration measured after centrifugation for a range of solvents plotted versus solvent surface tension and surface energy The horizontal arrow shows the approximate range of the reported literature values for the surface energy of graphite. (c) Graphene dispersions of varying concentration. Adapted from [78, 79]

and solvent surface energies. This expression predicts that good solvents for dispersion and debundling of CNTs will have surface energies close to that of the nanotubes. To test this, the nanotube concentration after centrifugation was measured for a range of solvents with a well-defined peak in concentration for solvents with surface energies in the range reported for CNTs.

Following on from this work, in 2008 two groups independently applied the same techniques to exfoliate graphite in a range of amide solvents [78, 80]. Hernandez et al showed graphene could be dispersed in solvents such as NMP and DMA using ultrasonication [78]. Figure 2.7b shows the correlation between solvent surface energy and dispersed concentration of nanotubes. As is the case for CNTs, effective solvents are characterised by a surface energy matching that of graphene. This method produced pale grey dispersions consisting of well exfoliated material but also a large number of aggregates that would fall out over time. The aggregates were easily

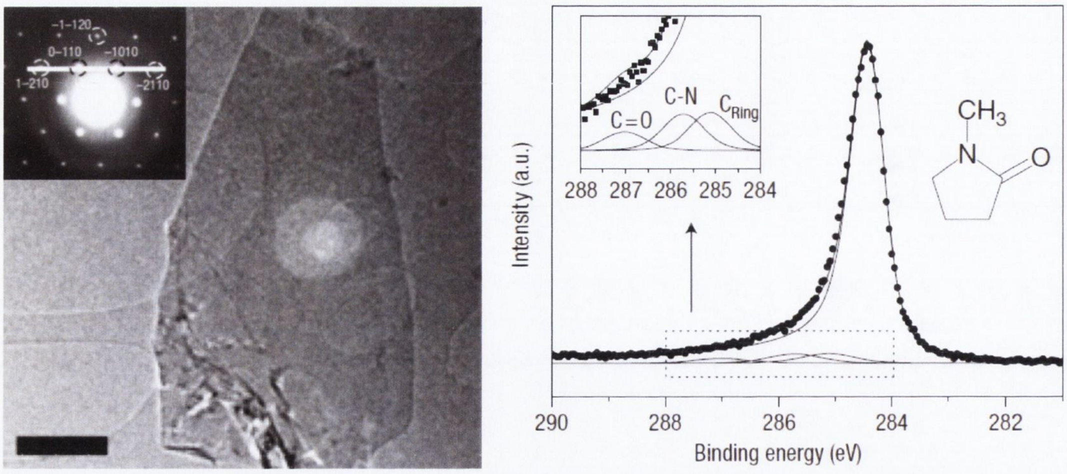

Figure 2.8: (a) High-resolution TEM image of solution-cast monolayer (scale bar 500 nm). Inset: Electron diffraction pattern of the sheet with the peaks labelled by Miller–Bravais. (b) A carbon 1s core-level XPS spectrum for a thin film vacuum-deposited from a graphene dispersion. Main fit line represents graphitic carbon (C–C). The smaller fit lines represent residual NMP. Left inset: enlarged view of the NMP fit lines Right inset: structure of NMP. Adapted from [78]

removed by mild centrifugation leaving behind a stable dispersion of few and monolayer material. The presence of this mono and few-layer material was confirmed by transmission electron microscopy (TEM) analysis of the supernatant. Figure 2.8 shows a representative image of the kind of graphene flake produced by this method. Both the size and aspect ratio vary from flake to flake with the former ranging from 10s of nanometres to a few microns. Although the thickness of the flakes also varies significantly, electron diffraction confirms the presence of monolayer graphene in reasonable quantities. This coupled with X-ray photoelectron spectroscopy (XPS) and Raman analysis shows the material produced to be of high quality and most importantly free of structural defects and functional groups. One major drawback to this method however is that the most effective solvents are predominantly toxic as well as having high boiling points making them both hazardous and difficult to remove after processing.

2.2.3.2 *Surfactant based Exfoliation*

Unfortunately the most useful solvent for liquid phase exfoliation, water, has a surface energy much too high to act as an exfoliant for pristine CNT bundles or graphite. However surfactants can be used to overcome the inherent hydrophobicity in pristine

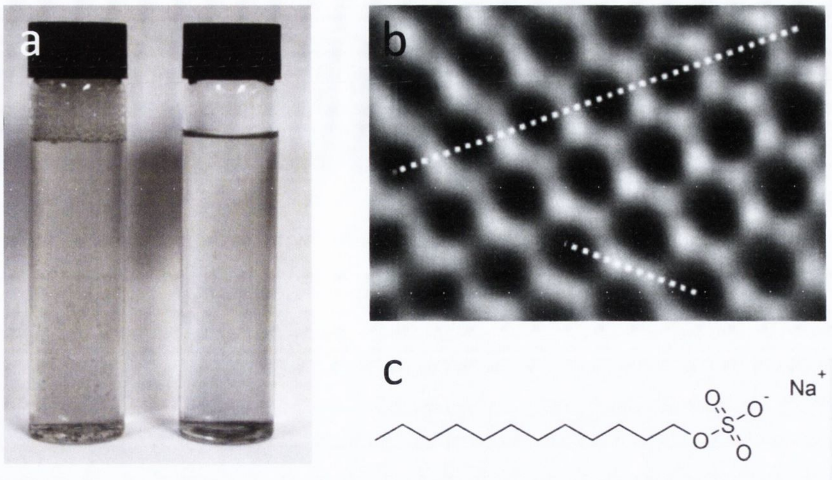

Figure 2.9: (a) Surfactant-stabilized graphite dispersions (left) before and (right) immediately after centrifugation. (b) Filtered HRTEM images of graphene monolayer. Intensity analysis of top and bottom dashed lines confirm hexagonal width and C-C bind length respectively. (c) Molecular diagram of surfactant used: sodium dodecylbenzene sulfonate (SDBS) Adapted from [81]

carbon nanomaterials. These are amphiphilic surface active molecules that act as a bridge between polar and non-polar media. The non-polar tail groups adsorb onto the hydrophobic particles while the polar head groups interact with the polar solvent stabilising them in dispersion. A more detailed discussion of this mechanism is presented in Chapters 3 and 5. The earliest work in CNT dispersion involved the use of surfactant stabilisation [82]. As the method was perfected it became possible to create stable dispersions with much less bundling with fluorescence measurements confirming the presence of well exfoliated material [20, 21, 23]. Subsequent work compared various surfactants examining their efficiency [83-86] and forms the basis for the work presented on Graphene surfactant dispersions presented in Chapter 5.

In 2009 Lotya et al, expanded upon this work to produce surfactant stabilised dispersion of graphene exfoliated from bulk graphite. The procedure for production was exactly the same as that used by Hernandez et al simply replacing the solvent with aqueous surfactant solution. The results were comparable with those already obtained from solvent exfoliation. Pale grey dispersions of mono and few-layer material were produced after sonication and centrifugation and were stable over a period of weeks. TEM analysis showed the flakes produced to have a similar distribution of size and thickness compared with solvent exfoliated samples. Atomic resolution HRTEM (Figure 2.9) showed good hexagonal symmetry in the lattice

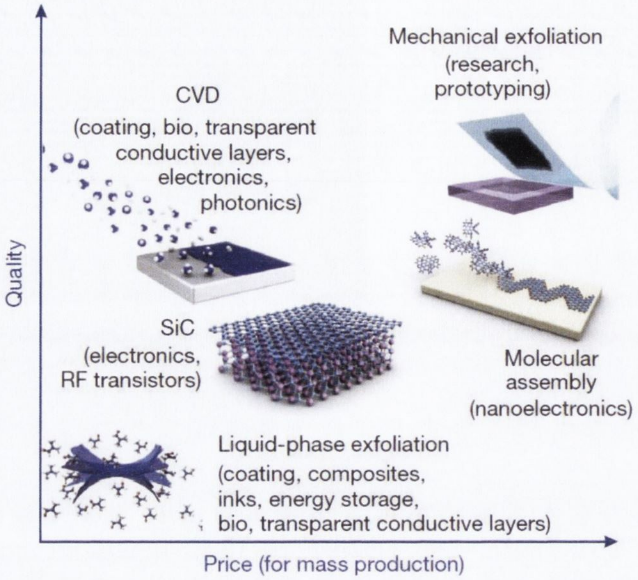

Figure 2.10: Quality versus cost for several graphene production methods [44]

suggesting good quality material. Raman spectroscopy of thin films cast from these dispersions further suggested low defect density while XPS analysis confirmed the presence of pristine carbon material with very low levels of oxidation.

Like GO or rGO, these dispersions can easily be vacuum filtered to make thin films. This method allows for deposition on a range of substrates by transfer of vacuum filtered films or by spray deposition. They can also be blended with polymers and other materials to make composites with tuneable electrical and physical properties [39, 40]. Nuvoli et al for example have successfully exfoliated graphene in organosilanes [87]. These dispersions can then be polymerised allowing for the production of polymer composites without the need to remove solvent. Unlike other liquid phase methods, this process produces defect free graphene. The functional groups associated with GO or structural defects of rGO are not present in the material produced by exfoliation in solvents and surfactants. This means that the solution processing does not interfere with the intrinsic properties of the material and hence makes it an attractive route for production. It is important to note that although the material is chemically unaltered, it is still polydispersed, i.e. comes in a range of thickness' and lateral flake dimensions. This represents a huge obstacle for application since the electrical properties of graphene have been shown to depend heavily on the number of layers. While an appreciable fraction of the material produced is monolayer graphene, the inability to precisely control the flake thickness means the electrical performance of the films produced do not compare favourably with micromechanically cleaved or CVD grown samples.

Despite some of the drawbacks previously discussed, liquid phase exfoliation using solvents or surfactants produces large quantities of material at room temperature making it a much more scalable and affordable process than CVD or mechanical exfoliation. Figure 2.10 compares the quality of material with production cost for a range of processing techniques. It is clear that more work is required in order to improve the quality of the material produced by gaining a greater control over the lateral flake dimensions as well as thickness. Improving the dispersed concentration of graphene is also of great importance when considering liquid phase exfoliation as a viable route to mass production. This thesis aims to further investigate and address both of these problems for surfactant based exfoliation.

2.3 INORGANIC LAYERED MATERIALS

In addition to carbon nanomaterials, many other low dimensional inorganic materials exist. This section will introduce the layered two-dimensional materials used in this thesis with particular emphasis on molybdenum disulphide. It is also appropriate for clarity at this stage to define a two dimensional material as a material in which the atomic organization and bond strength along two-dimensions are similar and much stronger than along a third dimension[88]

2.3.1. *Boron Nitride*

Hexagonal boron nitride (h-BN) is a structural analogue of graphite consisting of stacked sp^2 bonded sheets where alternating boron and nitrogen atoms substitute carbon atoms. The B-N bond length (1.45 Å), honeycomb spacing (2.50 Å) and interlayer spacing (0.33 nm) are almost identical to that of graphene (Figure 2.11)[89]. While graphene is predominantly AB stacked with carbon atoms sitting above or below the centre of the benzene ring in the adjacent layer, the stacking in h-BN crystals is different. They are predominantly AA' stacked with boron atoms sitting above nitrogen atoms in the neighbouring layer due to favourable electrostatic or polar interactions [89].

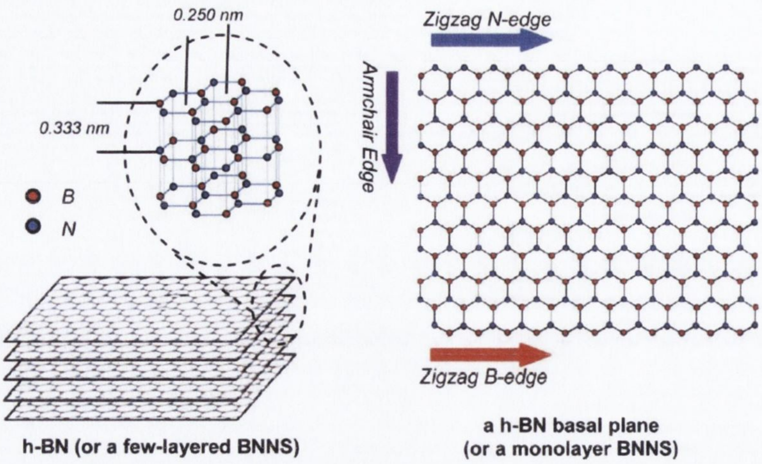

Figure 2.11: Structural basics of 2D BN nanostructures [89]

Like graphene, thin films of h-BN can have very high transparencies however unlike graphene these films are insulating rather than conducting. This is due to the very large bandgap in h-BN reported to be approximately 6.07 eV for monolayer material [90]. BN nanoribbons (BNNRs) have been shown to have a tuneable band gap while Terrones et al have shown ribbons with zigzag edges to have metallic properties [91]. The structural similarities with graphene yet different electrical properties have led to a great deal of interest in graphene-BN heterostructures. h-BN has been proposed for use as a gate dielectric or substrate for graphene transistors and has been shown to improve the performance of such devices [92].

Although there have been very few reported measurements of the stiffness and strength of h-BN nanosheets they have shown promise as a filler material for polymer composites. BN/PMMA (polymethyl methacrylate) composites displayed a 22% increase in elastic modulus accompanied by an 11% increase in strength for loadings as small as 0.3 wt% of BN sheets in the polymer [93]. h-BN is an excellent thermal conductor with conductivities >600 W/m/K reported for monolayer sheets[94]. It is also extremely thermally stable compared with graphite showing oxidation resistance at temperatures up to 1000°C [90]. The ability to enhance thermal conductivity without imparting any electrical conductivity makes h-BN an exciting material for composites despite lower values of k compared to graphene. Song et al reported thermal conductivities of 60 W/m/K for epoxy films with a 50 vol% of nanosheets [89, 95].

Despite the range of possible applications, BN has been the subject of much less intense research compared with graphene. One possible reason for this could be less well established routes to synthesis. While much of graphene synthesis built on existing methods for CNT production or heavy oxidation, these routes are less straightforward for h-BN due to its thermal stability. Other top down methods such as non-covalent chemical functionalization [96], mechanical cleavage [3] and most recently solvent mediated ultrasonication [93, 97] have been used to produce h-BN. Song et al. pioneered a CVD method to prepare large area, transferrable few-layered h-BN films with of areas up to a few cm^2 where Ammonia borane was decomposed at 1000°C on a Cu substrate utilising the similar lattice constants (2% mismatch) [98].

2.3.2. *Transition Metal Dichalcogenides*

Transition metal dichalcogenides (TMDs) have a general molecular formula of MX_2, where M is a transition metal from groups 4-10 and X is a chalogen. There are around 60 different types [99] with around two thirds forming graphite-like layered structures with thickness' typically ranging from 6-7 Å [100]. The individual sheets consist of a layer of metal atoms hexagonally packed and sandwiched between two layers of chalcogen atoms as shown in Figure 2.12. Like graphene, the in-plane bonding is covalent while the inter layer attraction is due to weak van der Waals interactions leading to anisotropy in the physical properties [99]. Single layer TMDs can exist in only two polymorphs where the coordination of the metal is either trigonal prismatic (2H) or octahedral (1T). The preferred phase depends on the number of d-electrons in the transition metal.

The electronic properties of TMDs are diverse - depending heavily on the coordination and oxidation state of the metal atoms. They range from semiconductors such as MoS_2 and WS_2 and semimetals such as WTe_2 and $TiSe_2$, to metals such as NbS_2 and VSe_2. A summary of electronic properties for TMDs is presented in Table 2.1. The chalcogen atoms also affect the electronic structure but far less drastically with a decrease in bandgap associated with increasing atomic number [99]. Like graphene, mono and few layer TMDs show dramatic changes in electronic properties compared to the bulk due to quantum confinement. This coupled with the diversity of

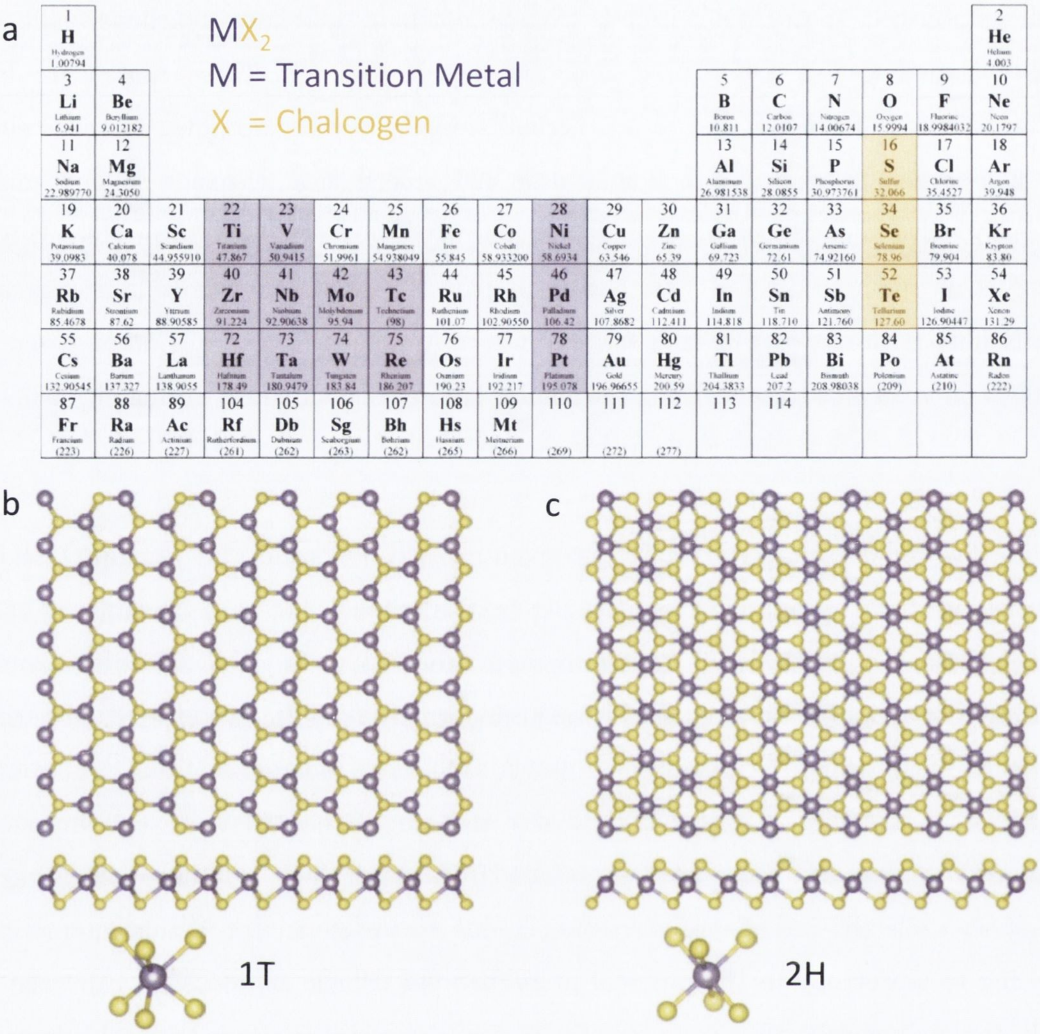

Figure 2.12: Structure of layered transition metal dichalcogenides. The transition metals (purple) and the three chalcogens (yellow) that predominantly crystallize in layered structures are highlighted in the periodic table. Single-layer TMD with trigonal prismatic (b) and octahedral (c) coordination. Adapted from [100]

Group	M	Properties
4	Ti, Hf, Zr	Semiconductors
5	V, Nb, Ta	Narrow band metals or semimetals
6	Mo, W	Sulfides & Selenides: semiconductors Tellurides: Semimetals
7	Tc, Re	Small-gap semiconductors
10	Pd, Pt	Sulfides & Selenides: semiconductors Tellurides: Metals

Table 2.1: Electronic properties of TMDs. Adapted from [100]

electronic properties makes TMDs of enormous interest to the scientific community with applications in catalysis [101] photovoltaics [102] and energy storage [103].

Top down methods of producing TMDs can be traced back to the mid-sixties where Frindt used mechanical cleavage to isolate layers of MoS_2 as thin as 3 nm [99]. More recently a similar method was employed by Novoselov to produce monolayer MoS_2 [35]. As is the case with graphene, mechanical cleavage is the processing method of choice to produce the highest quality samples however it is not a scalable technique. Mirroring progress in graphene production, several routes for synthesis of mono and few layer TMDs have emerged over the past few years and will be discussed below.

As discussed in the previous section, chemical vapour deposition can be used to deposit graphene layers on certain transition metal substrates using organic precursors. A similar approach has been applied to the growth of TMDs with most of the early efforts focused on MoS_2. CVD growth of MoS_2 can be divided into three main strategies: (i) vaporisation and decomposition of metal/chalcogen precursors (ii) direct sulfurization of metal and (iii) conversion of metal oxide. The first is a two-step process pioneered by Zhan et al which involved coating a substrate in ammonium thiomolybdates ($(NH_4)_2MoS_4$) and converting to MoS_2 by annealing at 500°C [104]. This is followed by second sulfurizing annealing step at 1000°C to improve the crystallinity of the material (Figure 2.13) Zhan and co-workers showed that thin films of molybdenum can also by sulfurized by annealing at high temperatures to produce mono and few layer MoS_2 [105]. Perhaps most promising is the conversion of MoO_3 to MoS_2 to produce large area monolayer sheets [106]. This method involves deposition

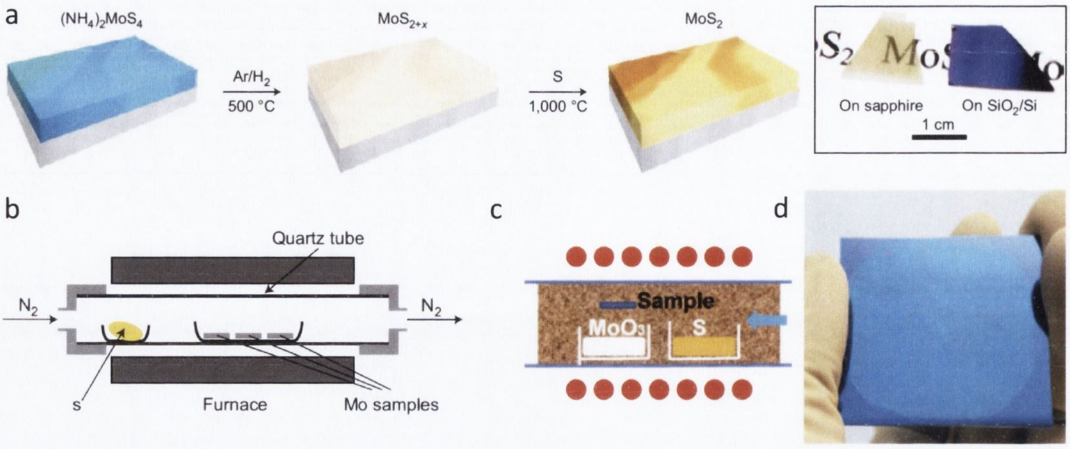

Figure 2.13: (a) MoS_2 layer deposited by two-step thermolysis, and the films obtained on a sapphire and silica substrate. (b) MoS_2 prepared by sulfurization of thin molybdenum films. **(c)** Growth of a MoS_2 monolayer on a substrate (sample) from MoO_3 and S powders through a gas-phase reaction. (d) Wafer-scale deposition and transfer of mono to few-layered MoS_2 films [100]

on a substrate by way of a gas phase interaction between MoO_3 and S_2 powders with Lee et al reporting that substrates pre-treated with aromatic molecules such as rGO can assist growth. Wafer scale production has been demonstrated on sapphire substrates as shown in Figure 2.13 [107].

The layered structure of TMDs allows for several liquid phase top down methods to be employed to produce mono or few-layer material. These layered structures can strongly adsorb molecules into their interlayer spacing forming inclusion complexes [79]. This allows for a process known as intercalation to occur whereby the inclusion of ions between the layers increases their spacing and hence weakens the bonds between them. These bonds can be further weakened by transfer of charge to the layers using intercalants such as n-butyllithium[108]. The overall effect is a reduction in the energy required to separate the layers and hence aids in exfoliation by ultrasonication [108, 109]. The exfoliated nanosheets can be stabilized against reaggregation by a surface charge or surfactant. Recent developments have allowed the successful intercalation and preparation of monolayer dispersions of MoS_2, WS_2, TiS_2 and TaS_2 [110]. Although ion intercalation can produce concentrations of up to 50mg/ml with almost 100% exfoliation to monolayers [111] there are some distinct disadvantages to the process. Lithium intercalation is extremely sensitive to ambient conditions and must be carried out at high temperatures for a period of days. The lithium intercalation must also be carefully controlled so as to prevent the formation of metal nanoparticles

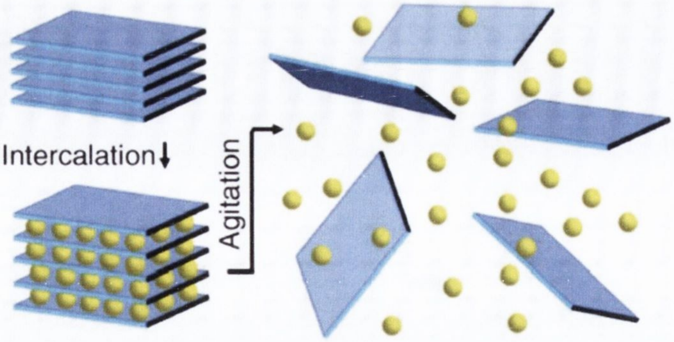

Figure 2.14: Ion intercalation. Ions (yellow spheres) are intercalated between the layers [79]

and precipitation of Li_2S. Perhaps most importantly, it does not produce an exfoliated version of the starting material. For instance, exfoliation of MoS_2 does not give pristine MoS_2 but lithiated MoS_2 (Li_xMoS_2). While it is possible to remove the lithium by washing, some will always remain. This poses a problem as the interaction of the Li ions results in partial electron transfer to the layers [112, 113]. This results in significant changes to the structural and electronic properties. In the case of MoS_2 intercalation of Li into layers leads to a structural transformation causing the geometry around the Mo atoms to shift from trigonal prismatic (2H) to octahedral (1T) [112]. This structural change is accompanied by a dramatic change in electronic properties which is retained after formation of the exfoliated layers into films [114] While these properties can be advantageous, the structural and electrical properties are not defined by the starting material alone but by the processing. It is therefore necessary to consider less pertubating systems for exfoliation in the liquid phase.

Recent work in the Coleman group has built on the success of solvent based exfoliation of graphite to produce dispersions of a range pristine TMDs such as MoS_2 and WS_2 [97]. As discussed in the previous sections good solvents are characterised by their surface energy. If this surface energy matches that of the TMD, the energy difference between the exfoliated and reaggregated states becomes much smaller. This allows for dispersions to remain stable after the bulk material has been exfoliated using ultrasoniation. The dispersions are made up of a range of flake sizes and thicknesses with a relatively low monolayer yield. They can be deposited on substrates or formed into thin films as well as being easily blended with polymers or other nanomaterials to form hybrids and composites. As with solvent exfoliation of graphene, one of the main drawbacks to this method is the solvents themselves. The majority have high toxicity as well as boiling points making them both hazardous and difficult to remove. This could be overcome by replacing the solvent media with aqueous surfactant solutions and will be covered in Chapter 7.

2.3.3.1 *Molybdenum disulphide*

While most TMDs are chemically synthesised, MoS_2 can be found in naturally occurring molybdenite ore and is hence the most common. MoS_2 in its bulk form, is a semiconductor with an intrinsic indirect bandgap of 1.29 eV and an in plane conductivity of 1.58×10^4 Ωcm^{-1} [112]. The band gap of MoS_2 increases with decreasing crystal thickness due to quantum confinement [108] with several studies also showing a transition from an indirect to direct band gap ($E_g = 1.90$ eV) for MoS_2 monolayers [115-117]. This induces a 10^4 fold enhancement of the photoluminescence (PL) quantum yield observed for monolayers. MoS_2 has been shown to possess robust mechanical properties, with a high Young's modulus of about 0.33 TPa reported for suspended nanosheets. This value for stiffness is about 1/3 that of graphene [118, 119] Bulk MoS_2 is widely used in dry lubrication or as a hydrodesulfurization catalyst to remove sulphur compounds from oil. It has generated interest for application in photovoltaic and photocatalytic devices due to its strong absorbance in the solar spectrum.

6.3.3. *Transition Metal Oxides*

Layered transition metal oxides (TMOs) represent a more diverse class of layered materials with a range of structures as well as interesting electronic and electrochemical properties. These oxides are composed of sheets of MO_6 octahedral units (M=Metal atoms such as Mo, Mn, Ti and Nb). The most used method of production for these materials is ion-exchange based exfoliation [120-122]. This method is based on the fact that many layered oxides exist as mixed valence compounds and hence contain an interlayer of charge balancing cationic counterions [121]. Soaking these materials in acid can cause these inter-layer ions to be exchanged for protons which in turn can be exchanged for more bulky organic ions. This leads to swelling of the layers much like oxidation of graphite or intercalation of TMDs. This swelling allows individual layers to be exfoliated by ultrasonication or shear mixing to give dispersions. These dispersions have been proposed for a range of applications from

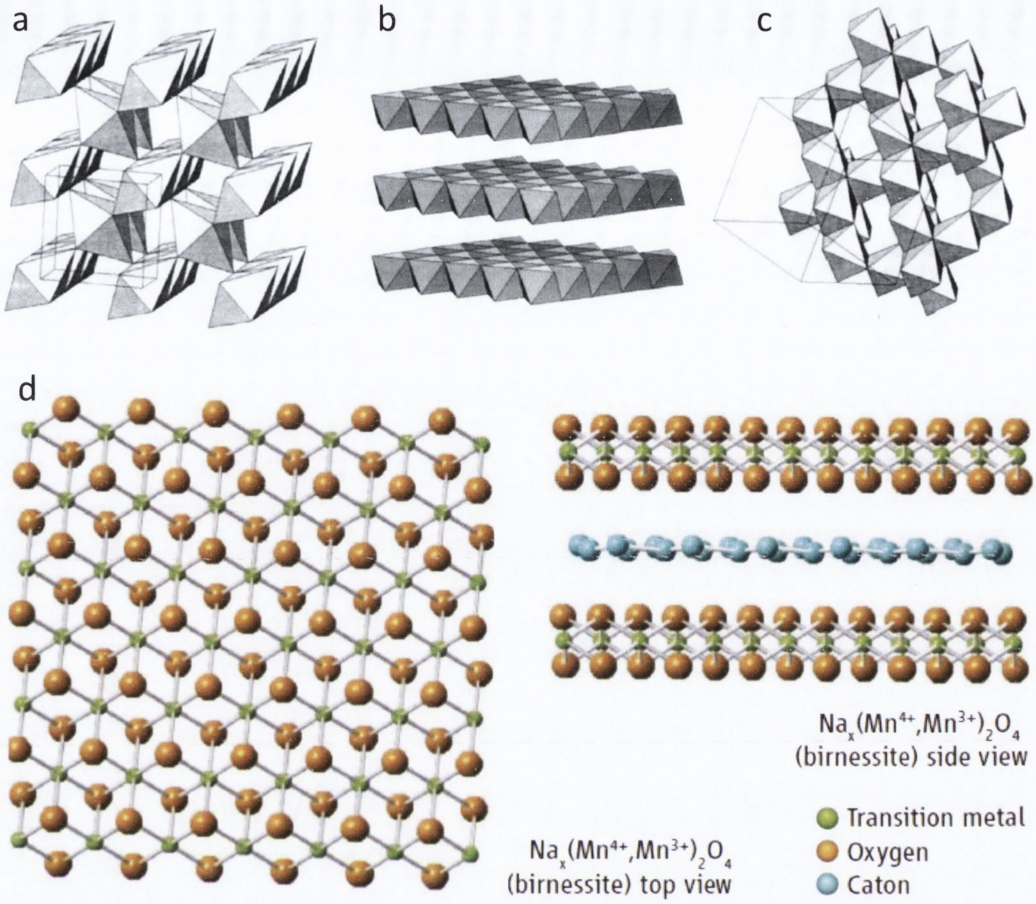

Figure 2.15: Structures of MnO_2 (a) pyrolusite b-MnO_2 (rutile-type) (b) birnessite type layered MnO_2 (c) spinel $\lambda-MnO_2$ (d) Atomic structure of layered MnO_2. Adapted from [79, 123][79, 122][79, 122][77, 120][77, 120]

high-κ dielectrics to to energy storage. The TMO studied in this thesis is manganese dioxide (MnO_2).

MnO_2 is one of the most stable of the manganese oxides and occurs naturally in many minerals. The structure of this oxide consists of MnO_6 octahedra sharing vertices and edges [123]. The large number of possible orientations and arrangements for these octahedra allows for the construction of 1D, 2D, or 3D tunnel structures as shown in Figure 2.15. These tunnels can be filled with water molecules or cations such as Li^+, Na^+ and K^+ [123]. The variety of structures coupled with the pseudocapacitve properties of manganese oxides [123-125] has generated a great deal of interest in large scale processing of the various polymorphs of MnO_2 [126-130]. In terms of energy storage, the layered birnessite type MnO_2 is of most interest due to its high surface area.

3

COLLOIDAL THEORY

3.1 INTRODUCTION

This thesis focuses on the exfoliation and stabilization of layered materials in the liquid phase, building on work pioneered by Hernandez et al in dispersing graphene in organic solvents [78]. Although the method of exfoliation (ultrasonication) has not changed with regard to this initial research, the mechanism for stabilization is very different. While exfoliation in organic solvents relies on favourable solution energetics to oppose re-aggregation of material, the work presented in this thesis employs electrostatic or steric stabilizing forces due to adsorbed surfactant molecules on the surface of the exfoliated nanosheets. This chapter introduces the mechanisms of stabilization by considering the attractive and repulsive forces acting on dispersed particles.

3.2 SURFACTANTS

Surfactants are usually long chained organic molecules containing both hydrophobic tails groups and hydrophilic head groups. These amphiphilic molecules tend to accumulate at interfaces between polar and non-polar media so as to minimize the number of polar solvent molecules in contact with the non-polar region of the surfactant molecules [131]. Both the ionic and non-ionic surfactants used in this thesis dissociate in aqueous media to form solutions at low concentrations. The local concentration of molecules tends to be greater at the air/water or container/water interfaces reducing contact between the hydrophobic tails groups and water molecules [132]. This also occurs at the interface between water and any dispersed hydrophobic material. The areal density of surfactant molecules at these interfaces increases with increasing surfactant concentration in solution reaching its peak once a monolayer coating is formed. This layer of adsorbed surfactant molecules can act as a stabilizer against aggregation aggregation of dispersed materials. Surfactant molecules can also

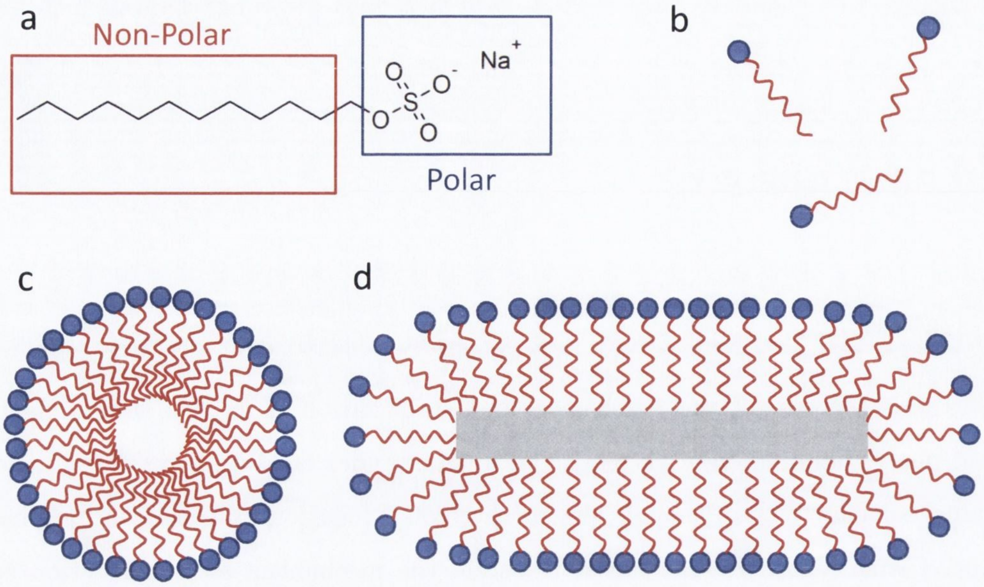

Figure 3.1: (a) Molecular structure of typical surfactant (in this case SDS). (b) randomly orientated free surfactant molecules in solution (c) self-assembled micelle structure (d) adsorption of surfactant at water/hydrophobic solid interface

interact with each other to form aggregates in solution in order to minimize the contact between hydrophobic tails groups and water. Above a critical concentration in solution, surfactant molecules will form clusters whereby their tail groups will form a core region surrounded by hydrophilic head groups as shown in Figure 3.1. These aggregates are known as micelles and will form mostly spherical aggregates however the exact size and shape will depend on a number of factors such as molecular geometry and concentration of the surfactant molecules or solution temperature and pH. The concentration at which these micelles are formed is known as the critical micelle concentration (CMC) and varies from surfactant to surfactant. To understand how surfactant molecules stabilize particles in colloidal dispersion it is first necessary to consider the interaction between particles, specifically the attractive potential between them.

3.3 VAN DER WAALS ATTRACTIVE POTENTIALS

The origin of attraction between colloidal particles are weak interactions known as van der Waals interactions. Van der Waals is a general term used to describe a number of interactions (Keesom, Debye and London dispersion) arising from permanent, induced and fluctuating dipole moments within atoms resulting in a net

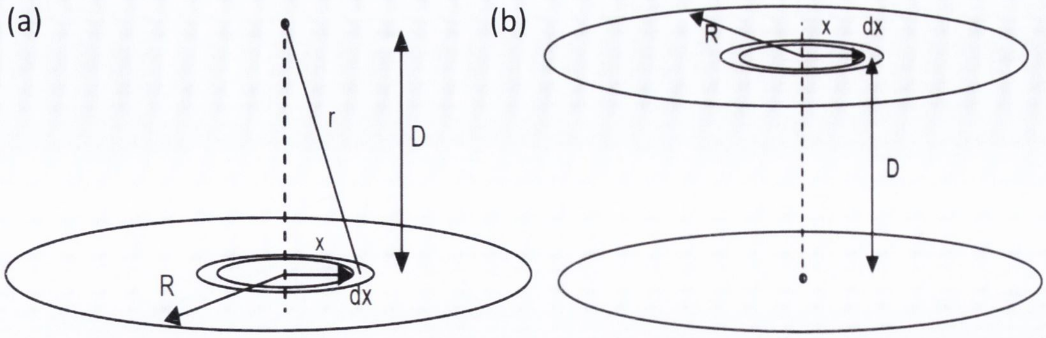

Figure 3.2: Diagram of van der Waals interaction between (a) an atom and a planar atomic sheet (b) two planar atomic sheets [81]

attractive force [131]. As all three interactions are between dipoles and have the same distance dependence it is useful to describe them in one general term.

The attractive van der Waals potential between two sheets can be approximated as a function of separation by first considering the interaction between a single free atom and a circular two-dimensional sheet with radius R separated by distance D. Considering a ring of atoms, of radius x and thickness dx, in the sheet such that the ring contains dN atoms where

$$dN = 2\pi\rho x dx \qquad (3.1)$$

where ρ is the areal number density of atoms per sheet. The free atom is attracted to the atoms in the ring by van der Waals interactions. The energy of interaction between the free atom and any one of the atoms in the ring is given by

$$V = \frac{C}{r^6} = \frac{C}{(x^2 + D^2)^3} \qquad (3.2)$$

where C is a constant dependant on the polarizability of the atoms [132]. Combining Equations 3.1 and 3.2 gives the total energy of interaction between the free atom and the entire ring

$$dV_{atom-sheet} = -\frac{2\pi\rho C x dx}{x^2 + D^2{}^{\ 3}} \qquad (3.3)$$

The total interaction energy between the atom and sheet can be found by integrating this over the area of the sheet. As van der Waals attractions are short range the upper limit can be set as ∞ rather than R

$$V_{atom-sheet} = -2\pi\rho C \int_0^\infty \frac{x dx}{x^2 + D^2{}^{\ 3}} = -\frac{\pi\rho C}{2D^4} \qquad (3.4)$$

This model can be extended by considering a second sheet of radius R, parallel and separated from the first by a distance D containing an identical ring of atoms in the second sheet of radius x and thickness dx. Every atom in this ring is attracted to the lower sheet with potential energy of attraction described in Equation 3.4. This means the total potential energy of interaction of all the atoms in the ring with the lower sheet is the product of Equations 3.1 and 3,4 such that

$$dV_{sheet-sheet} = -\frac{\pi^2\rho^2 C x dx}{D^4} \qquad (3.5)$$

The total van der Waals interaction (V_{vdW}) is found by integrating between $x = 0$ and $x = R$ to give

$$V_{vdW} = -\frac{\pi^2\rho^2 C}{D^4}\int_0^R x dx = -\frac{\pi^2\rho^2 R^2 C}{2D^4} \qquad (3.6)$$

It is important to note that this model is only an approximation as it is based primarily on the London inter-atomic potential which fails to take into account retardation effects. In order to create a stable dispersion of nanosheets, a repulsive potential must be introduced to oppose the attractive van der Waals potential. This means that the stability of any colloid will depend on the sum of the attractive and repulsive potentials as set out in DLVO (Derjaguin, Landau, Verwey and Overbeek) theory. The source of this repulsive potential can be electrostatic or steric in nature.

3.4 ELECTROSTATIC & STERIC REPULSION

Ionic surfactants dissociate in water forming a large molecular ion and counterion. As a result surfactant molecules adsorbed to the surface of a particle create a local increase in the concentration of counterions. This region is known as the electric double layer and can be divided into two parts. The first is the inner region where ion

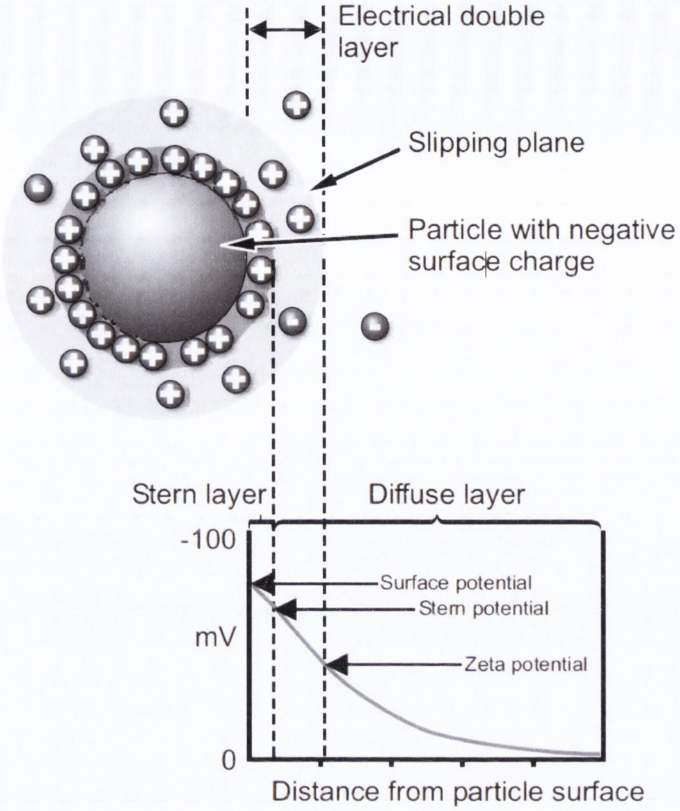

Figure 3.3: Electrostatic potential near a positively charged colloidal particle illustrating the source of the zeta potential.[133]

are strongly bound to the particle and is known as the Stern Layer. The second is a more diffuse layer of ions. The edge of this region is defined as the boundary inside which particles and ions form a stable entity i.e. when the particle moves these ions move with it. This boundary is known as the slipping plane. The electrostatic potential at any point a distance x from a charged surface has a general form

$$V = Be^{-\kappa x} \qquad (3.7)$$

where B is a constant and κ^{-1} is the Debye screening length and is a measure of the thickeness of the double layer [132, 134]. The electric potential at the edge of the slipping plane is known as the zeta potential. The magnitude of the zeta potential gives the best indication of stability within a charged colloidal system. If all the dispersed particles have large negative or positive zeta potentials the resulting repulsive electrostatic potential will be large enough to oppose the attractive van der Waals potential thus stabilizing particles against aggregation. Changes in pH of a system greatly affect the zeta potential and hence stability. For example, in the case of a negatively charged colloidal dispersion, the addition of acid will result in charge neutralization causing the magnitude of the zeta potential to decrease. The point at which a colloid has zero zeta potential due to charge neutralization is called the isoelectric point and is generally the least stable of the system [133].

A more widespread mechanism for stabilization of colloidal systems is steric stabilization. In this case particles are stabilized by an osmotic repulsive pressure between them caused by the interaction of long chain molecules adsorbed on their surfaces [131]. The steric stabilizing agents used in this thesis are non-ionic surfactants. For non-ionic surfactants the hydrophilic head group usually consists of polymeric organic molecules. These long chains are hydrophilic due to the presence of hydroxyl groups. The hydrophobic portion of the molecule adsorbs to the surface of the particle leaving these chains protruding outwards forming brush like coatings. When two particles with adsorbed layers approach each other, interaction of the two layers takes place. The degree of stabilization can be expressed quantitatively in terms of the energy change occurring upon the interaction of the adsorbed layers [132]. The free energy of mixing ΔG_{mix} of the of the adsorbed layers as particles approach each can be expressed

$$\Delta G_{mix} = \Delta H_{mix} + T\Delta S_{mix} \qquad (2.1)$$

If ΔG_{mix} is negative upon the overlap of the adsorbed layers, aggregation of the particles will occur, while a positive value will result in stabilization. As the adsorbed layers approach each other and segments begin to become compressed. These polymeric segments have fewer possible configurations in a compressed state than in an uncompressed state resulting in a decrease in configurational entropy. The result is a positive free energy of mixing and hence repulsion between the particles, preventing aggregation. Both mechanisms for stabilization of two-dimensional materials in aqueous surfactant solutions are discussed in more detail in Chapter 5 with specific regard to graphene.

4

METHODS AND CHARACTERISATION

4.1 INTRODUCTION

This chapter discusses the main sample preparation techniques and characterisation methods used in this work. Layered materials were exfoliated and dispersed by ultrasonication of bulk layered materials in aqueous surfactant media. The dispersions were centrifuged to remove any remaining unexfoliated starting material and large aggregates. Dispersions were characterised in the liquid phase using absorption spectroscopy to determine concentration as well as temporal stability. In addition, laser doppler velocometry was used to measure the zeta potential. The remaining characterisation techniques were performed on solid material filtered or deposited from the dispersions. Raman spectroscopy was used examine the composition of the dispersed and bulk materials while scanning electron microscopy was used to study thin films and powders deposited on silicon substrates. Transmission electron microscopy was used extensively to measure lateral dimensions and thickness of exfoliated flakes. All these techniques will be examined in more detail below.

4.2 SAMPLE PREPERATION

4.2.1. *Ultrasonication*

As discussed in Chapter 2, liquid phase exfoliation of layered compounds is a two-step process whereby the interlayer attractions are overcome and the resulting exfoliated material is stabilized electrostatically/sterically or by favourable solution energetics. While the first step can be aided by a reduction in the interlayer attractions afforded by certain processing techniques such as ion intercalation, some energy is always required in order to break these bonds completely. This can be provided in the form of thermal shock or ultrasonication.

Ultrasonication is the agitation of a sample through physical vibration. The transfer of vibration to the sample causes solvent molecules to oscillate, resulting in compression and rarefaction cycles. If the rarefaction is large enough then the critical molecular distance can be exceeded resulting in the formation of cavities within the solvent. The growth and collapse of these cavitations creates shock waves and sheer stress is applied to the material dispersed in the liquid [135]. As the interlayer attractions are considerably weaker than the interatomic bonds, the sheer stress cleaves individual and few-layer sheets from the bulk layered structure. Despite the anisotropy in bond strengths, experiments on low dimensional materials like CNT bundles have shown ultrasonication to result in scission as well as exfoliation [135-138]. The scission exhibits an inverse power law relationship with sonication time t, such that

$$L \propto \frac{1}{\sqrt{t}} \qquad (4.1)$$

where L is the longest axis of the nanomaterial [135]. Recent work on solvent exfoliation of graphene has reported a similar trend for two dimensional nanosheets [139]. The level of sonication induced exfoliation and scission varies significantly with a number of parameters such as time, energy density, frequency of implosion events and the spatial distribution of cavitations.

A sonicator is any device that converts and electrical signal into physical vibrations. There are two types of sonicator used in this work: an ultrasonic bath and an ultrasonic tip. The ultrasonic baths used in this work have a fixed frequency of 20 kHz with a 2L capacity. Of the two types of sonication, this has the lowest power output typically 25W. The sample are positioned and held inside the bath during sonication. While this is a reliable and cheap method of sonication, the low power means that long sonication times are required to achieve reasonable concentrations. The main problem however is with reproducibility. Interference of waves causes nodes to be formed in the bath leading to inhomogeneity in energy distribution. This coupled with changing water levels due to heating makes the sample reproducibility poor. As a result this method of sonication was not employed in any of the studies varying parameters in Chapters 5, 7 and 8. Instead sonic baths were used only to homogenise hybrid dispersions or to produce large volumes used to make composites. A more reproducible sonication technique involves using an ultrasonic probe rather than bath.

In this system the vibrations are transferred by a probe place within a sample rather than placing the sample into a bath. This allows the user to control the exact energy input into the sample by adjusting amplitude and sonication time. Much shorter sonication times are required to produce dispersions of reasonable concentrations due to the much higher power output (750W) compared with a bath. The probe can either be a point or a horn tip with the latter used more frequently in this work due to the larger volumes required. The ability to pulse the vibrations as well as the adaptability with coolant systems makes control over the ambient temperature in samples much more straightforward

.

4.2.2. *Centrifugation*

As previously discussed in Chapter 2, sonication assisted dispersion of layered materials in solvents and surfactant yields a mixture of mono, few and many-layer sheets as well as unexfoliated bulk and aggregated material. The earth's gravitational field is sufficient to separate the larger/higher density particles as they typically sediment at a faster rate than smaller or less dense particles. This sedimentation of particles, can be modelled approximately by the Stokes equation, which describes the movement of a sphere in a gravitational field [140]. The equation relates the velocity of sedimentation, v to five other parameters

$$V = \frac{d^2(\rho_p - \rho_m)g}{18\eta} \qquad (4.2)$$

where d is the diameter of the particle, η is the viscosity of the medium, g is acceleration due to gravity and ρ_p and ρ_m are the densities of the particle and medium respectively. The rates can be quite slow depending on the difference in densities between the particles and media and the size of the particles themselves. In addition, the gravitational force for smaller particles can often be insufficient to overcome the molecular forces in dispersion. It is therefore necessary to artificially increase the magnitude of the gravitational field in order to remove undesired large aggregates in a more timely fashion or indeed to aid effective separation of smaller stable particles in dispersion. This is achieved in the centrifuge by increasing the centrifugal force through increased rotational speed. The radial force generated by the spinning rotor in a centrifuge is sometimes expressed relative to the earth's gravitational force and is known as the relative centrifugal force (RCF). This will depend on both the rotational speed and radius of the rotor. In this work a Hettich Mikro 220R centrifuge was used for all samples with a constant temperature of 35°C. The machine has a variable rotation rate with a fixed 6 way rotor of radius 90mm. As such all centrifugation rates (CF) are quoted in revs per minute (RPM) for this rotor. Recent work in the Coleman group has shown that it is possible to tailor the lateral flake dimensions for dispersions of layered materials by using multiple centrifugation steps as well as varying rotational speeds. Chapter 9 contains similar work on surfactant stabilised MoS_2 while Chapter 5 presents an alternative method for separation that will be discussed in the next section. `

4.2.3. *Size exclusion column chromatography*

Size exclusion chromatography separates particles according to their different sizes as they pass through a porous filtration medium packed tightly into a column. In contrast to other chromatographic techniques such as ion exchange or affinity chromatography, particles do not bind to the medium. This is one of the principle advantages to this method allowing for a range of materials and solvents to be used. This kind of filtration technique is widely used for the separation of biomolecules but has more recently been applied to the purification of CNT dispersions [141-143].

The experimental setup consists of a medium often referred to as a “gel” packed tightly into a vertical column. This gel consists of small spherical particles with a controlled pore size. Silica is often used as it is critical that the gel medium be chemically and physically stable with low reactivity and adsorptive properties [144]. The rest of the column is filled with a buffer medium (in the case of liquid dispersions of particles, the buffer medium is composed of the dispersant/solvent used). When a polydispersed material is injected at the top of the column the volume available to particles varies depending on their diameter. Depending on the pore size of the media some particles will be able to enter whereas others cannot. These can be split up into three groups: (i) particles with no access to the pores (ii) particles with partial access and particles with complete access. Figure 4.1 shows the varying concentrations of sample components as they elute from the column in order of their size. Material that

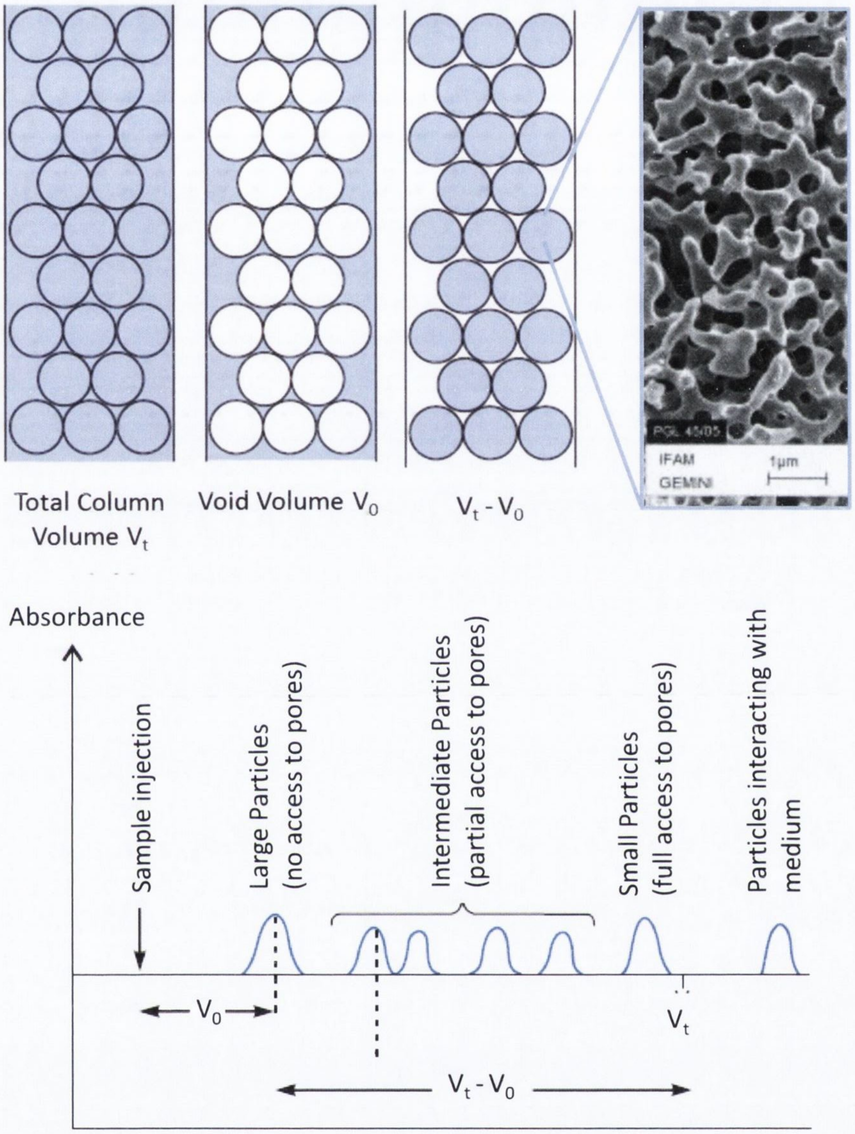

Figure 4.1: Size exclusion chromatography: Top: Column set up with SEM micrograph of porous silica gel. Bottom: Elution volumes for different particle sizes. Adapted from [144].

is too large to enter the pores passes directly through the column at the same rate as the buffer and hence is eluted at the void volume V_0. Molecules with partial access to the pores will elute at a slower rate compared to the buffer with smaller particles taking longer. Finally particles with full access to the pores will have a much slower elution rate and will generally elute around the total column volume.

While it can be rather straightforward to remove a group of smaller particles from a dispersion in this manner, fractionation requires high resolution. It is clear from Figure 4.1 that the resolution of the column is highest for particles with partial access to the pores. This means that the resolution for any fractionation will depend on the mean pore size compared to the size distribution of the starting dispersion. The size range over which a gel medium can separate particles is known as the selectivity of the medium and is the most crucial factor in ensuring good resolution. Many other parameters will also affect the final resolution of the column. These include sample to column volume ratio, column height, packing density, flow rate and viscosity of the buffer [144].

4.3 SAMPLE CHARACTERISATION

4.3.1. *Absorption spectroscopy*

Light can interact with a material in many different ways. Incident light can have its path altered by either reflection or refraction caused by an interface between two media however it is of more interest how the light behaves as it propagates through a given media. Absorption spectroscopy measures the attenuation of a beam of light as it passes through a sample. This can generate a great deal of physical information on a sample such as electronic structure and particle size. The two main processes contributing to attenuation of a beam of light when passed through a sample are scattering and absorption with the measured attenuation being the sum of the two processes.

Scattering occurs when photons interact with heterogeneous media causing them to change direction. This is an elastic process if no energy is exchanged between the photon and the medium and is generally known as Rayleigh scattering, however inelastic scattering also occurs. Absorption occurs when the frequency of the light matches electronic transitions in the medium. Depending on the material, valence

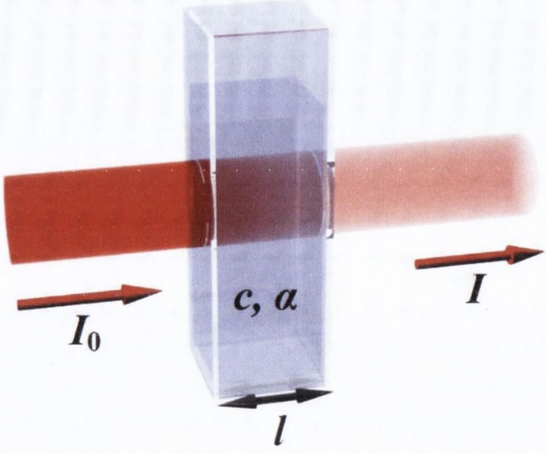

Figure 4.2: Illustration of Beer-Lambert law

electrons can be excited by light in the UV(200-400nm), visible (400-800nm) and near infrared (800-2500nm) ranges of the electromagnetic spectrum. An absorption spectrometer can probe the electronic properties of a material by simply measuring absorption over a range of wavelengths with characteristic spectra generated for different materials. The speed and ease of this measurement make this kind of spectroscopy extremely useful when dealing with dispersed nanomaterials. Luminescence can also occur when light interacts with a material. This is the process of spontaneous emission of light by excited atoms. While it is related to absorption it does not always accompany it as non-radiative relaxation processes can occur in some systems.

For liquid samples, the attenuation for a given wavelength will increase with increasing concentration as the number of scattering/absorbing particles increases. This is easily quantified and allows for quick and accurate determination of concentration. Consider the beam of monochromatic light passing through a sample of total thickness l as show in Figure 4.2. The reduction in intensity of the beam dl is proportional to the intensity of the incident beam, the number of scattering/absorbing particles (concentration) and the length such that

$$dI = -\beta ICdl \quad (4.3)$$

where β is a constant. Integrating over the length of the sample

$$\int_{I_o}^{I} \frac{dI}{I} = -\beta C \int_{0}^{l} dl \qquad (4.4)$$

$$\ln\left(\frac{I}{I_0}\right) = -\beta Cl \qquad (4.5)$$

This can be re-written in terms of logarithmic base 10 by introducing a constant α such that $\alpha = \beta ln10$

$$\log_{10}\left(\frac{I}{I_0}\right) = -\alpha Cl \qquad (4.6)$$

The absorbance is related to the transmittance by

$$A = -\log_{10} T = -\log_{10}\frac{I}{I_0} \qquad (4.7)$$

Hence by combining equations 4.6 and 4.7

$$A = \alpha Cl \qquad (4.8)$$

This is known as Beer-Lamberts law where α is known as the extinction coefficient. Knowledge of this value for a given wavelength/material allows concentration to be determined from measured absorbance. As the measured attenuation of the beam will be due to both absorbance and scattering, it is important to separate the two when analysing spectra and generating concentration values (i.e. absorption = extinction – scattering). This can be done by extrapolating the scattering background from regions where absorption is not the dominating phenomenon and subtracting it from the measured spectra. This method is discussed in more detail in Chapter 7.

All absorption measurements carried out for this work were performed using a Cary Varian 6000i spectrophotometer with a spectral resolution of 0.05nm over a scanning range of 190-1800 nm. Figure 2.3 shows a schematic of the spectrometer setup with a tungsten halogen lamp for NIR and visible wavelengths and a deuterium arc source for ultraviolet wavelengths [145]. A dual beam configuration allows for simultaneous measurement of absorbance across the sample and a reference. This reference contains

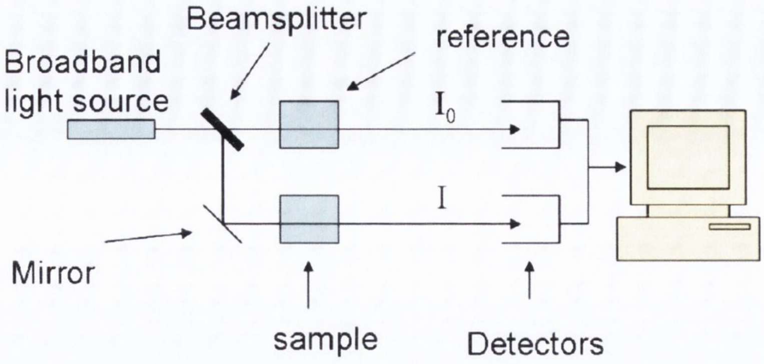

Figure 4.3: Schematic of UV-Vis-NIR spectrometer

an identical cuvette filled with the same solvent as the sample of interest. In the case of solid samples such as thin films, the reference consists of a matching substrate.

4.3.2. *Sedimentation Analysis*

Absorption measurements can also be used to assess the temporal stability of a dispersion of nanomaterials by recording the change in concentration over time. As large aggregates and unstable particles sediment out over time, the concentration will change and hence the optical absorbance will decrease. The total concentration, C can be expressed as the sum of the concentrations of the stable and sedimenting phases

$$C = C_0 + \sum_n C_n \qquad (4.9)$$

where C_0 is the concentration of the stable phase and C_n is the concentration of the sedimenting phases. Recent work on dispersed nanomaterials has shown the concentration of these unstable phases to decay exponentially with each phase having a characteristic time constant such that

$$C(t) = C_0 + \sum_n C_n e^{-t/\tau_n} \qquad (4.10)$$

where τ_n is the decay constant of phase n [146]. All sedimentation measurements for this work were carried out on a homemade apparatus consisting of four lasers (λ = 650 nm) and four photodiodes. The lasers were set to run, with synchronised pulse duration of 30ms over a period of days or weeks. The 4 transmission spectra of the laser light through the dispersion, was then averaged and converted to absorbance.

4.3.3. *Zeta Potential*

As previously discussed in Chapter 3, the zeta potential is a measure of the effective electric potential at the edge of the electric double layer surrounding charged colloidal particles. It is therefore an important and useful quantity to measure as the magnitude of the zeta potential will give some indication as to the stability of surfactant stabilized nanomaterials. If particles in dispersion have a large negative or positive zeta potential then they will tend to repel each other, however, if the particles have low zeta potential values then there can be insufficient force to prevent the particles coming together and aggregating. As a general rule, particles with zeta potentials of magnitudes greater than 30mV are normally considered stable.

Zeta potential measurements are made by examining the electrokinetic behaviour of the charged particles within a colloid. An electric field is applied across the sample resulting in charged particles migrating towards the electrode of opposite sign. Viscous forces tend to oppose this motion however when equilibrium is reached the particles move with a constant velocity. This is known as electrophoresis. The electrophoretic mobility (μ) of the particles will depend on this drift velocity as well as the strength of the electric field (E) such that $\nu = \mu E$. This can be used to determine the zeta potential (ζ) using the henry equation for spherical particles:

$$\zeta = \frac{3\eta\mu}{2\varepsilon_r\varepsilon_0 f(\kappa a)} \qquad (4.11)$$

where η is the viscosity of the medium $f \ \kappa a$ is henrys function, a is the particle radius and κ is the inverse of the Debye length [133].For water $f \ \kappa a = 1.5$ as the thickness of the electric double layer compared with the radius of the particle will be small and hence $\kappa a \gg 1$. This gives the Smoluchowski expression which holds for plate like particles [147].

From equation it is straightforward to calculate the zeta potential by measuring the electrophoretic mobility. All such measurements for this work were carried out on a Malvern Zetasizer Nano where samples are injected into capillary tubes with built in electrodes as shown in Figure 4.4. In this setup the velocity of the particles is

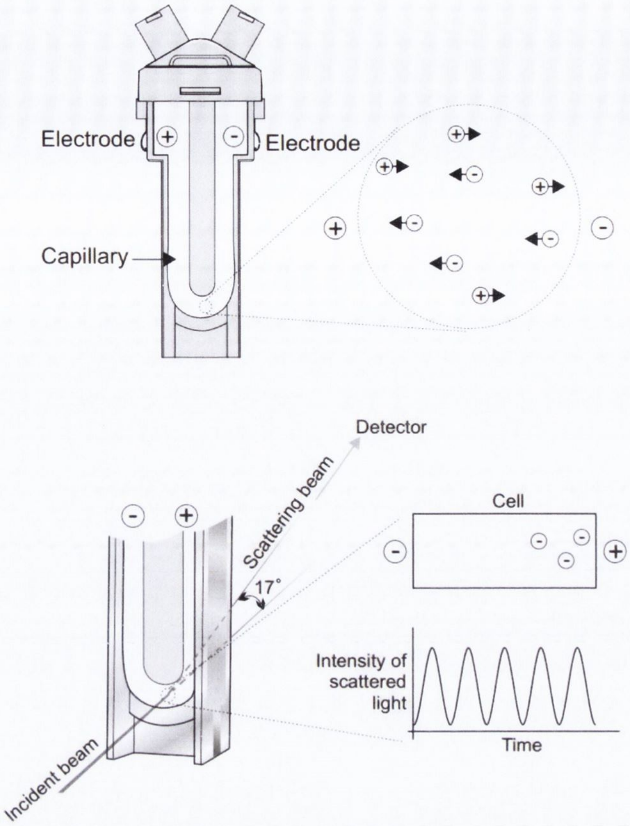

Figure 4.4: (a) Electrophoresis in a capillary cell (b) Diagram of laser Doppler velocimetry measurement. Adapted from [133]

measured using laser Doppler velocimetry. This technique analyses the scattered laser light through the cell. This produces a signal with oscillating intensity, the frequency of which is proportional to the speed of the particles. A similar technique has been applied by Lotya et al to determine the average flake size for dispersions of layer material using a dynamic light scattering measurement [148].

4.3.4. *Raman Spectroscopy*

While the vast majority of photons incident on a material will be Rayleigh scattered (elastically), some will be scattered inelastically. This will involve an energy exchange between the photon and the material characterized by a frequency shift in the scattered light. This effect was first observed by Indian physicist Chandrasekhar Venkata Raman in 1928 who was awarded the Nobel Prize two years later for his work in this field. Incident monochromatic light such as laser light is incident on a

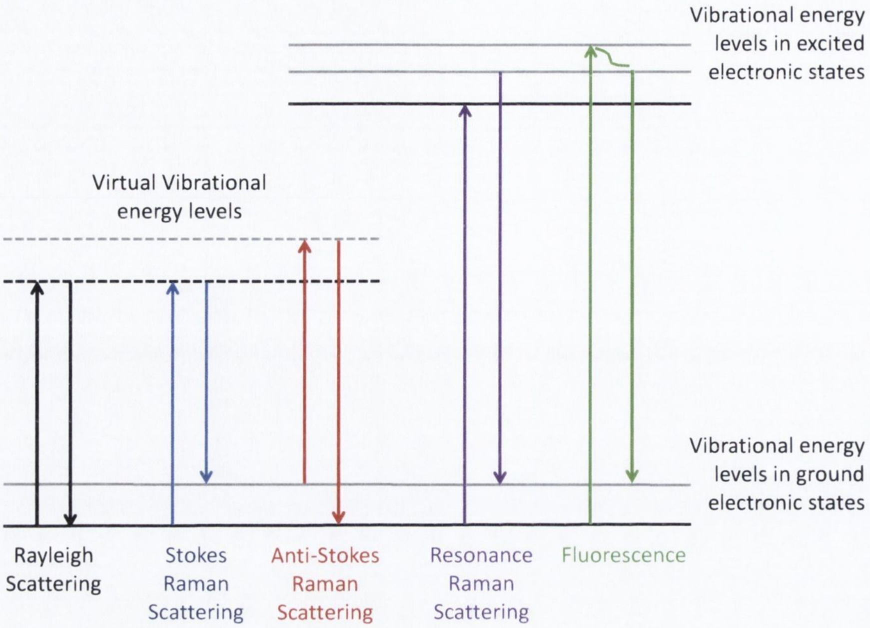

Figure 4.5: Diagram of relevant transitions in Raman Spectroscopy

material, photons interact with the molecules inducing a dipole moment which in turn radiates scattered light. The strength of the dipole moment will depend on the polarizability of the molecule - a material property that depends on the molecular structure and nature of the molecular bonds. For any bond, the individual atoms are confined to specific vibrational modes, in which the vibrational energy levels are quantized. Thus the excitation and emission process results in scattered photons with a characteristic frequency shift for each bond. This phenomenon makes Raman spectroscopy an extremely useful tool for probing the chemical bonding in materials.

The transitions involved in Raman scattering are summarised in Figure 4.5. Raman scattering events most commonly occur between ground state vibrational energy levels and virtual excited states. Upon interaction with the incident photon, the molecule is excited from its ground state to a virtual state. It then relaxes to another vibrational state of higher energy compared with the ground state by emission of a photon. This is known as Stokes Raman scattering and occurs when the material gains vibrational energy resulting in a scattered photon of reduced frequency. This frequency is determined by the energy difference between the ground and final relaxed states. Anti-Stokes Raman scattering occurs when the excited molecule returns to a lower energy level than the one it started in. In this case the emitted photon has gained energy when compared with the incident photon and hence will be of a higher frequency. In general Stokes scattering is much more intense than anti Stokes since it depends on the number of molecules in the ground state whereas anti Stokes can only occur for molecules in higher energy levels.

When the frequency of the incident photons matches that of an electronic transition, resonant Raman scattering can occur, significantly increasing the sensitivity of the measurement. Fluorescence can also occur under these conditions. This can obscure spectral features as more relaxations (the result of transitions between two excited electronic states) produce more scattered photons of different frequencies. A Raman spectrum is a plot of Raman scattering intensity versus the Raman shift υ,

$$\nu = \frac{1}{\lambda_i} - \frac{1}{\lambda_s} \qquad (4.12)$$

where λ_i is the wavelength of the incident light and λ_s the wavelength of the scattered light. The Raman shift is a measure of the energy of vibration for a given bond and can be considered a "fingerprint" for that bond. For a sample to be Raman active its polarisability must change when exposed to incident light. Molecules with pi-bonds are easily polarised and hence good Raman scatterers. This makes Raman spectroscopy a particularly important technique when investigating carbon materials.

Raman Spectroscopy of Graphene & MoS_2

The sp^2 and sp^3 type carbon materials are highly Raman active with well-defined spectral features [149], As a result Raman spectroscopy has proved to be a powerful tool in the characterization of fullerenes [150], CNTs [151-153] and most recently Graphene [154-157]. The Raman spectrum for graphite has three main features: the D, G and 2D bands at $1340cm^{-1}$, $1580cm^{-1}$ and $2700cm^{-1}$ respectively.

The D band is a related to the disorder and hence defects in sp^2 carbon materials. It is a second order process as the transition associated with it requires a defect in order to occur. This can be in the form of an edge, atomic vacancy or presence of functional groups. The G band is first order scattering process and is characteristic of all sp^2 hybridised carbon. Broadening of both the D and G bands are associated with increasing disorder. The 2D band often referred to as G' is a second order scattering process involving a second phonon rather than a defect. A relative in increase in the 2D band can be attributed to increased graphitization [158]

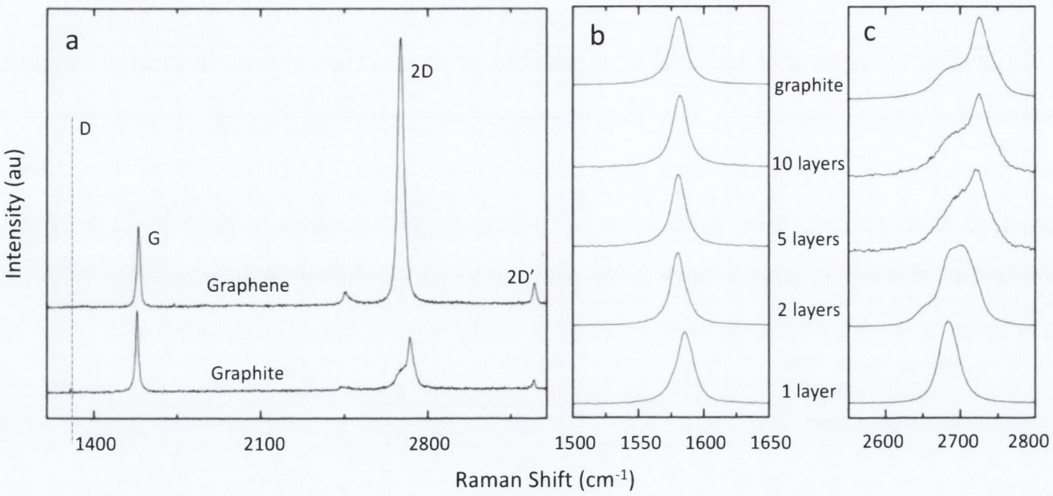

Figure 4.6: a) Raman spectra of bulk graphite and graphene. b-c) variation in G band (b) and 2D band (c) with number of layers. Adapted from [159]

In 2006 Ferrari et al. reported the effect of varying number of graphitic layers on these spectral features. Ferrari and co-workers used both a green and a red laser excitation on mechanically cleaved graphite with the results shown in Figure 4.6. The absence of a D band in these spectra indicates the absence of either edge or point defects in the lattice. This is due to the high quality (HOPG) starting material as well as the production method – yielding samples with crystallite sizes larger than that of the laser spot. The most striking difference between the spectra is the evolution of the 2D band from bulk graphite to few and monolayer graphene. While there are numerous contributions to the 2D band for bulk graphite, the signal for a monolayer is a single narrow Lorentzian peak. A D'-band around 1620 cm^{-1} can also appear and is associated with defects. The double-resonance 2D'-band can be seen in Figure 4.6a around 3240 cm^{-1}[193]. The intensity ratio I_{2D}/I_G is approximately 4 for monolayer graphene decreasing with increasing number of layers. This makes it possible to estimate the thickness of graphene layers from Raman spectra with scanning Raman spectroscopy particularly useful, allowing for the identification of defects and edges (I_D/I_G)[160, 161] and also layer thickness (I_{2D}/I_G) [161] over large areas. Recent studies have used Raman spectra to examine the effects of strain on graphene composites [162, 163]. This work has reported a characteristic red or blue shift in the 2D indicating tensile and compressive strain, respectively [164, 165]

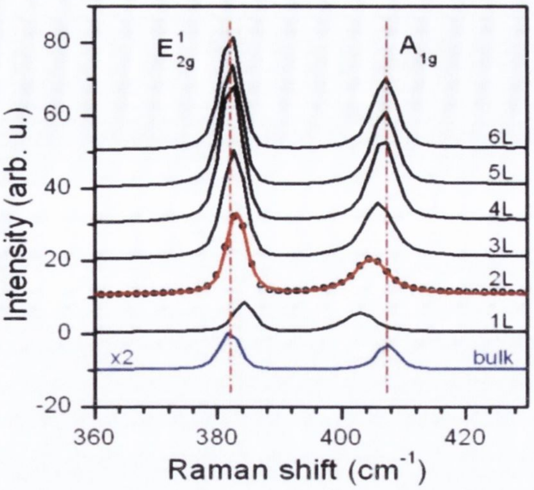

Figure 4.7: Evolution of MoS2 Raman spectrum for varying number of layers [166]

The two main Raman spectral features for MoS_2 are E^1_{2g} and the A_{1g} modes located at 383 cm^{-1} and 409 cm^{-1} respectively[166-168]. In plane vibrations are characterised by the E12g band while A1g band is associated with of out of plane vibrations. Lee et al were the first to report changes in these bands with varying number of atomic layers similar to Raman spectroscopy of graphene[166]. They demonstrated a change in frequency for both the A_{1g} and E^1_{2g} modes with decreasing number of layers, as seen in Figure 4.7. This means that the frequency change in both these modes can be used as a robust and straightforward means to quickly asses sample thickness using Raman spectroscopy.

4.3.5. *Electron Microscopy*

Electron microscopy is one of the most widely used techniques in the study of nanomaterials. The resolution of any microscope i.e. the smallest distance that can be resolved δ, can be approximated as

$$\delta \approx 0.6\lambda \qquad (4.13)$$

where λ is the wavelength of the incident radiation [169]. This means that for a conventional optical microscope using visible light, the maximum resolution is about 300nm making them unsuitable for detailed characterization of nanoscale materials

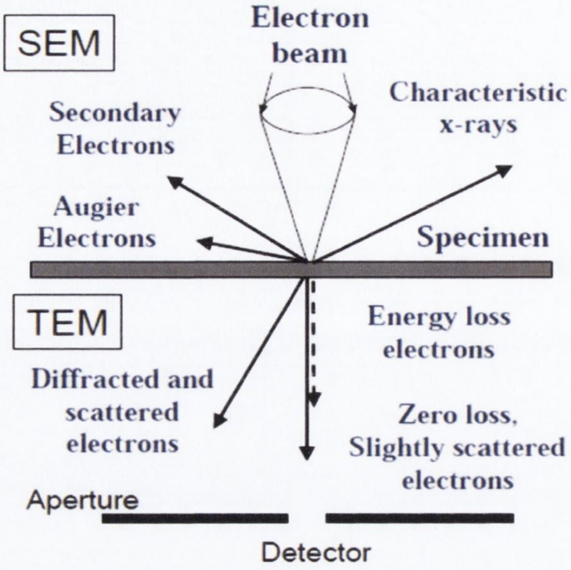

Figure 4.8: Interaction of electron beam with sample

and structures. In the late 1920's research began to focus on techniques using high energy electrons rather than photons to overcome the limits of conventional microscopy. The principle idea behind these techniques is the wavelike characteristics of electrons first proposed by de Broglie in 1925. De Broglie theorized that electrons had a wavelength much shorter than that of visible light and characterized by their energy such that

$$\lambda = \frac{h}{mv} \approx \frac{1.22}{E^{1/2}} \qquad (4.14)$$

where h is planks constant, m and v are the electon's mass and velocity respectively and E is the energy of the electron in electron volts (eV) [169]. Combining Equations 4.13 and 4.14 it is possible to estimate the resolution limit of a microscope using 100kV electrons to be ~ 4pm. At this point the advantages for such a system in the study of nanomaterials become clear as nanoscale features can be distinguished. All electron microscopes work in the same way. A coherent monochromatic beam of electrons is formed by a source through either thermionic emission or field emission and accelerated towards the specimen. The stream is confined and focused using a series of magnetic lenses and metal apertures. As shown in Figure 4.8, interactions occur inside the irradiated sample affecting the electrons emitted. It is the electrons detected that that differentiates the two main types of electron microscopy.

4.3.6. *Transmission Electron Microscopy*

Transmission electron microscopy (TEM) generates information about a sample by focusing a beam of high energy electrons on the sample under high-vacuum and examining the transmitted beam. Depending on their energy as well as the thickness of the sample, some electrons can pass through unimpeded while others will be scattered due to their interaction. The attenuation of this beam of electrons due to scattering is the source of contrast used to generate images with a TEM. A typical TEM can be divided up into 3 main components: the illumination system, the objective lens/stage and the imaging system.

The illumination system can be operated in two different modes: convergent beam and parallel beam. The first mode is mostly used for scanning transmission electron microscopy (STEM) while the second mode primarily used in this work. In this set up, the electron beam is generated by either a thermionic of field emission source for normal or high resolution work respectively. Condensing electromagnetic lenses are used to focus and manipulate the electron beam so that electrons are moving parallel to the sample before interaction occurs (Figure 4.9a). As the beam passes though the sample it becomes disrupted as electrons are scattered both elastically and inelastically with some passing straight through. Under normal imaging conditions as shown in Figure 4.9b an objective aperture is used to allow only unscattered electrons through cutting out the majority of diffracted beams. This increases the contrast when creating a final image. An intermediate lens is then used to focus an image of the sample onto a photographic plate or CCD.

Besides contrast for imaging, the electron beam can also be used to generate crystallographic information on a sample when used in diffraction mode. In this mode the objective aperture is removed with a selected area aperture used instead. This is placed in the first image plane and ensures that the beam carries only information from a selected area of the sample. If the samples are crystalline, the resulting diffraction patterns have spot positions governed by Bragg's law and can be used for the identification of mono and bi-layers of graphene.

Although Equations 4.13 and 4.14 imply a high theoretical resolution of 4pm for electron microscopy, the actual achievable resolution is limited by aberrations. Aberrations can be either spherical or chromatic in nature. Spherical aberrations are caused by inherent imperfections in the magnetic lenses used while chromatic

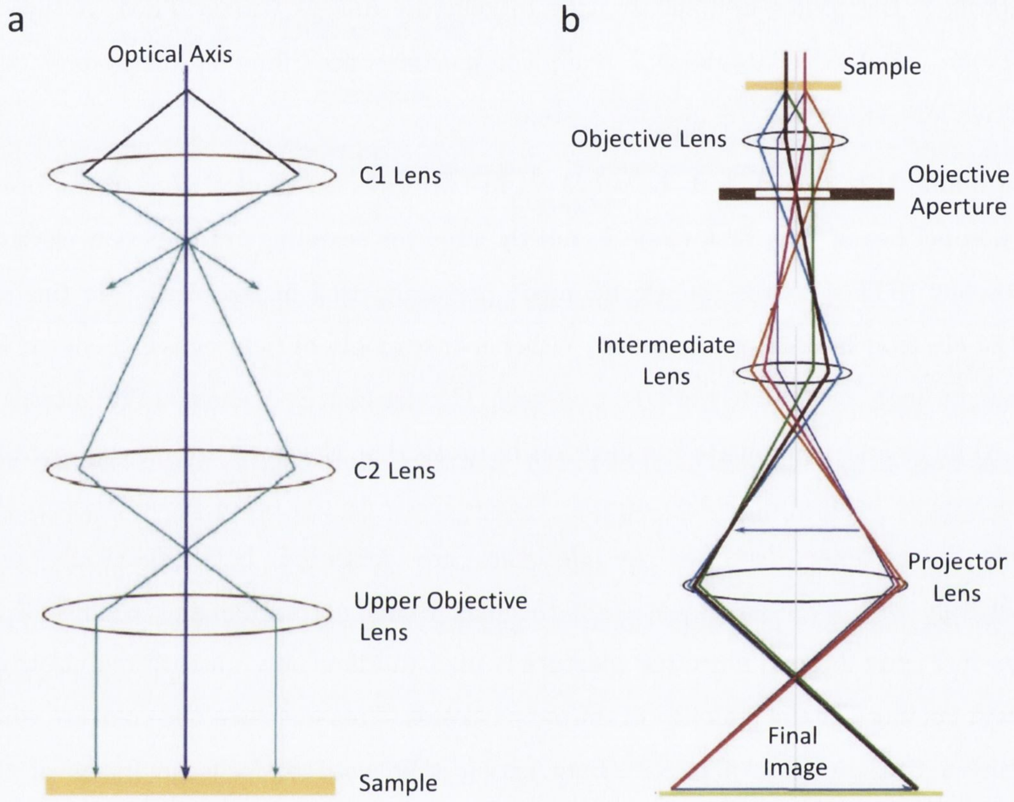

Figure 4.9: Schematic of TEM (a) illumination system (b) imaging system. Adapted from [169]

aberrations are caused by slight variations in electron energies within the beam incident on the sample. High resolution TEMs can reduce this with the use of aberration correcting lenses as well as use of a more monochromatic source. In this research normal TEM imaging was carried out using a Jeol 2100 operated at an accelerating voltage of 200 kV. This instrument has a LaB6 filament electron gun. All HRTEM was carried out by Dr. Valeria Nicolosi, then at the Department of Materials, University of Oxford using the Oxford-Jeol JEM2200MCO FEGTEM/STEM fitted with two CEOS Cs aberration correctors operating at 200 kV.

Statistical Analysis of dispersed material using TEM

In order to examine the exfoliated material produced in this work, dispersions were drop cast onto holey carbon grids using a pipette. Samples were diluted to a fixed low concentration with the same volume dropped in each case. The low concentration helps reduce aggregation while the constant deposited mass helped ensure the material distribution was the same in each case and hence better allowed for comparison of flake lengths/level of exfoliation between samples. All samples were mildly heated in a vacuum overnight to remove as much adsorbed surfactant and water as possible. Once placed in the microscope, careful adjustment of the focus, magnification and brightness allows for imaging of material deposited on the grid. The contrast between the carbon grid and graphene can be quite poor especially for thinner samples but the serendipitous alignment of flakes over the pores in the grid allows for good image contrast with the vacuum background. This is not an issue with materials containing elements of higher atomic number such as Mo as contrast improves.

Depending on the size of the object in question and the magnification, quantitative analysis can be performed on TEM images producing statistics on flake dimensions. The most easily obtained and reliable statistics are those concerning the lateral dimensions of the dispersed material. By carefully tuning the mass deposited on the grids, it is possible to ensure a reasonable areal density of flakes while still limiting aggregation. This allows several flakes to be captured in the same image and hence increases the number of counts per measurement decreasing the uncertainty in the mean values generated. As the flakes are of random shape, they were treated as rectangular with the length defined as the longest axis while the width was taken to

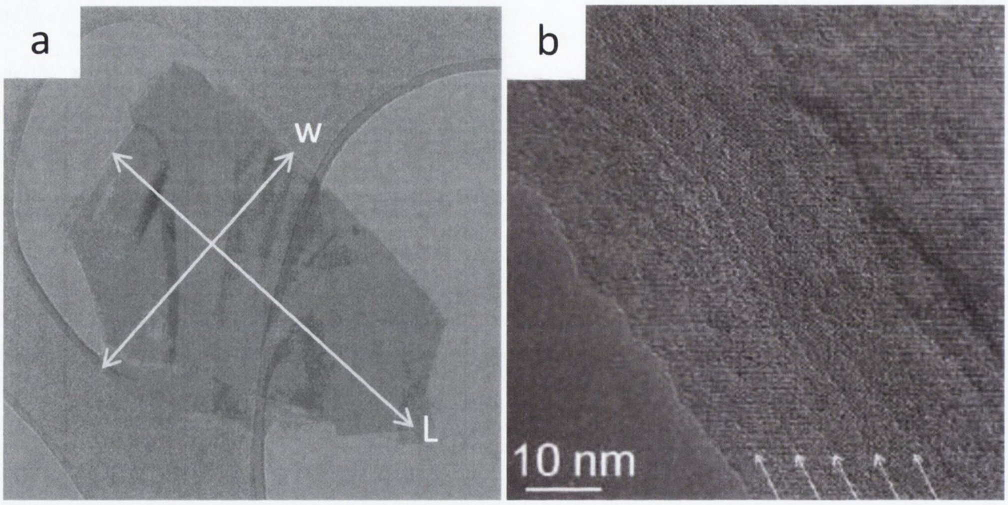

Figure 4.10: Representative images of the type used to generate (a) length and width statistics (b) layer statistics

be the largest measurement perpendicular to that axis. Figure 4.10 illustrates how these measurements were obtained.

Generating statistics on flake thickness i.e. number of layers N, is more difficult and requires more careful and selective imaging of individual flakes. This means that it is difficult to take larger sample sets and hence errors in the mean can be larger than those for lateral dimensions. This method relies on the observation that exfoliated sheets tend to have terraced edge structures with visible straight line contrast between these terraces corresponding to individual layers stacked to form multilayers. An example of the contrast seen at these edges is shown in Figure 4.10. By counting these edges, the number of layers per flake can be estimated. Although this method is not as robust as direct measurement such as AFM or electron intensity mapping using a carefully calibrated STEM, the mean values generated have proven to be in good agreement with those obtained by these techniques and will be discussed in more detail in Chapters 7 and 9.

4.2.7. *Scanning Electron Microscopy*

Like a TEM, a scanning electron microscope (SEM) uses a focused beam of electrons to probe a sample. The accelerating voltage and hence energy of the electrons is usually much lower than conventional TEM with 2 to 10 keV the most common voltages used. The optics are somewhat different than a TEM as the beam is rastered

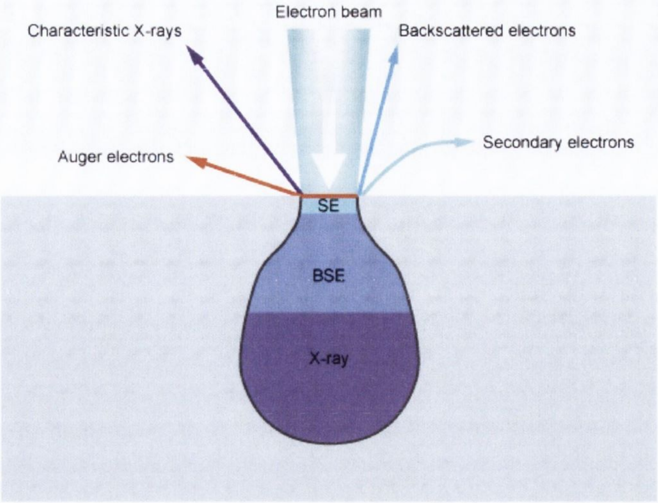

Figure 4.11: Breakdown of signals generated from interaction volume for scanning electron microscopy [170]

across the sample as secondary and scattered electrons are collected at various detectors generating a digital image. When the electron beam strikes the surface of a sample electrons penetrate to depths of about 1 µm interacting both elastically and inelastically. The volume of this interaction will depend on the energy of the incident electrons and will take the general tear drop shape shown in Figure 4.11. Due to interaction between the beam and the sample various types of radiation emerge, from this region. Backscattered electrons and secondary electrons can be used to generate images while characteristic x-rays can also be detected generating data on chemical composition.

Secondary electrons give good topographical information as they are generated by ionization of the sample by the incident beam. This means they have low energy around 3-5 eV and hence have a small escape depth of only a few nanometers. Backscattered electrons give good contrast between materials of varying atomic number as this affects the level of scattering. Backscattered electrons are high energy and inelastically scattered coming from much deeper inside the sample. All SEM analysis in this thesis was performed on a Zeiss Ultra Plus SEM using a Lab_6 source.

4.2.8. *Thermogravimetric Analysis*

Thermogravimetric analysis (TGA) is an analytical technique in which the mass of a sample is measured as a function of temperature or time as the sample is subjected to a controlled temperature under controlled atmospheric conditions. TGA can provide information about phase transitions such as vaporization, sublimations, adsorption and desorption. It can also provide information on sample composition based on characteristic decomposition, desolvation or oxidation and reduction [171]. The TGA operates by placing a small mass (3-5mg) of the material of interest into a sample pan supported by a precision balance. The pan is then inserted into a small electrically heated furnace equipped with a thermocouple and is heated up to 1000°C. with the mass of the sample monitored during the experiment. A sample purge gas controls the sample environment. This may be inert or a reactive gas that flows over the sample [171].

TGA can operate in two modes, either by measuring the time taken to achieve a constant rate of mass loss or by measuring the mass loss as the sample is heated at a constant rate. The former can provide information on reaction kinetics while the latter is used in compositional analysis. The thermogravimetry presented in Chapter 7 is used to estimate the surfactant content in thin films of MoS_2. This is achieved by comparing mass loss versus temperature curves for thin films of MoS_2 with the curves for the surfactant and MoS_2 powders alone. The apparatus used in this work was a Perkin Elmer Pyris TGA with a temperature range from 35 to 1000°C and a resolution of 5°C. All measurements carried out used a minimum of 3mg and had a constant heating rate of 10 °C per min. Besides material composition, TGA can be used to assess the thermal stability of sample over a desired temperature range as well as defining the upper temperature limits for use of a given material.

5

DISPERSION OF GRAPHENE IN AQEUOUS SURFACTANT MEDIA

5.1 INTRODUCTION

Over the last few years, it has become clear that graphene will be extremely useful both for fundamental studies and for a range of applications [19, 172]. Previous work has shown that graphene can be produced in large quantities by exfoliation of graphite in certain solvents [78, 139, 173, 174] or surfactants [81, 175, 176]. Of these methods, surfactant dispersion is perhaps the most promising because the use of toxic solvents is avoided. Although previous work has shown that such methods give reasonably large quantities of good-quality graphene, there is still much scope for improvement. For example, it is difficult to prepare high-concentration dispersions and flake sizes larger than 1μm^2. In addition, the dispersed graphene comes as both mono- and multilayers.

To improve the concentration and quality of surfactant-stabilized graphene dispersions, it is critical to gain an understanding of the physics and chemistry of the stabilization process. Such an understanding will aid surfactant choice and process optimization, resulting in better dispersions. In this chapter, a study of dispersibility of graphene in a range of surfactants is presented. The effect of surfactant choice on exfoliation state is investigated by TEM analysis of the dispersed material. Most importantly, a relationship between surfactant choice and dispersed concentration is established.

5.2 EXPERIMENTAL PROCEDURE

The surfactants used in this study were: sodiumdodecylsulfate (SDS), dodecylbenzenesulfonic acid (SDBS), lithium dodecyl sulfate (LDS), cetyltrimethyl ammoniumbromide (CTAB), tetradecyltrimethylammonium bromide (TTAB), sodium cholate (SC), sodium deoxycholate (DOC), sodium taurodeoxycholate (TDOC)

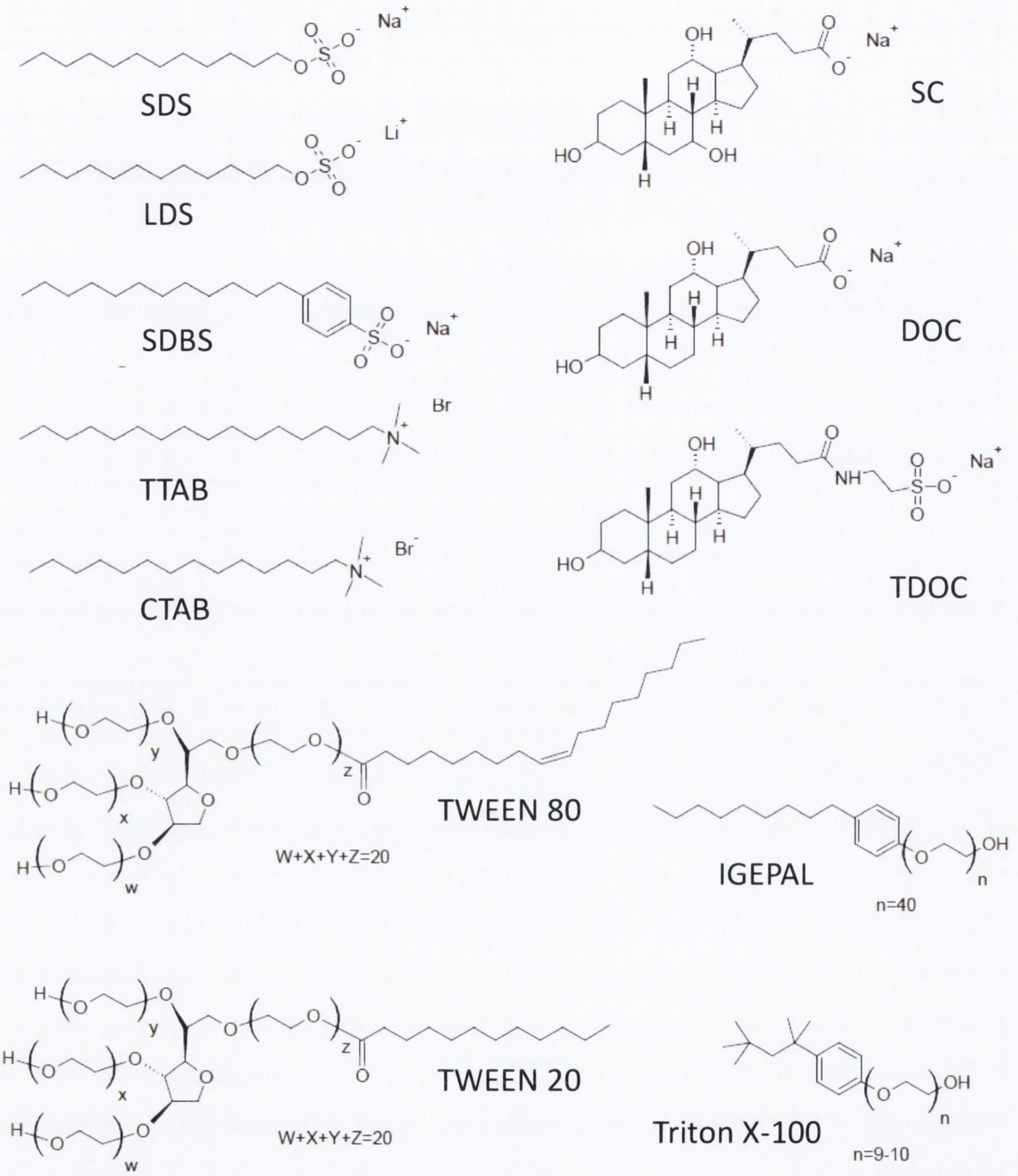

Figure 5.1: Molecular structures of surfactants used in this study

Igepal Co-890, Triton X-100, Tween 20 and Tween 80. All these surfactants are known to be efficient in dispersing carbon nanotubes [86, 177]. Molecular structures of the surfactants are shown in Figure 5.1. All surfactants were purchased from Aldrich and used as supplied.

For each surfactant type, 500 mg of graphite powder, purchased from Sigma–Aldrich (product number 332461), was added to 100 ml of aqueous surfactant solution (0.1 mg ml^{-1} surfactant concentration) to give an initial graphitic concentration of 5 mg ml^{-1}. This mixture was sonicated using a sonic tip (a Sonics VX-750 ultrasonic processor with a flat head tip) for 30 min at 75% of the maximum power (i.e. 75% of 750W nominal maximum power). The dispersion was left to stand overnight. The top 20 ml was decanted into a 28.5 ml vial and centrifuged (Hettich Mikro 22R) for 90 min at 1500 rpm. The top 10 ml was then decanted into a 14 ml vial.

UV–Vis–IR absorption spectroscopy (Varian Cary 6000i) measurements were then carried out immediately after centrifugation. The dispersions were then left to stand for 1 week undisturbed and the absorption spectrum was measured again. For each surfactant type, this procedure was performed three times. The reported values for the concentration (calculated from the absorption spectra) and zeta potential are the averages over these three dispersions.

Graphene films were made by vacuum filtration of the dispersions immediately after centrifugation. A controlled volume of dispersion with known concentration was filtered through a nitrocellulose membrane (pore size 25 nm) and dried overnight in vacuum. This was then transferred to glass and the cellulose was dissolved in acetone. These films were then characterized by Raman spectroscopy using a Horiba Jobin Yvon LabRAM with a 50X objective lens and 633 nm laser excitation. Ten spectra were collected from different parts of each film. The spectra were then normalized to the *G* peak and averaged. TEM grids (holey carbon) were prepared by drop casting immediately after centrifugation and dried overnight in vacuum. All TEM images were taken with a Jeol 2100 operated at 200 kV.

Zeta potential measurements were carried out immediately after centrifugation on a Malvern Zetasizer Nano system with irradiation from a 633 nm He–Ne laser. The samples were injected into folded capillary cells, and the electrophoretic mobility (μ) was measured using a combination of the electrophoresis and laser Doppler velocimetry techniques. All measurements were carried out at 20°C and at the natural pH of the surfactant solution, unless otherwise stated.

5.3 RESULTS AND DISCUSSION

5.3.1. *Characterization of surfactant-stabilized graphene*

In this study, powdered graphite was dispersed in water using 12 different surfactants as stabilizers. In all cases, the surfactant concentration was very low, 0.1 mg ml^{-1} and below the critical micelle concentration (CMC) for all surfactants except Tween 80 and Tween 20. The rationale behind this choice was twofold. Firstly, to aid direct comparison, it was necessary to prepare all dispersions identically. Previous work showed the optimum SC concentration to be 0.1 mg ml^{-1}[176]. However, the intrinsic advantage of using low surfactant concentrations is that there is less surfactant to remove if the dispersed graphene is to be deposited on a substrate for thin film applications. The downside of this strategy is that as the dispersed concentration depends critically on the surfactant content and hence these dispersions are not optimized.

The concentration of graphene remaining dispersed after centrifugation was calculated from the absorption spectra using an extinction coefficient of 6600 ml^{-1} g^{-1} [176]. These concentrations are shown in Figure 5.2 for all surfactants. The dispersed concentration varied from 0.011 mg ml^{-1} for SDS to 0.026 mg ml^{-1} for both SC and IGEPAL. It is important to note that the dispersed concentration was zero for a control sample using only water without surfactant. It is also interesting to note that the alkyl sulfate surfactants (red) are less effective than the other ionic surfactants (green) or non-ionic surfactants (blue).

The stability of these dispersions was measured by recording the absorption spectra (and so the concentration remaining dispersed) 7 days after sample preparation. It was found that a small amount of graphene had sedimented over this period (Figure 5.2); with the exception of TTAB, in all cases <8% of the graphene had fallen out over 7 days. In the case of TTAB, 17% fell out over the first week.

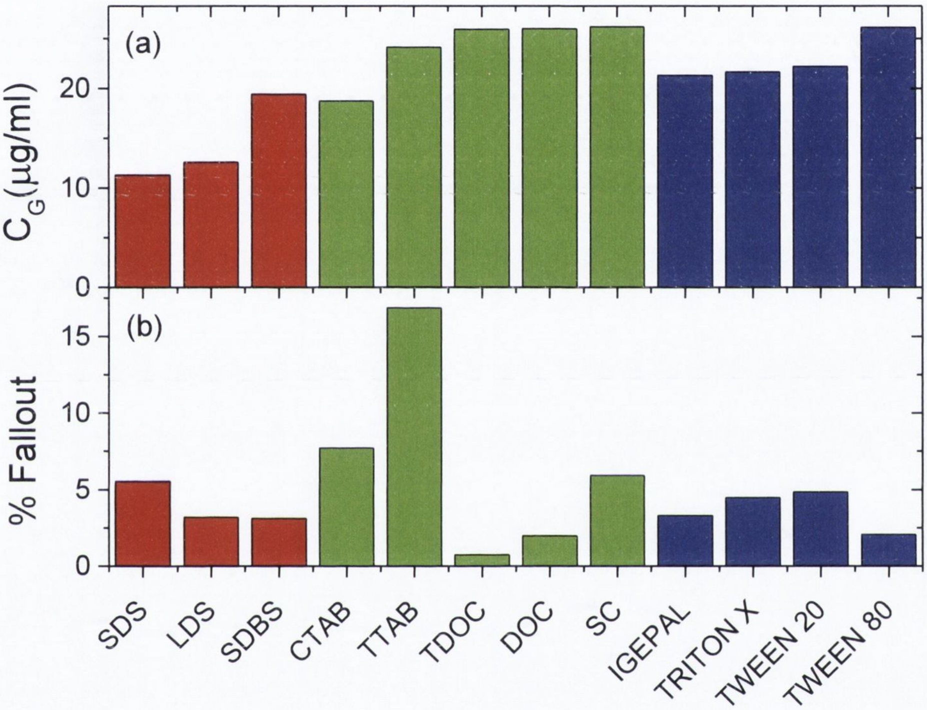

Figure 5.2: (A) Concentration of graphene remaining after centrifugation (B) Percentage sediment after 7 days of the original dispersed concentration. Alkyl sulfates (SDS, SDBS and LDS, red), other ionic surfactants (green) and non-ionic surfactants (blue).

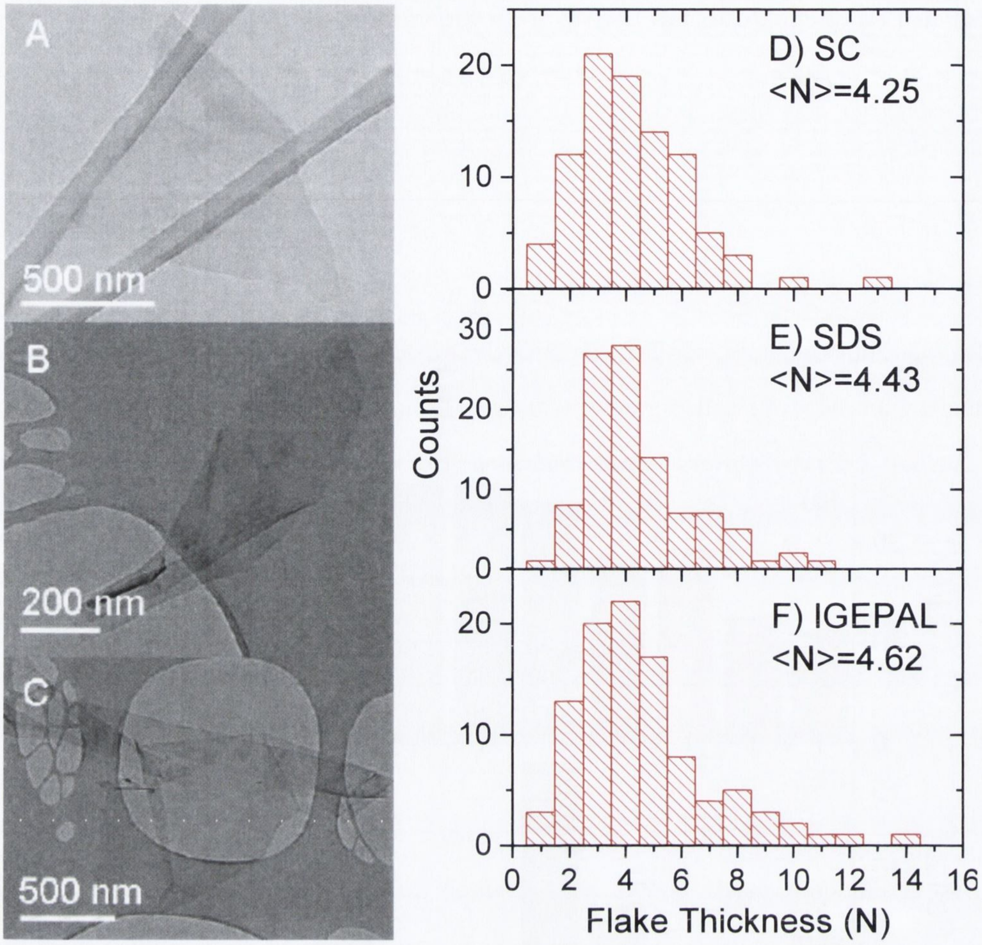

Figure 5.3: (A-C) TEM images of graphene flakes observed during this work. (D–F) Histograms showing flake thickness, expressed as the number of graphene monolayers per flake, for graphene dispersed in (D) SC, (E) SDS and (F) IGEPAL.

In order to determine the degree of graphene exfoliation, TEM analysis was performed on three of the dispersions (SC, IGEPAL and SDS). In all cases, large numbers of two-dimensional objects were observed. A selection of these is shown in Figure 5.3. Of these flakes, A and B appear to be monolayers, whereas C is a multilayer. Both broad flakes and ribbons were observed in all surfactants while all objects observed tend to be of the type shown in figure with no very large aggregates found. It is also important to estimate the degree of exfoliation of the flakes. This was achieved by measuring the flake thickness distribution for the same three surfactants by TEM image analysis used extensively in previous work [139]. The data is shown in Figure 5.3 as histograms of the number of monolayers per flake. In each case, flakes with thickness varying from 1 to 16 layers were observed with a mean flake thickness close to 4.5.

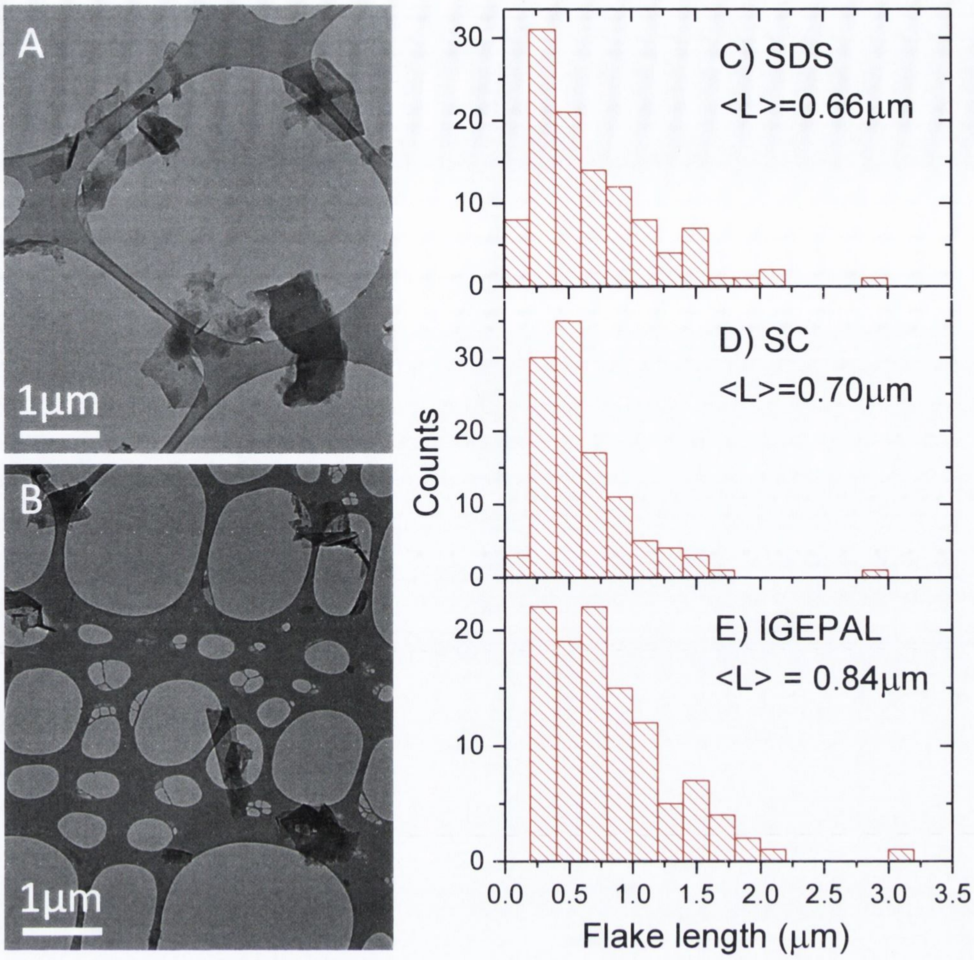

Figure 5.4: (A-B) Wide field TEM images of graphene flakes used to generate length statistics. (C–E) Histograms showing flake length as measured by TEM for graphene dispersed in (C) SC, (D) SDS and (E) IGEPAL.

The lateral size of the flakes is also important for a number of applications. For example, for mechanical reinforcement in composites or thin conducting films, large flakes will be required [178]. The length of the long axis of a large number of flakes was measured for the three surfactants discussed earlier: SDS, SC and IGEPAL. These surfactants were chosen because they represent one from each family (alkyl sulfates, other ionics, and the non-ionics). In addition, they span the full range of dispersed graphene concentration from the lowest (SDS) to the highest (SC and IGEPAL). This data is presented in the form of histograms in Figure 5.4. In each case, the flake length varies from 100 nm to 2μm. The mean length is close to 0.75μm in all cases. Such flake sizes are typical of graphene dispersed using solvents or surfactants [81, 139, 176, 179]. It is interesting that each surfactant appears capable of exfoliating graphene to approximately the same degree.

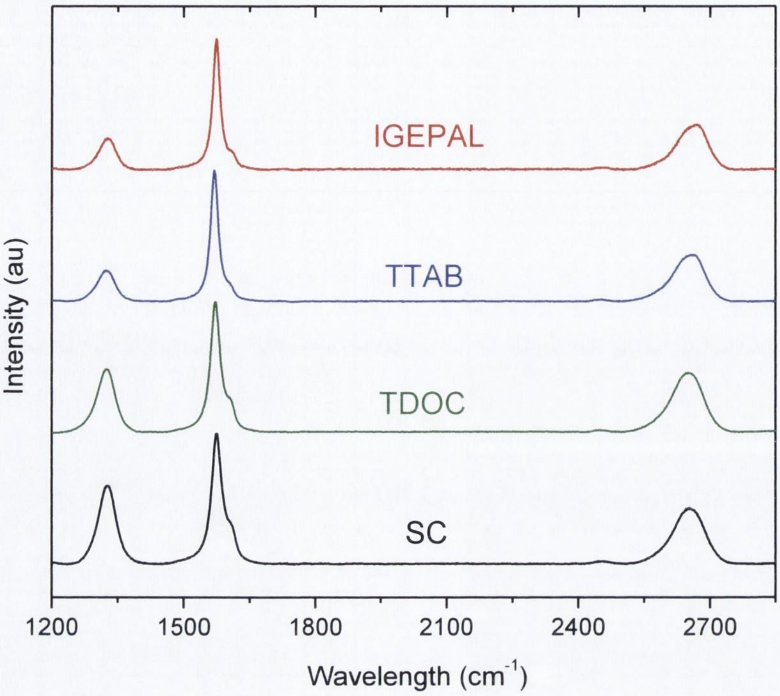

Figure 5.5: Averaged Raman spectra of thin films made from vacuum filtered dispersions of graphene in various surfactants.

Dispersions were also vacuum filtered to form films. Raman spectroscopy was used to characterize these films, measuring spectra at ten different positions before normalizing and averaging. In each case, the spectra display well-defined D, G and 2D bands as shown in Figure 5.5. The D/G ratio is between 0.25 and 0.6, typical of surfactant stabilized flakes in this size range [176]. As will be discussed in more detail in chapter 6, such ratios suggest a defect population dominated by edge defects but with a small cohort of basal plane defects.

5.3.2. *Stabilization mechanism for ionic surfactants*

Any nano-scale object coated by surfactants is stabilized against re-aggregation by the presence of repulsive interactions between nearby surfactant-coated objects. All surfactants consist of a hydrophobic tail group and a hydrophilic head group. The nature of the repulsive interaction is controlled by the structure of the head group. While non-ionic surfactants have a polar head group, ionic surfactants have an ionic head group. Thus, for ionic surfactants, these repulsions are electrostatic in nature,

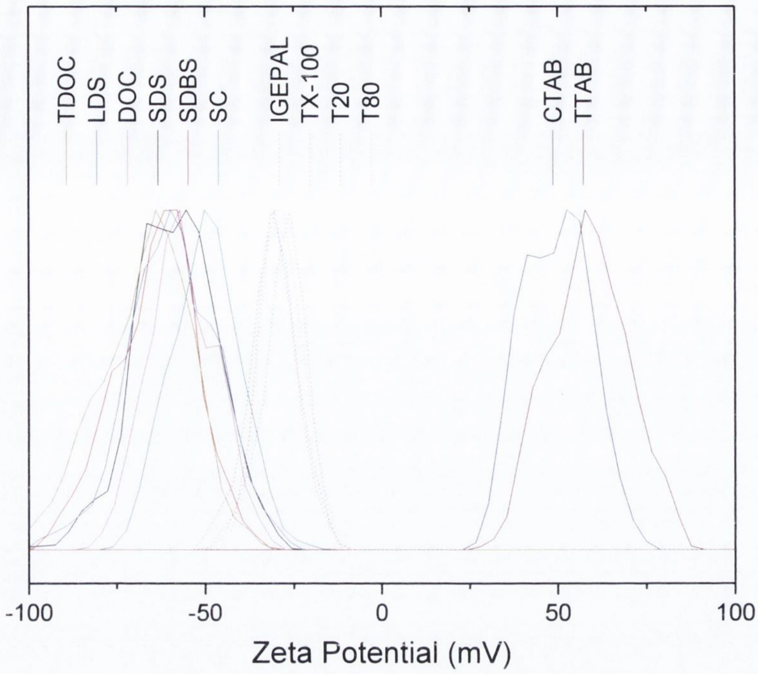

Figure 5.6: Zeta potential spectra for surfactant-stabilized graphene flakes for 12 different surfactants. The non-ionic surfactants are shown by dashed lines.

whereas for non-ionic surfactants, they can be due to a number of sources, such as steric interactions for molecules with bulky hydrophilic regions [131].

The source of the repulsions is most easily understood for ionic surfactants. In general, the surfactant tail group can adsorb by van der Waals (vdW) interactions onto non-polar objects, such as graphene flakes. In aqueous media, the head groups tend to disassociate, imparting an effective charge on the flake. The dispersed flakes will be stabilized by electrostatic repulsion between surfactant-coated flakes. In general, the effective charge is not what is considered but rather the electric potential at the edge of the layer of bound ions: the zeta potential, ζ [131]. The zeta potential can be measured in a straightforward manner for aqueous dispersions as described in chapter 4. It is reasonable to expect that the magnitude of the zeta potential would have an effect on the graphene concentration that can be attained. To test this, the zeta potential distributions for graphene dispersed with each surfactant was measured at the natural pH of the dispersion. These distributions are shown in Figure 5.6

The measured distributions are generally broad and asymmetric due to the range of flake sizes and possible contributions from free surfactant [180]. The distributions can clearly be divided into three sets: anionic, non-ionic and cationic. The zeta potential of the surfactant stabilized sheets was estimated to be the centre of the distribution. It

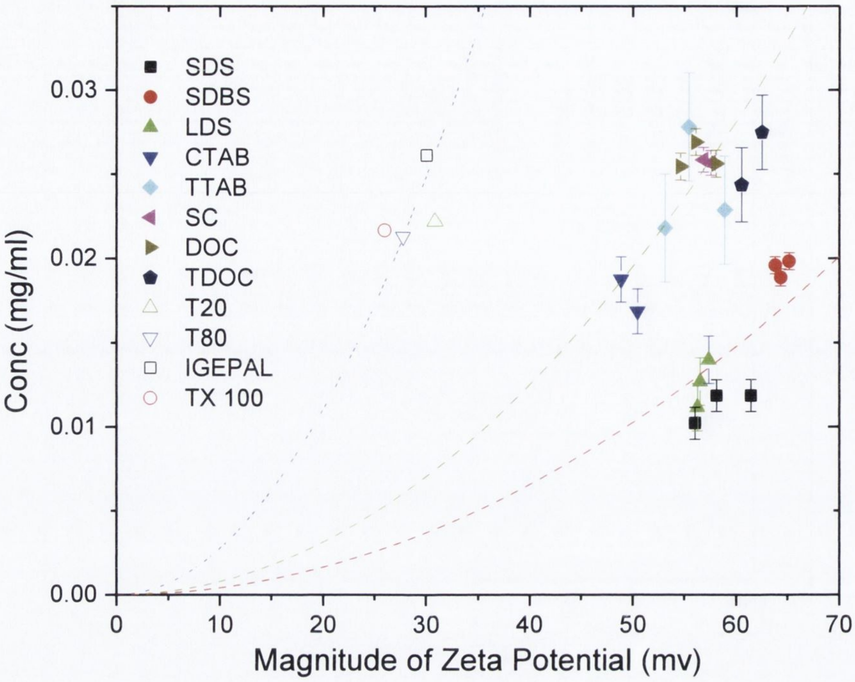

Figure 5.7: Dispersed graphene concentration (after centrifugation) plotted as a function of the measured zeta potential of the dispersion. The dashed line represents $C_G \propto \zeta^2$ behaviour

was found that the zeta potential varied from −64mV for SDBS to +57mV for TTAB. The anionic surfactant-coated sheets had zeta potentials in the range −50 to −64 mV, whereas the cationic surfactants displayed zeta potentials of 48 and 57mV. Interestingly, rather than being neutral, the graphene sheets coated by non-ionic surfactants displayed zeta potentials between −26 and −31 mV. This was previously observed for surfactant-stabilized nanotubes and may be due to adsorption of charged impurities [180]. This means that even the graphene sheets coated with non-ionic surfactants may be partially stabilized by electrostatic interactions.

To test the relationship between the magnitude of zeta potential and the dispersed concentration, it is useful plot C_G versus ζ in Figure 5.7. The data is clearly divided into three groups: the sulfides (SDS, SDBS and LDS), other ionic surfactants (TDOC, DOC, SC, TTAB and CTAB) and the non-ionic surfactants. Interestingly, for both groups of ionic surfactants, C_G clearly increases with increasing ζ. Such behaviour may occur for the non-ionic surfactant-stabilized systems, however the data is too clustered to say definitively.

To understand this behaviour more clearly, the stabilization mechanism must be considered in more detail. Within Derjaguin–Landau–Verwey–Overbeek (DLVO) theory, ionic surfactant stabilized colloids are considered in terms of a layer of bound molecular ions (tail groups) and a diffuse cloud of counter ions, the so-called double layer [131]. The repulsive DLVO potential energy for two charged surfaces is give

$$V_{DLVO} = 2A\varepsilon_r\varepsilon_0\kappa\zeta^2 e^{-\kappa D} \qquad (5.1)$$

where κ^{-1} is the Debye screening length (a measure of the double layer thickness):

$$\kappa^{-1} = \left(\frac{\varepsilon_r\varepsilon_0 kT}{2e^2 n_0}\right)^{1/2} \qquad (5.2)$$

where n_0 is the number of surfactant molecules per unit volume of solution [131]. It is important to note that this expression strictly holds only for $\zeta < 25$ mV making any numbers generated approximate. However, it is used it here merely to illustrate the mechanism. The repulsive interaction energy for two charged 2D sheets can be calculated by multiplying V_{DLVO} by 2 (to account for the fact that both sides of the sheets are charged). DLVO theory considers the balance of these repulsive interactions and attractive vdW interactions between adjacent colloids. The attractive vdW potential energy between two parallel 2D sheets can be approximated as the sum of pairwise inter-atom attraction energies. This can be calculated, in a manner similar to the method pioneered by Hamaker [181], to be

$$V_{vdw} = A\pi\rho^2 C/2D^4 \qquad (5.3)$$

where A is the sheet area, ρ is the number of atoms per unit area in the sheets, D is the sheet separation and C is the constant relating the inter-atomic vdW energy to the inter-atomic separation:

$$V = -C/r^6 \qquad (5.4)$$

The overall potential energy of two parallel 2D sheets can thus be approximated as

$$V_T \approx 4A\varepsilon_r\varepsilon_0\kappa\zeta^2 e^{-\kappa D} - A\pi\rho^2 C/2D^4 \qquad (5.5)$$

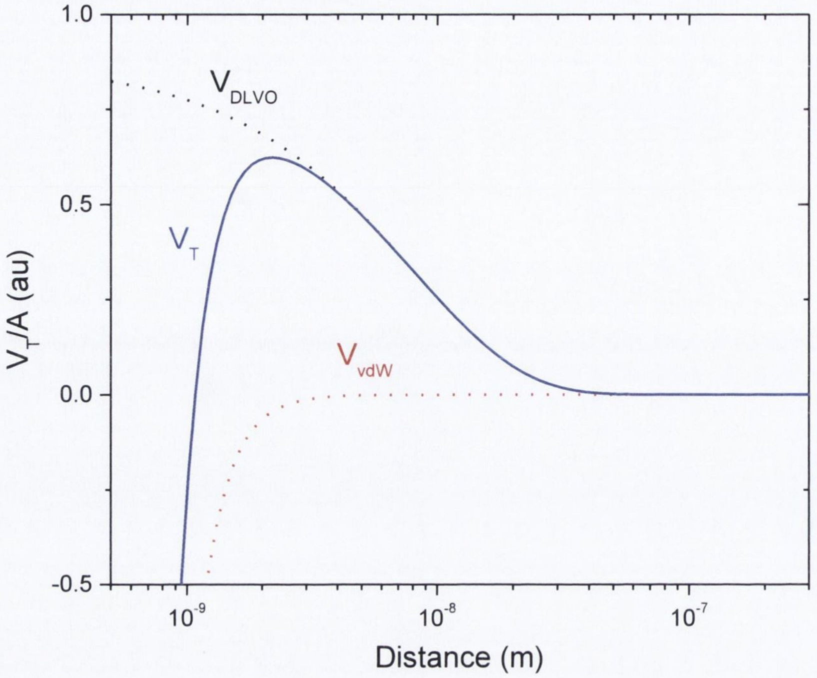

Figure 5.8: Plot of total interaction potential, V_T/A, as a function of separation D for two charged surfactant coated parallel sheets. Repulsive component V_{DLVO} and attractive component V_{vdW} represented by dotted lines.

This expression does not account for screening or retardation effects. This function describes a potential that increases as D decreases, reaches a peak and then drops rapidly to a potential well as shown in Figure 5.8. The well describes the case when the sheets are aggregated, while the peak represents a potential barrier against aggregation. It has been previously shown for graphene stabilized by SDBS [81], that the potential barrier, V_{BD}, can be approximated by taking the value of the repulsive component as D approaches zero:

$$V_{BD} \approx 4A\varepsilon_r\varepsilon_0\kappa\zeta^2 \qquad (5.6)$$

It is reasonable to suggest that the concentration of dispersed graphene may be strongly linked to the height of this potential barrier. In fact, each of the three groups of data in figure is consistent with $C_G \propto \zeta^2$ behaviour, suggesting that C_G may scale linearly with V_{BD} (dashed lines). This can be seen more clearly by plotting C_G as a function of $\kappa\zeta^2$ (equivalent to plotting C_G versus V_{BD}/A in arbitrary units), as shown in Figure 5.9. It is clear from this graph that the concentration of graphene stabilized by the non-alkyl sulfate ionic surfactants scales linearly with the barrier height with an intercept very close to zero. However, for the alkyl sulfates a different behaviour is

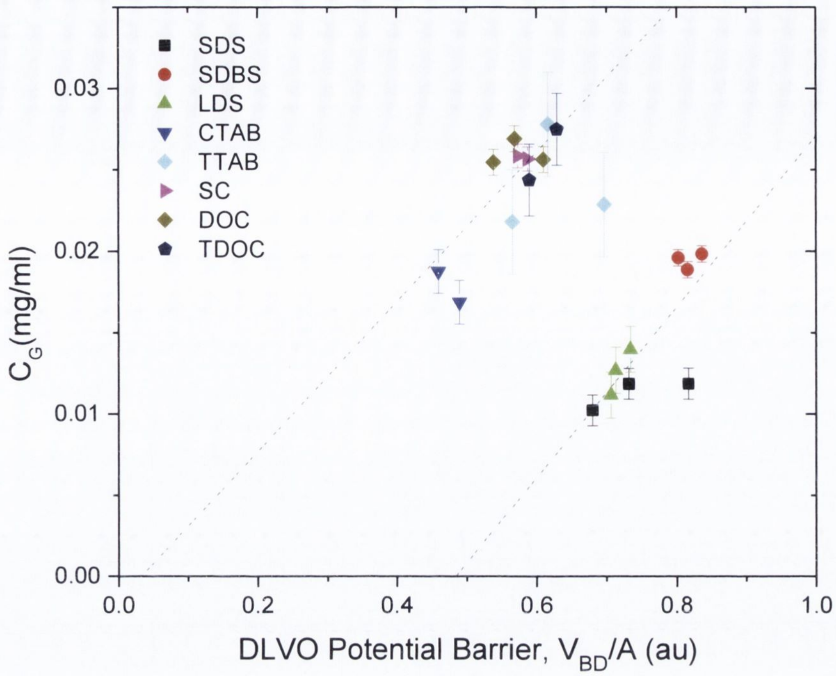

Figure 5.9: Dispersed graphene concentration (after centrifugation) plotted as a function of the calculated potential barrier height due to Derjaguin–Landau–Verwey–Overbeek (DLVO) interactions between ionic surfactant-coated sheets.

observed. While the dependence of C_G on V_{BD} is linear, there is a significant intercept on the V_{BD} axis. This means that graphene can only be dispersed for electrostatic potential barriers above some minimum value. This suggests that the inter-sheet attractive potential is stronger for alkyl sulfate-coated sheets than for the other ionic surfactants. The origin of this additional attractive interaction is unknown at present.

That the dispersed concentration scales with barrier height immediately suggests that the dispersed concentration can be increased by taking steps to increase V_{BD}, by increasing either ζ or κ. In practical terms, this would involve careful control of surfactant type and concentration. It is probably easiest to envisage increasing ζ by surfactant control. As ζ represents the electrostatic potential at the edge of the layer of bound ions, it can be increased by maximizing the surface charge in this layer. This could be achieved by choosing compact surfactants that pack tightly on the graphene surface to give high bound surfactant density. In addition, the charge per molecule could be increased by using multiply charged surfactants.

5.3.3. *Stabilization mechanism for non-ionic surfactants*

Although there is most likely some electrostatic stabilization due to charged impurities, the primary stabilization mechanism for non-ionic surfactants is slightly different. In each case, these surfactants have a hydrophobic tail and a long hydrophilic part. For such molecules, the stabilization mechanism tends to be based on steric effects[131]. The hydrophobic tail adsorbs on the graphene sheet, while the hydrophilic part extends into water. When two surfactant-coated sheets approach each other, the protruding hydrophilic groups begin to interact, resulting in an osmotic repulsion between the flakes. This results in a steric repulsive potential of the form:

$$V_S \approx \alpha AkTLe^{-\frac{\pi D}{L}} s^{-3} \qquad (5.7)$$

where α is a constant, A is the flake area, L is the length of the protruding group and s is the average distance between adsorbed groups [131]. This equation is appropriate for the case where the molecules are adsorbed at one end and closely packed on the surface. As is the case with ionic stabilization, the total potential is the sum of this repulsive term and the vdW attractive term,

$$V_T \approx \alpha AkTLe^{-\frac{\pi D}{L}} s^{-3} - A\pi\rho^2 C/2D^4 \qquad (5.8)$$

Assuming that, as with the electrostatic repulsive term above, one can approximate the potential barrier as the magnitude of the repulsive part as D approaches zero, the barrier height can be written as

$$V_{BS} \approx \alpha AkTLs^{-3} \qquad (5.9)$$

It is possible to estimate both L and s for the non-ionic polymers under study. To estimate s, the average separation between adsorbed surfactant molecules, it can be assumed that they are tightly bound onto the graphene surface. The combined area of the atoms in the hydrophobic part can be estimated by counting the number of C atoms and multiplying this by an area per atom. The hydrophobic part can be considered to be the region of the molecule to the left of the brackets in the structures of IGEPAL and Triton X-100 and to the right of the =O in the structures of Tween 20 and Tween 80 (Figure 5.1). The distance between molecules s was taken to

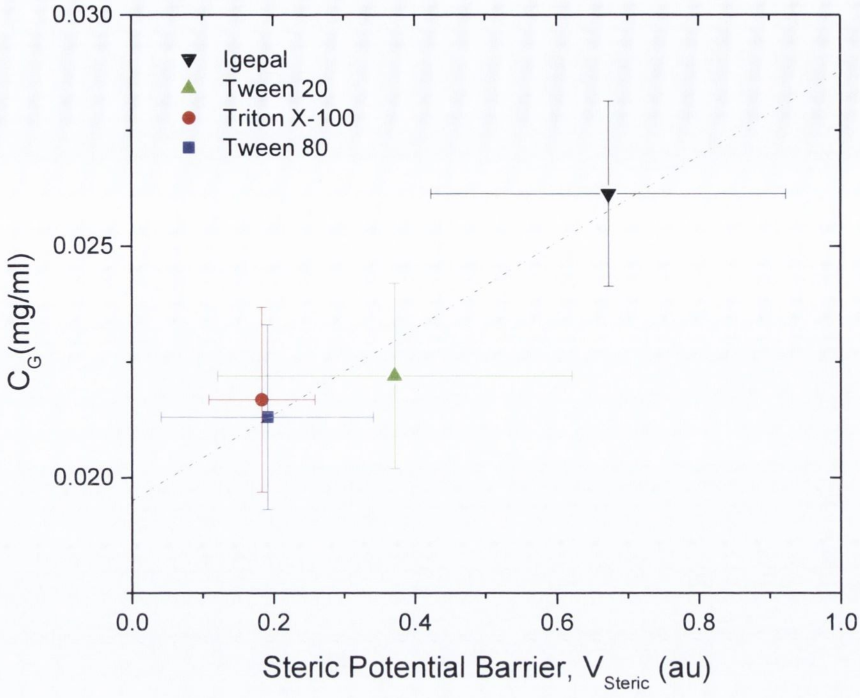

Figure 5.10: Dispersed graphene concentration (after centrifugation) plotted as a function of the calculated potential barrier height due to steric interactions between non-ionic surfactant coated sheets.

be the square root of the hydrophobic area. To estimate L, it is important to note that closely packed, adsorbed linear molecules form brush-like structures. Here, the molecules tend to protrude away from the surface with a length that is proportional to the actual length of the protruding part of the molecule. This length can be estimated from the number of bonds in the hydrophilic part of the molecule. While this is uncertain for the Tween surfactants, estimating the maximum and minimum lengths, gives a mean value. This allows L/s^3 and V_{BS} (in arbitrary units) to be calculated.

A plot of C_G versus V_{BS} in Figure 5.10 suggests the data scales linearly, consistent with the hypothesis that the dispersed concentration does indeed scale with the potential barrier for steric stabilization. However, there is a significant intercept on the concentration axis of 0.02 mg ml^{-1}. This suggests that even for very short, widely spaced protruding groups, a significant concentration of graphene would remain dispersed. This means that an additional stabilization mechanism must be present for these non-ionic surfactants. In fact the additional mechanism is most likely twofold. Each of the non-ionic groups has at least one acid group and many ether linkages. Such groups interact very strongly with water, making dispersion of surfactant-coated graphene flakes in water reasonably energetically favourable. In addition, the non-ionic surfactant-coated graphene have a negative zeta potential, possibly due to adsorbed impurities. Such a zeta potential would result in an additional potential barrier due to electrostatic repulsion, further stabilizing the flakes.

As in the case of ionic surfactants, it is possible to speculate on non-ionic surfactant structures that would maximize the potential barrier. It is clear that a compact yet strongly bound tail group is required to maximize the number of bound molecules per unit area of graphene sheet. The polar part of the surfactant must be very long and interact strongly with water via large numbers of hydrophilic.

5.4 CONCLUSIONS

This work has established that graphene can be dispersed with the aid of a range of surfactants at low surfactant concentration. The dispersed flake size and degree of exfoliation (flake thickness) vary very little from surfactant to surfactant. However, the dispersed concentration varied significantly from 11μg ml^{-1} for SDS to 26μg ml^{-1} for SC. It appears that for ionic surfactants, the concentration is largely controlled by the zeta potential of the surfactant-coated graphene sheet. Specifically, the concentration scales linearly with the repulsive electrostatic potential barrier that stabilizes surfactant-coated sheets against aggregation. Similarly, for non-ionic surfactants, the concentration scales linearly with a repulsive potential barrier that has steric origins. However, in this case, other repulsive interactions are present. These may be both electrostatic and thermodynamic in nature.

It is important to note that this study is merely a first step towards better understanding the factors affecting surfactant choice for exfoliation of graphene and other two dimensional materials. A more detailed study using optimized dispersions in each case is required in order to more accurately compare surfactants. A more quick and accurate means of determination of the distribution length and thickness of a dispersion will be crucial in order to fully assess the effect surfactant choice has on these parameters. This may be possible by more detailed analysis of the absorbance spectra of 2D materials and will be discussed in more detail in chapter 9.

6

LATERAL SIZE SELECTION OF SURFACTANT STABILISED GRAPHENE FLAKES USING SIZE EXCLUSION CHROMATOGRAPHY

6.1 INTRODUCTION

Due to its unique mechanical and electrical properties, graphene has recently generated intense interest among researchers [172]. While much of this work has been carried out on micromechanically cleaved samples, many future applications will require high throughput processing techniques [182]. As discussed in the previous chapter, exfoliation of graphite in organic solvents or surfactant solutions yields dispersions of pristine graphene [78, 81, 139, 175, 176, 179, 183]giving it the potential to be very useful in a wide range of applications. This method however suffers from one critical disadvantage. The flakes produced have a significant spread in both lateral flake size and number of layers that has so far proved difficult to control through adjustment of processing conditions. While some work has been done to separate dispersed flakes according to number of layers [175], relatively little progress has been made on separation by lateral size [66, 139] which can be very important when considering applications such as polymer reinforcement [165, 178].

Size exclusion chromatography is a well-established chromatographic method for separating particles according to their size as they pass through porous gel filtration medium packed tightly into a column [141]. This medium consists of porous spherical particles made of a chemically inert and physically stable material. As a sample moves through the column, particles diffuse in and out of these pores. Smaller particles have more available volume to diffuse into and hence have a retention volume. This means that larger particles leave the column first followed by smaller particles in order of their size. By collecting samples based on their elution time, separation based on particle size can be achieved. One significant advantage of this technique is that it has been studied for over 50 years which means that methodologies to increase resolution and throughput are well understood. In this chapter, surfactant exfoliated graphene flakes are separated according to their lateral dimensions using size exclusion chromatography. Raman spectroscopy and transmission electron microscopy are used to confirm size selection.

6.2 EXPERIMENTAL PROCEDURE

A graphene stock dispersion was prepared by adding graphite powder (Aldrich) at initial concentration $C_G = 20\text{mgmL}^{-1}$ to sodium cholate solution $C_{SC} = 0.3$ mg mL^{-1} as described previously in chapter 5. Ultra sonication was carried out using a high powered sonic tip (Sonics VX-750 ultrasonic processor) for approximately 8 h. The dispersion was left to sit overnight and then centrifuged. (Hettich Mickro 22R) at 500 rpm for 45 min to remove large aggregates. The dispersion was then placed in a rotary evaporator to remove 50% of the water present and hence double its concentration.

The volume of the glass column was measured to be ~50 mL. By using the known density of controlled pore glass (CPG, Purchased from Millipore, product No. CPG3000B, mean pore diameter 300 nm) the mass required to fill the column was calculated. The CPG was then added to a sodium cholate surfactant solution (0.3 mg/mL). The CPG/surfactant mixture was then packed tightly into the glass column. The stock dispersion was mixed with ethylene glycol at a ratio of 3:1 to increase the density of the dispersion. A syringe was used to add 3 mL of the resulting mixture to the column just above the top of the CPG mixture, the tap was opened and surfactant solution added to the top of the column. Fractions were collected for every 3 mL of dispersion.

Graphene films were made by vacuum filtration of the dispersions immediately after centrifugation. A controlled volume of dispersion with known concentration was filtered through a nitrocellulose membrane (pore size 25 nm) and dried overnight in vacuum. This was then transferred to glass and the cellulose was dissolved in acetone. These films were then characterized by Raman spectroscopy using a Horiba Jobin Yvon LabRAM with a 50X objective lens and 633 nm laser excitation. Ten spectra were collected from different parts of each film. The spectra were then normalized to the *G* peak and averaged. TEM grids (holey carbon) were prepared by drop casting immediately after centrifugation and dried overnight in vacuum. All TEM images were taken with a Jeol 2100 operated at 200 kV.

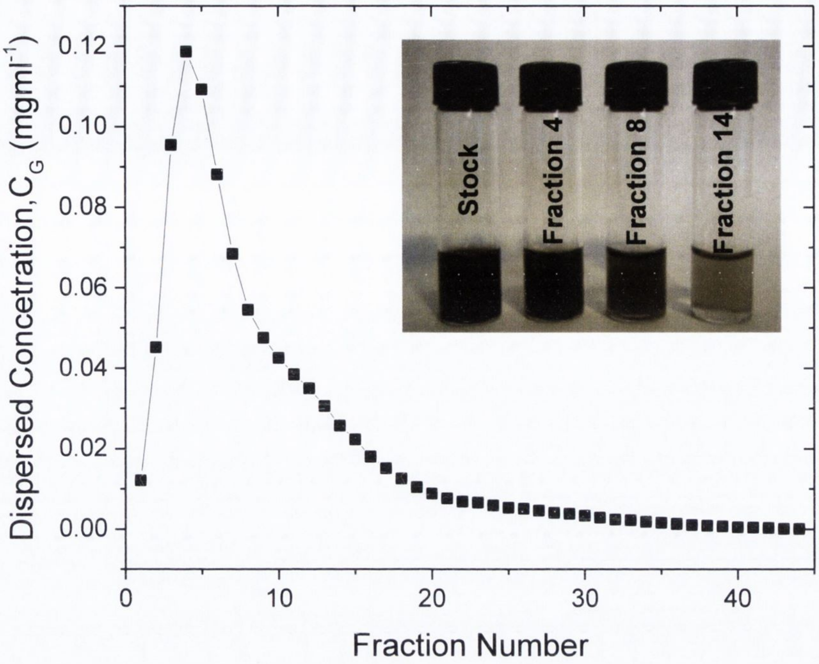

Figure 6.1: Concentration of dispersed graphene as a function of fraction number. Inset(Left to right): Original high concentration stock dispersion of graphene in sodium cholate solution. Fractions collected every 3ml after stock was passed through the size exclusion column.

6.3 RESULTS AND DISCUSSION

6.3.1. *Optical characterization of surfactant-stabilized graphene fractions*

After the dispersion was passed through the column, 44 samples were collected, each comprising of 3ml of dispersion. A sample set of these fractions is shown in the inset of Figure 6.1. All samples were of varying concentration with the initial few fractions appearing more concentrated than rest. In order to accurately determine the dispersed graphene concentration, optical absorption measurements were performed on the fractions. As with the study in the previous chapter, the extinction coefficient α, for graphene dispersed in surfactant was taken to be 6600 $Lg^{-1}m^{-1}$ at 660nm[176].

The data in Figure 6.1 clearly shows the concentration to increases dramatically with fraction number for the first few fractions before peaking around fraction 4 or 5. The concentration then falls off more smoothly with just over 50% of the total initial dispersed material contained in the first 7 fractions. This could suggest that there is a high mass fraction of large material present in the initial stock dispersion but could also mean that size exclusion has not been effective for the first few fractions.

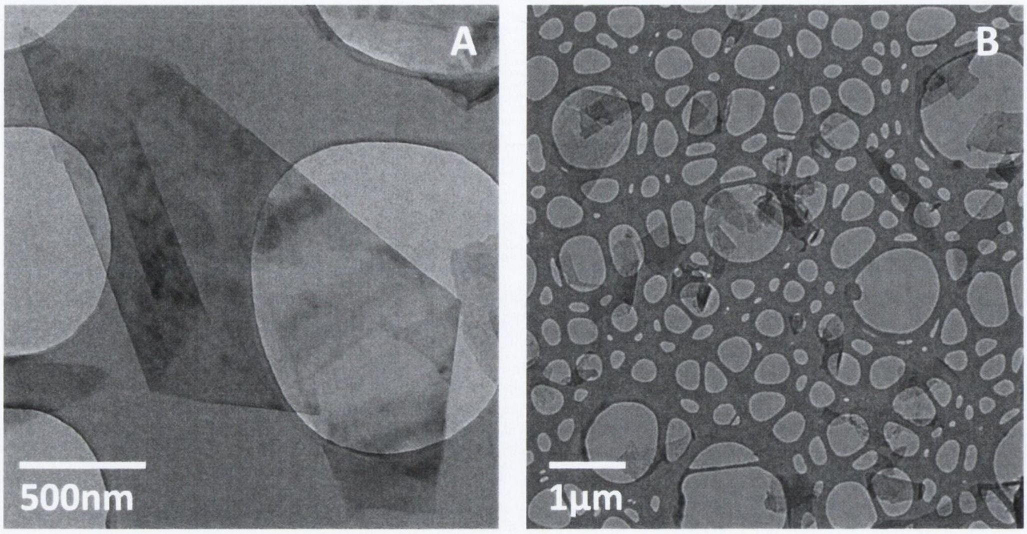

Figure 6.2: (A) TEM image of typical graphene flake found in dispersion. (B) Wide field TEM image of graphene flakes used to generate statistics.

In order to quantitatively analyse the fractions in terms of lateral dimensions, 6 samples were taken from the first 14 fractions (comprising 85% of the total dispersed graphene). An equal mass from each fraction as well as the stock dispersion was then dropped onto holey carbon grids and examined using TEM. A minimum of 100 flakes were counted per sample in order to generate statistics on the flake size distribution. Figure 6.2a shows a sample image of an exfoliated graphene flake. Each fraction predominantly contained few layer flakes such as this one with a range of thicknesses and aspect ratios present (mean aspect ratio close to 2). Figure 6.2b shows a wide field TEM image of deposited flakes of the type used to generate lateral flake length statistics for each fraction.

As can be seen from these statistics (Figure 6.3), there is a gradual shift in mean flake size, going from higher to lower fraction numbers. The average flake length decreased from ~1.2l µm for fraction 2, to ~0.5l µm for fraction 14. Indeed, the first 8 fractions yield dispersions with a significant increase in the mean flake length compared with the stock. Although the lateral flake size varied with fraction number, the average number of layers per flake did not appear to vary as significantly. This observation was not investigated quantitatively as flake thickness was not the main focus of this work and the edge counting technique required to assess this parameter is very time consuming for such a large sample set.

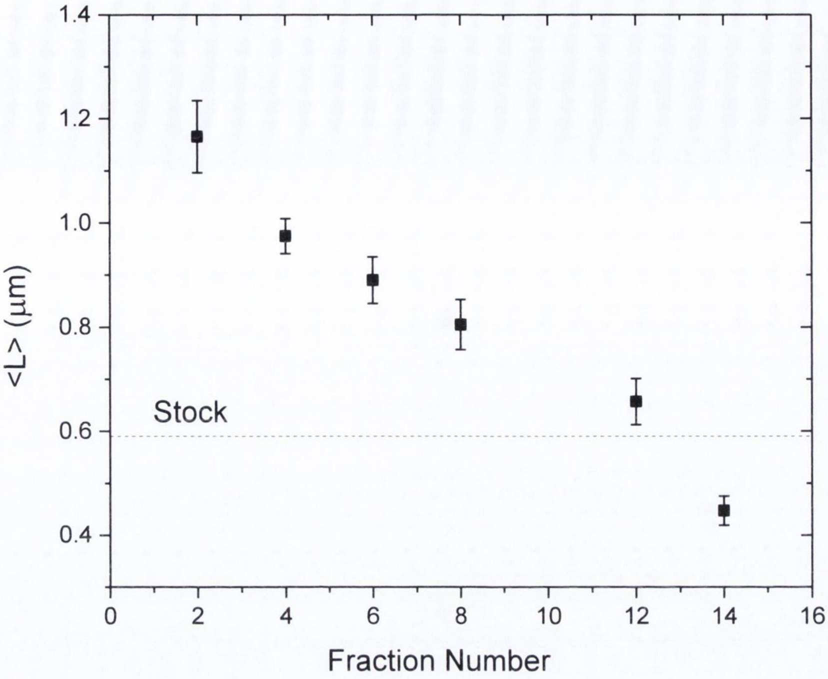

Figure 6.3: Average flake length as a function of fraction number. The mean flake size measured for the stock dispersion is shown by the dashed line

Besides average flake length, the distribution of sizes is an important factor in assessing the success of size exclusion chromatography. In this regard this method appears to fall short as the distributions for larger mean flake dimensions are rather broad (figure 6.4). This means that although some of the smaller material has been removed increasing the average flake length <L>, a large population of small material still remains in the initial fractions.

The reason for this is most likely a limit of this particular experimental setup rather than a fundamental limit of the process itself. The resolution of the column will depend on the ratio of the dispersion volume compared to the column volume. When a sample with too large a volume is placed in the column, the pores can become overloaded with material preventing them from effectively screening out objects with smaller dimensions from the initial fractions. This problem could be rectified by both increasing the volume of the column and decreasing the volume of the dispersion. Increasing the volume of the column simply requires a larger vessel and a greater mass of controlled pore glass however increasing the concentration of the dispersion is less straightforward. As concentration is increased the stability of the dispersion can decrease leading to aggregation of the flakes and hence large fallout of material. The dispersed graphene concentration of 0.3 mlml-1 used in this work represented the

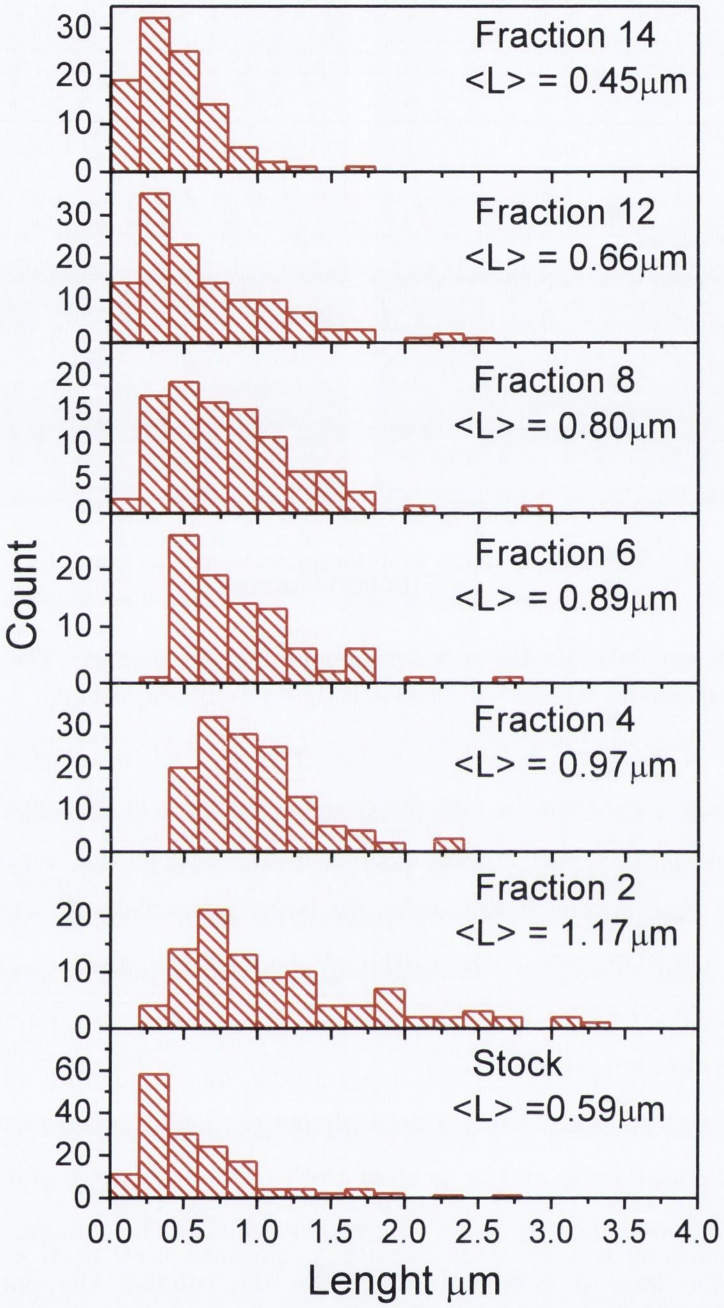

Figure 6.4: Histogram of flake size distributions generated using TEM images for different fractions as well as stock dispersion.

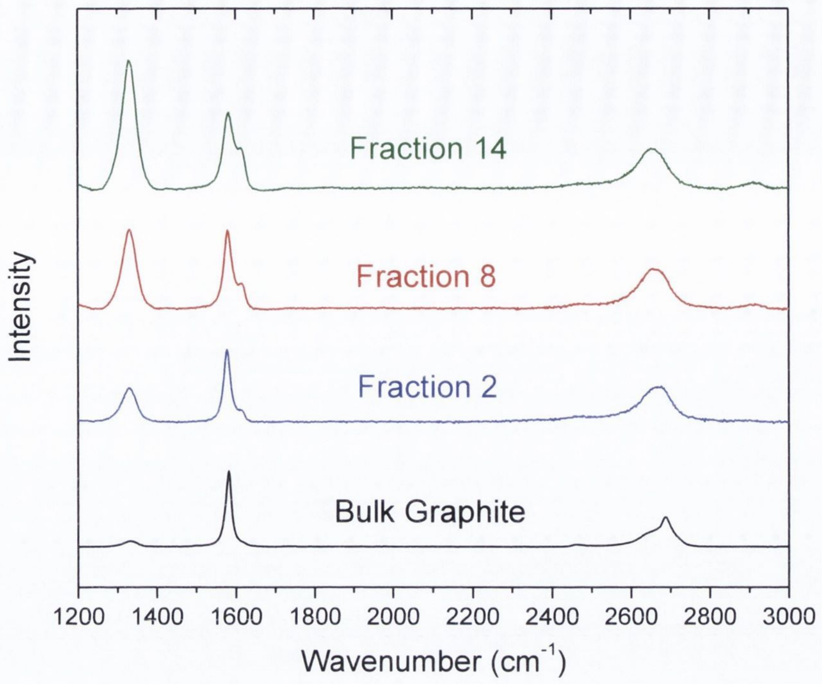

Figure 6.5: Representative Raman spectra of films filtered from various fractions as well as that of graphite powder.

upper limit for surfactant stabilized dispersion at the time this work was carried out. Recent work with similar surfactant stabilized dispersions of MoS_2, have achieved concentrations around 4mgm-1. If this method is also successful for graphene, then the resolution of this experiment could be increased significantly.

6.3.2. *Raman characterization of surfactant-stabilized graphene fractions*

Raman spectroscopy can be used to further characterize these fractions by assessing the quality of the graphene present in each. To that end, thin graphene films were prepared from each fraction by vacuum filtration onto porous mixed cellulose ester membranes (MF-Millipore mixed cellulose ester membrane, 25 nm pore size, 47mm diameter). These films could then be transferred to glass and analysed using a Raman spectrometer. Representative spectra for three fractions are shown in Figure 6.5 as well as the graphite powder.

In Raman spectroscopy, graphitic materials are generally characterized by the D, G, and 2D bands around 1350, 1580 and 2700 cm^{-1}, respectively[157, 159]. It is important to note the change in the 2D band for these graphene films compared to the bulk

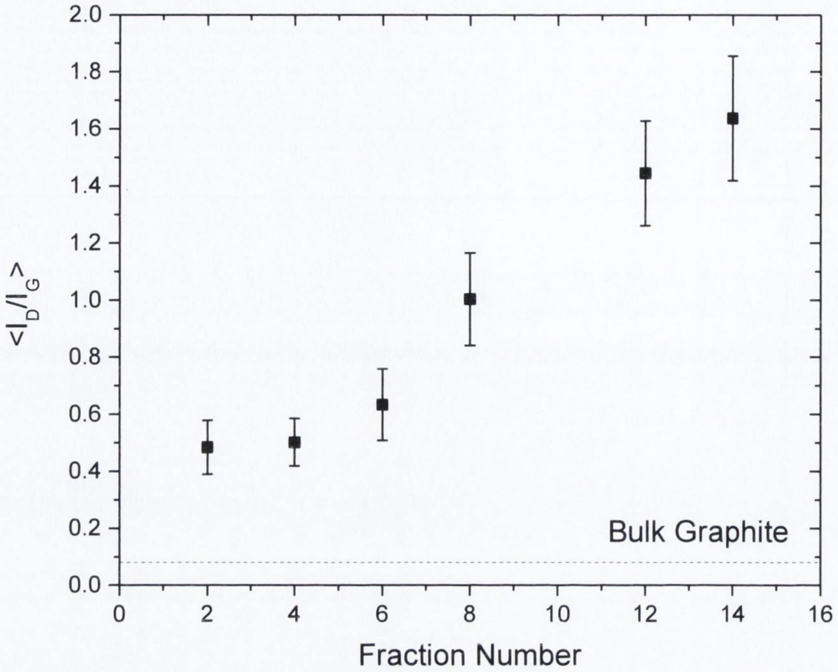

Figure 6.6: Average D band to G band ratio as a function of fraction number. The D/G ratio measured for the graphite powder is shown by the dashed line.

graphite is indicative of exfoliation and consistent with few layer material[157, 175]. The D band is particularly interesting in this case as the defect content is indicated by the intensity of the D band relative to the G band [160]. All spectra have D bands significantly larger than that of the starting powder, indicating that processing induces defects. Similarly, the growth of the shoulder at 1615 cm^{-1} also indicates defect creation [156].

To investigate this further the intensity of the D band to G band (I_D/I_G) was plotted as a function of fraction number. Figure 6.6 shows a steady increase in $<I_D/I_G>$ relative to the starting graphite as the fraction number is increased and the flake size decreases. This implies that smaller graphene flakes are much more defectious than their larger counterparts. To understand this it is important to consider the types of defects that can contribute to the D band intensity.

Defects in graphene are divided into two main types: body defects such as point defects on the basal plane and edge defects. It is important to distinguish between the contributions of these defect types. The introduction of edge defects is known to occur during processing as sonication cuts the initially large crystallites up into smaller flakes [139]. These smaller flakes have more edges per unit mass resulting in an increase in the population of edge defects. To establish the effect of flake dimensions on $<I_D/I_G>$, it is first necessary to consider the individual contributions to D and G intensities.

As previously stated, I_D will be proportional to the flake edge and hence by modelling the flakes as rectangles

$$I_D \propto \langle W \rangle + \langle L \rangle \quad (6.1)$$

where $\langle W \rangle$ and $\langle L \rangle$ are the mean flake width and lengths respectively. I_G is related to the total area of the flake and hence will also be proportional to the mean width and length such that

$$I_G \propto \langle W \rangle \langle L \rangle \quad (6.2)$$

By combining the previous two equations

$$I_D/I_G \propto \langle W \rangle + \langle L \rangle \ / \ \langle W \rangle \langle L \rangle \quad (6.3)$$

As discussed in the previous section, the mean aspect ratio of flakes appeared invariant with average size consistent with measurements in previous work [176]. It is possible then to define this aspect ratio $\langle L \rangle / \langle W \rangle$ as a constant, γ and rewrite equation as

$$I_D/I_G \propto \gamma + 1/\langle L \rangle \quad (6.4)$$

It is therefore instructive to plot I_D/I_G vs $\langle L \rangle^{-1}$ as shown in Figure 6.7. It is clear that the quantities scale linearly with an intercept close to I_D/I_G for the graphite powder. By considering the additional contribution of defects already present in the starting powder, the ratio of the D to G bands can be modelled as

$$I_D/I_G = I_D/I_G{}_{\ Powder} + k/\langle L \rangle \quad (6.5)$$

where k is a constant. Fitting this equation to the data (dotted line Figure 6.7), gives a value of 0.65 for k. This is significantly higher than the value of 0.3, observed for solvent exfoliated graphene [139, 184] but agrees well with what has previously been observed for surfactant exfoliated graphene [176]. The discrepancy between these two values suggest a difference in the basal plane defect densities of solvent and surfactant exfoliated flakes however

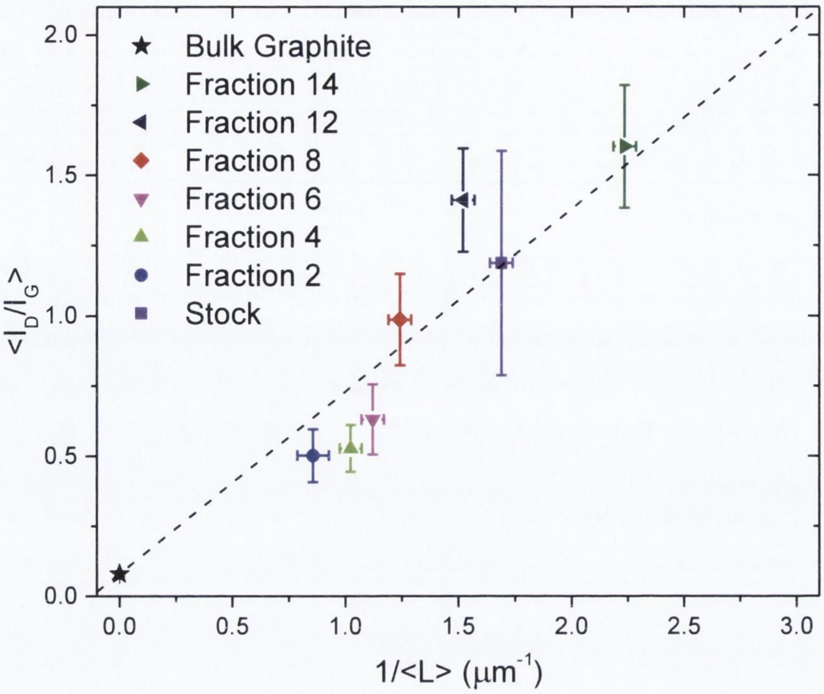

Figure 6.7: D band to G band ratio plotted as a function of 1/<L>

there is not enough data to support this conclusion. It is perhaps more likely that the difference in apparent I_D/I_G for a given average flake size is due to differences in processing conditions. For example, the less aggressive centrifuging regime in the solvent exfoliated samples could lead to a much broader distribution of sizes for each sample.

The consistency of this model with the measured data strongly indicates that the higher defect density present recorded for smaller flakes is due to the creation of edges as flakes are cleaved from the parent crystal and not an increased number of basal plane defects. This would suggest that processing is merely making the flakes smaller and not affecting the quality of the material produced.

6.4 CONCLUSIONS

Size selection column chromatography has successfully been used to separate typical aqueous graphene dispersion into several fractions according to their average lateral flake size. The separation has been confirmed by means of TEM analysis of the dispersions themselves and Raman spectroscopy of thin films cast from these fractions.

Effectively, this process has allowed for a 100% increase in the average flake size of a graphene dispersion through the removal of smaller flakes.

Although initial results are promising, some applications such as the use of graphene as a reinforcing material will require average flake sizes larger than those reported in this work[178]. It is reasonable to expect this to be made possible by two separate approaches. The first is to increase the population of large flakes in the initial stock dispersion through re-dispersing sediment as outlined in previous work done by the group [179]. The second is to increase the resolution of the column in order to be better able to isolate this population of large flakes. This can be done by increasing the column size relative to the volume of dispersion passed through it and hence can be achieved both by increasing initial concentration of stock dispersion as well as the volume of the column itself. All these options will be investigated in future work. In addition, this approach will be extended to surfactant exfoliated inorganic layered compounds such as MoS_2 in Chapter 7.

7

EXFOLIATION OF INORGANIC LAYERED COMPOUNDS IN AQUEOUS SURFACTANT MEDIA

7.1 INTRODUCTION

With high surface area and novel properties, 2D materials are potentially useful for a range of applications. In addition to graphite, a wide range of inorganic layered compounds exist. A good example is the family of transition metal dichalcogenides [99]. These form 2D layers of covalently bonded transition metal atoms, M, and chalcogen atoms, X in the stoichiometry MX_2, with examples such as MoS_2, $NbSe_2$, and $NiTe_2$ [99]. In addition, some transition metal oxides [185] form 2D structures, as do other materials such as BN, Bi_2Te_3, Sb_2Se_3, FeTe, etc. In general these 2D layers tend to bond via van der Waals interactions, stacking to form 3D crystals. These materials span the whole range of electronic structures from insulator to metal [99] and display interesting properties such as superconductivity and thermoelectricity[186, 187].

While micromechanically exfoliated [3] single flakes of materials such as MoS_2 are ideal for electronic devices [188], large-scale liquid-phase exfoliation methods could lead to a range of thin film applications such as nanoscale hybrids for use in thermoelectrics [189], supercapacitors [190], or Li-ion batteries [191]. Although a number of layered compounds can be exfoliated by ion intercalation [108], this method is time consuming, extremely sensitive to environmental conditions, and results in structural deformations in some TMDs [115]. Furthermore, removal of the ions results in reaggregation of the layers.

More promisingly, it has recently been shown that both TMDs and BN can be exfoliated in organic solvents [96, 97, 192, 193]. However, for large-scale applications, exfoliation in an aqueous environment would be hugely advantageous. While BN can be dispersed in water due to sonication-assisted hydrolysis, this method cannot be extended to other layered compounds [194]. The discovery of a facile, scalable method to exfoliate a range of layered materials in water would assist the production and characterization of a range of new materials and greatly facilitate the potential transfer of such technology to industry. This chapter presents a simple, large-scale method to exfoliate BN, transition metal dichalcogenides, and transition metal oxides down to very thin platelets in aqueous surfactant solutions.

7.2 EXPERIMENTAL PROCEDURE

The MoS_2 Powder used in all experiments was purchased from Sigma Aldrich (Fluka, Product Number: 69860). The other transition metal dichalcogenide powders used were purchased from a range of suppliers listed below: In all cases the powders were used as supplied. WS_2: Sigma Aldrich (Product Number: 24363-9) $MoTe_2$: Cerac Incorporated (Item Number: 36498-FW-081897) $MoSe_2$: Cerac Incorporated (Item Number: 300041-1) $TaSe_2$: Chemsavers (no product number could be found) $NbSe_2$: American elements (Product Number: NB-SE-028-P.325M) Oxide: MnO_2 was purchased from Alfa Aesar (Product number: MnO_2, 42250)

All surfactants were purchased from Sigma Aldrich, product numbers in brackets Sodium dodecyl sulphate, SDS (L6026), Sodium Dodecylbenzenesulphonate, SDBS (D2525), Lithium dodecyl sulphate, LDS (861901), Sodium cholate, SC (C6445), taurodeoxycholate, TDOC (T0875), IGEPAL CO-890, IGP (238678), Triton X-100, TX-100 (T9284)

The MoS_2 and other layered compounds were dispersed in sodium cholate/water solution (0.1 to 9 mg/ml) in a polished stainless steel pot (100ml) at an initial TMD concentration of 5 to 30 mg/ml by tip sonication (Sonics VX-750 ultrasonic processor with flat head tip, 750W at 75% Amplitude) for various times (15 – 480 mins). The dispersions were then transferred to a glass pot (100ml) and allowed to settle for 24 hours. The top 50 mls of dispersion was then decanted into 2 glass vials (28.5ml) and centrifuged using a Hettich Mickro 22R for 90 mins at various RPM's (500-5000). After centrifugation (CF), decantation was carried out by pipetting off the top half of the dispersion into a single glass vial (28.5ml).

Single walled carbon nanotube (Iljin nanotech) dispersions were prepared in a similar manner by adding nanotubes to a solution of sodium dodecyl sulphate surfactant in water (5 mg/mL SC) such that the nanotube concentration was 1 mg/mL. This dispersion was subjected to 5 min of high power tip sonication (VibraCell CVX; 750

W, 20% 60 kHz), then placed in a sonic bath for 1 h, and then subjected to another 5min of high-power sonication.

Absorbance measurements were made using a Varian Cary 6000i and quartz cuvettes (10 mm). Sedimentation measurements were performed with a homemade apparatus consisting of an array of synchronized, pulsed lasers and photodiodes. Zeta potential measurements were carried out on a Malvern Zetasizer Nano system with irradiation from a 633 nm He-Ne laser. The samples were injected in folded capillary cells, and the electrophoretic mobility (μ) was measured using a combination of electrophoresis and laser Doppler velocimetry techniques. The pH of the sample was controlled by the addition of 1M NaOH and HCL. Each zeta measurement is the average of 5 results. Samples for TEM were prepared by drop casting from the dispersion onto holey carbon grids (400 mesh). TEM images were taken with a Jeol 2100 operated at 200 kV and the Oxford-JEOL JEM2200MCO FEGTEM/STEM, fitted with two CEOS Cs aberration correctors, operated at 200kV.

Thin films were prepared by vacuum filtration immediately after CF. A controlled volume of dispersion with known concentration was filtered through nitrocellulose membranes (pore size 25nm). The deposited films were washed with 100 ml of Millipore water followed by a wet transfer to a PET substrate. For transfer to glass, quartz or Si/SiO_2, films were dried on a hotplate at 50C for 20 mins after vacuum filtration. They were then wetted with IPA and pressed against the substrate. The cellulose filter membrane was then removed by treatment with acetone vapour and subsequent acetone liquid baths in all cases.

Raman and SEM samples were prepared by transferring the films onto Si/SiO_2. Raman spectroscopy was carried out on a Horiba Jobin Yvon LabRAM using a 50X objective lens with a 633 nm laser excitation. Each spectra shown is an average of 5 taken on various spots of the film. SEM was carried out using a Zeiss Ultra Plus SEM. Sheet resistance measurements were made using the four-probe technique with silver electrodes of dimensions and spacings of approximately millimeter size and a Keithley 2400 source meter.

Electrical conductivity and Seebeck coefficient (S), also known as thermopower, were simultaneously measured by suspending 30 x 7 mm samples between two thermoelectric devices with thermal paste. These devices were spaced 20 mm apart and used to generate temperature gradients. Silver paste was used to apply four lines on each sample to allow I-V measurements, which verified the ohmic nature of the contacts. Temperature differences and thermoelectric voltages were measured using T-type thermocouples, containing copper leads with negligible thermopower attached to the metal lines on opposite ends of the sample strip.

MoS_2/CNT cathodes were characterised using 2032 coin cells. The cells were assembled by using lithium metal foil as the counter electrode in an argon-filled glove box. The electrolyte solution was 1M LiPF6 in ethylene carbonate/diethyl carbonate (EC/DEC, 1:2 v/v). Constant-current charge–discharge tests were performed in the range of 0.01–3.0 V at a current density of 100 mAg-1. EIS was performed by using an Ametek PARSTAT 2273 electrochemistry workstation. The ac amplitude was 5 mV. The frequency range applied was 100 kHz–0.01 Hz.

The Size exclusion column was prepared by first measuring the volume to be ~50 mL. By using the known density of controlled pore glass (CPG) (Purchased from Millipore, Product No. CPG3000B, Mean pore diameter 2966A) the mass required to fill the column was calculated to be 16.5g. The CPG was then added to surfactant solution of Sodium Cholate (4.5mg/mL). The mixture was then shaken repeatedly while under vacuum to replace any trapped air with surfactant solution. The CPG/ Surfactant mixture was then poured into the glass column with the tap open. While pouring more surfactant solution into the column, the sides were tapped with a rubber stopper to allow the mixture to settle homogeneously. It was then left overnight and tapped again.

MoS_2 dispersions for size exclusion chromatography were mixed with ethylene Glycol (purchased from Aldrich, Product No. 32,455-8) at a ratio of 3:1 to increase the density of the dispersion. 3 mL of the resulting mixture was then added to the column using a 5mL syringe just above the top of the CPG mixture. The tap was then opened and 17.5 mL of liquid was allowed run off before the first fraction was collected. This volume was calculated by multiplying the known pore volume by mass of CPG in the column. Each fraction was collected every 3mL of dispersion.

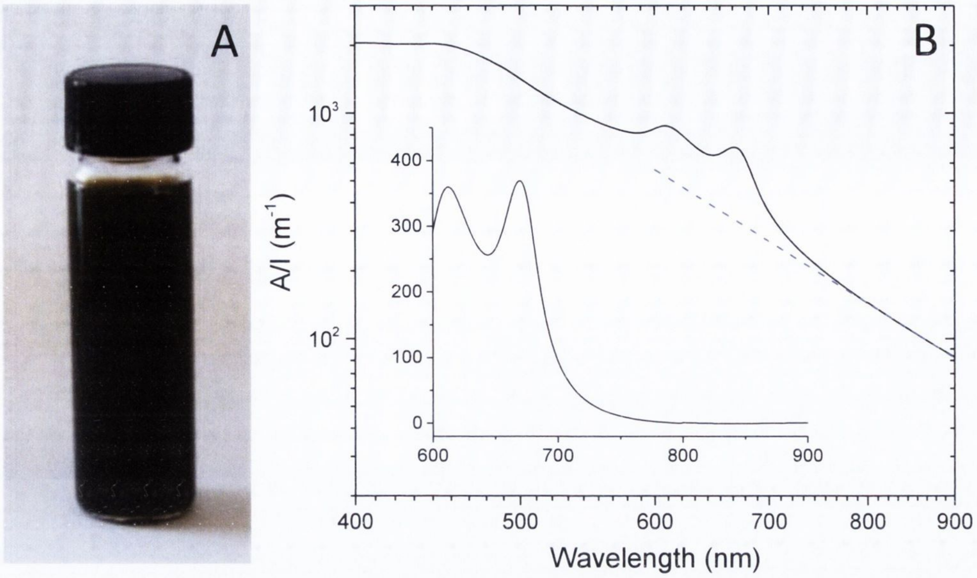

Figure 7.1: Surfactant exfoliation of MoS_2, A) A dispersion of MoS_2 flakes in water, stabilized by sodium cholate (SC) B) Absorption spectra of MoS_2/SC prepared by centrifuging at 1500rpm. Inset: The spectrum of the dispersion after subtraction of scattering background (dashed line in main figure)

7.3 RESULTS AND DISCUSSION

7.3.1. *Characterization of surfactant-stabilized MoS_2 dispersions*

In this study, MoS_2 powder at initial concentration, C_I = 5 mgmL^{-1}, was probe sonicated in an aqueous solutions of the surfactant sodium cholate of concentration, C_{SC} = 1.5 mg mL^{1} for 30 mins. The dispersions were centrifuged to remove unexfoliated powder resulting in dark supernatants as shown in Figure 7.1a. Optical absorption measurements gave spectra superimposed on a large power law background ($A \approx \lambda^{-a}$) shown in Figure 7.1b. Subtraction of this background gave spectra typical of MoS_2.

The power-law dependence of the absorbance on wavelength is characteristic of light scattering. To investigate this further, several MoS_2 dispersions were centrifuged at varying rates from 500 to 2000 rpm. The absorption spectra for these dispersions are shown in Figure 7.2a. For graphene dispersed in solvents or surfactants, as the centrifugation rate is increased, the flake size decreases and hence a similar phenomenon is expected here. It is clear that the slope of the scattering background (exponent, a) changes with centrifugation rate and hence flake size. The plot of

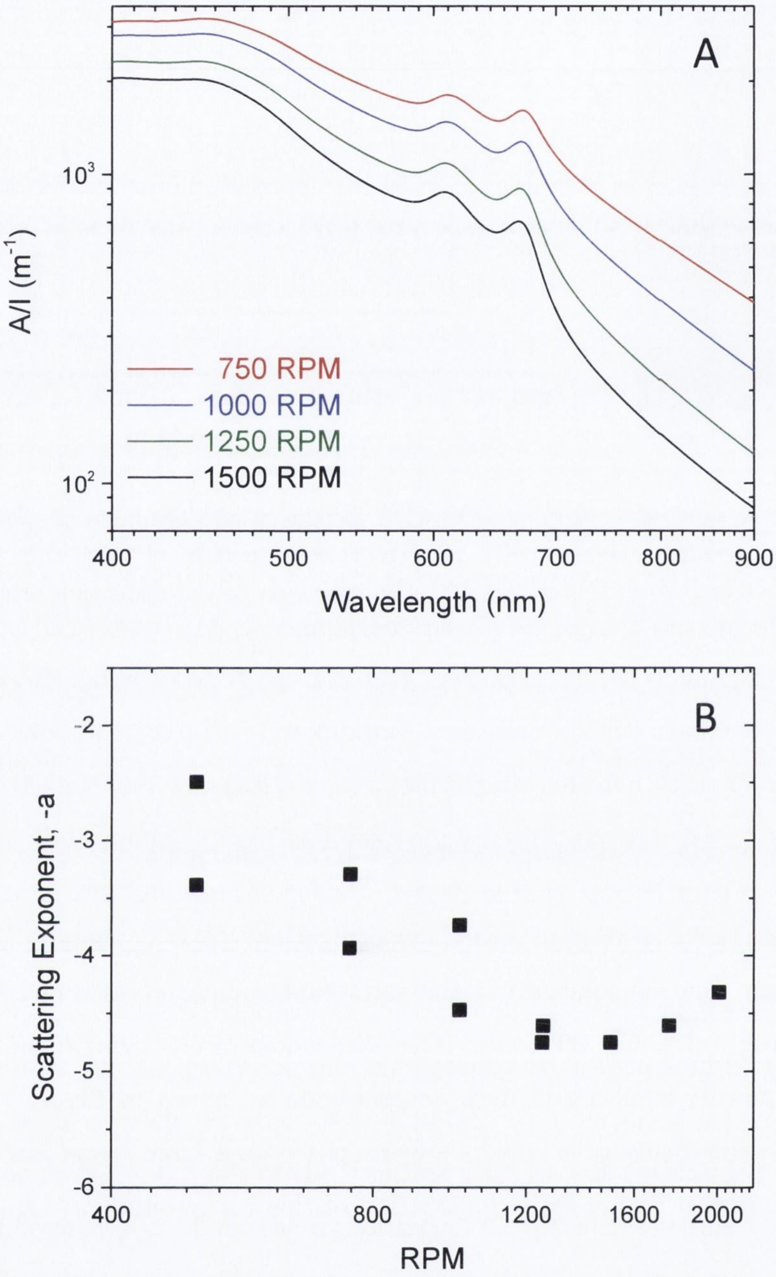

Figure 7.2: A) Absorption spectra for MoS_2 dispersions prepared with different centrifugation rates. B) The scattering exponent a, as a function of centrifugation rate.

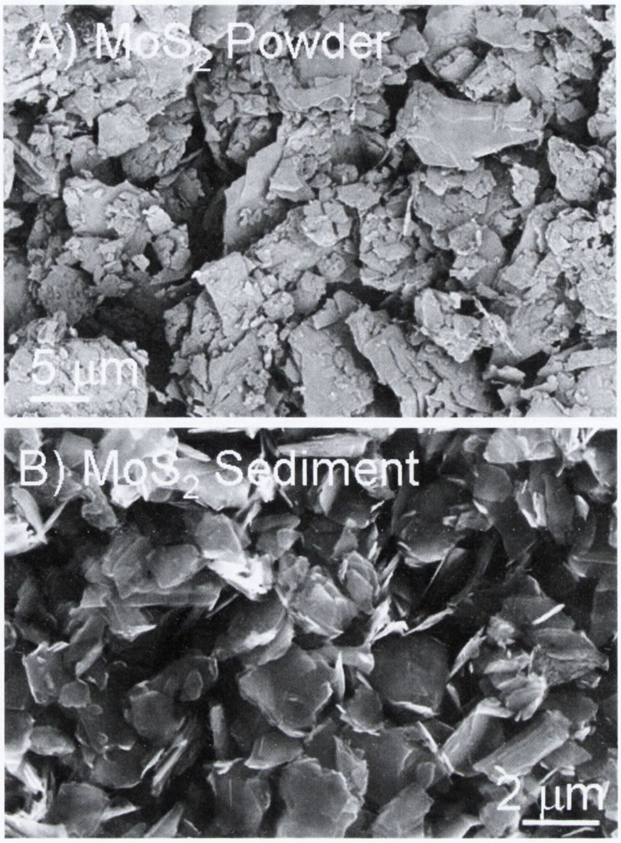

Figure 7.3: SEM images of A) the MoS_2 starting powder and B) the sediment collected after centrifugation.

scattering exponent a, against centrifugation rate in Figure 7.2b shows the exponent to decrease from -3 to -5 the centrifugation rate is increased. This particle size dependency further suggests that the background is due to light scattering [195, 196]. There are 3 possible types of light scattering for these dispersions: Rayleigh scattering, Tyndall scattering and Mie Scattering. Rayleigh scattering occurs when the scattering objects or molecules are much smaller in size than the wavelength of incident light whereas Tyndall scattering occurs for larger particles. Mie scattering theory covers the scattering between Rayleigh and Tyndall scattering regimes. Although this regime seems the most appropriate given the range of sizes of the dispersed flakes (Figure 7.9), it is worth noting that the exponent should not fall below -4 for mie scattering and hence further study is required to fully explain the scattering effects.

Both the starting powder and sediment collected after centrifugation were characterized using SEM as shown in Figure 7.3. The powder consists of flakes with a wide range of lateral sizes from 1 to 10s of microns. In contrast, the sediment

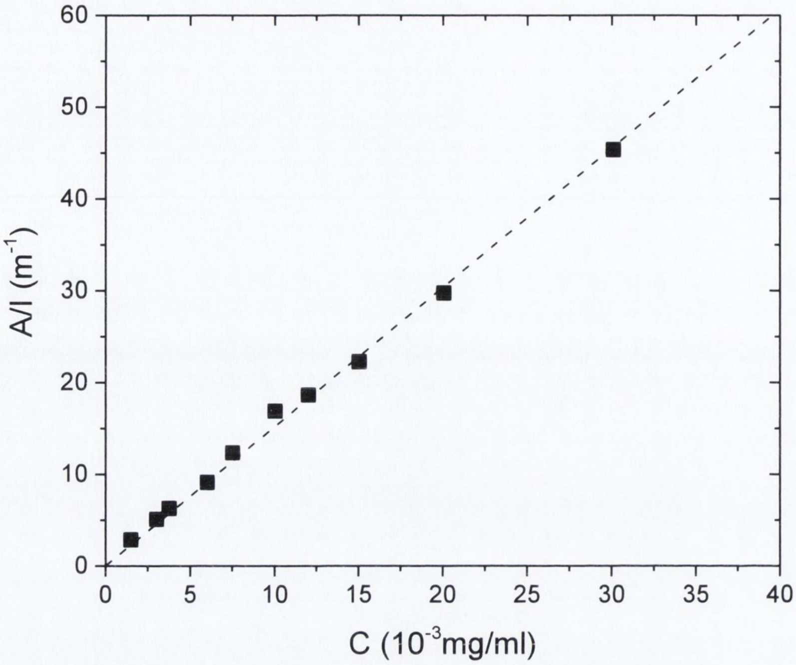

Figure 7.4: Absorbance per unit length (λ= 672 nm) as a function of dispersion concentration after centrifugation, C. Initial MoS_2 concentration C_I = 5 mg/ml with C_{SC} = 1.5 mg/ml.

consists of much smaller flakes with lateral size of only a few microns. This suggests that the sonication breaks up the MoS_2 crystallites, probably by sonication induced scission. Of the resulting dispersion of small flakes it is probable that only the smaller, thinner variety, are stable with the larger thicker phase falling out during centrifugation.

Optical absorbance of these dispersions scaled linearly with concentration (see Figure7.4) both before and after background subtraction. The dispersed concentration, C, was measured by filtration and weighing, allowing the estimation of the extinction coefficient α. Background subtracted spectra were used for these measurements as any measurement of α using raw spectra would be flake size dependent. The dispersed concentrations of all dispersions could then be measured using the Lambert–Beer law, $A/l = \alpha C$, where A / l is the absorbance per cell length.

To determine α, a high-volume dispersion (2000 ml) was prepared. A precisely measured volume of the dispersion (1400mL) was filtered under high vacuum onto a nitrocellulose membrane of known mass. The resulting thick film was washed with 800 ml of water and dried overnight in a vacuum oven at room temperature. The mass of material in the filtered volume of stock dispersion was then determined using a

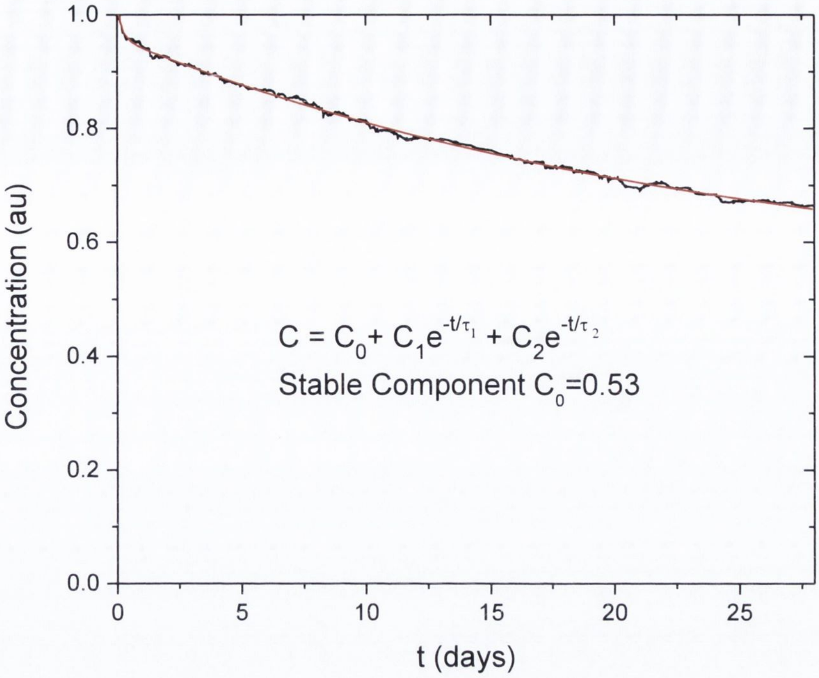

Figure 7.5: Concentration remaining as a function of sedimentation time for a MoS_2/SC dispersion over the course of one month. The data has been fitted to sedimentation theory for two sedimenting components (1 and 2) and a stable component (0). The fit constants are $C_0 = 0.53$, $C_1 = 0.43$, $C_2 = 0.05$, $t_1 = 24$ days, and $t_2 = 5.5$ hours.

microbalance to be 84.25 mg. Knowledge of the mass of MoS_2 in the film allowed the final concentration of the stock dispersion to be determined. A sample of the stock dispersion was then serially diluted with 1.5 mg/ml SC solution, allowing the measurement of the absorbance per unit length (A/l) versus concentration of MoS_2 (after centrifugation, C) The background was subtracted from each spectra and the A/l value at 672 nm was plotted versus dispersion concentration. The slope of this curve gave the absorption coefficient to be a=1517 L/g/m

After centrifugation, sedimentation measurements [146] were performed in order to quantitatively assess the temporal stability of these dispersions. The optical absorbance of the sample at 650 nm was monitored as a function of time as shown in Figure 7.5. The measured absorbance fell sharply at first then steadily over a period of weeks indicating that just fewer than 50% of the material had fallen out of the dispersion.

A biexponential fit to the data suggests one stable phase and two sedimenting phases: one rapid and one slowly. The rapidly sedimenting phase constitutes approximately 5% of the dispersed material while the slower sedimenting phase about

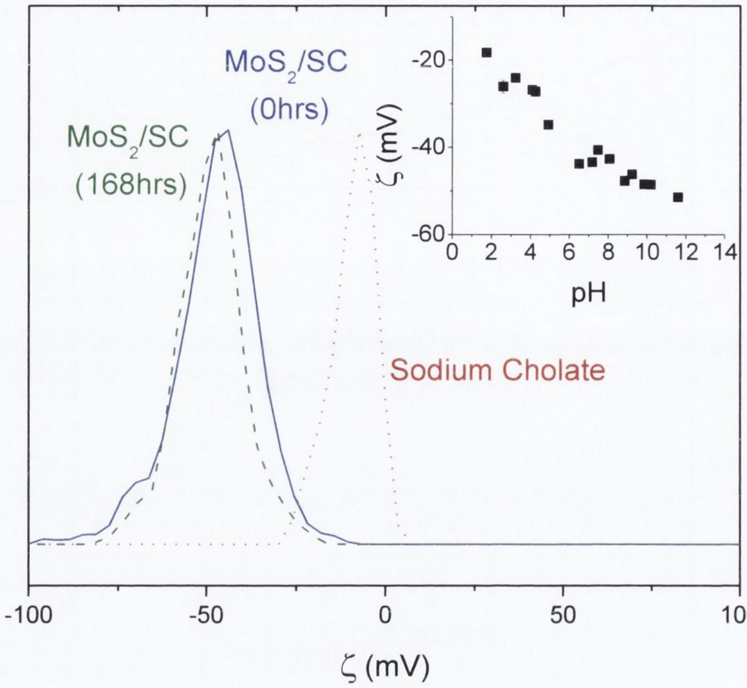

Figure 7.6: Zeta potential spectra for SC solution and MoS_2/SC dispersions immediately after preparation (solid) and after 1 week (dashed). Inset: Zeta potential of MoS_2/SC dispersions as a function of pH (adjusted by addition of 1M HCl and NaOH)

45%. The rapidly sedimenting phase is most likely due to residual unexfoliated material while the slowly sedimenting phase is more likely to be larger less stable flakes. The fact that over half the MoS_2 remains dispersed means that the temporal stability of these dispersions compares very favourably with their graphene counterparts[81]. It is also worth noting that the observation of such stable dispersions at relatively low zeta potential suggests that previous estimates of the MoS_2 surface energy may be too high [197].

Surfactant-coated nanoparticles are usually stabilized by electrostatic repulsion as characterized by the zeta potential [81, 86]. At neutral pH, the zeta potential of the sodium cholate coated MoS_2 was measured to be stable over weeks at –40 mV (Figure7.6) and was extremely robust against changes in pH. The pH of the fresh dispersion was varied by addition of HCl and NaOH with the results shown in the inset of Figure 7.6. As the pH is raised, the zeta potential trends towards more negative values suggesting that the repulsions between the flakes are increased as more negative OH- charges are added to the flakes. As the pH is lowered, there is a trend towards a less negative zeta potential, consistent with charge neutralization and destabilization of the dispersions. This zeta potential versus pH trend is in line with

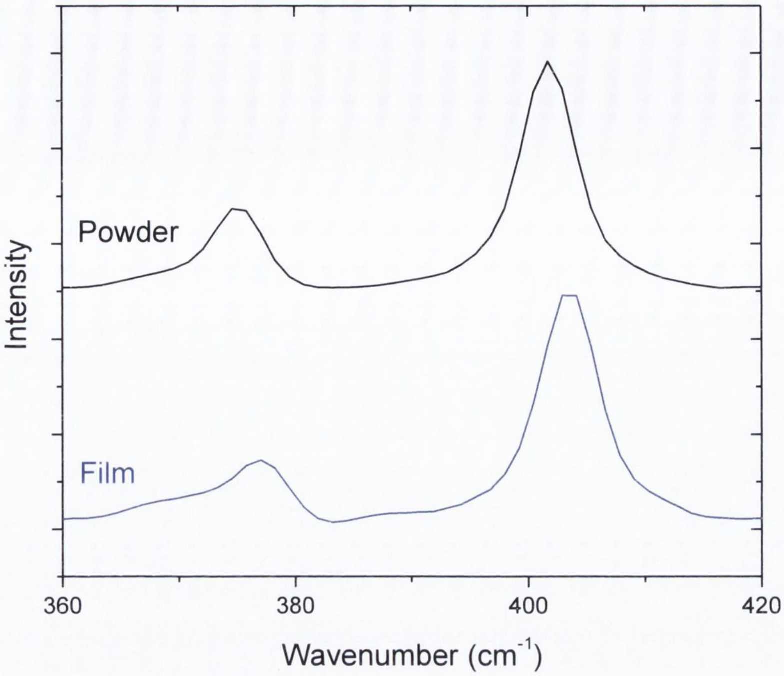

Figure 7.7: Raman spectra Raman spectra of both the starting powder and a MoS_2 film deposited on SiO_2 wafer.

trends reported for graphene and graphene oxide colloids [81] By lowering the pH, the zeta potential approaches the limit of stability for colloidal dispersions however it does not pass through the isoelectric point. This may be due to very high surface coverage of graphene flakes by sodium cholate molecules, something which will be discussed in the next section.

As previously discussed in chapter 4, the Raman spectra of MoS_2 has two main peaks of interest: the E^1_{2g} and the A_{1g} bands located at 383 cm^{-1} and 409 cm^{-1} respectively. Raman scans were performed on both the starting powder and a thin film deposited on an SiO_2 wafer. The spectra shown in figure have intense peaks at positions close to reported values from the literature with very little shift in peak positions or relative intensities between the MoS_2 powder and thin film, This strongly suggests the structure to be undistorted 2H MoS_2.[166] in contrast to ion-exfoliated MoS_2 , which generally becomes distorted from the bulk 2H structure [112, 198].

It is critical to ascertain the nature of the dispersed MoS_2. TEM examination of material deposited from the dispersion showed the presence of large quantities of extremely thin 2D flakes such as the one shown in Figure7.8a. It is reasonable to conclude that these flakes consist of a small number of stacked MoS_2 monolayers. High

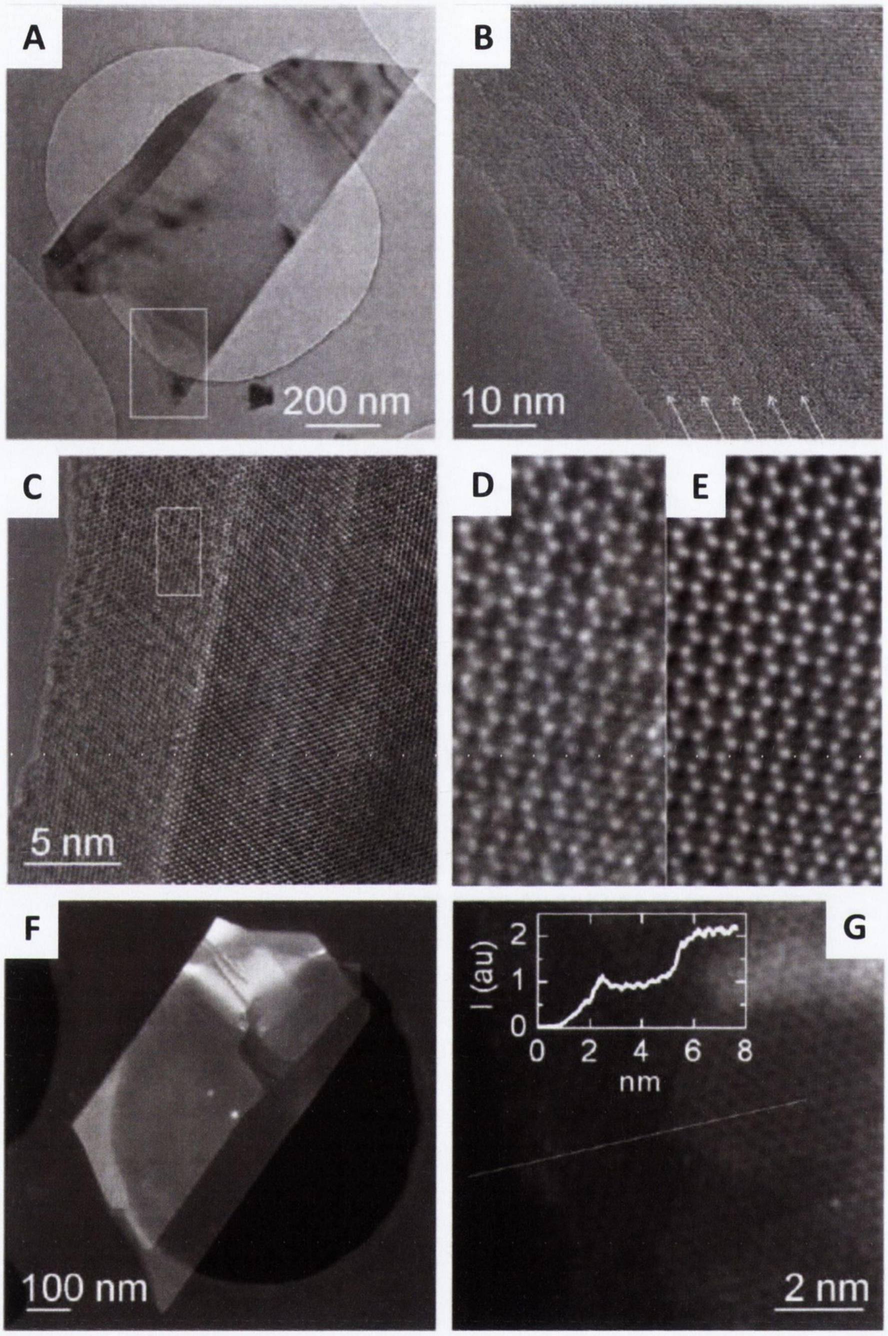

Figure 7.8: A) Typical bright field TEM image of MoS_2 flake. B,C) Phase contrast HRTEM images of a thin MoS_2 flakes showing layer edges. D) A zoomed image of the region in (C) indicated by the white square showing the MoS_2 atomic structure. E) A digitally filtered low-pass fast Fourier transform with spot masking and a 25-point smoothing image. F) Dark field scanning TEM image of a thin flake G) An unfiltered aberration corrected high-angle annular dark field (HAADF) STEM image. Inset: Average signal intensity plotted over the dashed line.

resolution TEM and STEM imaging was carried out by collaborators at the University of Oxford (Prof. Valeria Nicolosi and co-workers) The high resolution images in Figure 7.8e show clean, well-defined, hexagonally symmetric structures while the diffraction pattern in the inset Figure 7.8a is consistent with an undistorted lattice. Annular dark-field STEM imaging gives better layer contrast for MoS_2 than for graphene as the electron energy loss is proportional to the square of the atomic number. This technique was used to observe individual layer edges near the periphery of these flakes (Figure 7.8g).

As previously discussed in chapters 5 & 6, low-res TEM images of a highly populated grid can be used to generate statistics on flake dimensions for a given dispersions. Figure 7.9a shows the lateral size distribution for a standard dispersion of MoS_2. The Mean flake diameter is approximately 280 nm. For graphene flakes, it has been shown that edge counting can be a reasonably reliable way to approximate the number of layers [81, 176]. These layers can be clearly seen at the flake edge for the MoS_2 shown in Figure 7.8b. Flake thickness analysis was performed using careful edge-counting, in the same manner as for graphene with exfoliated flakes estimated to be between 2 and 9 layers thick.

The high contrast of STEM imaging provides an opportunity to improve on the reliability of these measurements by using fixed microscope conditions and a precisely calibrated annular dark-field detector. This allows the use of intensity cross sections at flake edges to reliably count layer number as shown in the inset of Figure 7.8g. However, such analysis requires special equipment, is time consuming and can be complicated by sample contamination caused by the STEM probe. Improvement of this technique will be crucial in generating fast and accurate statistics on flake thickness distributions in the future.

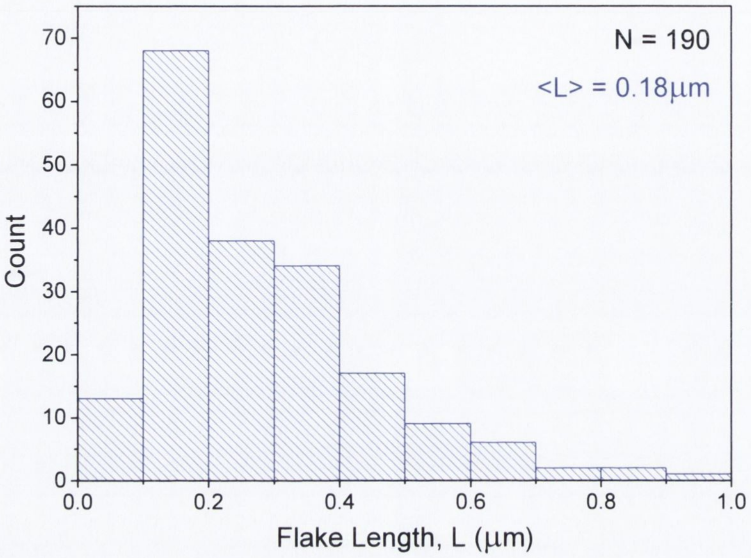

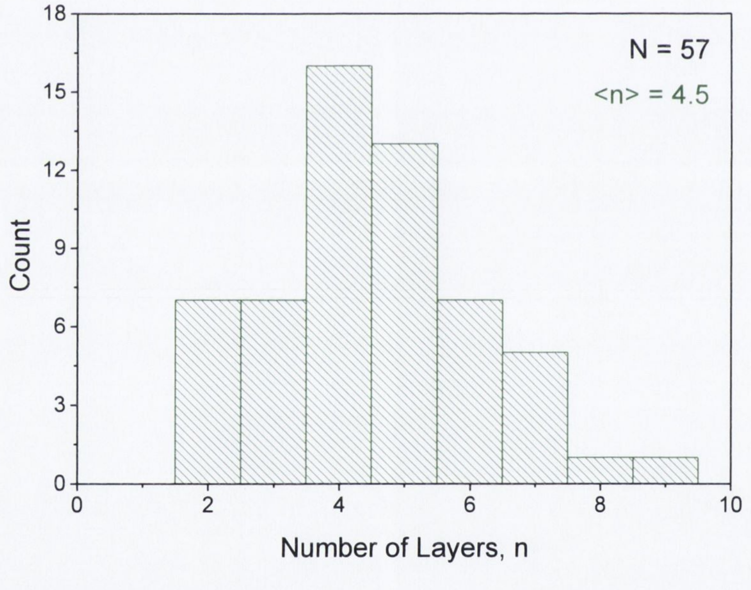

Figure 7.9: A) Flake length histogram for a standard dispersion. B) Histogram of flake thickness for a standard dispersion. These are estimated by examination of the edges of the flakes as has been described for graphene.

7.3.2. *Optimisation of surfactant-stabilized MoS_2 dispersions*

Using dispersed concentration C as a metric, the effect of varying processing parameters was investigated in order to obtain fully optimized dispersions of MoS_2. The main parameters considered were the initial MoS_2 concentration C_I , the surfactant concentration C_{SC}, the sonication time t_{sonic} and the sonication power.

The first part of this study investigated the effect of varying C_{SC} using fixed parameters $C_I = 5$ mg/ml, $t_{sonic} = 30$ mins and CF time 90 min at $w = 1500$ rpm. The initial MoS_2 concentration, sonication time and CF rate were chosen based on previous work with graphene dispersed using surfactants as discussed in chapter 5. It was found that the dispersed concentration increased monotonically with surfactant concentration as shown in Figure 7.10a before tapering off around $C_{SC}=0.3C_I$. It is important to note that this is well below the CMC.

This trend can be explained by considering the interactions between the surfactant molecules the dispersed flakes. As the surfactant concentration is increased, more surfactant molecules adsorb onto the surface of the flakes increasing their effective charge. This increases the size of the repulsion between the flakes which has been linked to dispersed concentration in Chaprter 5. This trend would indicate that maximum surface coverage is reached around $C_{SC}=0.3C_I$. As no more surfactant molecules can be packed onto the surface of the flakes, no more surface charges can be added. This means that the addition of more surfactant is no longer having a large effect on the repulsions between surfactant coated flakes and hence the dispersed concentration is unaffected. This high surface coverage of surfactant would also explain why the zeta potential of these dispersions is so robust to changes in the pH.

The initial concentration of MoS_2 was also varied keeping C_{SC} fixed at $0.3C_I$ and all other parameters as in the previous experiment. The dispersed concentration was found to scale linearly with the starting concentration for $C_I < 20$ mg mL^{-1} shown in Figure7.10b. This allows definition of a yield, Y ($C=YC_I$). The dotted line represents a yield of ~1 %

One advantage of tip sonication over bath is the ability to vary as well as directly measure the energy output. It is clear from the data presented in Figure 7.11a, that the dispersed concentration scales linearly with the power output of the tip. While increasing the power is key to increasing the concentration of these dispersions, it is

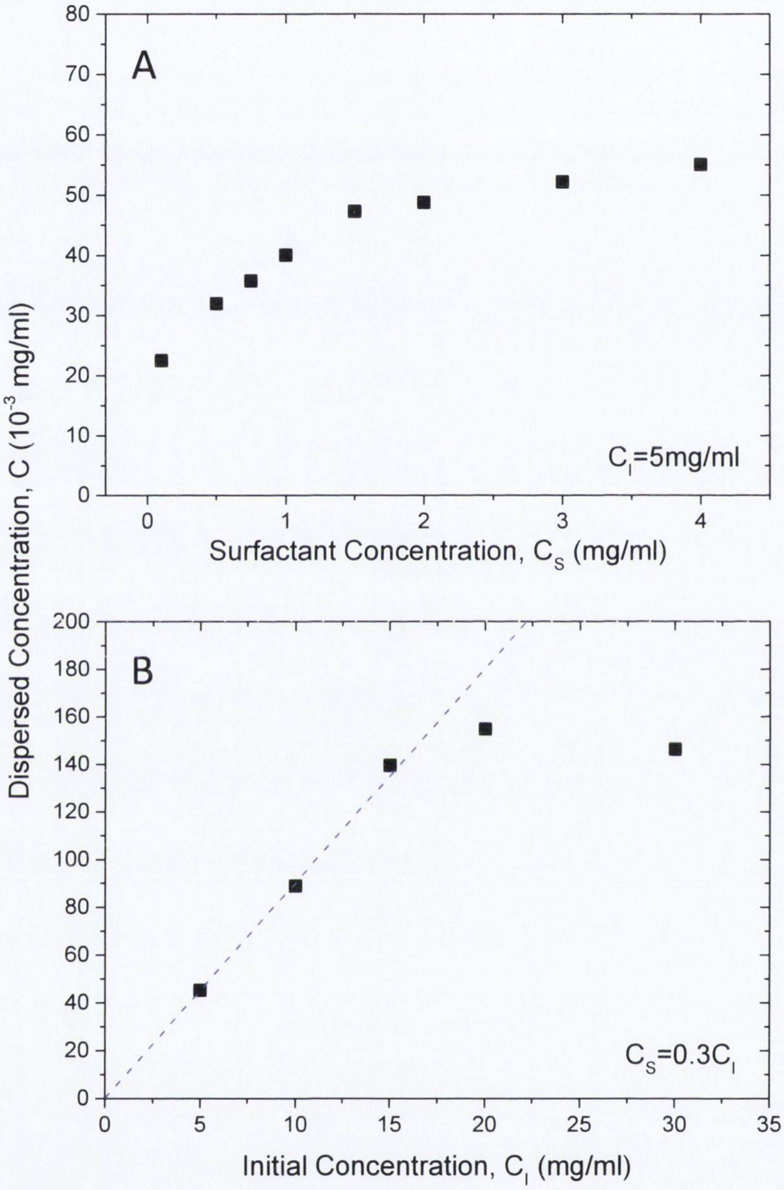

Figure 7.10: Dispersed concentration of MoS_2 C, of as a function of: A) Sodium cholate concentration C_{SC}. B) Initial concentration C_I.

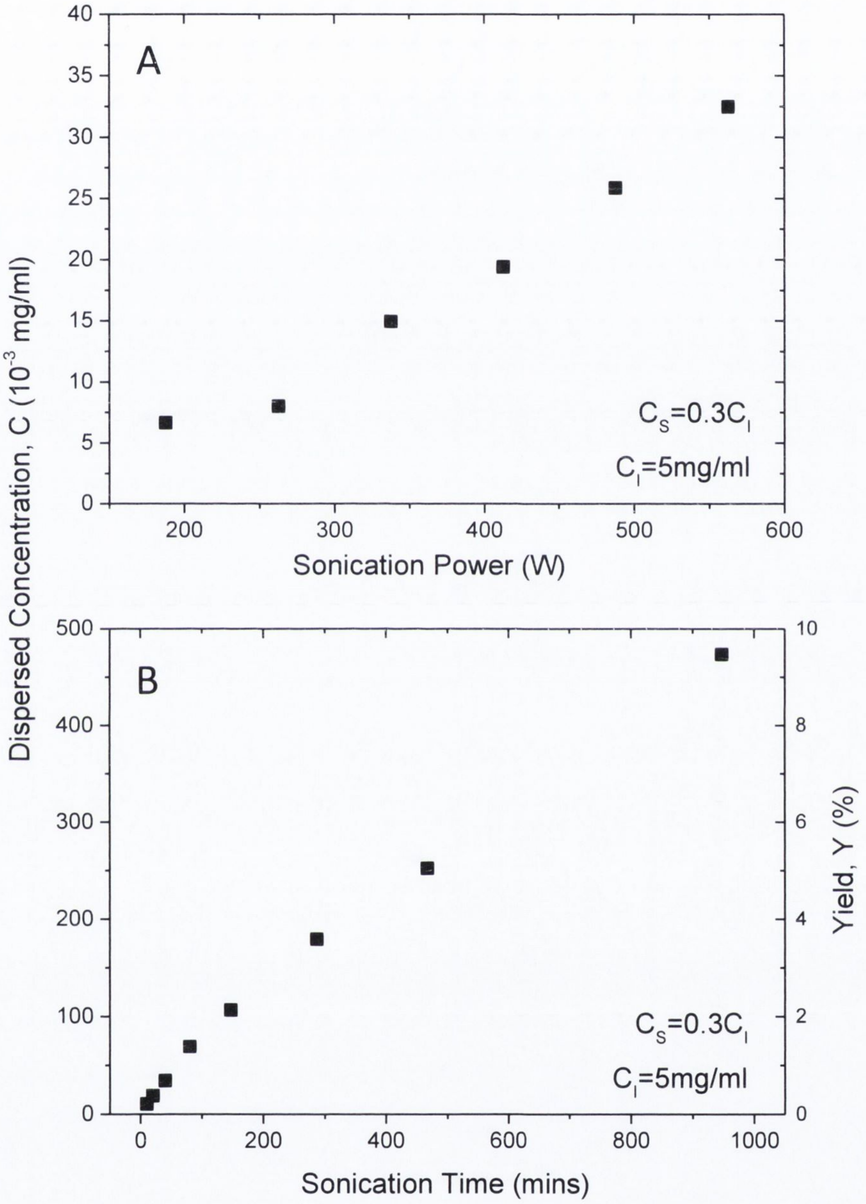

Figure 7.11: Dispersed concentration of MoS_2 C, of as a function of: A) Sonication Power. B) Sonication time t_{sonic}.

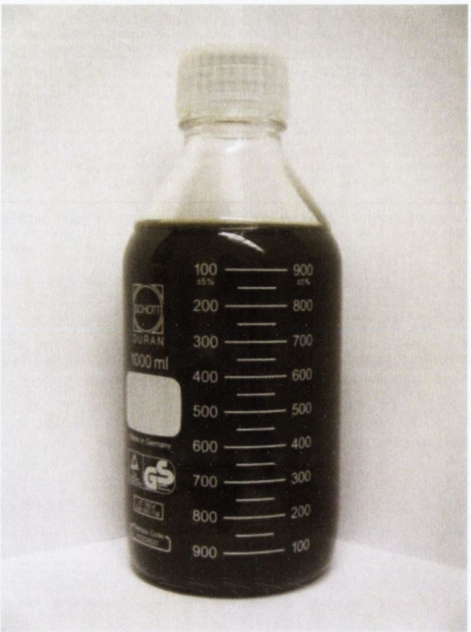

Figure 7.12: Litre of MoS_2 dispersed in sodium cholate. The sample was produced in less than 24 hours.

perhaps more important for large scale production, to maximise the dispersed yield i.e. the fraction of starting material dispersed. To this end, dispersions with low C_I were sonicated for long times, up to 16 hours. It was found that the yield increased with sonication time, up to ~10% as shown in Figure 7.11b. However, although high, this still means that ~90% of the MoS_2 does not become dispersed. To address this, the sediment was collected after 16 hours of sonication and added to 100 mL, of surfactant solution ($C_{SC}=0.3C_I$), sonicated for a further 16 hours and then centrifuged as before. This approach was successful in redispersing the sediment at a concentration of 0.37 $mgml^{-1}$ (Y=7.5%). This means that the total yield can be increased to 17.5% in a two-step process suggesting that the total effective yield could greatly be increased by efficient recycling of MoS_2 in multiple steps.

This method can easily be used to produce dispersions on the scale of litres. Ten 100ml dispersions were prepared by tip sonication to produce the litre of MoS_2 shown in Figure 7.12. The initial concentration was $15mgml^{-1}$ and sonication time 40 mins, allowing the production of a litre of reasonable concentration and stability (0.26 $mgml^{-1}$ after CF at 1500RPM) in less than a day. High volume of dispersion can also be produced with very little care and attention by a method whereby a sonic bath is used instead of a sonic tip. The sonication time required to obtain a reasonable concentration is much higher (~99 hours) due to the much lower power output of the

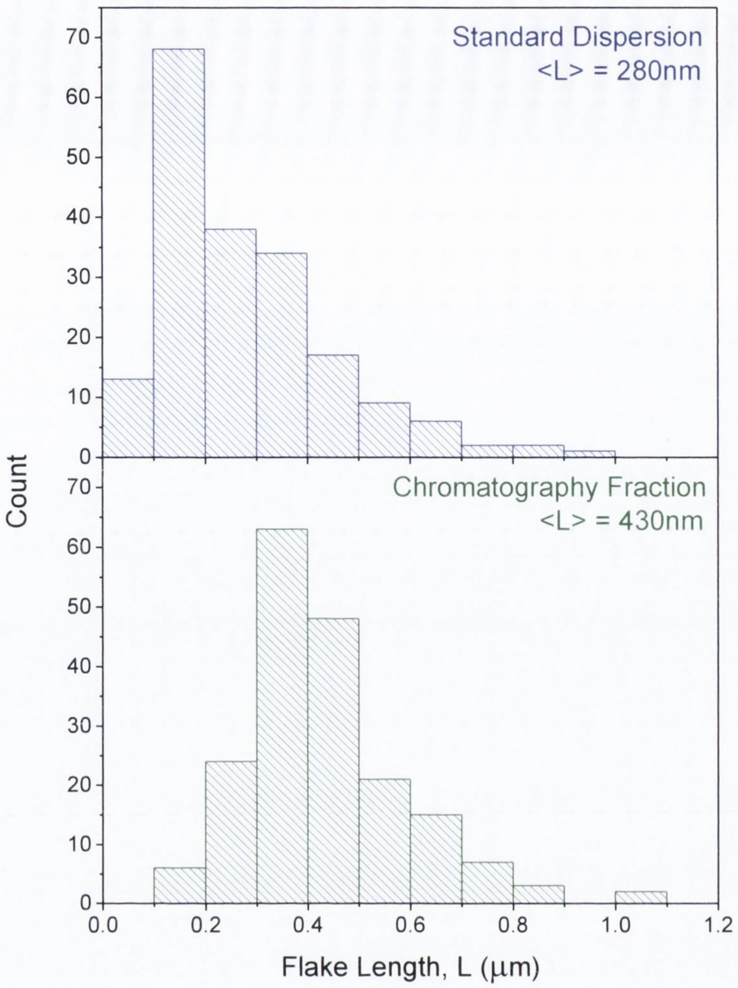

Figure 7.13: Lateral Flake size histograms for both a standard dispersion (Top) and the largest fraction separated by size exclusion chromatography.

bath compared to the tip. Another problem with bath sonication is reproducibility. The energy inputted into the sample by the bath is not as easily controlled or fixed compared to the tip making it more difficult to finely tune dispersion parameters. Bath sonication does have its advantages as much larger volumes can be sonicated at once.

For a number of applications, it would be advantageous to have control over the flake size in these dispersions. To this end, size exclusion chromatography (as discussed in Chapter 6 was used to isolate the fraction of larger flakes within a standard dispersion. The first fraction contained only surfactant solution but the second fraction contained well defined, exfoliated flakes. These were imaged with TEM and the flake length measured for over 100 flakes (Figure7.13). The flake length follows a broad distribution with a mean at <L>=430 nm which is significantly larger than for a standard dispersion. It is clear from the comparison with the size distribution of a standard dispersion that the chromatography has been effective in completely separating out flakes smaller than 100nm. As discussed in chapter 6, the resolution of this separation could be improved by increasing the dispersion concentration thus decreasing the volume required. The column volume could also be increased or multiple chromatography set ups could be used with varying pore sizes.

In order to compare the dispersibility of MoS_2 in a selection of surfactants, MoS_2 powder was dispersed in aqueous surfactant solutions using the following dispersion parameters: C_{Surf}= 1.5 mg/mL, C_I= 5 mg/ml, t_{sonic} = 30mins, centrifugation rate = 1500rpm, centrifugation time = 90 mins. Various ionic and non-ionic surfactants were tested in order to compare the success of both electrostatic and steric stabilization of MoS_2 in aqueous media. After centrifugation the samples were decanted and the absorption spectra measured (Figure7.14a). The absorption spectra are similar to those presented in previous sections consisting of resonant transitions typical of MoS_2 superimposed on a scattering background.

Using the measured absorption coefficient, the background-subtracted absorbance was used to calculate the dispersed MoS_2 concentration for each sample. The measured values for C are shown in Figure 7.14b and vary from 0.06 to 0.09mgml^{-1}. Although the concentrations are significantly higher than for similar work with graphene dispersions in chapter 5, the spread in concentrations is very similar to that seen in Figure 5.1 suggesting the two systems are very similar. Indeed the large difference in dispersed concentration could be due to the factor of ten increase in surfactant concentration for MoS_2 samples compared with graphene.

It is important to note that in all cases, the scattering backgrounds have similar slopes (scattering exponents) with the exception of TDOC and Triton X. The value for these scattering exponents is close to those obtained for sodium cholate dispersions centrifuged at a lower RPM. This would imply that there is an increase in average flake size for the TDOC and Triton X dispersions. While the initial work with graphene in chapter 5, has shown the flake size to vary slightly with surfactant, further study is required to fully assess the effect that surfactant choice has on parameters such as flake length and thickness for these dispersions.

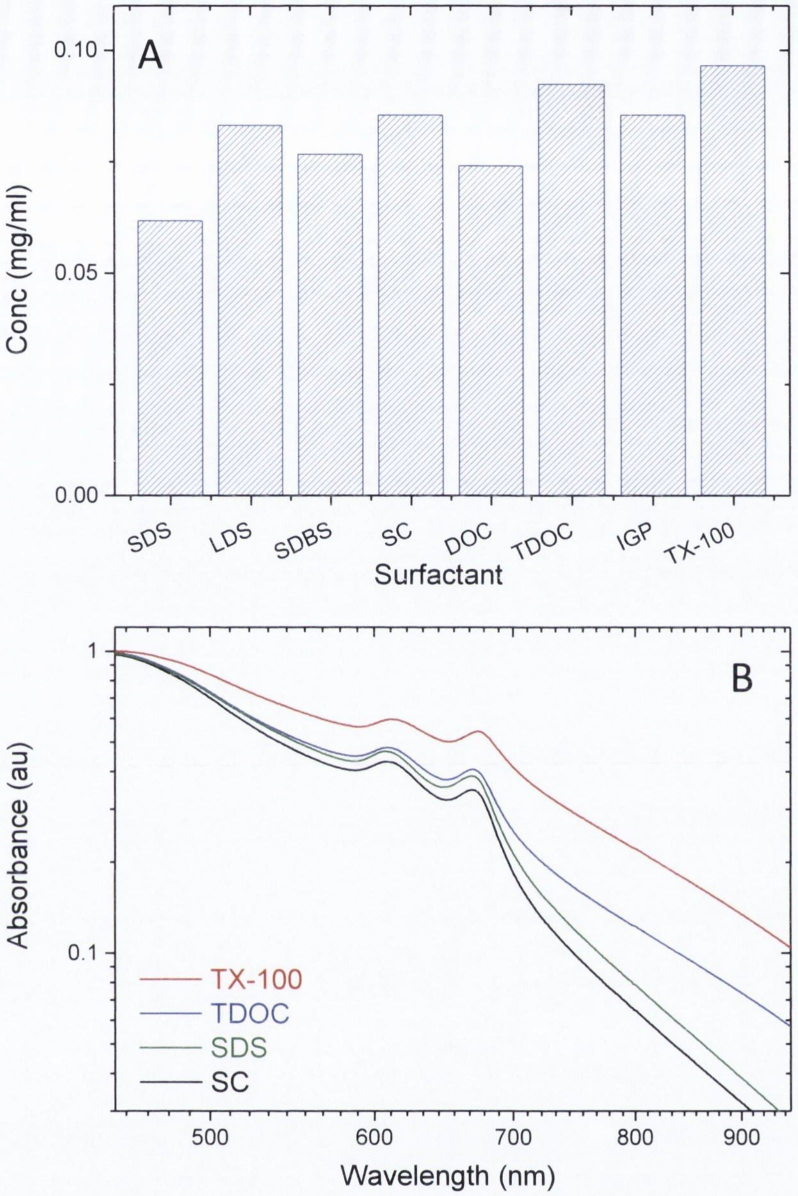

Figure 7.14: A) Dispersed concentration of MoS$_2$ C, for seven different surfactants. C_I, C_{surf}, t_{sonic} and ω were kept constant across the samples to aid comparison. B) Absorbance spectra for MoS$_2$ dispersed in four different surfactants.

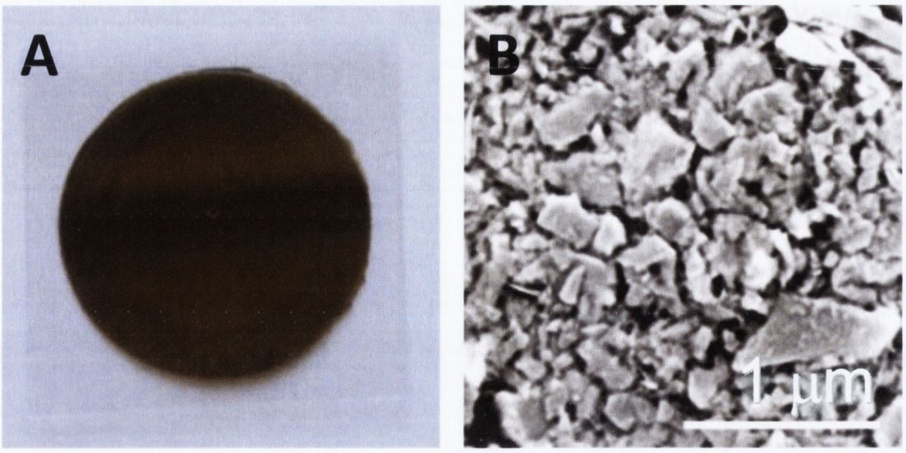

Figure 7.15: A) Thin vacuum filtered film of MoS_2 transferred onto a PET substrate. B) SEM micrograph of film identical to that shown in A, transferred onto an SiO_2 substrate.

7.3.3. *MoS_2 thin films*

Exfoliation of layered materials in an aqueous environment can be considered a gateway technology because it allows a wide range of processing techniques to be applied. Once a stable, environmentally robust dispersion has been prepared, it is straightforward to prepare films by vacuum filtration with thickness from nanometers to tens of micrometers. It is also straightforward to transfer these thin films to a number of substrates for various analytical techniques or for possible use as coatings. Figure 7.15a shows a thin film of MoS_2 (~200nmthick) transferred onto a flexible PET substrate. SEM imaging of an identical thin film deposited on SiO_2, shows a disordered array of MoS_2 flakes stacked predominately in-plane (Figure7.15b). The distribution of flake sizes in this image is consistent with those measured using TEM analysis of the dispersions themselves.

For samples with maximum observed yield, the surfactant was related to the starting MoS_2 concentrations by: $C_{SC}=0.3C_I$. This means that for a high-concentration dispersion (0.5 $mgml^{-1}$), the surfactant concentration will be 3 times that of the dispersed MoS_2. This much surfactant may be a problem for subsequent applications. To explore this, Thermogravimetric analysis was performed on an MoS_2 film prepared by vacuum filtration to estimate the surfactant content. This data is shown in Figure 7.16a and clearly shows three oxidation events at temperatures of ~280C (blue arrow), ~400C and ~750C (red arrows). The material burning during these events can be

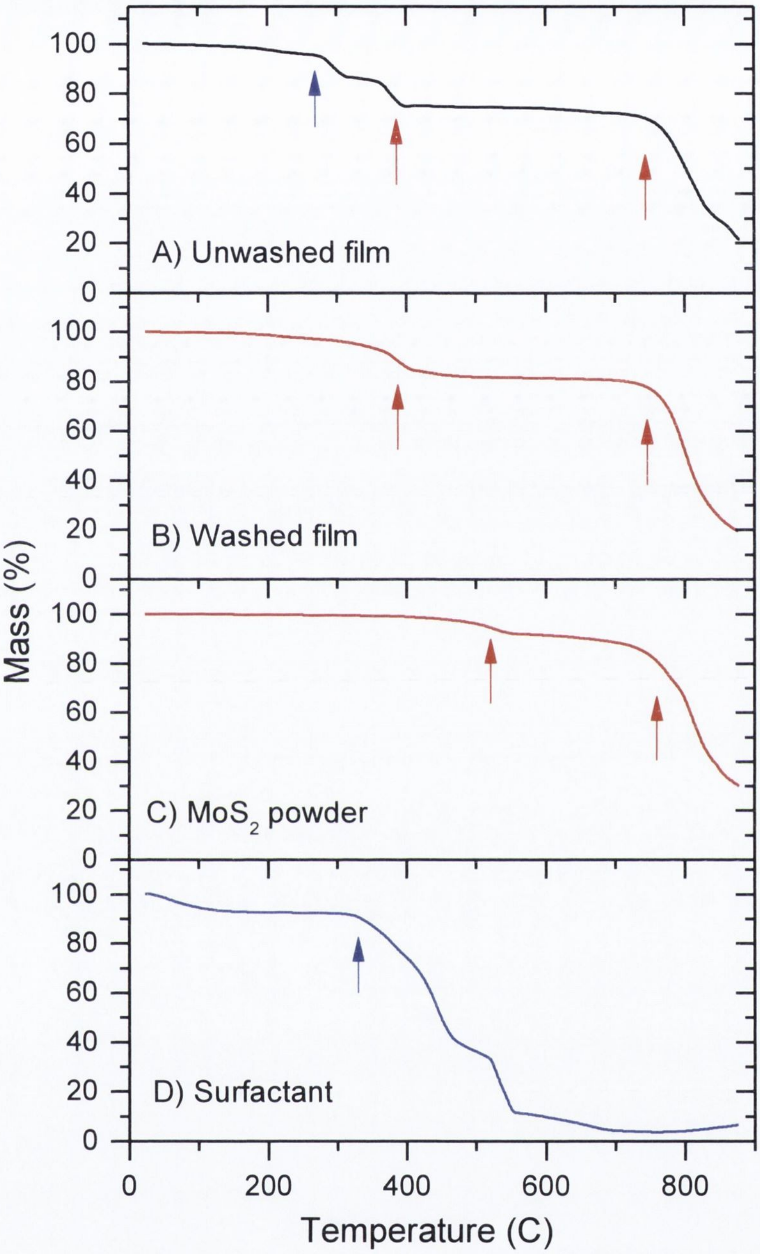

Figure 7.16: Thermogravimetric analysis data for A) an as-prepared MoS_2 film, B) a film after washing with excess water, C) the MoS_2 starting powder and D) the starting surfactant powder. Surfactant used was sodium cholate.

identified by comparison with the TGA curves for the starting MoS_2 powder and the starting surfactant powder (Figure 7.16c-d).

The MoS_2 powder displays two oxidation events at ~500°C and ~750°C (red arrows). These events have been observed in the literature and are known to occur at temperatures that depend on particle size with smaller particles having a lower oxidisation temperature [199]. Exfoliated flakes are of a much smaller size than those in the starting powder so it is reasonable to suggest a down shift in oxidisation temperature for the film compared to the starting powder. Thus, the peaks marked by the red arrow in Figure 7.16a can be identified as MoS_2 peaks. The powdered surfactant displays a main oxidation event at ~330°C. Again, it is reasonable to associate the peak at ~280°C in Figure 7.16a with surfactant as the dispersed surfactant molecules should have a lower oxidizing temperature than the much larger surfactant powder.

The data suggests that the MoS_2 film contains ~12wt% surfactant consistent with results for similar graphene films [176]. It is likely that the rest of the surfactant (the vast majority) was washed through the film during filtration. The simplest way to attempt to remove the residual surfactant is by simply washing the film with 400mL of water while is still on the membrane in the Buchner funnel. The TGA data for such a washed film is shown in Figure 7.16b. It is clear from the data that the surfactant peak identified at ~280C has disappeared. This demonstrates that the vast majority of residual surfactant can be removed by simply washing the films.

7.3.4. *MoS_2 hybrid films*

The relatively low electrical conductivity of TMDs is a major stumbling block when considering them for use in applications such as thermoelectric devices, Li ion batteries or supercapacitors. However, the conductivity would be increased dramatically by incorporation of conducting nanostructures into the TMD films. To demonstrate this, graphene and single-walled nanotubes were debundled in aqueous sodium cholate solutions at known concentrations. These were then blended with an aqueous MoS_2/SC dispersion in various ratios to give MoS_2/graphene and MoS_2/SWNT dispersions with a range of compositions. These could then be formed

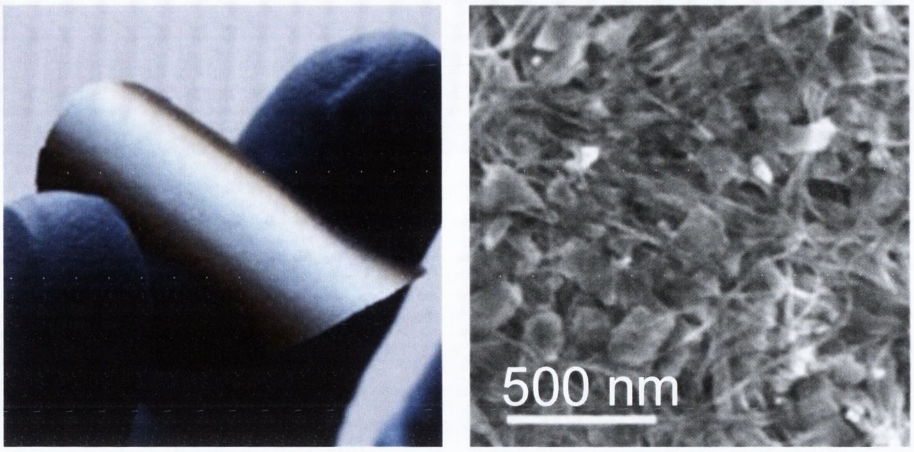

Figure 7.17: Photograph and SEM image of a thin MoS_2/SWNT hybrid film.

into free-standing films by vacuum filtration. Figure 7.17 shows a free standing MoS2/SWNT composite. While the free standing MoS_2 films are rather brittle, the addition of SWNTs greatly enhances the mechanical properties making them more flexible under strain. SEM analysis shows the MoS_2/graphene films to be similar in morphology to the MoS_2-only films (Figure 7.18:inset), while for the MoS_2/SWNT films, the flakes appear to be embedded in the SWNT network (Figure7.17). Addition of the nanoconductors increases the film conductivity, σ_{DC} , dramatically from $\approx 10^{-5}$ Sm^{-1} for the MoS_2 alone to 1000 Sm^{-1} for 100% graphene and 2×10^{5} S m^{-1} for 75% SWNTs (Figure 7.19a). Having tuneable electronic properties makes these films useful for a range of applications with two discussed in this section.

Increasing the DC conductivity of nanostructured materials without degrading the Seebeck coefficient is an important goal in thermoelectric research [189]. Figure 7.19 shows the DC conductivity of the hybrid films to increases in a percolation-like fashion as $\sigma_{DC} \propto M_f^{\ n}$ with n=0.84. For M_f values of 50% and above, the conductivity was above 10^5 S/m. This compares with approximate measurements of the out of plane conductivity for MoS_2 of $\sim 10^{-6}$ S/m showing that the addition of nanotubes results in extremely large increases in conductivity. The Seebeck coefficient was found to decrease slightly on addition of nanotubes remaining close to $S = 25$ μ VK^{-1} up to 75 wt% SWNT. The decrease was linear with a slope of dS/dMf=16.8 mV/K, suggesting that the Seebeck coefficient may follow a rule of mixtures-type relationship with material composition. Importantly, the power factor increased with nanotube content (Figure 7.19c), reaching $S^2\sigma_{DC} = 87$ μ $Wm^{-1}K^{-2}$ for 75 wt% before falling off

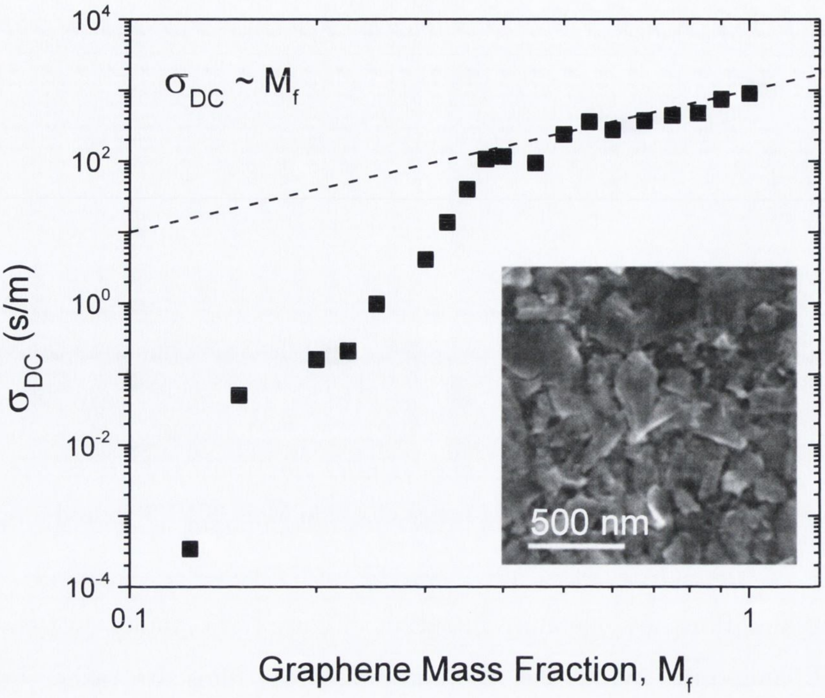

Figure 7.18: Electrical properties of MoS_2/graphene films as a function of mass fraction, M_f (thickness ≈ 200 nm)

at higher nanotube contents. This work clearly shows that addition of nanotubes increases the power factor dramatically compared to the MoS_2 only film.

It is important to note that it was not possible measure the Seebeck coefficient for an MoS_2 only film. The value of 34 mV/K suggested by the intercept in Figure 7.19b is much lower than the reported value for single crystal MoS_2 (600mV/K). It is expected that the value for the disordered films as reported here would be considerably lower than single crystal. The thermoelectric power factor for single crystal MoS_2 is approximately 0.02 mW/mK2 (S2sDC=(600mV/K)2´0.05 S/m). As suggested above, the power factor for a disordered film should be considerably lower than this.

It should be possible to extend this work to other layered compounds such as WSe_2 or TiS_2 which have very large Seebeck coefficients (900 and 1800 mV/K respectively). Thus it is reasonable to suggest that this approach could lead to hybrid materials with extremely large power factors. It is important to note that low thermal conductivities are also a requirement for thermoelectric materials. It has previously been shown that the thermal conductivity increases as nanotubes are added to WS_2 from ~1 W/mK to ~30 of W/mK for samples with nanotube content >25%. While the

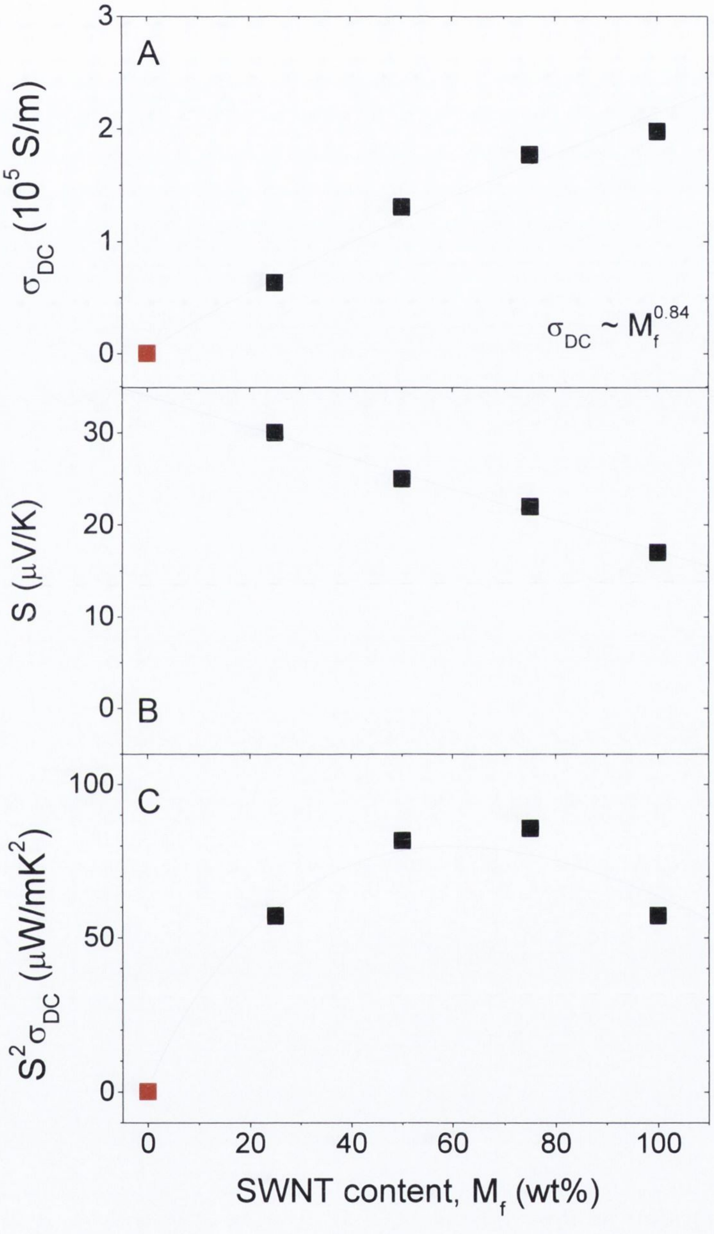

Figure 7.19: Thermoelectric properties of SWNT/MoS_2 composites studied in this work. A) DC conductivity, B) Seebeck coefficient, C) Power factor. In figure C, the dashed line was found by multiplying the percolation-like power law fit (dashed line in A) by the square of the rule of mixtures-like behaviour (dashed line in B)

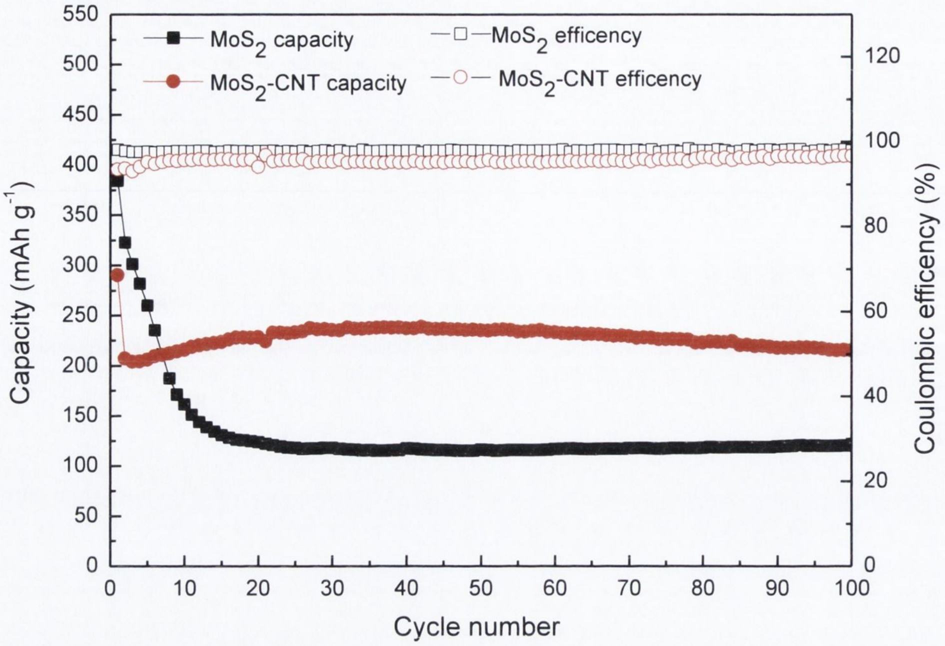

Figure 7.20: Lithium capacity (left axis) and Coulombic efficiency (right axis) for Li ion batteries with cathodes made from MoS2 or MoS2/SWNT hybrid films

thermal conductivity increases much slower than the electrical conductivity, such increases would be enough to remove the possibility of efficient thermoelectric materials. A significant challenge for the future will be to develop methods to increase the electrical conductivity while maintaining the thermal conductivity at a low level.

MoS_2/SWNT hybrids may also be of use as cathodes in Li- ion batteries. The layered structure of MoS_2 allows lithium ions to intercalate between the layers resulting in a conversion from 2H to 1T structure [200]. Li-ion cells using MoS_2 electrodes use a process whereby Li^+ ions are reversibly exchanged via an electrolyte. This can be written as

$$xLi + MoS_2 \leftrightharpoons Li_xMoS_2.$$

Initial testing of the hybrid films indicated a marked improvement in performance over MoS2 only films. Figure 7.20 shows data for a pure MoS_2 film and an 80% MoS_2-20% SWNT hybrid film. This work was done in collaboration with researchers in the universities of Wollongong and Sydney (Dr. Chen and Prof. Minet). The MoS_2 film shows a large decrease in capacity over the first 10 cycles, with 70% of capacity lost by the 25th cycle. This large decrease in capacity can be attributed to aggregation during charge/discharge cycling. The hybrid film performed better with 70% of the initial capacity retained after 100 cycles. These results compare favourably with literature values for other MoS_2-based lithium batteries [200, 201]. In this hybrid structure, the MoS_2 flakes are embedded in a mechanically robust nanotube network helping to minimize aggregation. The CNT network also serves as an efficient conducting matrix, facilitating electron transfer during the charge-discharge process.

The Coulombic efficiency is also shown in Figure 7.20. This gives an indication as to the energy loss during charge/discharge cycles. The Coulombic efficiency was quite high at above 95% for both systems, suggesting very good electrochemical performance can be achieved from these materials.

7.3.5. *Characterization of surfactant-stabilized dispersions of other layered compounds*

In order to investigate whether this process could be extended to other materials, several layered compounds (BN, WS_2, $TaSe_2$, $MoTe_2$, $MoSe_2$, and $NbSe_2$) were dispersed in aqueous surfactant solutions using the following parameters: C_{SC}= 1.5 mgml^{-1}, C_I= 5 mg/ml, t_{sonic} = 30mins, centrifugation rate = 1500rpm, centrifugation time = 90 mins. After centrifugation the samples were decanted giving stable dispersions of varying colour and concentration as shown in Figure 7.21. Although dispersions were not optimized for each individual material they were reasonably stable of a number of weeks with very little sediment present upon optical examination. The similarity in results for this range of materials using the same processing parameters as for MoS_2 and graphene, further highlights the ubiquity of this method for exfoliating and stabilizing 2D materials in aqueous media.

Similar to MoS_2, these dispersions could easily be formed into films by vacuum filtration (Figure 7.21). The films were easily transferred to a range of substrates in all cases except BN. Films of boron nitride were mechanically unstable during transfer decomposing in the acetone baths. As such, any thin film applications using this material would require a mechanically robust network to aid transfer such as carbon nanotubes. Recent work has also used BN as a filler material in polymer composites with promising reinforcement results comparable to graphene[202].

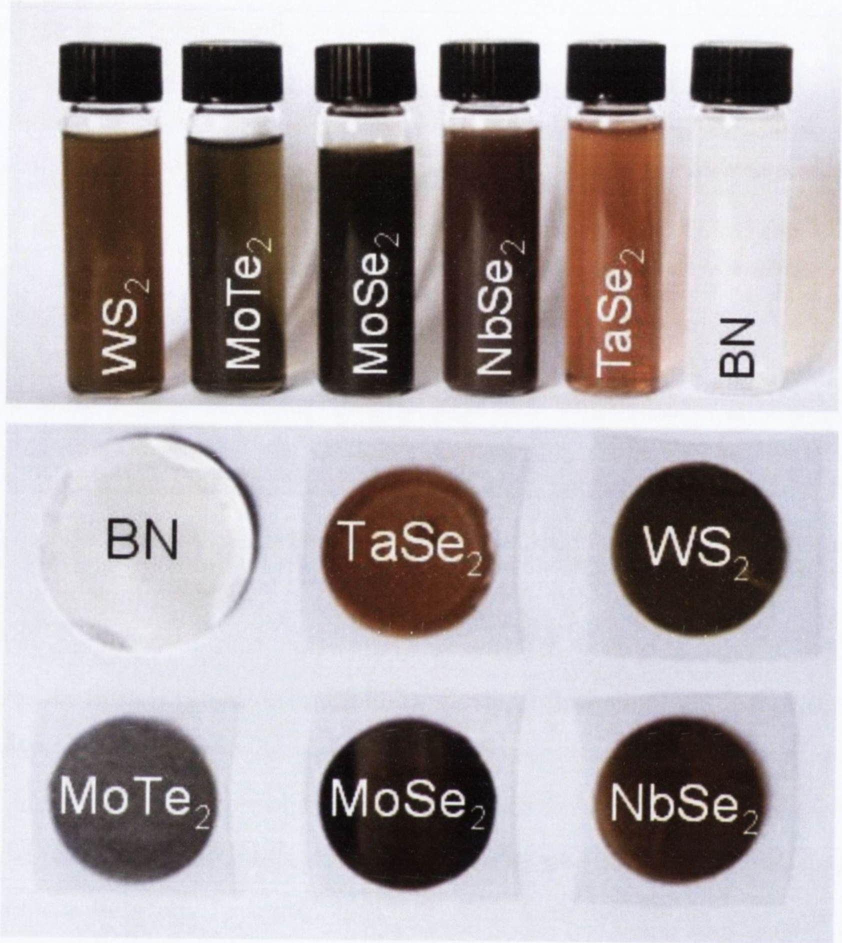

Figure 7.21: Photograph of: Dispersions of WS_2, $MoTe_2$, $MoSe_2$, $NbSe_2$, $TaSe_2$, and BN all stabilized in water by sodium cholate (Top). Vacuum filtered films of the same dispersions (Bottom).

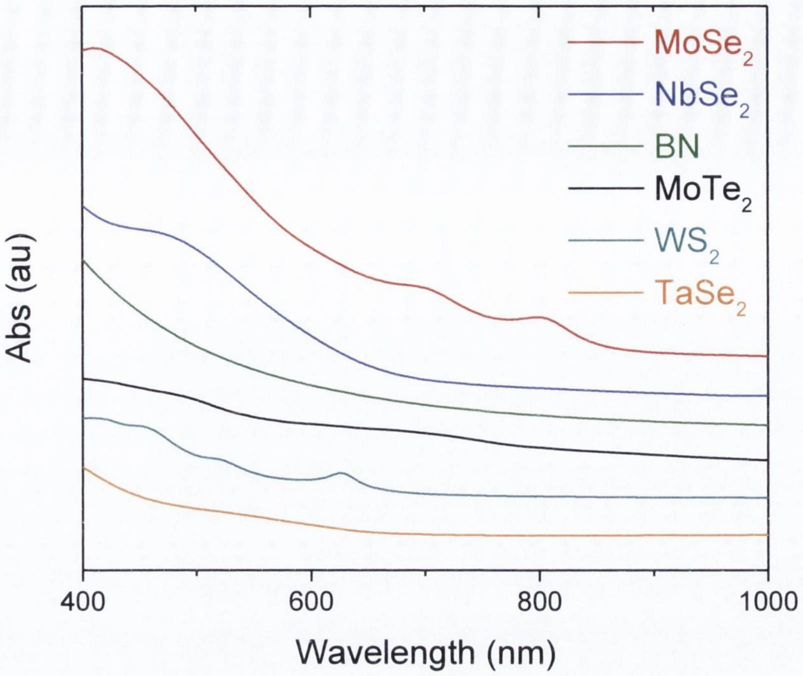

Figure 7.22: Absorption spectra of dispersions shown in Figure 7.21

The measured absorbance spectra of these dispersions (Figure7.21) were close to those expected for these materials [99]. As in the case of MoS_2, all spectra were superimposed on a power law background most likely due to scattering. Figure 7.21 highlights the diversity of electronic properties present in these materials and hence their usefulness for hybrid applications.

Due to the large number of materials it was not possible to quantitatively asses the exfoliation state and dimensions of each dispersion as was done for MoS_2. However, qualitative TEM analysis was carried out for each material with similar results for all dispersions. In each case, the dispersion consisted of a large number of two-dimensional objects ranging from about 50nm to 2 microns in lateral dimensions with a range of aspect ratios. Figure 7.22 shows representative images of flakes from each of the dispersions. All the flakes present in the dispersion were quite electron transparent and hence were exfoliated to some reasonable degree. It is likely that the centrifugation regime was sufficient to remove any large aggregates present in the initial dispersion though more extensive TEM and sedimentation analysis of the dispersions will be required to confirm this hypothesis.

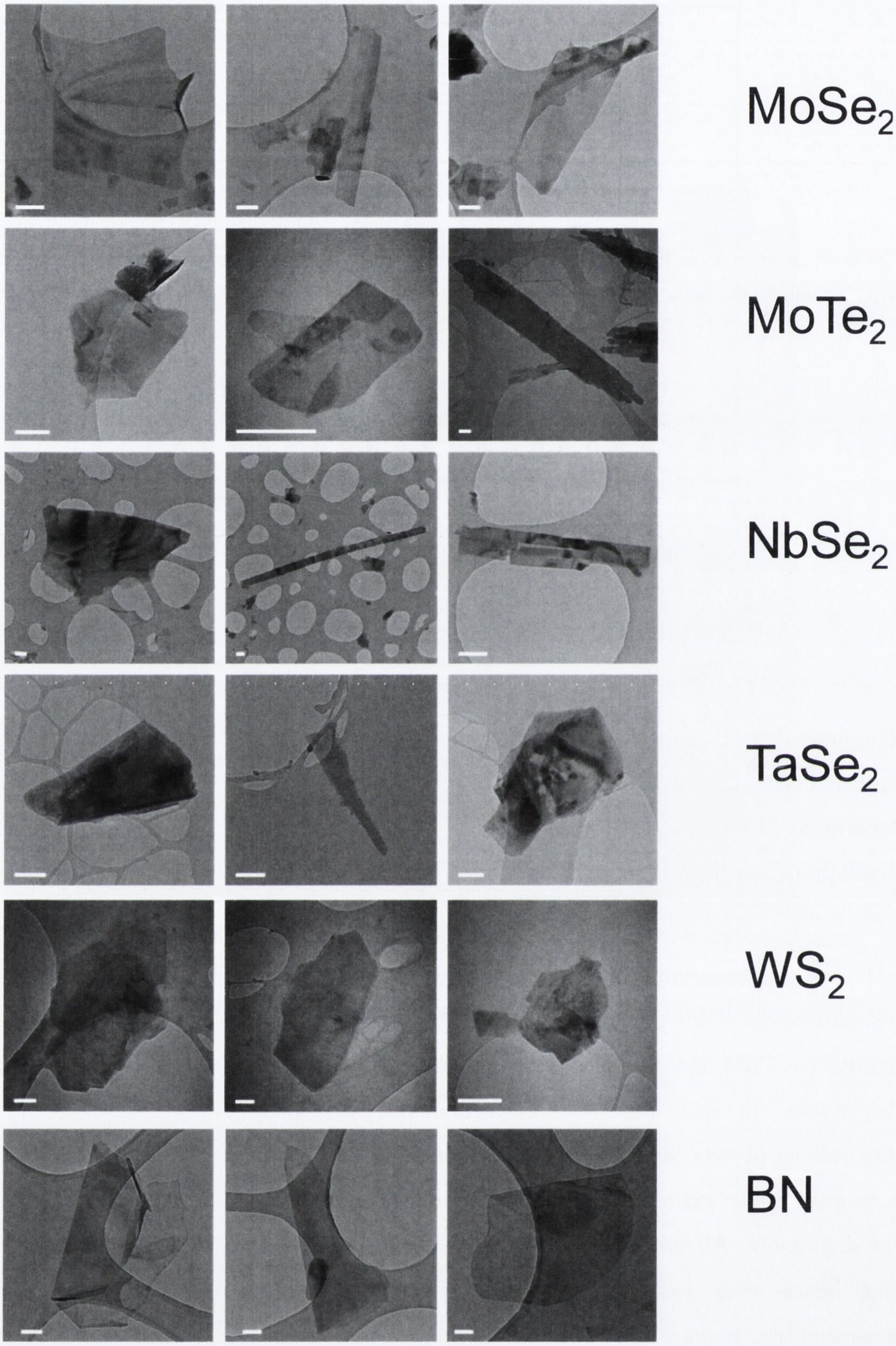

Figure 7.23: Representative TEM images of the TMD and BN flakes observed in this study. In all cases the scale bar is 100 nm.

7.4 CONCLUSIONS

The work presented in this chapter proposes a general exfoliation method that should apply to the vast majority of layered compounds. Unlike ion exfoliation methods, this process is quick, easy, and insensitive to ambient conditions. While the degree of exfoliation is inferior to ion-exfoliated dispersions, this is more than compensated by the versatility of the procedure. Most importantly this process does not introduce any significant structural or electrical changes to the starting material in contrast with ion exfoliation. The surfactant molecules interact with the layered materials by van der Waals interactions. Such interactions are known to only perturb the electronic properties of dispersed nanomaterials very slightly as evidenced by many studies on the optical properties of surfactant stabilised carbon nanotubes [20]. In fact, Raman spectroscopy of surfactant exfoliated MoS_2 flakes show the material to be of the same 2H-polytype as the bulk.

The effect of each individual processing parameter on dispersed concentration has been investigated for MoS_2. This will allow for scale up of the process in terms of quantity produced however the quality (exfoliation state of the material) has proven difficult to affect. In order to improve on monolayer yield, the effect of processing parameters on flake thickness will have to be quantitatively examined. Similarly, control over the lateral dimensions of the flakes produced would be useful. While column chromatography has proved successful in isolating fractions of flake sizes, the effect of processing parameters on lateral flake dimensions should be thoroughly investigated.

This method also enables the production of thin films of inorganic layered compounds with many possible applications in batteries and devices or as coatings or lubricants. In addition, it is clear that the available materials span the entire gamut of electrical properties from insulator to metal. By utilizing the processing methods discussed in this chapter, liquid phase exfoliation of these materials could become a powerful tool in the construction of a diverse group of hybrid materials tailored to specific electrical and physical properties.

8

EXFOLIATION OF MANGANESE OXIDE IN AQUEOUS SURFACTANT MEDIA

8.1 INTRODUCTION

Due to their high surface area, thin two-dimensional (2D) transition metal oxides have potential applications in catalysis[203, 204], batteries [205] and supercapacitors [130, 206]. manganese oxide in particular is a promising material for energy storage due to its high theoretical capacitance, low cost and environmentally friendly properties [125]. Although layered MnO_2 thin films can be prepared by the sol–gel method [206], electrostatic spray[207], ion intercalation [208] and electrodeposition [209-211], scaling up these processes for industrial application will prove difficult due to their harsh reaction conditions.

Chapters 5 and 7 have already shown liquid phase exfoliation of graphene and transition metal dichalcogenides (TMDs) to be a simple, robust and cost effective method for production of high quality samples as well as hybrid films and composites. The aim of this work is to determine whether or not this method can be applied to exfoliate two dimensional transition metal oxides, specifically manganese oxide. Ionic surfactants were chosen as stabilizers due to their van der Waals binding to the nanosheets and subsequent electrostatic stabilization.

8.2 EXPERIMENTAL PROCEDURE

The MnO_2 Powder used in all experiments was purchased from Alfa Aesar (product number: MnO_2, 42250). Sodium cholate was purchased from sigma Aldrich (C6445). The MnO_2 was dispersed in sodium cholate/water solutions (0.75 to mgmL^{-1}) in a polished stainless steel pot (100ml) at an initial concentration of 5 to 30 mgmL^{-1} by tip sonication (Sonics VX-750 ultrasonic processor with flat head tip, 750W at 75% Amplitude) for various times (5 – 60 minutes). The dispersions were then transferred to a glass pot (100ml) and allowed to settle for 24 hours. The top 50 mls of dispersion was then decanted into 2 glass vials (28.5ml) and centrifuged using a Hettich Mickro 22R for 90 mins at various RPM's (500-1500). After centrifugation (CF), decantation was carried out by pipetting off the top half of the dispersion into a single glass vial (28.5ml).

Absorbance measurements were made using a Varian Cary 6000i and quartz cuvettes (10 mm). Sedimentation measurements were performed with a homemade apparatus consisting of an array of synchronized, pulsed lasers and photodiodes. Samples for TEM were prepared by drop casting from the dispersion onto holey carbon grids (400 mesh). TEM images were taken with a Jeol 2100 operated at 200 kV.

Dispersion concentration was measured filtering a known volume under high vacuum onto a nitrocellulose membrane of known mass. The resulting thick film was washed with 400 ml of water and dried overnight in a vacuum oven at room temperature to remove residual surfactant. The mass of material in the filtered volume of stock dispersion was then determined using a microbalance.

Zeta potential measurements were carried out on a Malvern Zetasizer Nano system with irradiation from a 633 nm He-Ne laser. The samples were injected in folded capillary cells, and the electrophoretic mobility (µ) was measured using a combination of electrophoresis and laser Doppler velocimetry techniques. The pH of the sample was controlled by the addition of 1M NaOH and HCL.

Thin films were prepared by vacuum filtration immediately after CF. A controlled volume of dispersion with known concentration was filtered through nitrocellulose membranes (pore size 25nm). The deposited films were washed with 400 ml of Millipore water and then dried on a hotplate at 50C for 20 mins. They were then wetted with IPA and pressed against the ITO coated glass substrate. The cellulose filter membrane was then removed by treatment with acetone vapour and subsequent acetone liquid baths in all cases.

Raman and SEM samples were prepared by transferring the films onto Si/SiO_2. Raman spectroscopy was carried out on a Witec Alpha 300 R Raman spectrometer with an excitation wavelength of 532 nm using an 100x objective lens. SEM was carried out using a Zeiss Ultra Plus SEM. P3 carbon nanotube dispersions were blended in the ratio required to give the desired MnO_2/nanotube volume fraction. The mixture was then sonicated for 10 min in a sonic bath to homogenize. The resulting dispersions were vacuum-filtered. The thickness of these films was kept constant-controlled by the volume of dispersion filtered and hence the deposited mass.

Electrochemical characterization consisted of cyclic voltammetry using a three electrode electrochemical cell and Gamry Reference 600 potentiostat. A three electrode electrochemical cell consisted of an Ag/AgCl reference electrode and carbon counter electrode. Cyclic voltammagrams of film electrodes were obtained using a 0.5 M Na_2SO_4 electrolyte at a range of scan rates (2-1000 mVs^{-1}), and a potential window of 0-0.8 V vs. Ag/AgCl. The area of electrode exposed to the electrolyte was 0.7 cm^2 in all cases. The capacitance of the film electrodes was evaluated by integrating the current passed during discharge phase of the CV, over the potential window 0.8 to 0 V vs. Ag/AgCl.

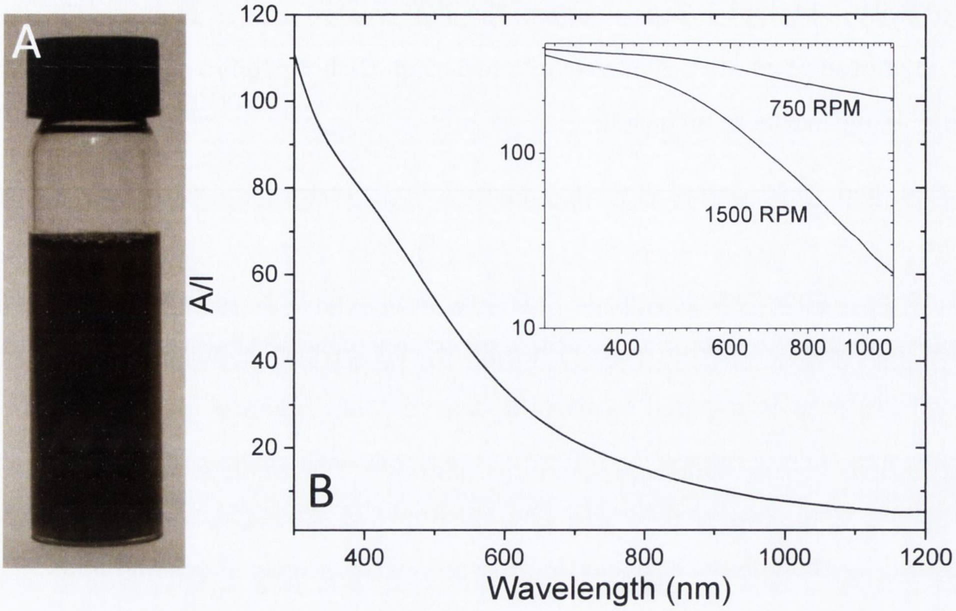

Figure 8.1: Surfactant exfoliation of MnO_2, A) A dispersion of MnO_2 flakes in water, stabilized by sodium cholate (SC) B) Absorption spectra of MnO_2/SC prepared by centrifuging at 1500rpm. Inset: Log-log plot of 2 spectra with different centrifugation rates.

8.3 RESULTS AND DISCUSSION

8.3.1. *Characterization of surfactant-stabilized MnO_2 dispersions*

In order to assess the dispersability of manganese oxide, MnO_2 powder was probe sonicated at initial concentration C_I=10 $mgml^{-1}$ in aqueous solution of surfactant sodium cholate of concentration 2 $mgml^{-1}$ for 30 minutes. The resulting dispersion was then centrifuged to remove large aggregates and unexfoliated powder. The supernatant was then separated giving the dark brown liquid shown in Figure 1b. Optical absorption measurements gave the spectra consistent with MnO_2 [212] shown in Figure 8.1b superimposed on a large power law background most likely due to light scattering. The change in exponent with lower RPM is consistent with a change in scattering due to an increase in average particle size (Figure 8.1b inset).

A high-volume dispersion (1000 ml) was prepared with a precisely measured volume of the dispersion (800mL) was filtered under high vacuum onto a nitrocellulose membrane of known mass. The resulting thick film was washed with 800 ml of water

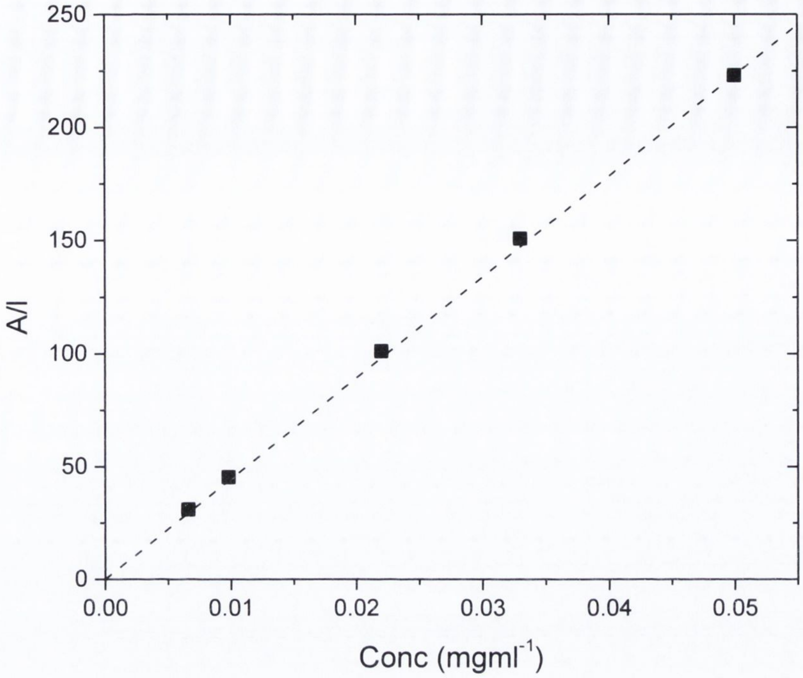

Figure 8.2: Absorbance per unit length (λ= 374 nm) as a function of dispersion concentration after centrifugation, C. Initial MnO_2 concentration C_I = 10 mg/ml with C_{SC} = 2 mg/ml.

and dried overnight in a vacuum oven at room temperature. The mass of material in the filtered volume of stock dispersion was then determined using a microbalance to be 40 mg. Knowledge of the mass of MnO_2 in the film allowed the final concentration of the stock dispersion to be determined (0.16 mgml^{-1}). A sample of the stock dispersion was then serially diluted with 2 mg/ml SC solution, allowing the measurement of the absorbance per unit length (A/l) versus concentration of MnO_2 (after centrifugation, C) Optical absorbance of these dispersions scaled linearly with concentration (see Figure 8.2) showing Beer-Lamber behaviour. The slope of this curve would suggest an absorption coefficient, α around 4460 L/g/m.

It is however, not possible to accurately determine a value for α that is independent of centrifugation rate due to the contribution of scattering to the measured absorbance. Unlike MoS_2, MnO_2 does not have sharp enough features in its absorbance spectra to allow for easy distinction between scattering and absorbance contributions making subtraction of the scattering background impossible. This means that any measured absorbance will have an unknown contribution from scattering that will change with flake size. The flake size dependence of the absorbance therefore

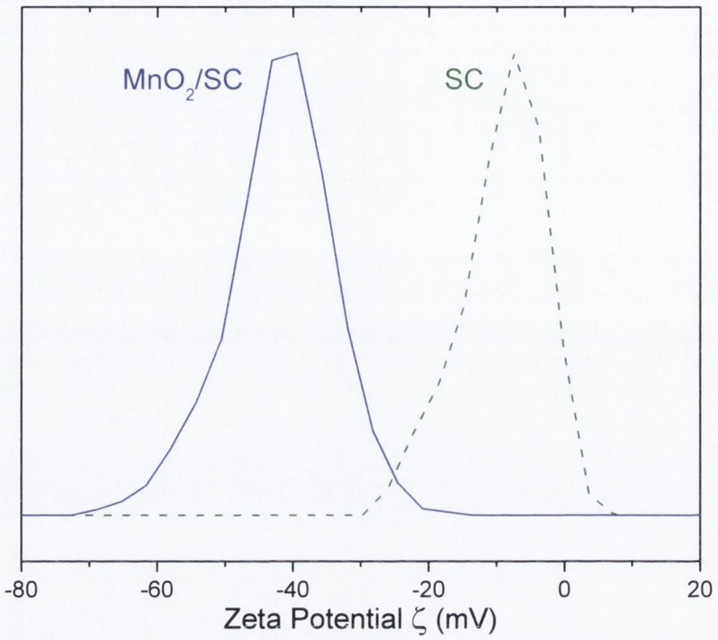

Figure 8.3: Zeta potential spectra for SC solution and MnO_2/SC dispersions immediately after preparation (solid).

makes accurate determination of dispersed concentration using Beer Lambert law impossible. Carefully determining α for a range of flake sizes or use of an integrating sphere for absorbance methods may overcome this obstacle in the future but for the purposes of this initial study, all concentrations were determined by filtration and weighing.

As discussed in Chapter 3, DLVO theory states that the electrostatic stabilization in colloids can be characterised using the zeta potential [131]. Zeta Potential is a measure of the effective charge surrounding colloidal particles due to the electric double layer of bound ions (tail groups) and diffuse cloud of counter ions (head groups). The observed zeta potential distribution for a fresh dispersion was centred around -43mV (Figure 8.3). The distribution is broad an asymmetric due to the range of flake sizes and possible contributions from free surfactant[180]. A peak zeta potential of -43mV is well above the accepted value for colloidal stability of -25mV indicating aggregation should be minimised.

To test this, sedimentation measurements were performed after centrifugation. The optical absorbance of the sample at 650 nm was monitored as a function of time as shown in Figure 8.4. The measured absorbance fell steadily over a period of days

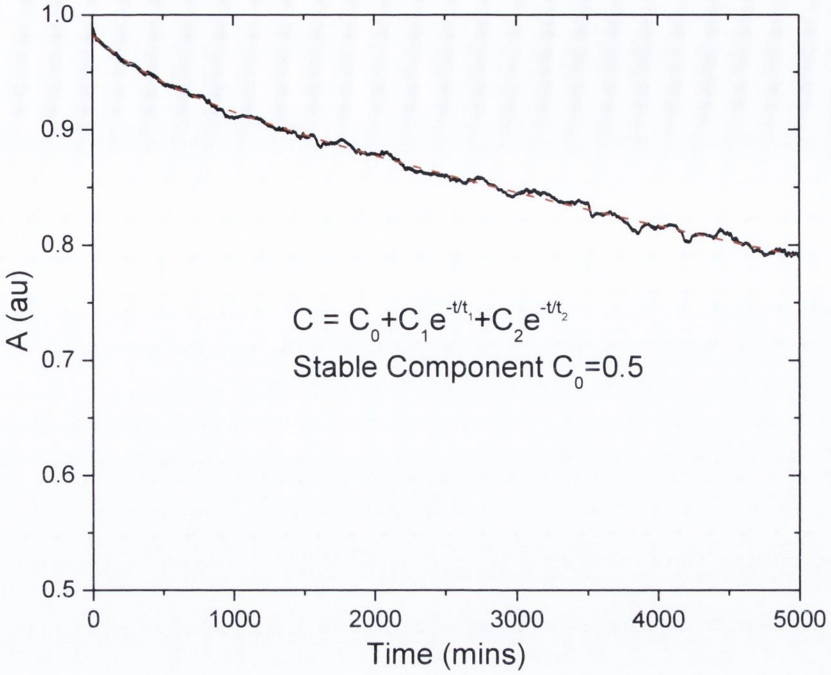

Figure 8.4: Concentration remaining as a function of sedimentation time for an MnO_2/SC dispersion over the course of 5000 mins. The data has been fitted to sedimentation theory for two sedimenting components (1 and 2) and a stable component (0). The fit constants are $C_0 = 0.52$, $C_1 = 0.43$, $C_2 = 0.04$, $t_1 = 7.5$ days, and $t_2 = 7.6$ hours.

indicating that just under 50% of the material had fallen out of the dispersion. A biexponential fit to the data suggests one stable phase and two sedimenting phases: one rapid and one slowly. The rapidly sedimenting phase constitutes approximately 5% of the dispersed material while the slower sedimenting phase comprises about 45% of the total dispersed material. The rapidly sedimenting phase is most likely due to residual unexfoliated material while the slowly sedimenting phase is more likely to be larger less stable flakes. The fact that over half the MnO_2 remains dispersed means that the temporal stability of these dispersions compares very favourably with their graphene and MoS_2 counterparts.

Raman Spectroscopy of vacuum filtered thin films and powder gave the spectra shown in Figure 8.7. A careful examination of the literature shows discrepancies in reports of the Raman spectra for manganese dioxides possibly due to its low Raman activity[207]. Kapteijn et al. reported MnO_2 to be Raman inactive [213], whereas Julien et al. reported well-defined spectra [214, 215]. The features most generally associated with the Raman spectra of MnO_2 are peaks around 510-515, 575-585, and

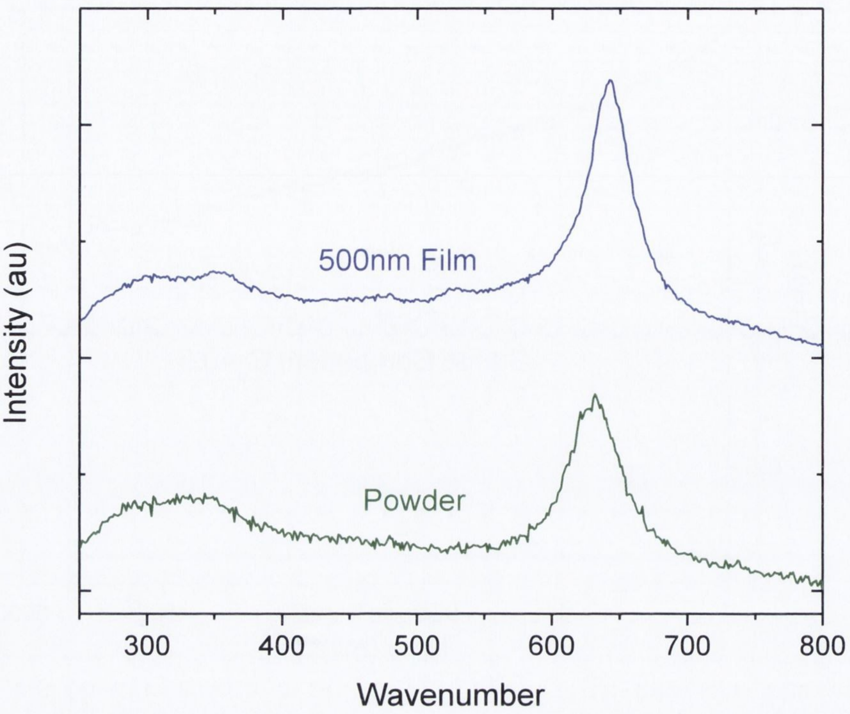

Figure 8.5: Raman spectra of both the starting powder and an MnO_2 film deposited on SiO_2 wafer.

630-640 cm^{-1} [207, 216]. The peaks shown in Figure 8.5 at 520 and 640 are consistent with those present in birnessite type MnO_2 [216, 217]. The features shown ~310 and 350 cm^{-1} are characteristic of Mn_3O_4. This can be formed during the spectrum acquisition because of the local heating of the samples causing the decomposition of MnO_2 to Mn_3O_4 [216]. However as low laser power was used to try minimize heating effects, it could indicate the presence of impurities in both the starting powder and dispersed material

TEM analysis of material deposited from the dispersion showed the presence of large quantities of extremely thin 2D flakes such as the one shown in Figure 8.6. As is the case with Graphene and MoS_2, these flakes appear to consist of a small number of stacked MnO_2 monolayers. As previously discussed, low-res TEM images of a highly populated grid can be used to generate statistics on flake dimensions for a given dispersion. Figure 8.7 shows the lateral size distribution for a standard dispersion of MnO_2. The mean flake diameter is approximately 150nm.

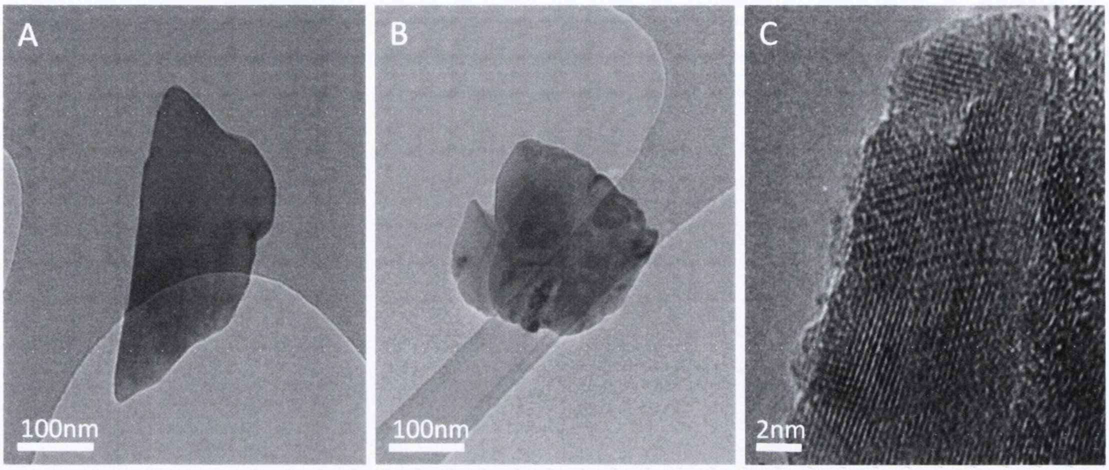

Figure 8.6: A, B) Typical bright field TEM image of MnO_2 Flake C) HRTEM image of MnO_2 showing layer edges.

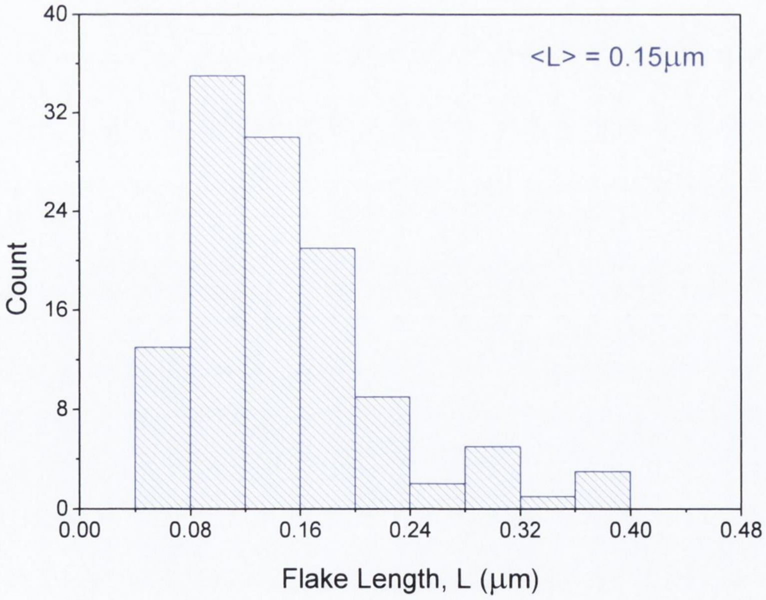

Figure 8.7: A) Flake length histogram for a standard dispersion.

8.3.2. *Optimisation of surfactant-stabilized MnO_2 dispersions*

Using dispersed concentration C as a metric, the effect of varying processing parameters was investigated in order to obtain fully optimized dispersions of MnO_2. The two parameters considered were the initial MnO_2 concentration C_I and the surfactant concentration C_{SC}..

The first part of this study investigated the effect of varying C_{SC} using fixed parameters $C_I = 5$ mg/ml, $t_{sonic} = 30$ mins and CF time 90 min at $w = 1500$ rpm. The initial MnO_2 concentration, sonication time and CF rate were chosen based on previous work with graphene and MoS_2 dispersed using surfactants as discussed in Chapters 5 and 7. It was found that the dispersed concentration increased sharply with surfactant concentration from no dispersion achieved below 0.75mgml^{-1} SC to a maximum around 1.5mgml^{-1} as shown in Figure 8.8.

The upper limit of this trend is most likely due to maximum surface coverage of surfactant molecules on the nanosheets. As discussed in Chapter 7, increasing the surfactant concentration increases the number of surfactant molecules adsorbed onto the surface of the flakes and hence increases their effective charge. This in turn increases the size of the repulsion between the flakes which has been linked to dispersed concentration in Chapter 5. Unlike graphene and MoS_2, there is a relatively high minimum surfactant concentration required to disperse MnO_2. As can be seen from Figure 8.8 dispersion was impossible for solutions below C_{SC}=0.75mgml^{-1}. This suggests a minimum electrostatic barrier required for dispersal which in turn implies and increased attractive potential between MnO_2 sheets compared with Graphene or MoS_2.

Initial concentration of MnO_2 was also varied keeping C_{SC} fixed at $0.2C_I$ and all other parameters as in the previous experiment. The dispersed concentration was found to scale linearly with the starting concentration for $C_I < 30$ mgml^{-1} shown in Figure 8.9. This allows definition of a yield, $Y(C = YC_I)$. The dotted line represents a yield of ~0.35 %. This is compares unfavourably with a yield of 1% for similar experiments with MoS_2. An increased attractive potential between MnO_2 flakes compared with MoS_2 could explain the disparity in results.

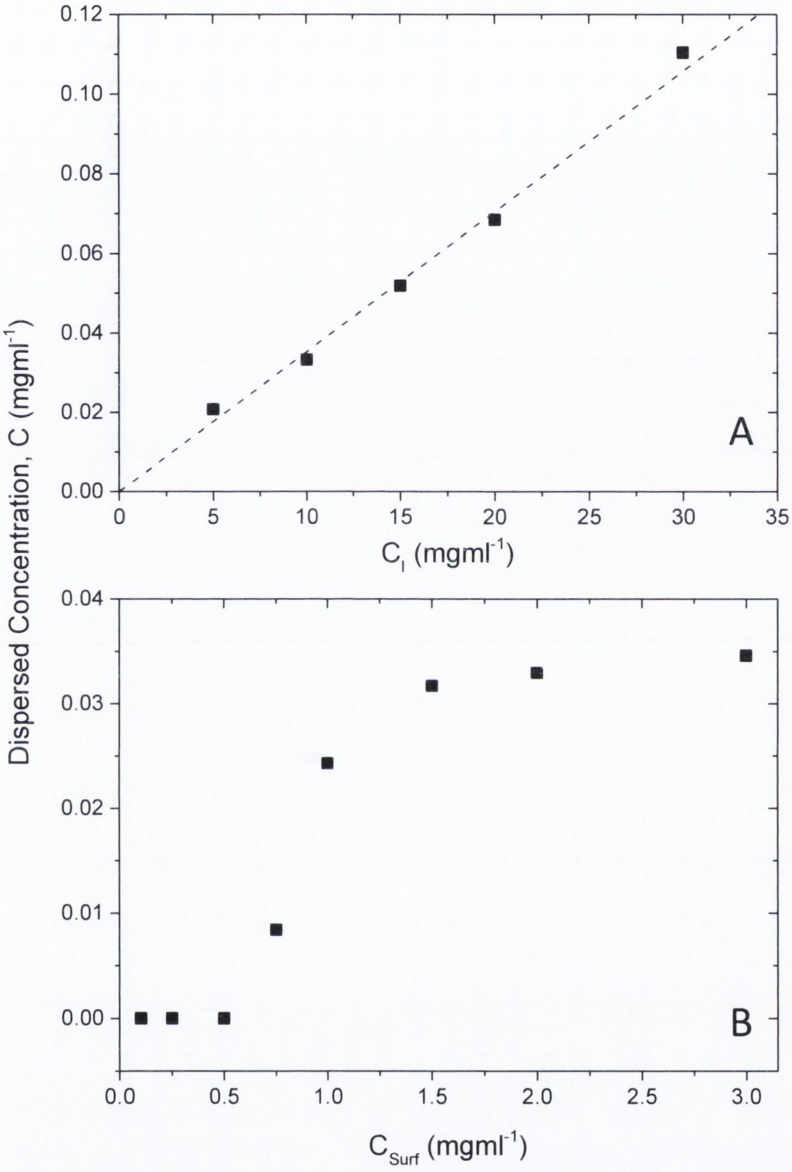

Figure 8.8: Dispersed concentration of MnO_2 C, of as a function of: A) Sodium cholate concentration C_{SC}. B) Initial concentration C_I.

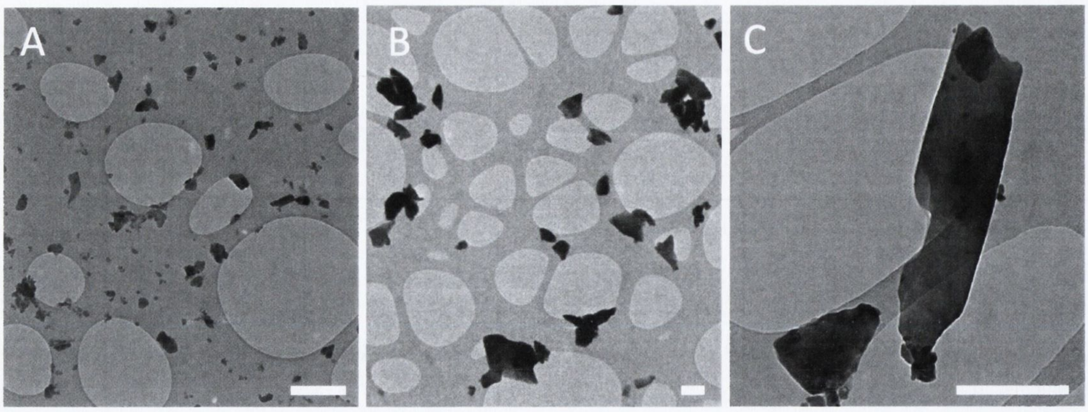

Figure 8.9: A, B) Wide field TEM images of MnO_2 flakes from a standard (A) and size selected (B) dispersions. Several of these images are used to generate statistics shown in Figure 8.10. C) Bright field TEM image of Typical MnO_2 flake from a size selected dispersion. All scale bars are 400nm.

Control over lateral flake dimensions can be essential for a number of applications. In order to investigate the possibility of increasing the lateral flake dimensions of these dispersions, the sediment post centrifugation (1500 RPM) was collected and redispersed in fresh sodium cholate solution (C_{SC}=1mgml^{-1}) using a sonic bath. The resulting dispersion was then centrifuged at 1000 RPM and the supernatant removed. The sediment post centrifugation (1000 RPM) was again collected and redispersed in fresh sodium cholate solution (C_{SC}=1mgml^{-1}) using a sonic bath. The final dispersion was then centrifuged at 500 RPM to remove any unexfoliated material. The final concentration of dispersed material was 0.1 mgml^{-1}, representing an increase on yield to 1% using this two-step process.

The first two centrifugation steps help to increase the final mean flake dimensions by reducing the number of smaller flakes present while the final centrifugation step eliminates any unexfoliated material present in the sediment. This process has previously been used Khan et al using high concentration graphene dispersions. It achieves similar results to size exclusion chromatography with a much higher throughput. TEM analysis of the size selected dispersion showed a dramatic increase in average flake size from 150 nm to 500nm.

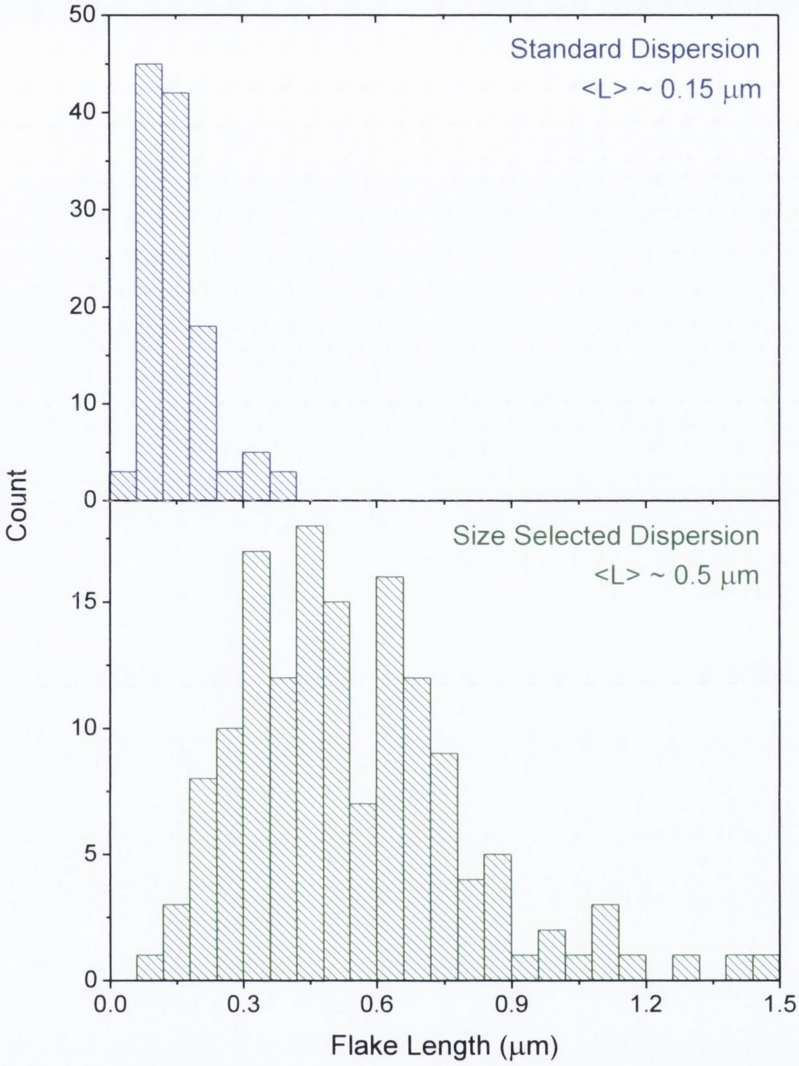

Figure 8.10: Lateral Flake size histograms for both a standard dispersion (Top) and the largest fraction separated by multiple centrifugation steps (Bottom).

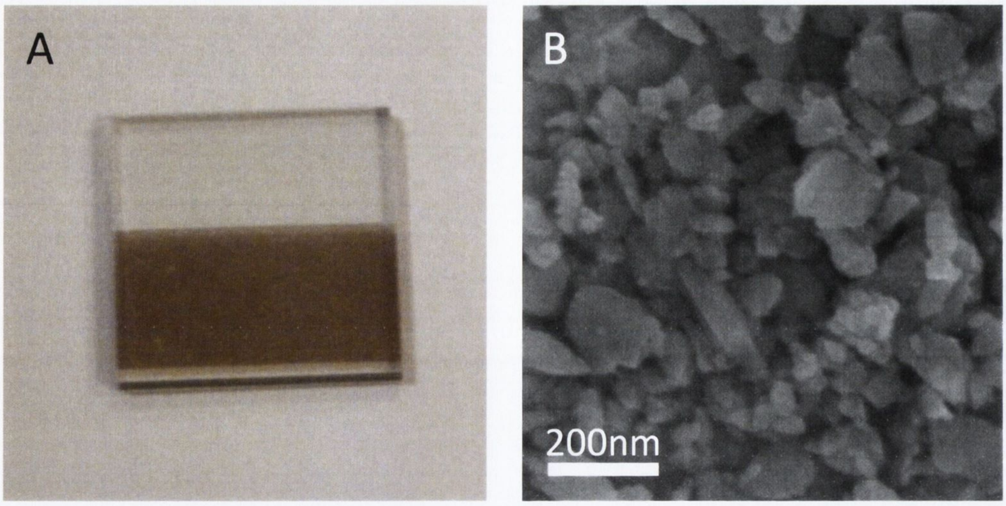

Figure 8.11: A) Thin vacuum filtered film of MnO_2 transferred onto an ITO coated glass substrate. B) SEM micrographs of thin film of MnO2 hybrid film of MnO2/P3 Nanotubes transferred onto a SiO_2 substrate.

83.3. *MnO_2 thin films & Hybrids*

As discussed in Chapter 7, exfoliation of layered materials in the liquid phase allows for the processing of thin films by vacuum filtration or spray deposition. It is also straightforward to prepare hybrid films by mixing of dispersed materials in the liquid phase at desired mass fractions and filtering or spraying the hybrid dispersion. All films prepared in this work were prepared by vacuum filtration and transferred to a desired substrate by dissolving the nitrocellulose membranes in acetone vapour and baths. Figure 8.11a shows an image of typical, MnO_2 films transferred onto ITO coated glass. This substrate was chosen so that the ITO could at as a current collector during electrochemical measurements of these films which will be discussed below.

Figure 8.11b shows an SEM micrograph of a thin MnO_2 film. These films consist of an array of randomly orientated flakes packed in plane with sizes ranging from 10s to 100s of nanometers. The hybrid films are composed of the same flakes but embedded in a network of one dimensional nanotubes shown in Figure 8.12. Nanotubes can enhance both the electrical and mechanical properties of thin films depending on their loading. Figure 8.12 shows a crack in the film, common for MnO_2 due to its small flakes size compared with graphene. Nanotubes can bridge these cracks and help maintain structural stability of the film as well as ensuring good electrical contact of the flakes throughout the hybrid.

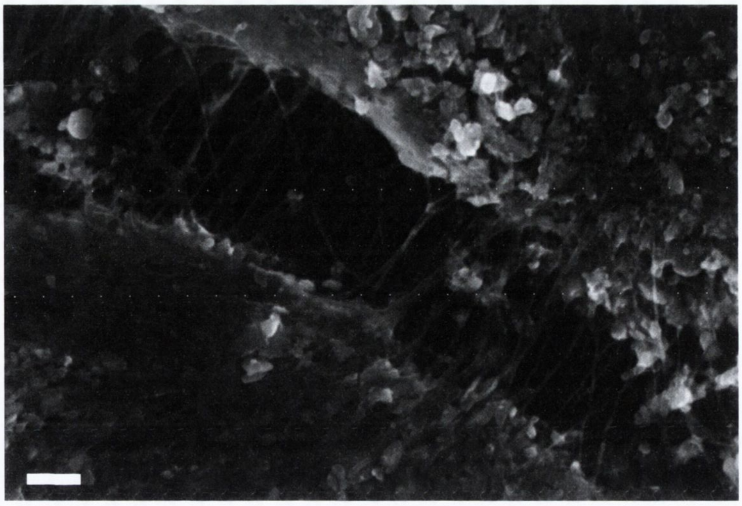

Figure 8.12: SEM micrograph of MnO_2/P3 hybrid film transferred onto a SiO_2 substrate. Scale bar is 200nm.

Supercapacitor electrodes which make use of transition metal oxides can improve the energy able to be stored by an electrode through rapid and reversible conversion between different oxidation states. The charge passed during such redox processes is a function of the applied potential and therefore is effectively a capacitance termed a pseudocapacitance to distinguish it from the non-Faradaic capacitance associated with charging the electrochemical double layer. Low electrical conductivity of MnO_2 is a key impediment for its use as a supercapacitor electrode. This limitation can be addressed to some extent by the inclusion of other nanoscale conductors. An equally important factor when assessing the suitability of MnO_2 for supercapacitor applications is the available surface area. Reports have shown that the specific capacitance of MnO_2 for electrodes decreases with increasing mass deposited [207]. This is most likely due to two main factors: (1) limiting the electrical contact between the surface and the current collector as film thickness is increased and (2) decreasing in the available surface area per mass as material begins to stack. The incorporation of nanotubes into thin films can increase porosity and hence increase the available surface area. To that end the electrochemical response of MnO_2 and MnO_2/Nanotube hybrid films was examined in collaboration with Thomas Higgins (Trinity College Dublin) with the results shown in Figure 8.13.

The current response of MnO_2 films approaches ideal capacitive behaviour indicated by the rectangular and symmetric shape of the CVs shown in Figure 8.13a. The specific capacitance at a scan rate of 25 mVs^{-1} was ~ 30 Fg^{-1}. This is quite low when compared with similar MnO_2 electrodes. The low specific capacitance could be due to

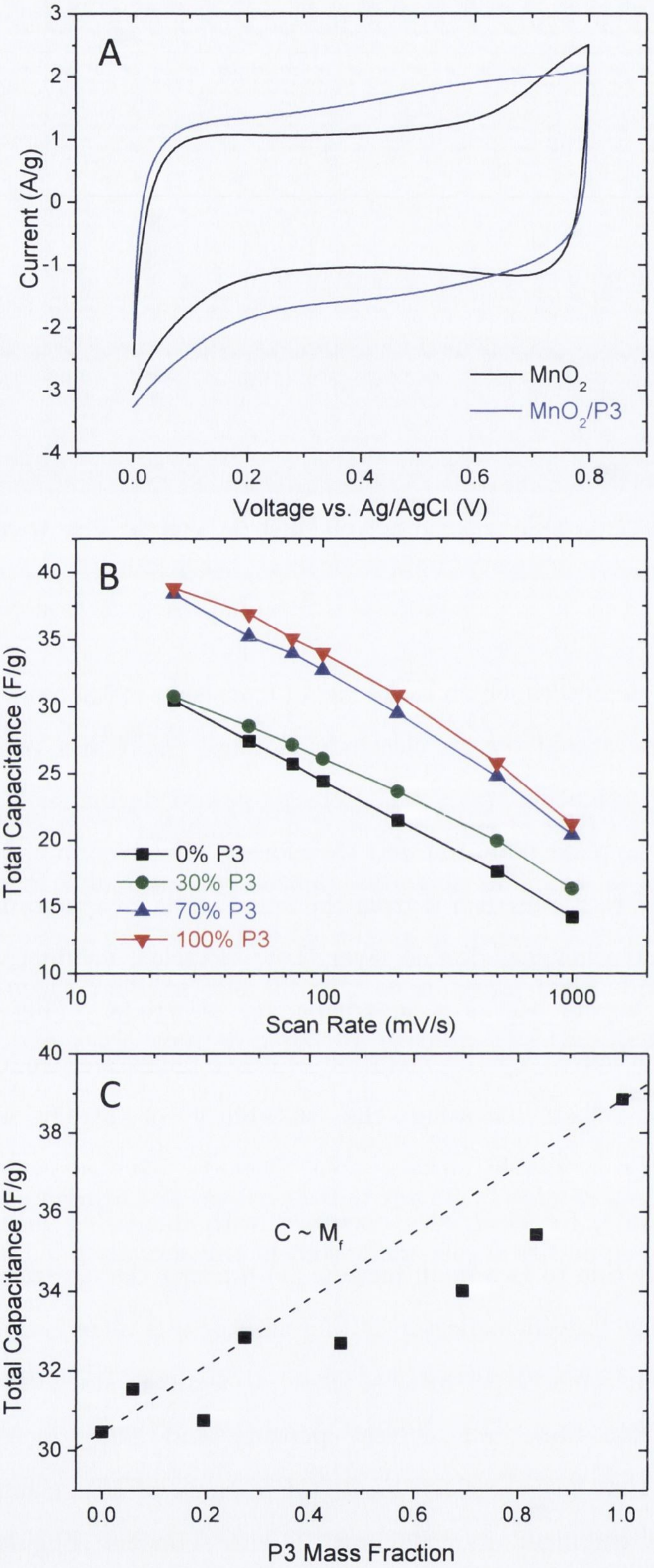

Figure 8.13: A) Cyclic voltagramme for MnO_2 and MnO_2/P3 hybrid electrodes. B) Capacitance as a function of scan rate for MnO_2 and MnO_2/P3 hybrid electrodes (C) Capacitance as a function of Nanotube mass fraction. Dotted line represents $C \sim M_f$ behaviour.

the presence of Mn_3O_4 with reported values as low as 10 Fg^{-1} for specific capacitance [218]. Analysis of the scan-rate dependence of capacitance can provide useful information concerning the charge storage mechanisms in an electrode material. Figure 8.13b shows a large decrease in the capacitance with increased cycling rate. This trend is consistent with charge storage due to faradaic bulk and surface reactions as well as capacitive surface reactions [123]. As previously outlined, the addition of nanotubes enhance an electrodes electrical properties.

Figure 8.13c shows the capacitance versus nanotube mass fraction for a number of composite electrodes. It is clear that the addition of nanotubes is increasing the capacitance however the rule of mixtures type behaviour would suggest that this is merely due to the increased specific capacitance of a nanotube films when compared with MnO_2 only electrodes. While the nanotubes have increased electrical contact with the flakes and thus increased current collection throughout the film, this has had no effect on specific capacitance suggesting that poor electrical conductivity is the limiting factor in the electrochemical performance of these films. Although the addition of nanotubes should increase the porosity of the films and hence increase available surface area there is no evidence to suggest that this has improved electrochemical performance either. It is difficult to quantify the effect on electrode porosity with addition of nanotubes without direct measurement and nitrogen adsorption may indicate this in the future. In fact the effect may be quite negligible given the very small average flake size and hence larger packing density within the film. Despite possible surface induced limitations due to the structures of these electrodes it would appear that the main limitation is the specific capacitance of the dispersed material. This is most likely due to impurities in the commercially available powder used as a starting material recently reported by Nicolosi et al [79].

7.4 CONCLUSIONS

The work presented in this chapter extends the general exfoliation method proposed in Chapter 7 to include layered transition metal oxides. The effect of each individual processing parameter on dispersed concentration has been investigated for MnO_2. Similarly, control over the lateral dimensions of the flakes produced has been demonstrated. The electrochemical performance of thin films cast from these dispersions has also been investigated though values derived for capacitance are lower than those reported in the literature. The incorporation of a network of nanoconductors has failed to improve specific capacitance of the exfoliated material however further study is merited. Any future work in this area will have to address the issue of impurities present in the starting material. This could be overcome by use of direct synthesis rather than purchasing powder from a supplier. The effect of various separation techniques such as column chromatography or multiple centrifugation could also be investigated in order to assess the suitability of post purification.

9

ONGOING AND FUTURE WORK

9.1 INTRODUCTION

This chapter introduces research currently being undertaken to expand on the work presented in this thesis. A discussion of possible future applications and scope for further research into liquid phase exfoliation is also presented. The main aims for ongoing and future research in this area are three fold: (i) to develop techniques to finely adjust both thickness and lateral dimensions of nanosheets produced by liquid phase exfoliation. (ii) to gain better control over the architecture of nanostructures constructed from these materials and (iii) to further explore the use of these materials in applications such as energy storage.

9.2 ABSORBANCE METRICS FOR DISPERSED NANOSHEETS

As previously discussed, nanosheets produced by liquid phase exfoliation in solvent and surfactant systems are polydisperse, in both lateral dimensions and thickness. While the work presented in Chapter 6 along with other publications from the Coleman group attempt to address part of this problem by developing methods to separate the nanosheets by size [219, 220], separation by thickness has proved much more problematic. Green et al were the first to report density gradient centrifugation of dispersions of layered materials whereby the dispersed material is separated out according to number of layers by changes in their buoyant densities [175]. Although this method gives good separation of layers it is quite laborious and the monolayer yield quite low due to low populations in the initial dispersion. In order to increase this yield and narrow both the size and thickness distributions, it is necessary to develop a simple, quick and reliable method of measuring these quantities so that the effect of varying processing parameters can be studied in more detail. Current

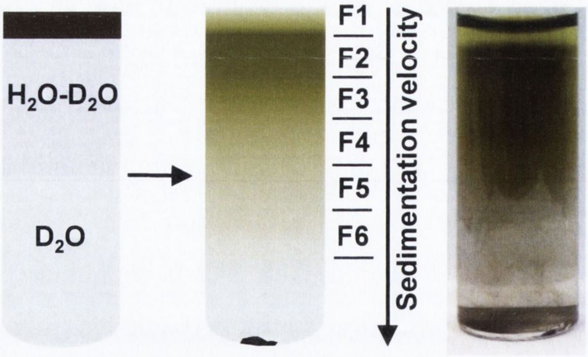

Figure 9.1: Diagram of band sedimentation centrifugation. Centrifugation leads to a continuous spread of the material throughout the vial separated sedimentation velocities.

methods for determining nanosheet dimensions are rather tedious, requiring time-consuming AFM or TEM statistical analysis. Lotya et al have demonstrated that approximate in-situ measurements of lateral size can be made optically [148], though this method cannot yield information on the nanosheet thickness. It is clear that a new method is required to measure nanosheet dimensions in dispersion.

Current work in collaboration with Dr Claudia Backes is attempting to address these requirements by examining the optical absorbance spectra of exfoliated TMDs. A combination of band sedimentation and homogenous centrifugation has been used to separate liquid phase exfoliated dispersions of MoS_2 into fractions with reasonably narrow size distributions. TEM and AFM statistical analysis has been used to generate quantitative relationships between spectral features and nanosheet dimensions. This is due to confinement and edge effects which result in thickness dependent shifts in excitonic positions and length-dependent changes to relative spectral intensities respectively. A summary of the results obtained so far follows.

The size exclusion chromatography and multiple centrifugation steps, introduced in Chapters 6 and 7 have proven to be effective techniques in size separation of dispersed nanomaterials. In addition to these methods, this work also uses band sedimentation to separate material according to size and thickness similar to techniques already used for sorting of dispersed nanomaterials by lateral dimensions [221-223]. This method involves layering a stock dispersion on top of a race layer of higher density followed by centrifugation (Figure 9.1). This results in fractionation with material separating out

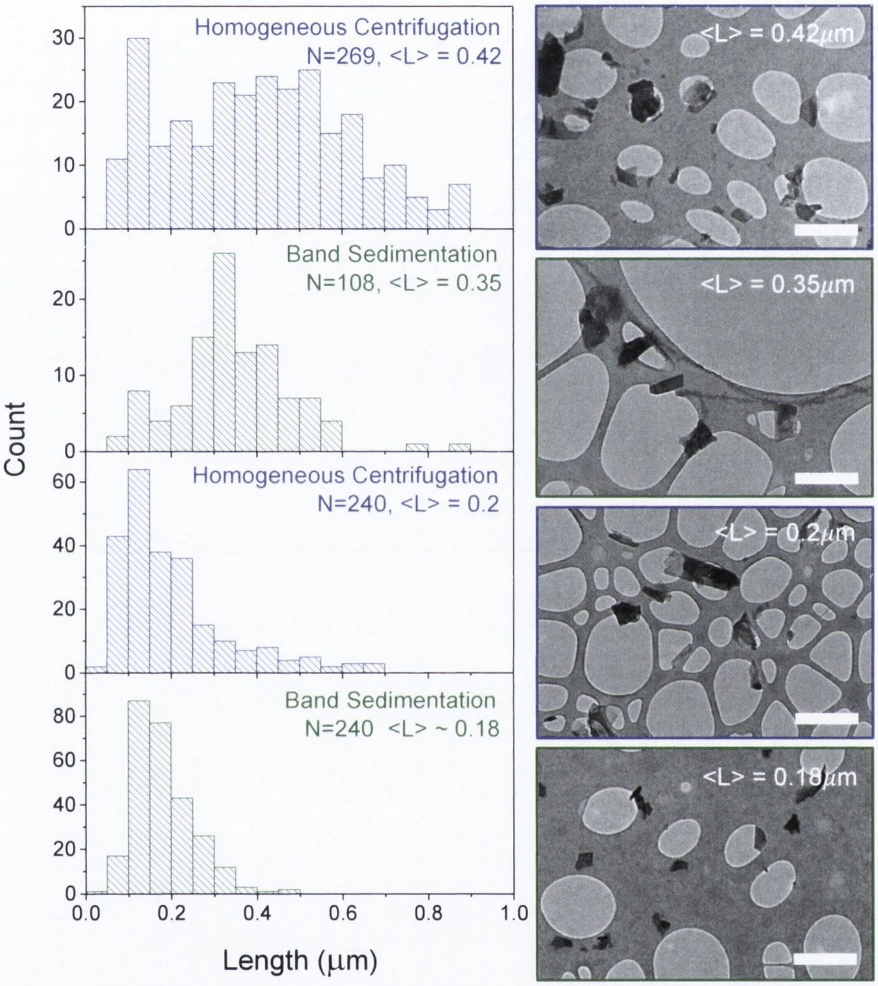

Figure 9.2: TEM Statistical analysis of size selected dispersions prepared by homogeneous centrifugation (Blue) and band sedimentation (Green). Both histograms and representative images show band sedimentation to produce narrower size distributions.

according to its centrifugation velocity. The first fraction, taken from the top of the vial contains the slowest sedimenting material and hence is composed of the smallest thinnest material while the size and thickness increase with fraction number. The effectiveness of this method is highlighted when comparing the size distributions for dispersions prepared by band sedimentation with homogenous centrifugation measured by TEM analysis (Figure 9.2). The distribution of sizes for fractions produced using band sedimentation is much narrower than those achieved by conventional centrifugation allowing for better control over the dispersed flake size.

Figure 9.3 shows normalized absorbance spectra for fractions of a stock dispersion of MoS_2/SC separated using band sedimentation. Although the excitonic transitions are typical of MoS2, there are significant spectral changes from fraction to fraction. The most prominent trend is the shift in the A-exciton (E_A) position. Eda et al. have previously correlated this shift with the number of layers per sheet [108], A plot of E_A versus fraction number (Figure), shows a clear trend, as the peak is red shifted with increasing fraction number (i.e. increased number of layers). This implies that the energy of the A-exciton can be used as a metric to calculate flake thickness for surfactant stabilised MoS_2.

In addition to shifts in excitonic energy there is also a change in the relative intensity of these peaks. This trend can be illustrated by plotting the ratio of absorbance at the B exciton peak, Abs(λ_B) to that at the local minimum Abs(λ_{345}) with an almost fourfold increase in this ratio from fraction 1 to fraction 6 (Figure). When taken in conjunction with the observed shifts in E_A, it would appear that this trend might also be due to changes in the number of layers per nanosheet, however no such observations have been made for films of restacked chemically exfoliated MoS_2 of varying thickness [108]. This strongly suggests that the changes in relative intensities are due to changes in the lateral flake size.

These size dependent relative intensities are most likely the effect of flake edges on the local electronic structure and hence local absorption coefficient. In this case the flakes can be considered to consist of two electronically distinct regions: edge (E) and bulk (B) with absorption coefficients α_E and α_B respectively.

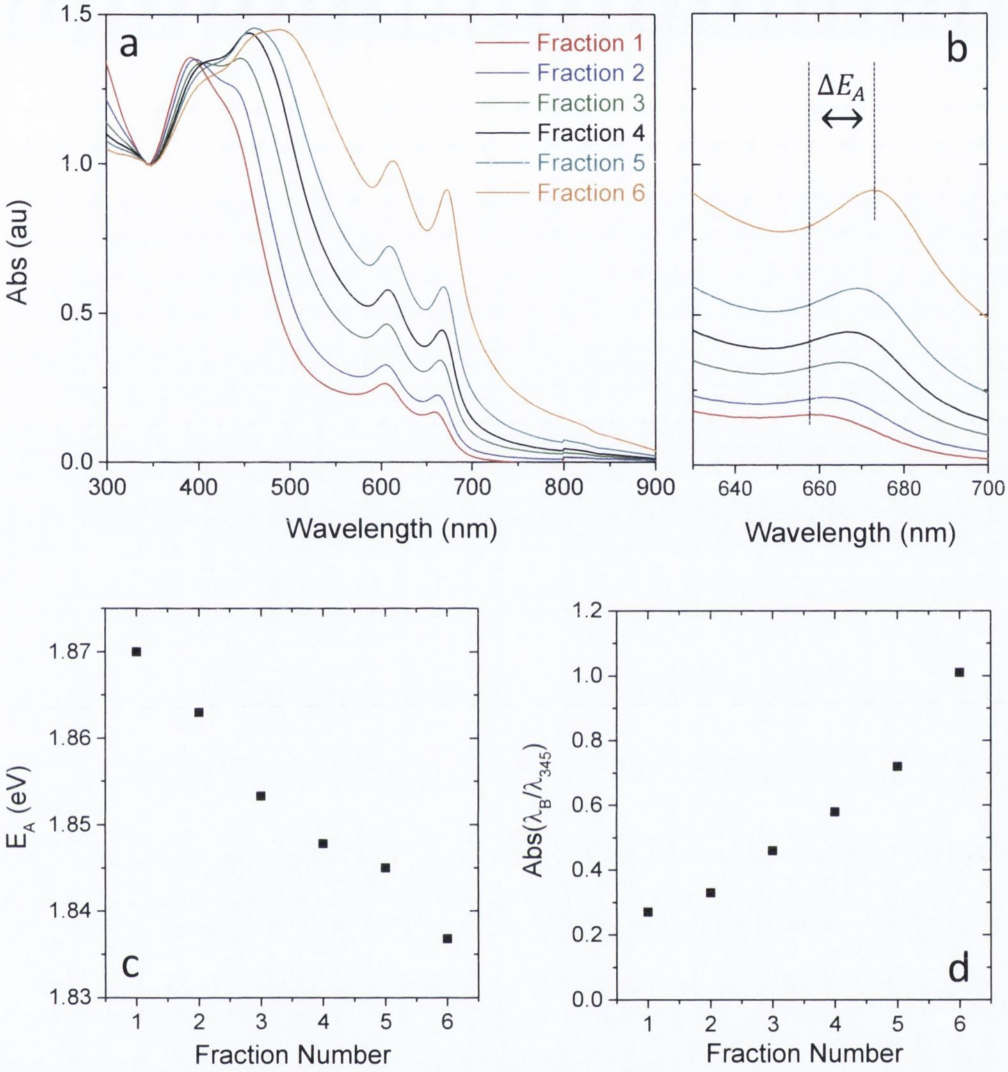

Figure 9.3: (a) Absorbance spectra of the fractions normalised to the local minimum at 345 nm (b) evolution of A-exciton position with varying fraction c) Energy of the A-exciton as a function of fraction number. d) Changes in intensity peak ratios of the B exciton / 345 nm as a function of fraction number.

The flakes can be modelled as rectangles of length L, and width W, with an edge region of width x such that the area of the edge region is given

$$A_{edge} \approx 2Lx + 2Wx \qquad (9.1)$$

assuming that x<<L, the area of the bulk is given by

$$A_{bulk} \approx LW \qquad (9.2)$$

$$\frac{A_{edge}}{A_{bulk}} \approx \frac{2Lx + 2Wx}{LW} \qquad (9.3)$$

taking the aspect ratio l/w to be constant k then

$$\frac{A_{edge}}{A_{bulk}} = \left(\frac{2x}{L}\right)\ k + 1 \qquad (9.5)$$

The absorption at a given wavelength will be related to the weighted sum of the absorption at both edge and bulk such that

$$Abs\ \lambda\ \propto\ \alpha_B + \left(\frac{2x}{L}\right)\ k + 1\ \alpha_E \qquad (9.6)$$

By taking the mean aspect ratio to be 2, this can be used to derive and expression for the ratio of absorbance intensities at two distinct wavelengths λ_1 and λ_2.

$$\frac{Abs(\lambda_1)}{Abs(\lambda_2)} = \frac{\alpha_B\ \lambda_1\ + 6x\alpha_E(\lambda_1)/L}{\alpha_B\ \lambda_2\ + 6x\alpha_E(\lambda_2)/L} \qquad (9.7)$$

In order to quantitatively correlate the change in peak intensities with changes in lateral flake dimensions several dispersions of varying flake size were prepared by both band sedimentation and homogenous centrifugation. The average flake lengths were determined by TEM analysis and plotted against Abs(λ_B)/Abs(λ_{B345}). This data along with a fitting of Equation 9.6 is shown in Figure 9.4. The measured data appears to fit model previously outlined quite well with some deviation at smaller flake sizes when x becomes larger compared with L. With knowledge of the fit parameters, equation 9.5 can be rearranged to give a quantitative relationship between

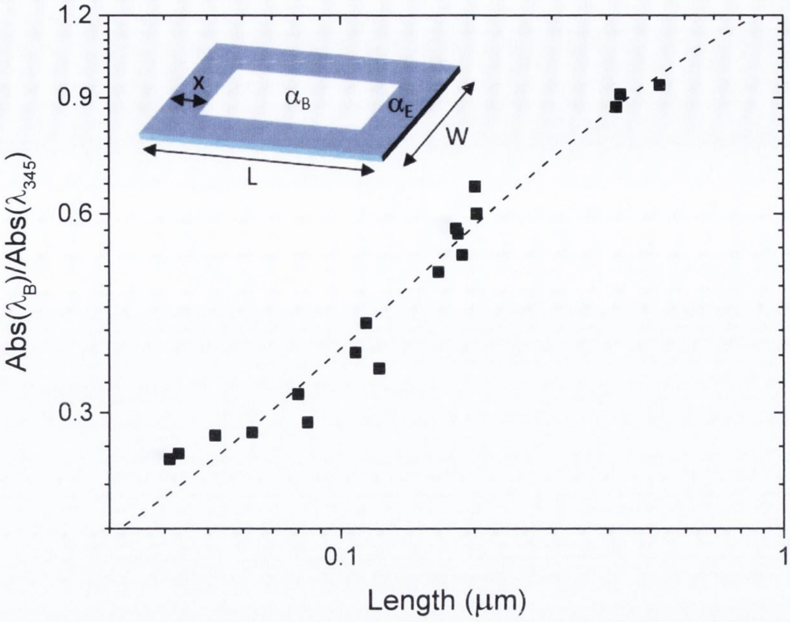

Figure 9.4: Ratio of absorbance at B-exciton to that at 345 nm, plotted versus the lateral dimensions of the flake (expressed as mean length, L, obtained by statistical TEM analysis). The line is a fit to equation 9.7. The inset schematically shows the division of a nanosheet into edge and central regions.

L and Abs(λ_B)/Abs(λ_{345}) allowing this ratio to be used as a metric to assess the flake length for surfactant stabilized MoS_2 dispersions.

While the TEM allows for relatively straightforward determination of average flake length, it is far more difficult and time consuming to generate statistics on flake thickness. As such, nanosheets were deposited from a number of samples onto Si/SiO_2 wafers and atomic force microscopy (AFM) was used to correlate the shift in excitonic peaks with number of layers with measurements carried out by Dr. Claudia Backes. Conversion of the measured height into the actual number of monolayers per flake, N, can be challenging due to the presence of adsorbed surfactant on both flakes and substrate. This can be resolved by careful examination of the edges. As discussed earlier in relation to TEM analysis, the edges of multi-layered exfoliated MoS_2 flakes are made up of terraces separated by steps. By measuring this step height for a large number of flakes and plotting these values in ascending order, it is clear that each terrace is separated by a multiple of 1.9nm suggesting this corresponds to a monolayer. This is larger than expected for monolayer MoS_2 with previous reported

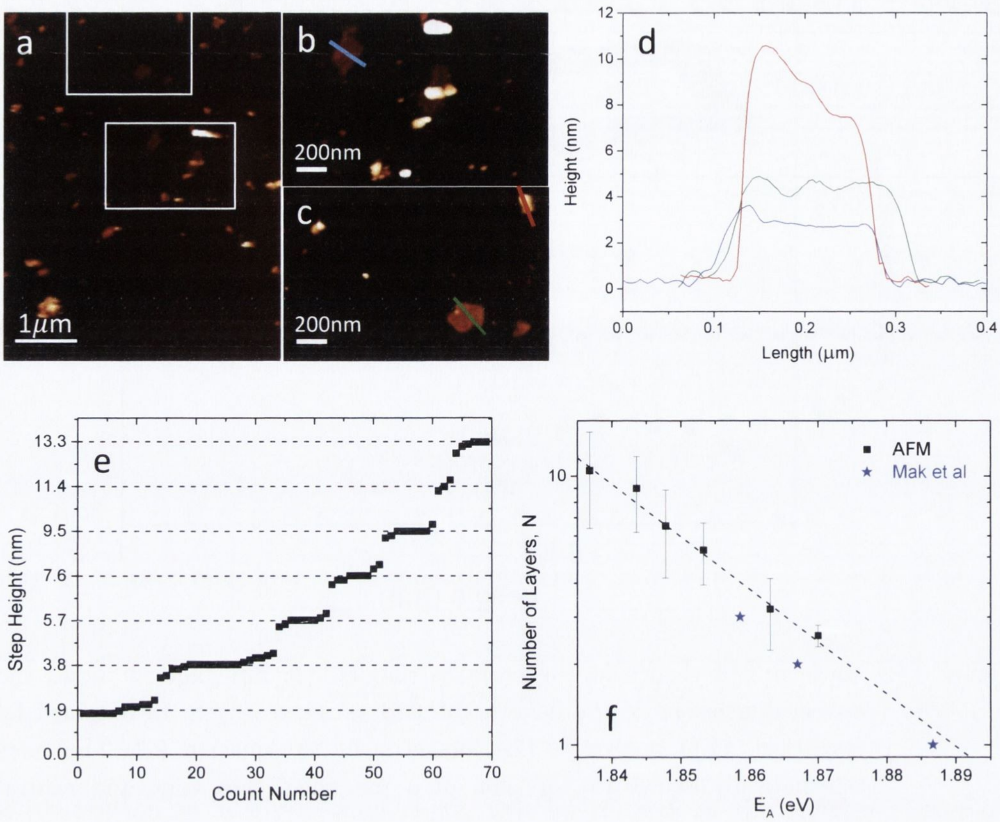

Figure 9.5: (a) Representative overview AFM images of a surfactant-exfoliated MoS_2 dispersion deposited on Si/SiO_2 wafers. b/c) Zoomed-in AFM images of the regions indicated in a. d) Height profiles of the nanosheets in b/c). e) Heights of steps observed on deposited MoS_2 nanosheets f) Plot of the mean number of layers as obtained from AFM thickness analysis *versus* the energy of the A-exciton in the absorbance spectra. The experimental findings are consistent with literature data (blus stars) on the photoluminescence of freestanding MoS_2 extracted from Mak *et al* [112]

values of 1.1nm[108] but is most likely due to the presence of adsorbed surfactant on the edges. This is consistent with the 3nm heights measured for the smallest flakes as these layers would have approximately 1nm of surfactant coating top and bottom.

Figure 9.5e plots the average number of layers per nanosheet, N, and the measured A-exciton position, E_A for several dispersions. These results were tested by comparing them to reported values for A-exciton position for mono-, bi- and tri-layer mechanically exfoliated MoS_2 reported by Mak et al with both sets of data in close agreement [115]. The data in figure 3h clearly shows an exponential relationship between N and E_A with $N = 8.36 \times 10^{36} e^{-45E_A}$ allowing for the determination of average thickness for surfactant stabilised MoS_2 flakes. This is an important result given the time consuming nature of conventional methods of measurement such as AFM and TEM. The absorbance metrics outlined in this section are based on changes in the electronic structure due to edge and confinement effects. This implies that this technique could be applied to a wide range TMDs and other layered materials.

9.3 HYDROGEN EVOLUTION CATALYSIS

Due to the ever increasing demand for renewable sources of energy, storage has become a topic of great interest and debate. While energy demands may be met by renewable sources such as wind and solar power, these processes cannot produce continuous supply and hence the electricity they generate must be stored. One of the most promising strategies to solve this problem is the conversion of electricity to hydrogen. The most abundant source of hydrogen is water with electrolysis producing resulting in the overall reaction

$$H_2O \longrightarrow H_2 + 0.5O_2 \qquad (9.8)$$

This is the sum of two half-cell reactions

$$2H^+ + 2e^- \longrightarrow H_2 \qquad (9.9)$$

$$OH^- \longrightarrow 0.5O_2 + H^+ + 2e^- \qquad (9.10)$$

The hydrogen evolution reaction (HER) represented by Equation 9.8 requires a catalyst whose effectiveness is characterised by the strength of the intermediate bonds formed with adsorbed hydrogen ions prior to evolution of H_2. The most effective catalysts to date are rare metals such as Platinum and Ruthenium but the cost of these materials prohibits their use for mass production. Although it is most commonly used in industry as a hydrodesulfurization catalyst, MoS_2 is generating increased interest as a HER catalyst [101, 224-226]. The catalytic HER performance of this material is currently limited by the density of active sites and poor electrical transport. The density of active sites will depend on the structure of the MoS_2. Recent studies have linked the catalytic activity with the edge sites of 2D MoS_2 nanosheets [225].

This implies that catalytic activity can be improved by increasing the number of

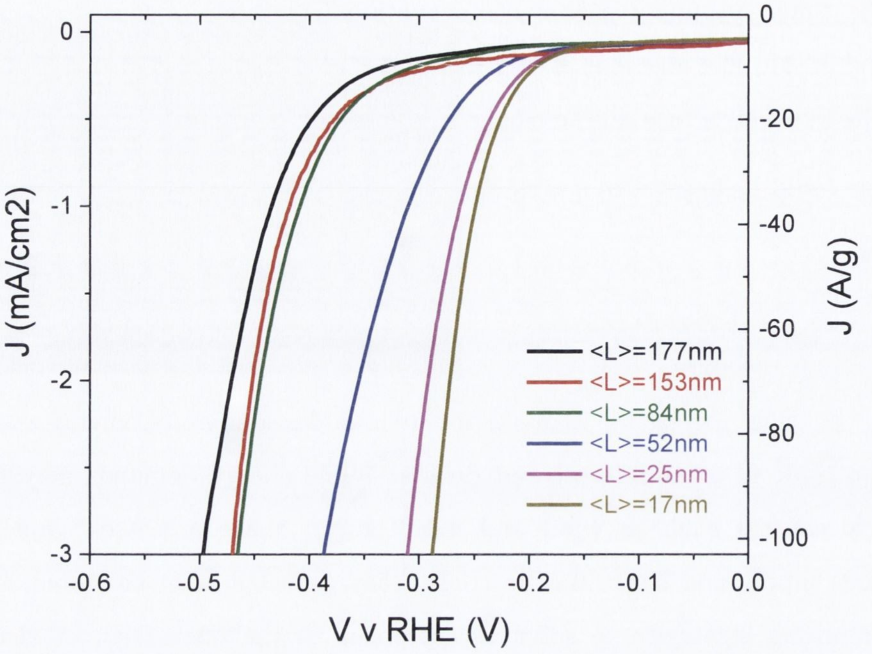

Figure 9.6: Linear sweep voltammograms (5 mV/s) of lateral dimension selected MoS_2 on ITO substrates, comparing the electrocatalytic response towards hydrogen evolution reaction.

edge sites per nanosheet, Current work in the Coleman group is attempting to control the number of edge sites by careful size selection of surfactant stabilised MoS_2 dispersions. By decreasing the average lateral dimensions of the dispersed flakes, the catalytic activity can be increased. To that end, a stock dispersion of MoS_2 was centrifuged at various rates (500 to 15000 RPM). The average flake size for each dispersion was determined by TEM analysis of drop cast grids with <L> ranging from 17 to 177nm shown in Figure. The dispersions were then vacuum filtered to give thin films of equal mass, transferred onto ITO coated glass substrates and characterised for electrocatalytic activity for hydrogen evolution. The sample behaves as expected with a decrease in the overpotential with decreasing flake size. To generate current densities of 3 mA/cm^2 required overpotentials of 500 mV for the 177 nm flakes compared with less than 300 mV for the 17 nm flakes at the same mass loading (Figure 9.6). While these results are promising, the numbers generated could be improved in a number of ways. Besides the number of active sites, there are a number of factors that could be tailored to increase catalytic activity. The use of low boiling point solvents, lower surfactant concentrations or more rigorous washing techniques could ensure the absence of adsorbed surfactant on the electrode increasing availability of active sites. The addition of conductive nanostructures such as CNTs at

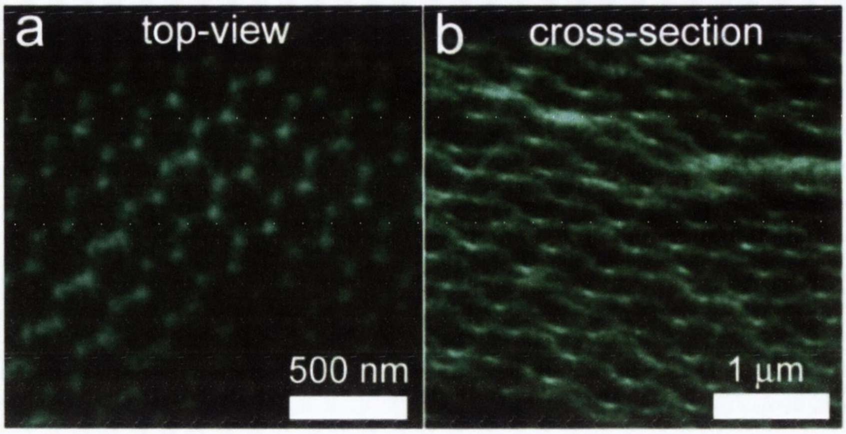

Figure 9.7: SEM of graphene assembled at the interstitial sites of highly ordered polymer latex matrix. (a) top-view and (b) cross-section of a composite containing 0.4 wt. % of graphene. Images taken by Dr. Izabella Jurewicz.

low fractions will increase the electrical transport properties of the electrode while hybrids with other nanomaterials such as TiO_2 have been shown to enhance electrocatalytic behaviour [227, 228]

9.4 CONTROLLED MORPHOLOGY OF NANOSTRUCTURED MATERIALS

The majority of applications for layered materials outlined in this thesis rely on the ability to make thin films from colloidal dispersions with vacuum filtering and spray deposition the most commonly used techniques. While these methods allow for good control over film thickness, the resulting films lack any long range order as they consist of an uncontrolled and inhomogeneous distribution of flakes. In addition, the porosity of these films is quite low leading to increasingly inaccessible surface areas as film thickness is increased. This is a particular problem when considering applications requiring high surface areas such as supercapacitors electrodes.

Recent work in collaboration with Dr. Alan Dalton and Dr. Izabella Jurewicz (University of Surrey, UK) has focused on the formation of hierarchical graphene structures by incorporating exfoliated graphene into aqueous polymer latex in method similar to that used for CNTs [229]. During this process, graphene is added to a polymer latex matrix in the liquid stage allowing it to be well dispersed during film formation. As these films dry, capillary forces trap the graphene [230] in the

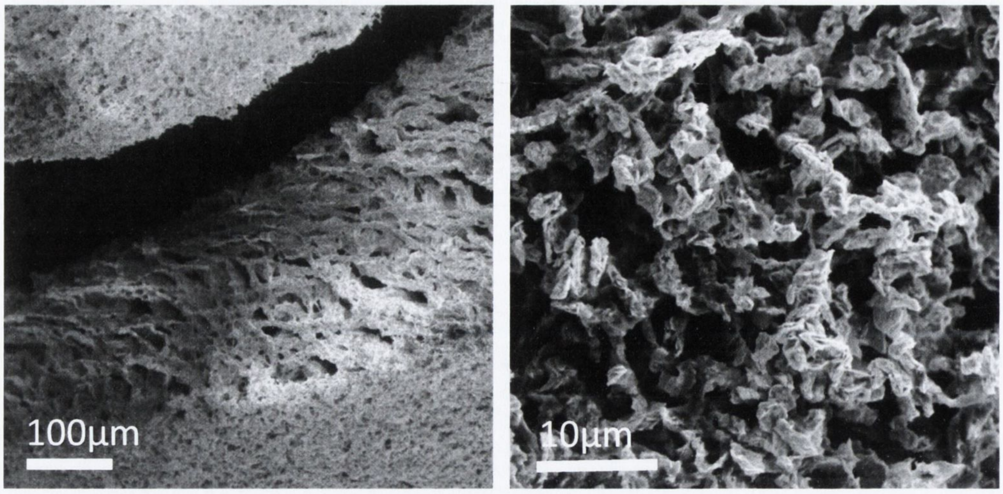

Figure 9.8: SEM of freeze-cast MoS_2 structures. Porosity is increased by significantly compared with vacuum filtered films. Images were taken by Tiffany Williams.

interstitial spaces between polymer particles resulting in highly ordered 3D petal-like graphene assemblies. This technique relies on the ability of nanosheets to bend and fit into the spaces between polymer particles and hence depends heavily on the average size and thickness of the nanosheets. In order for this method to produce structures exhibiting long range order for a wide variety of dispersed nanosheets, greater control over flake dimensions will be required.

Another route towards controlled film morphology is freeze casting. This involves freezing the dispersion in a cold bath followed by removal of the frozen solvents via sublimation under vacuum. This leads to the formation of porous structures with tuneable pore size and volume depending on processing conditions [231]. The pores themselves are a result of voids left behind by the removal of solvent and thus the frozen solvent acts as a template or scaffold for the resulting nanostructure. This is a well-established technique and has been used to create porous structures from aqueous polymer dispersions of both CNTs [232] and Graphene [233]. Initial work in collaboration with the Giannelis group (Cornell University, USA), has produced macroporous structures of MoS_2 nanosheets from surfactant stabilised dispersions. If this method proves viable in terms of structural stability, then it could be expanded to other hybrids dispersions for use in supercapacitor devices or batteries

10

CONCLUSIONS

The aim of this thesis was to investigate and perfect a large scale method of production for two dimensional materials building on initial liquid phase work on graphene [78]. Liquid phase exfoliation of bulk material in aqueous surfactant solutions has been demonstrated to be an effective as well as general method for isolation and stabilisation of two dimensional nanosheets.

In order to gain a better understanding of the physics and chemistry underlying surfactant stabilisation of these nanosheets, the dispersibility of graphene in various surfactants was measured. The results showed the dispersed concentration to depend critically on the size of the repulsive potential barrier, introduced by adsorbed surfactant molecules on the surface of dispersed flakes. The ability to disperse graphene in ionic and non-ionic surfactants is also an important result as charge neutrality or pH insensitivity may be important for some processes. Further study is required however as surfactants have yet to be compared at optimum concentrations. This will vary per surfactant due to different molecular structures. Long chain surfactants such as SDS which are less effective at low concentrations compared with SC could be useful for surfactant blends where surface coverage is optimised by increasing packing density of molecules.

The polydispersed nature of the material produced by liquid phase exfoliation is a major impediment for their use in many applications. Size exclusion chromatography has been used to separate dispersed flakes according to their lateral dimensions. The separation was confirmed by means of TEM analysis of the dispersions themselves and Raman spectroscopy of thin films cast from fractions. The process allowed for a 100% increase in the average flake size of a graphene dispersion essentially through the removal of smaller flakes. Although this is a promising result, the use of graphene as a reinforcing material will require average flake sizes larger than those reported in this work[178] It is reasonable to expect this to be made possible by increasing both the population of large flakes in the initial dispersion through re-dispersing sediment and the resolution of the column in order to be better able to isolate this population of large flakes.

The method of exfoliation established for graphene has also been expanded to include transition metal dichalcogenides and transition metal oxides. The parameter base for the process has been investigated extensively in terms of effect on dispersed concentration and stability allowing for scale up. TEM and Raman analysis has confirmed that the process does not introduce any significant structural or electrical changes to the starting material in contrast similar methods such as ion exfoliation. This method also enables the production of thin films of inorganic layered compounds whose electrical properties range from insulator to metal. By blending different dispersions, liquid phase exfoliation of layered materials could become a powerful tool in the construction of a diverse group of hybrid materials with unique electrical and physical properties tailored to specific requirements.

This has been explored somewhat by blending nanotubes with MoS_2 for use in a range of applications. The nanotubes in these hybrids increase the DC conductivity of the films without significantly degrading the Seebeck coefficient making them a promising material for use in thermoelectric devices. Further research on the thermal conductivity of these films will be required before any more progress can be made, although the use of other layered compounds with higher Seebeck coefficients may improve the power factor. As well as increasing the DC conductivity, the nanotubes can enhance the structural integrity of the films. This can be useful for energy storage in Li-ion batteries as cracking of the electrodes can occur after multiple cycles. The hybrid battery electrodes constructed have shown increased cyclability when compared with MoS_2 only samples.

Despite some promising initial results there still remains a great deal to be learnt about liquid phase exfoliation of layered materials before it can meet the stringent material demands for modern applications. Greater control over the size and thickness of the material produced is the most pressing need with little quantitative information on the effect of varying processing parameters on flake dimensions. The new absorbance metrics discussed in Chapter 9 may allow for fast and comprehensive studies on this possibly allowing for greater control over flake dimensions through careful control of the exfoliation conditions. Control over the architecture of nanostructures formed from these dispersions will also be essential in order to exploit intrinsic material properties such as high surface area. Initial work on freeze casting as well as latex templating has been promising and merits further development. Finally the changing chemistry with lateral dimensions of some layered materials could be exploited for catalysis with some encouraging results shown in Chapter 9. The effectiveness of MoS_2 electrodes for Hydrogen evolution could also be improved by the addition of nanoconductors such as graphene or CNTs. Despite the material diversity demonstrated in this thesis, this work has only scratched the surface in terms of layered materials and their possible applications. A new frontier in material science has been revealed with many untapped resources waiting to be discovered.

1. Kroto, H.W., J.R. Heath, S.C. O'Brien, R.F. Curl, and R.E. Smalley. (1985) C60: Buckminsterfullerene. *Nature 318*, 162-163.
2. Iijima, S. (1991) Helical microtubules of graphitic carbon. *Nature 354*, 56-58.
3. Novoselov, K.S. (2005) Two-dimensional atomic crystals. *Proceedings of the National Academy of Sciences 102*, 10451-10453.
4. Scarselli, M., P. Castrucci, and M. De Crescenzi. (2012) Electronic and optoelectronic nano-devices based on carbon nanotubes. *J Phys Condens Matter 24*, 313202.
5. Yu, M. (2000) Strength and Breaking Mechanism of Multiwalled Carbon Nanotubes Under Tensile Load. *Science 287*, 637-640.
6. Durkop, T., S.A. Getty, E. Cobas, and M.S. Fuhrer. (2004) Extraordinary Mobility in Carbon Nanotubes. *Nano Letters 4*, 35-39.
7. Wei, B.Q., R. Vajtai, and P.M. Ajayan. (2001) Reliability and current carrying capacity of carbon nanotubes. *Applied Physics Letters 79*, 1172.
8. Kane, C.L. and E.J. Mele. (1997) Size, Shape, and Low Energy Electronic Structure of Carbon Nanotubes. *Physical Review Letters 78*, 1932-1935.
9. Sumio, I. and I. Toshinari. (1993) Single-shell carbon nanotubes of 1-nm diameter. *Nature 363*, 603-605.
10. Coleman, J.N., U. Khan, W.J. Blau, and Y.K. Gun'ko. (2006) Small but strong: A review of the mechanical properties of carbon nanotube–polymer composites. *Carbon 44*, 1624-1652.
11. Hongjie Dai, A.G. Rinzler, P. Nikolaev, A. Thess, D.T. Colbert, and R.E. Smalley. (1996) Single-wall nanotubes produced by metal-catalyzed. *Chemical Physics Letters 260*, 471-475.
12. Voggu, R., K.V. Rao, S.J. George, and C.N.R. Rao. (2010) A Simple Method of Separating Metallic and Semiconducting Single-Walled. *Journal of the American Chemical Society 132*, 5560-5561.
13. De Volder, M.F., S.H. Tawfick, R.H. Baughman, and A.J. Hart. (2013) Carbon nanotubes: present and future commercial applications. *Science 339*, 535-9.
14. Bakshi, S.R., D. Lahiri, and A. Agarwal. (2010) Carbon nanotube reinforced metal matrix composites - a review. *International Materials Reviews 55*, 41-64.
15. Marty, L., A. Iaia, M. Faucher, V. Bouchiat, C. Naud, M. Chaumont, T. Fournier, and A.M. Bonnot. (2006) Self-assembled single wall carbon nanotube field effect transistors and AFM tips prepared by hot filament assisted CVD. *Thin Solid Films 501*, 299-302.

16. Zhang, T., S. Mubeen, N.V. Myung, and M.A. Deshusses. (2008) Recent progress in carbon nanotube-based gas sensors. *Nanotechnology 19*, 332001.

17. Kim, B., H. Chung, and W. Kim. (2012) High-performance supercapacitors based on vertically aligned carbon nanotubes and nonaqueous electrolytes. *Nanotechnology 23*, 155401.

18. Bordjiba, T. and D. Bélanger. (2009) Direct Redox Deposition of Manganese Oxide on Multiscaled Carbon Nanotube/Microfiber Carbon Electrode for Electrochemical Capacitor. *Journal of The Electrochemical Society 156*, A378.

19. Geim, A. and K. Novoselov. (2007) The Rise of Graphene. *Nature Materials 6*, 183-191.

20. Bachilo, S.M., M.S. Strano, C. Kittrell, R.H. Hauge, R.E. Smalley, and R.B. Weisman. (2002) Structure-assigned optical spectra of single-walled carbon nanotubes. *Science 298*, 2361-6.

21. O'Connell, M.J., S.M. Bachilo, C.B. Huffman, V.C. Moore, M.S. Strano, E.H. Haroz, K.L. Rialon, P.J. Boul, W.H. Noon, C. Kittrell, J. Ma, R.H. Hauge, R.B. Weisman, and R.E. Smalley. (2002) Band gap fluorescence from individual single-walled carbon nanotubes. *Science 297*, 593-6.

22. Strano, M.S., V.C. Moore, M.K. Miller, M.J. Allen, E.H. Haroz, C. Kittrell, R.H. Hauge, and R.E. Smalley. (2003) The role of surfactant adsorption during ultrasonication in the dispersion of single-walled carbon nanotubes. *Nanoscience and Nanotechnology 3*, 81-86.

23. Moore, V.C., M.S. Strano, E.H. Haroz, R.H. Hauge, R.E. Smalley, J. Schmidt, and Y. Talmon. (2003) Individually Suspended Single-Walled Carbon Nanotubes in Various Surfactants. *Nano Letters 3*, 1379-1382.

24. Bergin, S.D., V. Nicolosi, H. Cathcart, M. Lotya, D. Rickard, Z.Y. Sun, W.J. Blau, and J.N. Coleman. (2008) Large Populations of Individual Nanotubes in Surfactant-Based Dispersions without the Need for Ultracentrifugation. *Journal of Physical Chemistry C 112*, 972-977.

25. Coleman, J.N., A.B. Dalton, S. Curran, A. Rubio, A.P. Davey, A. Drury, B. McCarthy, B. Lahr, P.M. Ajayan, S. Roth, R.C. Barklie, and W.J. Blau. (2000) Phase separation of carbon nanotubes and turbostratic graphite using a functional organic polymer. *Advanced Materials 12*, 213-216.

26. Hasan, T., V. Scardaci, P.H. Tan, A.G. Rozhin, W.I. Milne, and A.C. Ferrari. (2008) Dispersibility and stability improvement of unfunctionalized nanotubes in amide solvents by polymer wrapping. *Physica E: Low-dimensional Systems and Nanostructures 40*, 2414-2418.

27. Giordani, S., S.D. Bergin, V. Nicolosi, S. Lebedkin, M.M. Kappes, W.J. Blau, and J.N. Coleman. (2006) Debundling of Single-Walled Nanotubes by

Dilution:Observation of Large Populations of Individual Nanotubes in Amide Solvent Dispersions. *Journal of physical Chemistry B* 15708–15718.

28. Bergin, S.D., V. Nicolosi, P.V. Streich, S. Giordani, Z. Sun, A.H. Windle, P. Ryan, N.P.P. Niraj, Z.-T.T. Wang, L. Carpenter, W.J. Blau, J.J. Boland, J.P. Hamilton, and J.N. Coleman. (2008) Towards Solutions of Single-Walled Carbon Nanotubes in Common Solvents. *Advanced Materials 20*, 1876-1881.

29. Novoselov, K.S., A. Geim, S.V. Morozov, D. Jiang, Y. Zhang, and S.V. Dubonos. (2004) Electric Field Effect in Atomically Thin Carbon Films. *Science 306*, 666-669.

30. Zhang, Y., Y.W. Tan, H.L. Stormer, and P. Kim. (2005) Experimental observation of the quantum Hall effect and Berry's phase in graphene. *Nature 438*, 201-4.

31. Pisana, S., M. Lazzeri, C. Casiraghi, K.S. Novoselov, A.K. Geim, A.C. Ferrari, and F. Mauri. (2007) Breakdown of the adiabatic Born-Oppenheimer approximation in graphene. *Nat Mater 6*, 198-201.

32. Lu, X., M. Yu, H. Huang, and R.S. Ruoff. (1999) Tailoring graphite with the goal of achieving single sheets. *Nanotechnology 10*, 269-272.

33. Balandin, A.A. (2011) Thermal properties of graphene and nanostructured carbon materials. *Nat Mater 10*, 569-81.

34. Bunch, J.S., S.S. Verbridge, J.S. Alden, A.M.v.d. Zande, J.M. Parpia, H.G. Craighead, and P.L. McEuen. (2008) Impermeable atomic membranes from graphene sheets. *Nano Letters 8*, 2458-2462.

35. Novoselov, K.S., A.K. Geim, S.V. Morozov, D. Jiang, M.I. Katsnelson, I.V. Grigorieva, S.V. Dubonos, and A.A. Firsov. (2005) Two-dimensional gas of massless Dirac fermions in graphene. *Nature 438*, 197-200.

36. Du, X., I. Skachko, A. Barker, and E.Y. Andrei. (2008) Approaching ballistic transport in suspended graphene. *Nature Nanotechnology 3*, 491-495.

37. Y.-M. Lin, C. Dimitrakopoulos, K.A. Jenkins, D.B. Farmer, H.-Y. Chiu, A. Grill, and P. Avouris. (2010) 100-GHz transistors from wafer-scale epitaxial graphene. *Science 327*, 662.

38. Lee, C., X. Wei, J.W. Kysar, and J. Hone. (2008) Measurement of the Elastic Properties and Intrinsic Strength of Monolayer Graphene. *Science 321*, 385-388.

39. Alzari, V., V. Sanna, S. Biccai, T. Caruso, A. Politano, N. Scaramuzza, M. Sechi, D. Nuvoli, R. Sanna, and A. Mariani. (2014) Tailoring the physical properties of nanocomposite films by the insertion of graphene and other nanoparticles. *Composites Part B: Engineering 60*, 29-35.

40. Nuvoli, D., V. Alzari, R. Sanna, S. Scognamillo, J. Alongi, G. Malucelli, and A. Mariani. (2013) Synthesis and characterization of graphene-based

nanocomposites with potential use for biomedical applications. *Journal of Nanoparticle Research 15*, 1-8.

41. Nair, R.R., P. Blake, A.N. Grigorenko, K.S. Novoselov, T.J. Booth, T. Stauber, N.M.R. Peres, and A.K. Geim. (2008) Fine Structure Constant Defines Visual Transparency of Graphene. *Science 320*, 1308.

42. Bae, S., H. Kim, Y. Lee, X. Xu, J.S. Park, Y. Zheng, J. Balakrishnan, T. Lei, H.R. Kim, Y. Song, K.S. Kim, B. Ozyilmaz, J.H. Ahn, B.H. Hong, and S. Iijima. (2010) Roll-to-roll production of 30-inch graphene films for transparent electrodes. *Nature Nanotechnology 5*, 574-578.

43. De, S., P.J. King, P.E. Lyons, U. Khan, and J.N. Coleman. (2010) Size Effects and the Problem with Percolation in Nanostructured Transparent Conductors. *ACS Nano 4*, 7064-7072.

44. Novoselov, K.S., V.I. Fal'ko, L. Colombo, P.R. Gellert, M.G. Schwab, and K. Kim. (2012) A roadmap for graphene. *Nature 490*, 192-200.

45. Stoller, M.D., S. Park, Y. Zhu, J. An, and R.S. Ruoff. (2008) Graphene-Based Ultracapacitors. *Nano Letters 8*, 3498-3502.

46. Yoo, E., T. Okata, T. Akita, M. Kohyama, J. Nakamura, and I. Honma. (2009) Enhanced electrocatalytic activity of Pt subnanoclusters on graphene nanosheet surface. *Nano Letters 9*,

47. Yuan, W. and G. Shi. (2013) Graphene-based gas sensors. *Journal of Materials Chemistry A 1*, 10078.

48. Schedin, F., A.K. Geim, S.V. Morozov, E.W. Hill, P. Blake, M.I. Katsnelson, and K.S. Novoselov. (2007) Detection of individual gas molecules adsorbed on graphene. *Nature Materials 6*, 652-655.

49. Deheer, W., C. Berger, X. Wu, P. First, E. Conrad, X. Li, T. Li, M. Sprinkle, J. Hass, and M. Sadowski. (2007) Epitaxial graphene. *Solid State Communications 143*, 92-100.

50. Ohta, T., A. Bostwick, T. Seyller, K. Horn, and E. Rotenberg. (2006) Controlling the electronic structure of bilayer graphene. *Science 313*, 951-4.

51. Ueta, H. (2004) Highly oriented monolayer graphite formation on Pt(111) by a supersonic methane beam. *Surface Science 560*, 183-190.

52. Sutter, P.W., J.I. Flege, and E.A. Sutter. (2008) Epitaxial graphene on ruthenium. *Nat Mater 7*, 406-11.

53. Li, X., W. Cai, J. An, S. Kim, J. Nah, D. Yang, R. Piner, A. Velamakanni, I. Jung, E. Tutuc, S.K. Banerjee, L. Colombo, and R.S. Ruoff. (2009) Large-area synthesis of high-quality and uniform graphene films on copper foils. *Science 324*, 1312-4.

54. Kim, K.S., Y. Zhao, H. Jang, S.Y. Lee, J.M. Kim, K.S. Kim, J.-H. Ahn, P. Kim, J.-Y. Choi, and B.H. Hong. (2009) Large-scale pattern growth of graphene films for stretchable transparent electrodes. *Nature 457*, 706-710.

55. Yang, X., X. Dou, A. Rouhanipour, L. Zhi, H.J. Ra¨der, and K. Mullen. (2007) Two-Dimensional Graphene Nanoribbons. *Journal of the American Chemical Society 130*, 4216.

56. Wu, J., W. Pisula, and K. Mullen. (2007) Graphenes as Potential Material for Electronics. *Chem. Rev. 107*, 718-747.

57. Brodie, B.C. (1859) On the Atomic Weight of Graphite. *Philosophical Transactions of the Royal Society of London 149*, 249.

58. Hummers, W.S. and R.E. Offeman. (1958) Preparation of Graphitic Oxide. *Journal of the American Chemical Society 80*,

59. Li, X., G. Zhang, X. Bai, X. Sun, X. Wang, E. Wang, and H. Dai. (2008) Highly conducting graphene sheets and Langmuir–Blodgett films. *Nature Nanotechnology 3*, 538-542.

60. Suk, J.W., R.D. Piner, J. An, and R.S. Ruoff. (2010) Mechanical Properties of Monolayer Graphene Oxide. *ACS Nano 4*, 6557.

61. Tung, V.C., M.J. Allen, Y. Yang, and R.B. Kaner. (2008) High-throughput solution processing of large-scale graphene. *Nature Nanotechnology 4*, 25-29.

62. Gilje, S., S. Han, M. Wang, K.L. Wang, and R.B. Kaner. (2007) A Chemical Route to Graphene for Device Applications. *Nano Letters 7*, 3394.

63. Li, D., M.B. Müller, S. Gilje, R.B. Kaner, and G.G. Wallace. (2008) Processable aqueous dispersions of graphene nanosheets. *Nature Nanotechnology 3*, 101-105.

64. Eda, G., G. Fanchini, and M. Chhowalla. (2008) Large-area ultrathin films of reduced graphene oxide as a transparent and flexible electronic material. *Nature Nanotechnology 3*, 270-274.

65. Lomeda, J.R., C.D. Doyle, D.V. Kosynkin, W.-F. Hwang, and J.M. Tour. (2008) Diazonium Functionalization of Surfactant-Wrapped Chemically Converted Graphene Sheets. *Journal of the American Chemical Society 130*, 16201-16206.

66. Eda, G. and M. Chhowalla. (2009) Graphene-based Composite Thin Films for Electronics. *Nano Letters 9*, 814-818.

67. Park, S. and R.S. Ruoff. (2009) Chemical methods for the production of graphenes. *Nature Nanotechnology 4*, 217-224.

68. Williams, G., B. Seger, and P.V. Kamat. (2008) TiO_2-Graphene Nanocomposites. UV-Assisted Photocatalytic Reduction of Graphene Oxide. *ACS Nano 2*, 1487.

69. Stankovich, S., D. Dikin, R. Piner, K. Kohlhaas, A. Kleinhammes, Y. Jia, Y. Wu, S. Nguyen, and R. Ruoff. (2007) Synthesis of graphene-based nanosheets via chemical reduction of exfoliated graphite oxide. *Carbon 45*, 1558-1565.

70. Schniepp, H.C., J.-L. Li, M.J. McAllister, H. Sai, M. Herrera-Alonso, D.H. Adamson, R.K. Prud'homme, R. Car, D.A. Saville, and I.A. Aksay*. (2006) Functionalized Single Graphene Sheets Derived from Splitting Graphite Oxide. *Journal of Physical Chemistry B 110*, 8535.

71. Ausman, K.D., R. Piner, O. Lourie, R.S. Ruoff, and M. Korobov. (2000) Organic Solvent Dispersions of Single-Walled Carbon Nanotubes: Toward Solutions of Pristine Nanotubes. *The Journal of Physical Chemistry B 104*, 8911-8915.

72. Furtado, C.A., U.J. Kim, H.R. Gutierrez, L. Pan, E.C. Dickey, and P.C. Eklund. (2004) Debundling and Dissolution of Single-Walled Carbon Nanotubes in Amide Solvents. *Journal of the American Chemical Society 126*, 6095-6105.

73. Tan, Y. and D.E. Resasco. (2005) Dispersion of Single-Walled Carbon Nanotubes of Narrow Diameter Distribution. *The Journal of Physical Chemistry B 109*, 14454-14460.

74. Bergin, S.D., V. Nicolosi, S. Giordani, A.d. Gromard, L. Carpenter, W.J. Blau, and J.N. Coleman. (2007) Exfoliation in ecstasy: liquid crystal formation and concentration-dependent debundling observed for single-wall nanotubes dispersed in the liquid drug γ-butyrolactone. *Nanotechnology 18*, 455705.

75. Bergin, S.D., Z. Sun, D. Rickard, P.V. Streich, J.P. Hamilton, and J.N. Coleman. (2009) Multicomponent Solubility Parameters for Single-Walled Carbon Nanotube−Solvent Mixtures. *ACS Nano 3*, 2340-2350.

76. Cheng, Q., S. Debnath, E. Gregan, and H.J. Byrne. (2008) Effect of Solvent Solubility Parameters on the Dispersion of Single-Walled Carbon Nanotubes. *The Journal of Physical Chemistry C 112*, 20154-20158.

77. Ham, H.T., Y.S. Choi, and I.J. Chung. (2005) An explanation of dispersion states of single-walled carbon nanotubes in solvents and aqueous surfactant solutions using solubility parameters. *Journal of Colloid and Interface Science 286*, 216-223.

78. Hernandez, Y., V. Nicolosi, M. Lotya, F.M. Blighe, Z. Sun, S. De, I.T. McGovern, B. Holland, M. Byrne, Y.K. Gun'Ko, J.J. Boland, P. Niraj, G. Duesberg, S. Krishnamurthy, R. Goodhue, J. Hutchison, V. Scardaci, A.C. Ferrari, and J.N. Coleman. (2008) High-yield production of graphene by liquid-phase exfoliation of graphite. *Nature Nanotechnology 3*, 563-568.

79. Nicolosi, V., M. Chhowalla, M.G. Kanatzidis, M.S. Strano, and J.N. Coleman. (2013) Liquid Exfoliation of Layered Materials. *Science 340*,

80. Blake, P. and P. Brimicombe. (2008) Graphene-Based Liquid Crystal Device. *Nano Letters 8*, 5.

81. Lotya, M., Y. Hernandez, P.J. King, R.J. Smith, V. Nicolosi, L.S. Karlsson, F.M. Blighe, S. De, Z. Wang, I.T. McGovern, G.S. Duesberg, and J.N. Coleman. (2009) Liquid Phase Production of Graphene by Exfoliation of Graphite in Surfactant/Water Solutions. *Journal of the American Chemical Society 131*, 3611-3620.

82. Bonard, J.-M., T. Stora, J.-P. Salvetat, F. Maier, T. Stöckli, C. Duschl, L. Forró, W.A. de Heer, and A. Châtelain. (1997) Purification and size-selection of carbon nanotubes. *Advanced Materials 9*, 827-831.

83. Grossiord, N., P. van der Schoot, J. Meuldijk, and C.E. Koning. (2007) Determination of the Surface Coverage of Exfoliated Carbon Nanotubes by Surfactant Molecules in Aqueous Solution. *Langmuir 23*, 3646-3653.

84. Rastogi, R., R. Kaushal, S.K. Tripathi, A.L. Sharma, I. Kaur, and L.M. Bharadwaj. (2008) Comparative study of carbon nanotube dispersion using surfactants. *Journal of Colloid and Interface Science 328*, 421-428.

85. Haggenmueller, R., S.S. Rahatekar, J.A. Fagan, J. Chun, M.L. Becker, R.R. Naik, T. Krauss, L. Carlson, J.F. Kadla, P.C. Trulove, D.F. Fox, H.C. DeLong, Z. Fang, S.O. Kelley, and J.W. Gilman. (2008) Comparison of the Quality of Aqueous Dispersions of Single Wall Carbon Nanotubes Using Surfactants and Biomolecules. *Langmuir 24*, 5070-5078.

86. Sun, Z., V. Nicolosi, D. Rickard, S.D. Bergin, D. Aherne, and J.N. Coleman. (2008) Quantitative Evaluation of Surfactant-stabilized Single-walled Carbon Nanotubes: Dispersion Quality and Its Correlation with Zeta Potential. *Journal of Physical Chemistry C 111*, 13684-13690.

87. Nuvoli, D., V. Alzari, R. Sanna, S. Scognamillo, M. Piccinini, L. Peponi, J. Kenny, and A. Mariani. (2012) The production of concentrated dispersions of few-layer graphene by the direct exfoliation of graphite in organosilanes. *Nanoscale Research Letters 7*, 1-7.

88. Sheneve Z. Butler, Shawna M. Hollen, Linyou Cao, Yi Cui, Jay A. Gupta, Humberto R. Gutierrez, Tony F. Heinz, Seung Sae Hong, Jiaxing Huang, Ariel F. Ismach, Ezekiel Johnston-Halperin, Masaru Kuno, Vladimir V. Plashnitsa, Richard D. Robinson, Rodney S. Ruoff, Sayeef Salahuddin, Jie Shan, Li Shi, Michael G. Spencer, Mauricio Terrones, Wolfgang Windl, and J.E. Goldberger. (2013) Progress, Challenges, and Opportunities in Two-Dimensional Materials Beyond Graphene. *ACS Nano 7*, 2898-2926.

89. Lin, Y. and J.W. Connell. (2012) Advances in 2D boron nitride nanostructures: nanosheets, nanoribbons, nanomeshes, and hybrids with graphene. *Nanoscale 4*, 6908-39.

90. Kim, K.K., A. Hsu, X. Jia, S.M. Kim, Y. Shi, M. Hofmann, D. Nezich, J.F. Rodriguez-Nieva, M. Dresselhaus, T. Palacios, and J. Kong. (2012) Synthesis

of monolayer hexagonal boron nitride on Cu foil using chemical vapor deposition. *Nano Lett 12*, 161-6.

91. M. Terrones, J.C. Charlier, A. Gloter, E. Cruz-Silva, E. Terrés, Y. B. Li, A. Vinu, Z. Zanolli, J. M. Dominguez, H. Terrones, Y. Bando, and D. Golberg. (2008) Experimental and theoretical studies suggesting the possibility of metallic boron nitride edges in porous nanourchins. *Nano Letters 8*, 1026-1032.

92. Dean, C.R., A.F. Young, I. Meric, C. Lee, L. Wang, S. Sorgenfrei, K. Watanabe, T. Taniguchi, P. Kim, K.L. Shepard, and J. Hone. (2010) Boron nitride substrates for high-quality graphene electronics. *Nat Nanotechnol 5*, 722-6.

93. Zhi, C., Y. Bando, C. Tang, H. Kuwahara, and D. Golberg. (2009) Large-Scale Fabrication of Boron Nitride Nanosheets and Their Utilization in Polymeric Composites with Improved Thermal and Mechanical Properties. *Advanced Materials 21*, 2889-2893.

94. Lindsay, L. and D.A. Broido. (2011) Enhanced thermal conductivity and isotope effect in single-layer hexagonal boron nitride. *Physical Review B 84*,

95. Song, W.L., P. Wang, L. Cao, A. Anderson, M.J. Meziani, A.J. Farr, and Y.P. Sun. (2012) Polymer/boron nitride nanocomposite materials for superior thermal transport performance. *Angew Chem Int Ed Engl 51*, 6498-501.

96. Han, W.-Q., L. Wu, Y. Zhu, K. Watanabe, and T. Taniguchi. (2008) Structure of chemically derived mono- and few-atomic-layer boron nitride sheets. *Applied Physics Letters 93*, 223103.

97. Coleman, J.N., M. Lotya, A. O'Neill, S.D. Bergin, P.J. King, U. Khan, K. Young, A. Gaucher, S. De, R.J. Smith, I.V. Shvets, S.K. Arora, G. Stanton, H.Y. Kim, K. Lee, G.T. Kim, G.S. Duesberg, T. Hallam, J.J. Boland, J.J. Wang, J.F. Donegan, J.C. Grunlan, G. Moriarty, A. Shmeliov, R.J. Nicholls, J.M. Perkins, E.M. Grieveson, K. Theuwissen, D.W. McComb, P.D. Nellist, and V. Nicolosi. (2011) Two-Dimensional Nanosheets Produced by Liquid Exfoliation of Layered Materials. *Science 331*, 568-571.

98. Song, L., L. Ci, H. Lu, P.B. Sorokin, C. Jin, J. Ni, A.G. Kvashnin, D.G. Kvashnin, J. Lou, B.I. Yakobson, and P.M. Ajayan. (2010) Large scale growth and characterization of atomic hexagonal boron nitride layers. *Nano Lett 10*, 3209-15.

99. Wilson, J.A. and A.D. Yoffe. (1969) The transition metal dichalcogenides discussion and interpretation of the observed optical, electrical and structural properties. *Advances in Physics 18*, 193-335.

100. Chhowalla, M., H.S. Shin, G. Eda, L.J. Li, K.P. Loh, and H. Zhang. (2013) The chemistry of two-dimensional layered transition metal dichalcogenide nanosheets. *Nat Chem 5*, 263-75.

101. Laursen, A.B., S. Kegnæs, S. Dahl, and I. Chorkendorff. (2012) Molybdenum sulfides—efficient and viable materials for electro - and photoelectrocatalytic hydrogen evolution. *Energy & Environmental Science 5*, 5577.

102. Puthussery, J., S. Seefeld, N. Berry, M. Gibbs, and M. Law. (2011) Colloidal iron pyrite (FeS2) nanocrystal inks for thin-film photovoltaics. *J Am Chem Soc 133*, 716-9.

103. Ding, S., D. Zhang, H.B. Wu, Z. Zhang, and X.W. Lou. (2012) Synthesis of micro-sized SnO2@carbon hollow spheres with enhanced lithium storage properties. *Nanoscale 4*, 3651-4.

104. Liu, K.K., W. Zhang, Y.H. Lee, Y.C. Lin, M.T. Chang, C.Y. Su, C.S. Chang, H. Li, Y. Shi, H. Zhang, C.S. Lai, and L.J. Li. (2012) Growth of large-area and highly crystalline MoS2 thin layers on insulating substrates. *Nano Lett 12*, 1538-44.

105. Zhan, Y., Z. Liu, S. Najmaei, P.M. Ajayan, and J. Lou. (2012) Large-area vapor-phase growth and characterization of MoS(2) atomic layers on a SiO(2) substrate. *Small 8*, 966-71.

106. Lee, Y.H., X.Q. Zhang, W. Zhang, M.T. Chang, C.T. Lin, K.D. Chang, Y.C. Yu, J.T. Wang, C.S. Chang, L.J. Li, and T.W. Lin. (2012) Synthesis of large-area MoS2 atomic layers with chemical vapor deposition. *Adv Mater 24*, 2320-5.

107. Lin, Y.C., W. Zhang, J.K. Huang, K.K. Liu, Y.H. Lee, C.T. Liang, C.W. Chu, and L.J. Li. (2012) Wafer-scale MoS2 thin layers prepared by MoO3 sulfurization. *Nanoscale 4*, 6637-41.

108. Eda, G., H. Yamaguchi, D. Voiry, T. Fujita, M. Chen, and M. Chhowalla. (2011) Photoluminescence from chemically exfoliated MoS2. *Nano Lett 11*, 5111-6.

109. Eda, G., T. Fujita, H. Yamaguchi, D. Voiry, M. Chen, and M. Chhowalla. (2012) Coherent atomic and electronic heterostructures of single-layer MoS2. *ACS Nano 6*, 7311.

110. Zhiyuan, Z., Y. Zongyou, H. Xiao, L. Hai, H. Qiyuan, L. Gang, B. Freddy, and Z. Hua. (2011) Single-Layer Semiconducting Nanosheets: High-Yield Preparation and Device Fabrication. *Angewandte Chemie International Edition 50*, 11093-11097.

111. Yang, D. and R.F. Frindt. (1996) Li-intercalation and exfoliation of WS2. *Journal of Physics and Chemistry of Solids 57*, 1113-1116.

112. Frey, G.L., K.J. Reynolds, R.H. Friend, H. Cohen, and Y. Feldman. (2003) Solution-Processed Anodes from Layer-Structure Materials. *Journal of the American Chemical Society 125*, 5998.

113. Golub, A.S., I.B. Shumilova, Y.V. Zubavichus, Y.L. Slovokhotov, Y.N. Novikov, A.M. Marie, and M. Danot. (1999) From single-layer dispersions of

molybdenum disulfide towards ternary metal sulfides: incorporating copper and silver into a MoS2 matrix. *Solid State Ionics 122*, 137-144.

114. Gordon, R., D. Yang, E. Crozier, D. Jiang, and R. Frindt. (2002) Structures of exfoliated single layers of WS2, MoS2, and MoSe2 in aqueous suspension. *Physical Review B 65*,

115. Mak, K., C. Lee, J. Hone, J. Shan, and T. Heinz. (2010) Atomically Thin MoS2: A New Direct-Gap Semiconductor. *Physical Review Letters 105*,

116. Splendiani, A., L. Sun, Y. Zhang, T. Li, J. Kim, C.-Y. Chim, G. Galli, and F. Wang. (2010) Emerging Photoluminescence in Monolayer MoS2. *Nano Letters 10*, 1271-1275.

117. Korn, T., S. Heydrich, M. Hirmer, J. Schmutzler, and C. Schüller. (2011) Low-temperature photocarrier dynamics in monolayer MoS2. *Applied Physics Letters 99*, -.

118. Castellanos-Gomez, A., M. Poot, G.A. Steele, H.S.J. van der Zant, N. Agraït, and G. Rubio-Bollinger. (2012) Elastic Properties of Freely Suspended MoS2 Nanosheets. *Advanced Materials 24*, 772-775.

119. Bertolazzi, S., J. Brivio, and A. Kis. (2011) Stretching and Breaking of Ultrathin MoS2. *ACS Nano 5*, 9703-9709.

120. Osada, M. and T. Sasaki. (2009) Exfoliated oxide nanosheets: new solution to nanoelectronics. *Journal of Materials Chemistry 19*, 2503-2511.

121. Ma, R. and T. Sasaki. (2010) Nanosheets of Oxides and Hydroxides: Ultimate 2D Charge-Bearing Functional Crystallites. *Advanced Materials 22*, 5082-5104.

122. Osada, M. and T. Sasaki. (2012) Two-Dimensional Dielectric Nanosheets: Novel Nanoelectronics From Nanocrystal Building Blocks. *Advanced Materials 24*, 210-228.

123. Brousse, T., M. Toupin, R. Dugas, L. Athouel, O. Crosnier, and D. Belanger. (2006) Crystaline MnO2 as Possible Alternatives to Amorphous Compounds in Electrochemical Supercapacitors, *Journal of The Electrochemical Society 153*, A2171-A2180.

124. Chen, C.-Y., S.-C. Wang, Y.-H. Tien, W.-T. Tsai, and C.-K. Lin. (2009) Hybrid manganese oxide films for supercapacitor application prepared by sol–gel technique. *Thin Solid Films 518*, 1557-1560.

125. Wei, W., X. Cui, W. Chen, and D.G. Ivey. (2011) Manganese oxide-based materials as electrochemical supercapacitor electrodes. *Chem Soc Rev 40*, 1697-721.

126. Chu, Y.-H., C.-C. Hu, and K.-H. Chang. (2012) Electrochemical quartz crystal microbalance study of amorphous MnO2 prepared by anodic deposition. *Electrochimica Acta 61*, 124-131.

127. Chou, S., F. Cheng, and J. Chen. (2006) Electrodeposition synthesis and electrochemical properties of nanostructured γ-MnO2 films. *Journal of Power Sources 162*, 727-734.

128. Yuan, J., Z.-H. Liu, S. Qiao, X. Ma, and N. Xu. (2009) Fabrication of MnO2-pillared layered manganese oxide through an exfoliation/reassembling and oxidation process. *Journal of Power Sources 189*, 1278-1283.

129. Jiang, R., T. Huang, J. Liu, J. Zhuang, and A. Yu. (2009) A novel method to prepare nanostructured manganese dioxide and its electrochemical properties as a supercapacitor electrode. *Electrochimica Acta 54*, 3047-3052.

130. Hu, Y., H. Zhu, J. Wang, and Z. Chen. (2011) Synthesis of layered birnessite-type manganese oxide thin films on plastic substrates by chemical bath deposition for flexible transparent supercapacitors. *Journal of Alloys and Compounds 509*, 10234-10240.

131. Israelachvili, J. *Intermolecular and Surface Forces*. Academic Press: New York. 1991

132. Hunter, R. *Introduction to modern colloid science*. Oxford University Press New York. 1993

133. *Malvern-Instruments, Zetasizer Nano Series User Manual.* 2004.

134. Overbeek, J.T.G. (1977) Recent developments in the understanding of colloid stability. *Journal of Colloid and Interface Science 58*, 408-422.

135. Hennrich, F.K., R. (2007) The mechanism of cavitation-induced scission of single-walled carbon nanotubes, *Journal of Physical Chemistry B 111*, 1932-1937.

136. Huang, Y.Y. and E.M. Terentjev. (2012) Dispersion of Carbon Nanotubes: Mixing, Sonication, Stabilization, and Composite Properties. *Polymers 4*, 275-295.

137. Huang, Y.Y., T.P.J. Knowles, and E.M. Terentjev. (2009) Strength of Nanotubes, Filaments, and Nanowires From Sonication-Induced Scission. *Advanced Materials 21*, 3945-3948.

138. Lucas, A., C.c. Zakri, M. Maugey, M. Pasquali, P.v.d. Schoot, and P. Poulin. (2009) Kinetics of Nanotube and Microfiber Scission under Sonication. *The Journal of Physical Chemistry C 113*, 20599-20605.

139. Khan, U., A. O'Neill, M. Lotya, S. De, and J.N. Coleman. (2010) High-Concentration Solvent Exfoliation of Graphene. *Small 6*, 864-871.

140. R.H. Burdon, P.H.v.K. and T.S. Paul. *Laboratory Techniques in Biochemistry and Molecular Biology*. Elsevier. 1988

141. Duesberg, G.S., M. Burghard, J. Muster, G. Philipp, and S. Roth. (1998) Seperation of carbon nanotubes by size exclusion chromatography. *Chemical Communications 3*, 435.

142. Flavel, B.S., M.M. Kappes, R. Krupke, and F. Hennrich. (2013) Separation of Single-Walled Carbon Nanotubes by 1-Dodecanol-Mediated Size-Exclusion Chromatography. *ACS Nano 7*, 3557-3564.

143. Duesberg, G.S., J. Muster, V. Krstic, M. Burghard, and S. Roth. (1998) Chromatographic size separation of single-wall carbon nanotubes. *Applied Physics A 67*, 117-119.

144. *Gel Filtration: Principles and Methods*. Amersham Biosciences. 2002

145. *Varian Cary 50 and 4000, 5000, 6000i UV-VIS Specifications.* . Varian.

146. Nicolosi, V., D. Vrbanic, A. Mrzel, J. McCauley, S. O'Flaherty , C. McGuinness, G. Compagnini, D. Mihailovic, W. J. Blau , and J.N. Coleman. (2005) Solubility of $Mo_6S_{4.5}I_{4.5}$ Nanowires in Common Solvents: A Sedimentation Study. *Journal of Physical Chemistry B 109*, 7124.

147. Ohshima, H. *Theory of Colloid and Interfacial Electric Phenomena*. Elsevier. 2006

148. Lotya, M., A. Rakovich, J.F. Donegan, and J.N. Coleman. (2013) Measuring the lateral size of liquid-exfoliated nanosheets with dynamic light scattering. *Nanotechnology 24*, 265703.

149. Tuinstra, F. and J.L. Koenig. (1970) Raman Spectrum of Graphite. *The Journal of Chemical Physics 53*, 1126-1130.

150. Dresselhaus, M.S., G. Dresselhaus, and P.C. Eklund. (1996) Raman Scattering in Fullerenes. *Journal of Raman Spectroscopy 27*, 351-371.

151. Duesberg, G.S., W.J. Blau, H.J. Byrne, J. Muster, M. Burghard, and S. Roth. (1999) Experimental observation of individual single-wall nanotube species by Raman microscopy. *Chemical Physics Letters 310*, 8-14.

152. Alvarez, L., A. Righi, T. Guillard, S. Rols, E. Anglaret, D. Laplaze, and J.-L. Sauvajol. (2000) Resonant Raman study of the structure and electronic properties of single-wall carbon nanotubes. *Chemical Physics Letters 316*, 186-190.

153. Strano, M.S., S.K. Doorn, E.H. Haroz, C. Kittrell, R.H. Hauge, and R.E. Smalley. (2003) Assignment of (n, m) Raman and Optical Features of Metallic Single-Walled Carbon Nanotubes. *Nano Letters 3*, 1091-1096.

154. Dresselhaus, M.S., A. Jorio, M. Hofmann, G. Dresselhaus, and R. Saito. (2010) Perspectives on Carbon Nanotubes and Graphene Raman Spectroscopy. *Nano Letters 10*, 751-758.

155. Graf, D., F. Molitor, K. Ensslin, C. Stampfer, A. Jungen, C. Hierold, and L. Wirtz. (2007) Raman imaging of graphene. *Solid State Communications 143*, 44-46.

156. Malard, L.M., M.A. Pimenta, G. Dresselhaus, and M.S. Dresselhaus. (2009) Raman spectroscopy in graphene. *Physics Reports 473*, 51-87.

157. Ferrari, A. (2007) Raman spectroscopy of graphene and graphite: Disorder, electron–phonon coupling, doping and nonadiabatic effects. *Solid State Communications 143*, 47-57.

158. Lee, Y.-J. (2004) The second order Raman spectroscopy in carbon crystallinity. *Journal of Nuclear Materials 325*, 174-179.

159. Ferrari, A.C., J.C. Meyer, V. Scardaci, C. Casiraghi, M. Lazzeri, F. Mauri, S. Piscanec, D. Jiang, K.S. Novoselov, S. Roth, and A.K. Geim. (2006) Raman Spectrum of Graphene and Graphene Layers. *Physical Review Letters 97*,

160. Casiraghi, C., A. Hartschuh, H. Qian, S. Piscanec, C. Georgi, A. Fasoli, K.S. Novoselov, D.M. Basko, and A.C. Ferrari. (2009) Raman Spectroscopy of Graphene Edges. *Nano Letters 9*, 1433-1441.

161. Graf, D., F. Molitor, K. Ensslin, C. Stampfer, A. Jungen, C. Hierold, and L. Wirtz. (2007) Spatially Resolved Raman Spectroscopy of Single- and Few-Layer Graphene. *Nano Letters 7*, 238-242.

162. Ni, Z.H., T. Yu, Y.H. Lu, Y.Y. Wang, Y.P. Feng, and Z.X. Shen. (2008) Uniaxial Strain on Graphene: Raman Spectroscopy Study and Band-Gap Opening. *ACS Nano 2*, 2301-2305.

163. Yu, T., Z. Ni, C. Du, Y. You, Y. Wang, and Z. Shen. (2008) Raman Mapping Investigation of Graphene on Transparent Flexible Substrate: The Strain Effect. *The Journal of Physical Chemistry C 112*, 12602-12605.

164. Srivastava, I., R.J. Mehta, Z.-Z. Yu, L. Schadler, and N. Koratkar. (2011) Raman study of interfacial load transfer in graphene nanocomposites. *Applied Physics Letters 98*, -.

165. Gong, L., I.A. Kinloch, R.J. Young, I. Riaz, R. Jalil, and K.S. Novoselov. (2010) Interfacial stress transfer in a graphene monolayer nanocomposite. *Adv Mater 22*, 2694-7.

166. Lee, C., H. Yan, L.E. Brus, T.F. Heinz, J. Hone, and S. Ryu. (2010) Anomalous Lattice Vibrations of Singleand Few-Layer MoS2. *ACS Nano 4*, 2695.

167. Molina-Sánchez, A. and L. Wirtz. (2011) Phonons in single-layer and few-layer MoS_{2} and WS_{2}. *Physical Review B 84*, 155413.

168. Li, H., Q. Zhang, C.C.R. Yap, B.K. Tay, T.H.T. Edwin, A. Olivier, and D. Baillargeat. (2012) From Bulk to Monolayer MoS2: Evolution of Raman Scattering. *Advanced Functional Materials 22*, 1385-1390.

169. Williams, D. and C. Carter. *Transmission electron microscopy: a textbook for materialsscience*. Springer. 2009

170. *Electron-matter interactions*. 2013; Available from: http://www.ammrf.org.au/.

171. Coats, A.W. and J.P. Redfern. (1963) Thermogravimetric analysis. A review. *Analyst 88*, 906-924.

172. Geim, A.K. (2009) Graphene: Status and Prospects. *Science 324*, 1530-1534.

173. Bourlinos, A.B., V. Georgakilas, R. Zboril, T.A. Steriotis, A.K. Stubos, and C. Trapalis. (2009) Aqueous-phase exfoliation of graphite in the presence of polyvinylpyrrolidone for the production of water-soluble graphenes. *Solid State Communications 149*, 2172-2176.

174. Hamilton, C.E., J.R. Lomeda, Z. Sun, J.M. Tour, and A.R. Barron. (2009) High-Yield Organic Dispersions of Unfunctionalized Graphene. *Nano Letters 9*, 3460-3462.

175. Green, A.A. and M.C. Hersam. (2009) Solution Phase Production of Graphene with Controlled Thickness via Density Differentiation. *Nano Letters 9*, 4031-4036.

176. Lotya, M., P.J. King, U. Khan, S. De, and J.N. Coleman. (2010) High-Concentration, Surfactant-Stabilized Graphene Dispersions. *ACS Nano 4*, 3155-3162.

177. Wenseleers, W., I.I. Vlasov, E. Goovaerts, E.D. Obraztsova, A.S. Lobach, and A. Bouwen. (2004) Efficient Isolation and Solubilization of Pristine Single-Walled Nanotubes in Bile Salt Micelle. *Advanced Functional Materials 14*, 1105-1112.

178. May, P., U. khan, A. O'Neill, and J.N. Coleman. (2011) Approaching the theoretical limit for reinforcing polymers with graphene. *Carbon*

179. Khan, U., H. Porwal, A. O'Neill, K. Nawaz, P. May, and J.N. Coleman. (2011) Solvent-Exfoliated Graphene at Extremely High Concentration. *Langmuir* 110630105928057.

180. White, B., S. Banerjee, S. O'Brien, N.J. Turro, and I.P. Herman. (2007) Zeta-Potential Measurements of Surfactant-Wrapped Individual Single-Walled Carbon Nanotubes. *The Journal of Physical Chemistry C 111*, 13684-13690.

181. Hamaker, H.C. (1937) The London-van der Waals attraction between spherical particles *Physica 4*, 1058-1072.

182. Ruoff, R. (2008) Graphene: Calling all chemists. *Nature Nanotechnology 3*, 10-11.

183. Smith, R.J., M. Lotya, and J.N. Coleman. (2010) The importance of repulsive potential barriers for the dispersion of graphene using surfactants. *New Journal of Physics 12*, 125008.

184. O'Neill, A., U. Khan, P.N. Nirmalraj, J. Boland, and J.N. Coleman. (2011) Graphene Dispersion and Exfoliation in Low Boiling Point Solvents. *The Journal of Physical Chemistry C 115*, 5422-5428.

185. Osada, M. and T. Sasaki. (2009) Exfoliated oxide nanosheets: new solution to nanoelectronics. *Journal of Materials Chemistry 19*, 2503.

186. Friend, R.H. and A.D. Yoffe. (1987) Electronic-properties of intercalation complexes of the transition metal dichalcogenides. *Advances in Physics 36*, 95.

187. Tang, X., W. Xie, H. Li, W. Zhao, Q. Zhang, and M. Niino. (2007) Preparation and thermoelectric transport properties of high-performance p-type Bi[sub 2]Te[sub 3] with layered nanostructure. *Applied Physics Letters 90*, 012102.

188. Radisavljevic, B., A. Radenovic, J. Brivio, V. Giacometti, and A. Kis. (2011) Single-layer MoS2 transistors. *Nat Nanotechnol 6*, 147-50.

189. Dresselhaus, M.S., G. Chen, M.Y. Tang, R.G. Yang, H. Lee, D.Z. Wang, Z.F. Ren, J.P. Fleurial, and P. Gogna. (2007) New Directions for Low-Dimensional Thermoelectric Materials. *Advanced Materials 19*, 1043-1053.

190. Soon, J.M. and K.P. Loh. (2007) Electrochemical Double-Layer Capacitance of MoS[sub 2] Nanowall Films. *Electrochemical and Solid-State Letters 10*, A250.

191. Feng, C., J. Ma, H. Li, R. Zeng, Z. Guo, and H. Liu. (2009) Synthesis of molybdenum disulfide (MoS2) for lithium ion battery applications. *Materials Research Bulletin 44*, 1811-1815.

192. Lin, Y., T.V. Williams, and J. W. Connell (2010) Soluble, Exfoliated Hexagonal Boron Nitride Nanosheets. *The Journal of Physical Chemistry Letters 1*, 227.

193. Warner, J.H., M.H. Rummeli, A. Bachmatiuk, and B. Buchner. (2010) Atomic resolution imaging and topography of boron nitride sheets produced by chemical exfoliation. *ACS Nano 4*, 1229.

194. Lin, Y., T.V. Williams, T.-B. Xu, W. Cao, H.E. Elsayed-Ali, and J.W. Connell. (2011) Aqueous Dispersions of Few-Layered and Monolayered Hexagonal Boron Nitride Nanosheets from Sonication-Assisted Hydrolysis: Critical Role of Water. *The Journal of Physical Chemistry C 115*, 2679-2685.

195. C. F. Bohren, D.R.H. *Absorption and Scattering of Light by Small Particles.* 1998

196. He, G.S., H.-Y. Qin, and Q. Zheng. (2009) Rayleigh, Mie, and Tyndall scatterings of polystyrene microspheres in water: Wavelength, size, and angle dependences. *Journal of Applied Physics 105*, 023110.

197. Fuhr, J.D., J.O. Sofo, and A. Saul. (1999) Adsorption of Pd on MoS2: Ab initio electronic-structure calculations. *Physical Review B 60*, 8313.

198. Jiménez Sandoval, S., D. Yang, R. Frindt, and J. Irwin. (1991) Raman study and lattice dynamics of single molecular layers of MoS2. *Physical Review B 44*, 3955-3962.

199. Lavik, M.T. and G.D. Moore. (1967) Oxidation data for MoS2 WS2 WSe2 TaS2 and TaSe2 by thermogravimetric analysis. *Lubrication Engineering 23*, 224.

200. Du, G., Z. Guo, S. Wang, R. Zeng, Z. Chen, and H. Liu. (2010) Superior stability and high capacity of restacked molybdenum disulfide as anode material for lithium ion batteries. *Chem Commun (Camb) 46*, 1106-8.

201. Xiao, J., D. Choi, L. Cosimbescu, P. Koech, J. Liu, and J.P. Lemmon. (2010) Exfoliated MoS2Nanocomposite as an Anode Material for Lithium Ion Batteries. *Chemistry of Materials 22*, 4522-4524.

202. Khan, U., P. May, A. O'Neill, A.P. Bell, E. Boussac, A. Martin, J. Semple, and J.N. Coleman. (2013) Polymer reinforcement using liquid-exfoliated boron nitride nanosheets. *Nanoscale 5*, 581-7.

203. Cheng, F., J. Shen, B. Peng, Y. Pan, Z. Tao, and J. Chen. (2011) Rapid room-temperature synthesis of nanocrystalline spinels as oxygen reduction and evolution electrocatalysts. *Nat Chem 3*, 79-84.

204. Kudo, A. and Y. Miseki. (2009) Heterogeneous photocatalyst materials for water splitting. *Chem Soc Rev 38*, 253-78.

205. Kim, G., C. Jo, W. Kim, J. Chun, S. Yoon, J. Lee, and W. Choi. (2013) TiO2 nanodisks designed for Li-ion batteries: a novel strategy for obtaining an ultrathin and high surface area anode material at the ice interface. *Energy & Environmental Science 6*, 2932.

206. Lin, C.-K., K.-H. Chuang, C.-Y. Lin, C.-Y. Tsay, and C.-Y. Chen. (2007) Manganese oxide films prepared by sol–gel process for supercapacitor application. *Surface and Coatings Technology 202*, 1272-1276.

207. Nam, K.-W. and K.-B. Kim. (2006) Manganese Oxide Film Electrodes Prepared by Electrostatic Spray Deposition for Electrochemical Capacitors. *Journal of The Electrochemical Society 153*, A81.

208. Liu, Z.-h., K. Ooi, H. Kanoh, W.-p. Tang, and T. Tomida. (2000) Swelling and Delamination Behaviors of Birnessite-Type Manganese Oxide by Intercalation of Tetraalkylammonium Ions. *Langmuir 16*, 4154-4164.

209. Nam, K.-W., C.-W. Lee, X.-Q. Yang, B.W. Cho, W.-S. Yoon, and K.-B. Kim. (2009) Electrodeposited manganese oxides on three-dimensional carbon nanotube substrate: Supercapacitive behaviour in aqueous and organic electrolytes. *Journal of Power Sources 188*, 323-331.

210. Cross, A., A. Morel, A. Cormie, T. Hollenkamp, and S. Donne. (2011) Enhanced manganese dioxide supercapacitor electrodes produced by electrodeposition. *Journal of Power Sources 196*, 7847-7853.

211. Babakhani, B. and D.G. Ivey. (2011) Effect of electrodeposition conditions on the electrochemical capacitive behavior of synthesized manganese oxide electrodes. *Journal of Power Sources 196*, 10762-10774.

212. Wang, L.O., Y. (2003) Fabrication and Characterization of Multilayer Ultrathin Films of Exfoliated MnO2 Nanosheets and Polycations. *Chem. Matter 15*, 28732878.

213. Kapteijn, F., A.D. Vanlangeveld, J.A. Moulijn, A. Andreini, M.A. Vuurman, A.M. Turek, J.M. Jehng, and I.E. Wachs. (1994) Alumina-Supported Manganese Oxide Catalysts: I. Characterization: Effect of Precursor and Loading. *Journal of Catalysis 150*, 94-104.

214. Julien, C.M., M. Massot, and C. Poinsignon. (2004) Lattice vibrations of manganese oxides: Part I. Periodic structures. *Spectrochimica Acta Part A: Molecular and Biomolecular Spectroscopy 60*, 689-700.

215. Julien, C., M. Massot, R. Baddour-Hadjean, S. Franger, S. Bach, and J.P. Pereira-Ramos. (2003) Raman spectra of birnessite manganese dioxides. *Solid State Ionics 159*, 345-356.

216. Buciuman, F., F. Patcas, R. Craciun, and D. R. T. Zahn. (1999) Vibrational spectroscopy of bulk and supported manganese oxides. *Physical Chemistry Chemical Physics 1*, 185-190.

217. Julien, C. (2003) Raman spectra of birnessite manganese dioxides. *Solid State Ionics 159*, 345-356.

218. Xia, H., M.O. Lai, and L. Lu. (2011) Nanostructured Manganese Oxide Thin Films as Electrode Material for Supercapacitors. *Journal of Minerals, Metals and Materials Society 63*, 54-56.

219. Khan, U., A. O'Neill, H. Porwal, P. May, K. Nawaz, and J.N. Coleman. (2012) Size selection of dispersed, exfoliated graphene flakes by controlled centrifugation. *Carbon 50*, 470-475.

220. O'Neill, A., U. Khan, and J.N. Coleman. (2012) Preparation of High Concentration Dispersions of Exfoliated MoS2with Increased Flake Size. *Chemistry of Materials 24*, 2414-2421.

221. Fagan, J.A., M.L. Becker, J. Chun, and E.K. Hobbie. (2008) Length Fractionation of Carbon Nanotubes Using Centrifugation. *Advanced Materials 20*, 1609-1613.

222. Fagan, J.A., M.L. Becker, J. Chun, P. Nie, B.J. Bauer, J.R. Simpson, A. Hight-Walker, and E.K. Hobbie. (2008) Centrifugal Length Separation of Carbon Nanotubes. *Langmuir 24*, 13880-13889.

223. Sun, X., D. Luo, J. Liu, and D.G. Evans. (2010) Monodisperse Chemically Modified Graphene Obtained by Density Gradient Ultracentrifugal Rate Separation. *ACS Nano 4*, 3381-3389.

224. Merki, D., S. Fierro, H. Vrubel, and X. Hu. (2011) Amorphous molybdenum sulfide films as catalysts for electrochemical hydrogen production in water. *Chemical Science 2*, 1262.

225. Jaramillo, T.F., K.P. Jorgensen, J. Bonde, J.H. Nielsen, S. Horch, and I. Chorkendorff. (2007) Identification of active edge sites for electrochemical H2 evolution from MoS2 nanocatalysts. *Science 317*, 100-2.

226. Lukowski, M.A., A.S. Daniel, F. Meng, A. Forticaux, L. Li, and S. Jin. (2013) Enhanced hydrogen evolution catalysis from chemically exfoliated metallic MoS2 nanosheets. *J Am Chem Soc 135*, 10274-7.

227. Xiang, Q., J. Yu, and M. Jaroniec. (2012) Synergetic effect of MoS2 and graphene as cocatalysts for enhanced photocatalytic H2 production activity of TiO2 nanoparticles. *J Am Chem Soc 134*, 6575-8.

228. Zhou, W., Z. Yin, Y. Du, X. Huang, Z. Zeng, Z. Fan, H. Liu, J. Wang, and H. Zhang. (2013) Synthesis of few-layer MoS2 nanosheet-coated TiO2 nanobelt heterostructures for enhanced photocatalytic activities. *Small 9*, 140-7.

229. Jurewicz, I., P. Worajittiphon, A.A. King, P.J. Sellin, J.L. Keddie, and A.B. Dalton. (2011) Locking carbon nanotubes in confined lattice geometries--a route to low percolation in conducting composites. *J Phys Chem B 115*, 6395-400.

230. Jurewicz, I., J.L. Keddie, and A.B. Dalton. (2012) Importance of capillary forces in the assembly of carbon nanotubes in a polymer colloid lattice. *Langmuir 28*, 8266-74.

231. Qian, L., A. Ahmed, A. Foster, S.P. Rannard, A.I. Cooper, and H. Zhang. (2009) Systematic tuning of pore morphologies and pore volumes in macroporous materials by freezing. *Journal of Materials Chemistry 19*, 5212.

232. Lau, C., M.J. Cooney, and P. Atanassov. (2008) Conductive Macroporous Composite Chitosan–Carbon Nanotube Scaffolds. *Langmuir 24*, 7004-7010.

233. Tkalya, E., M. Ghislandi, A. Alekseev, C. Koning, and J. Loos. (2010) Latex-based concept for the preparation of graphene-based polymer nanocomposites. *Journal of Materials Chemistry 20*, 3035.